Linear Digital Ion Trap Mass Spectrometry
and its Application for Cryogenic Ion Spectroscopy

By

Casey J. Howdieshell

A dissertation submitted in partial fulfillment of
the requirements for the degree of

Doctor of Philosophy
(Chemistry)

at the
UNIVERSITY OF WISCONSIN- MADISON
2021

Date of final oral examination: 05/07/2021

The dissertation is approved by the following members of the Final Oral Committee:

Etienne Garand, Professor, Chemistry

Timothy H. Bertram, Professor, Chemistry

Lloyd M. Smith, Professor, Chemistry

John C. Wright, Professor, Chemistry

Abstract

LINEAR DIGITAL ION TRAP MASS SPECTROMETRY

AND ITS APPLICATION FOR CRYOGENIC ION SPECTROSCOPY

Casey J. Howdieshell

Under the supervision of Professor Etienne Garand

At the University of Wisconsin-Madison

Cryogenic Ion Spectroscopy (CIS) is an established field of research centered around the collection of highly resolved spectroscopic data for molecules of interest. Said molecules are ionized through various means, contained in the gas phase by electric fields, collisionally cooled with an inert buffer gas, then struck with varying wavelengths of light to produce an observable phenomenon that can elucidate structural information relating to the original analyte. Typical methodologies for these experiments utilize Time-of-Flight Mass Spectrometry (TOF-MS), which while effective, offers minimal selectivity of ions prior to an ion-laser interaction. This, coupled with the spatial constraints of an ever-growing lab, have led to development of a smaller, more robust instrument, affectionately named "QTPI".

QTPI utilizes a compact Linear Digital Ion Trap (LDIT) operated by square waveforms. The manipulation of these waveforms facilitates sequential radial ejection of increasing ion mass by means of a stepped frequency sweep. This functionality allows for a direct replacement to TOF-MS based mass analysis. Prior to mass analysis, the applied square wave frequency and duty cycle can be tailored such that isolating a sub-set of the total population of masses present in the LDIT is possible. Future introduction of preexisting cryostat and laser systems will allow for CIS experiments. Additionally, complex square waveforms consisting of multiple frequencies can be applied to the LDIT to selectively exclude any undesired ions prior to mass analysis, facilitating future CIS studies involving complex ion species.

Additional to the instrumentation developed, two ion manipulation techniques also utilizing square waveforms have been development. These techniques allow for the mass isolation or mass exclusion of any ion population present in a digital ion trap (DIT). The function and application of these techniques are shown throughout this thesis. Immediate and future ion chemical reaction schemes only possible through the use of per cryogenic ion trap ion manipulation is also presented here.

Table of Contents

List of Figures

Acknowledgements

The amount of people who have facilitated the generation of this thesis is enormous. Thank you to Dr. Darrin Smith, my undergraduate advisor, whose class on Mass Spectrometry first sparked my interest in the analytical tool. Second, to Etienne for providing me with a sandbox of vacuum pump oil, an electronics inventory reminiscent of a 1990’s Radioshack, and at least half of the Kurt Lesker catalog. A very big thank you to Dr. Pete Reilly and Dr. Nathan Hoffman for providing the needed circuit designs for successful square wave integration, I do not think this project would have gotten off the ground without you two. To Dr. Martha Vestling and Dr. Lloyd Smith for their donations of respective MALDI-TOF and Thermo LCQ instrumentation, of which critical QTPI components were harvested. A very big thank you to machine shop crew, Steve Meyers, James Mullarkey, Kendall Schneider, and Matt Martin for all of the help fabricating items in a timely manner, advising me on CAD design, and helping me fabricate parts under supervision. Working with the four of you has really sparked an interest in CAD design and fabrication. An additional thanks to Matt for quite frankly performing miracles on mechanical pumps that are older than I am. Thanks to Blaise Thomson for being a good friend, collaborator, and for introducing me to an area of employment I would have never thought of. To all of you this project would have never been completed, and for that you have my eternal gratitude.

On a personal level, the people of the Garand group have facilitated my education, provided needed emotional support, and frankly dragged me through the rough patches of graduate school. Jon Voss and Steve Kregel, you two were like the big brothers I never had. Jon you taught me so much about how to value myself, keep a positive outlook, and you are one of the best people I have ever had the pleasure of meeting. Steve, despite your curmudgeon exterior you really are a caring person. Thank you for teaching me basically everything I know about how to build both software and hardware. You were a great mentor, and you are a great friend. Kaitlyn and Darien, thank you for always being down to disc golf

or play board games, and thanks for carrying me through John’s spectroscopy class. To the “old guard” of the Garand group, thanks for all of the great memories, the degree is nice, but the time spent with you all is really what I am happy to take away from graduate school.

And to the new guard, to Cole and Summer, thanks for being good friends and forcing me to socialize when I otherwise did not want to. I wish I could have been to you what Jon and Steve were to me. Cole, thanks for all of the late night super smash sessions in the office, for following me down the rabbit hole of “enthusiast” coffee, and I am sorry I got you into my expensive PC gaming hobbies. Summer thanks for answer all of my stupid questions that I was too lazy to look up, but I knew you had the answer. And thanks for all of the dog advice, Maple appreciates it! To both of you, thanks for always being there to talk when I was frustrated and needed to vent, this past year has been difficult, and I am not sure I would have made it without you two. To Gina and Kathy, thank you for challenging the status quo of the group when it needed it most. You both have a level of enthusiasm for the work you are doing that makes me glad to see. Gina, thank you for listening to the ramblings of a madman when it came to square waves and Mathieu equations. I am glad you wrote some of it down!

Next, I would like to thank the people who mean the world to me, my family. Mom and Popps thank you so much for everything you have done these past 29 years. You gave me a stable home, encouraged me to push myself academically, provided a means for me to attend higher education and believed in me every step of the way. I am sorry for how distant I have been these past six years. To Jo and Dale, thank you for being my in-person parent substitutes, you both have given me some great live advice and a nice place to call home away from home.

Last but certainly not least, I would like to thank my wife, Lyndsey. You are my world, and if it were not for meeting you I can all but guarantee I would not be writing thesis. You have seen me at rock bottom and dragged me, sometimes kicking and screaming, to push through it. You make the highs feel like mountaintops and the lows feel like flat plains. You mean more to me than you will ever know. You have done so much to help me through this that if I could, I would gladly write your name alongside mine on this thesis and this degree. You are the only person aside from myself that I definitely know has actually read this document all the way through! I cannot wait for what comes next for us, but more importantly I cannot wait to tackle it together, with you. I love you.

Chapter 1 Introduction

Section 1.1 The Need for Molecular Characterization

There is an ever present need to accurately characterize otherwise unknown samples on a molecular level. From impurity identification in petroleum refining processes[1] to pharmaceutical product characterization of compounds for drug development,[2] the vast majority of analytical chemistry exists to better characterize observable chemical systems. Many approaches for doing so are available. For example, Tandem Mass Spectroscopy (MS^n) ionizes an analyte of interest and sequentially fragments sub-structures into observable ion species.[3] Ion Mobility Spectrometry (IMS) provides collisional cross-section data used to correlate molecular modelling of large chemical structures.[4] Nuclear Magnetic Resonance (NMR) observes perturbations of local magnetic fields, which can be correlated to adjacent functional groups present in a sample. A major limitation to the above methods is the scale of characterization information obtained. Fragment ions in MS^n only yield mass-to-charge (m/z) values of whole functional groups. IMS only provides an elution time based overall shape, and NMR only probes atoms with appropriate spin states. Overall, none of these methods have the capacity to determine discrete bonding interactions within an analyte to use for molecular characterization. Infrared spectroscopy is a tool that can address this problem.

Every bond in a molecule of interest between two atoms can oscillate at some frequency that is dependent on the relative masses of the bonded atoms. Additionally, the local environments surrounding the atoms perturb these oscillations. By striking the molecules with a wavelength of infrared light resonant with one of these oscillations, absorption occurs. This absorption can be detected and correlated to elucidate per-bond molecular characterization in the original sample. Typically, these spectroscopic interrogations are done at room temperature and utilize liquid or solid samples. Boltzmann distributions of energy states for room temperature samples and the sheer density of molecules in the condensed phase make accurately identifying key structural properties of analytes difficult. Transitioning molecules of interest to the gas phase alleviates the sample density and cryogenically cooling these ions minimizes the energy state distribution of samples present. To further this compound the sampling capacity, Mass Spectrometry (MS) is separate molecules in the original sample based on their mass-to-charge ratios. By coupling MS with Infrared Spectroscopy (MS-IR), both high resolution IR spectrum of small analyte concentration can be attained in a technique termed Cryogenic Ion Spectroscopy (CIS).

Section 1.2 Cryogenic Ion Spectroscopy

Typical commercial spectroscopic instruments are designed with rapidity, robustness, ease of sample introduction, and ease of interpretation in mind. What these instruments sacrifice by doing so, however, is spectral resolution and experimental complexity. Recent instrumental developments have addressed these limitations by transitioning analytes to the gas phase from either solid or liquid (condensed) phases, ionizing sample molecules to constrain them in 3D space by means of electric fields, bombarding them with cryogenically cooled neutral gas molecules to reduce thermal motion, then subjugating cryogenic ions to variable wavelength lasers, producing extremely well resolved spectroscopic data. By transitioning the analytes to the gas phase, the sampling density of the condensed phase is solved and by cryogenically cooling the gas phase ions, the Boltzmann distribution of energy states is reduced greatly. Additionally, through the use of action spectroscopy, which will be covered below, the power requirements of the variable wavelength lasers is greatly reduced. All of these techniques combine to generate extremely detailed IR spectroscopic data of a gas phase ion which can be correlated to the original sample molecule. These data can be supplemented by theoretical computation to gain accurate structural information of either the original molecule pre-ionization or about ion-neutral chemical reactions performed in the gas phase. CIS has been used recently to characterize reaction intermediates of catalytically driven water oxidation reactions,[5] to monitor structural changes of biologically relevant ions as a function of solvation,[6] to determine the structure of small ammonium bisulfate clusters and the atmospheric impact they have,[7] and many more. **Figure 1.1** illustrates a simplified CIS process from post-ion generation to post-laser interaction, which will be covered below.

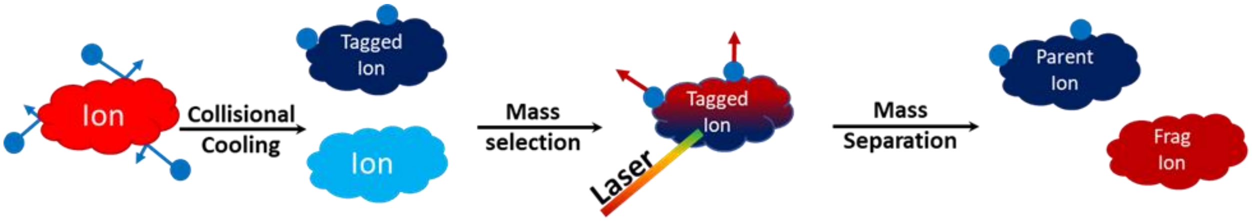

Figure 1.1 Reaction schematic of CIS. Temperature indicates temperature.

Direct measurement of light absorbed by cryogenically cooled ions is incredibly difficult, therefore the use of small, neutrally charged, structurally non-perturbative molecules, such as Helium and molecular Hydrogen (H_2), are more commonly used to perform "action" spectroscopy, which detect laser absorption by an orthogonal means (i.e., m/z abundance for MS-IR). These molecules act as spectroscopic "tags," non-covalently adhering to ions when appropriate temperatures are reached, typically ones to tens of Kelvin.[8] Binding energies of these tags are quite low (≈300-500 cm^{-1}) such that absorption from a single photon (e.g., 600-4000 cm^{-1} in the IR range) is capable of disrupting the adherence, thus providing minimal power requirements of tunable wavelength lasers used. This absorption causes an increase in internal energy until the tagged ion's temperature is above the spectroscopic tag's condensation temperature, thus causing a dissociation of the tag and now "hot" ions (dark red in **Figure 1.1**). This warming effect only occurs when the wavelength of light used resonates with an optical transition (i.e., vibrational or electronic state). Thus, by repeating this process of ionization, collisional cooling and tagging, then variable wavelength ion-laser interactions, a production of high-resolution spectroscopic data occurs.

To accomplish this spectroscopic tagging, a buffer gas seeded with small concentrations of these tags is introduced into a structure whose function is to spatially confine ions, called an ion trap. Once generated, ions (light red in **Figure 1.1**) are restricted in ion traps by electric fields from metal electrodes. By using an external cryogenic refrigerant, these electrodes can be cooled to temperatures less than 30 Kelvin. Upon multiple gas-electrode collisions, the introduced gas mixture containing the spectroscopic tags approach their condensation temperature. The now cold gas mixture cryogenically cools ions inside the ion trap by means of multiple ion-neutral inelastic collisions. Upon reaching favorably cold temperatures, a non-covalent attraction occurs between the cold ion (light blue in **Figure 1.1**) and spectroscopic tag, creating complex ion populations of cold-but-never-tagged ions and tagged ions (dark blue in **Figure 1.1**) in the ion trap.

Two major problems arise from this methodology. First, there is a need to detect the presence and amount of an ion population that has lost its tag by means of an ion-laser interaction, called a “de-tagged” ion. Mass Spectrometry (MS) is an analytical tool specifically designed for this application. Diverse in its methods,[9–13] the goal of any mass spectrometer is to take a collection of ions with different mass-to-charge ratios (m/z) and separate from lower m/z to higher m/z, producing a mass spectrum. Indirect detection of light absorbed is achieved by monitoring the de-tagged mass channel as a function of laser wavelength. As the laser wavelength is moved to resonant frequencies, the population of the tagged species will decrease, and the de-tagged species will increase.

The second problem, when using MS, is that the post-laser de-tagged ion and never-tagged ion species have the same m/z. This can be solved via two separate methods. The first is to monitor the loss of amplitude of the tagged mass channel and/or the additional amplitude of the de-tagged/never-tagged mass channel as a function of laser wavelength. Sample instability of generated ions across the many instrument cycles needed for spectroscopic data collection makes this method non-ideal. The second involves removing the entirety of the never-tagged ion species prior to mass analysis. If accomplished, only the de-tagged species would be present in the never-tagged/de-tagged mass channel at the laser interaction, thus allowing for the monitor of only the de-tagged ion species. This pre-laser mass filtering allows for de-tagged ion amplitude vs. wavelength data collection independent of sampling fluctuations. **Figure 1.2**[14] illustrates a typical workflow from post-collision cooling to spectroscopic data collection utilizing this method. In lieu of H_2, molecular Deuterium (D_2) is used to further separate the tagged species due to the mass spectrometer's ability to resolve peaks. By first removing any ions of lower m/z than the $[M^+ \cdot (D_2)_2]$ species, de-tagged ion amplitude vs. wavelength that is free of source instability is achieved. The result is high resolution spectroscopic data that can be directly compared to computational models to confidently identify and characterize structural phenomenon in the original sample.

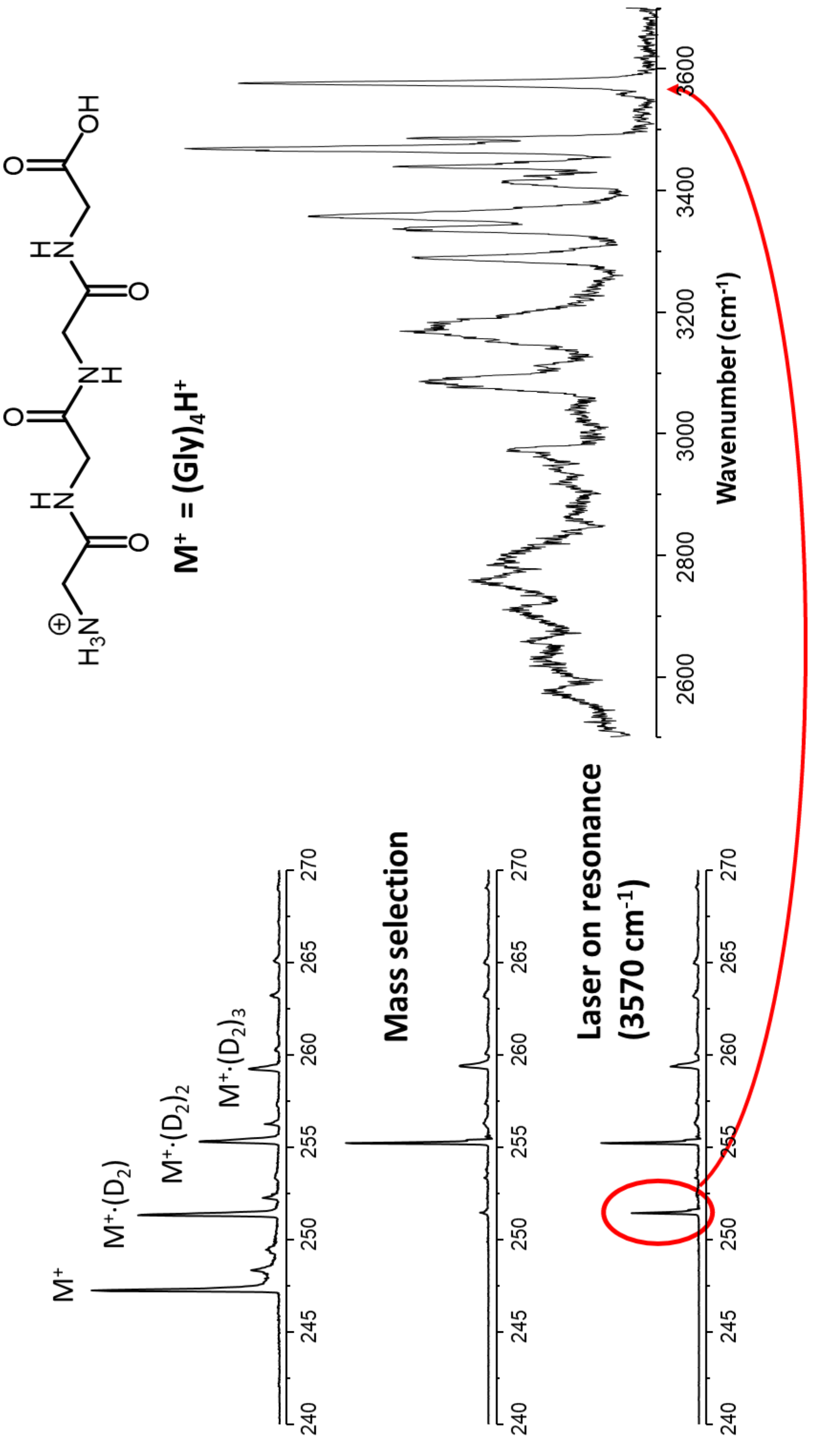

Figure 1.2 CIS workflow utilizing MS-IR with a mass separation step.

Section 1.3 Time-of-Flight Mass Analyzers and Their Limitations

A collection of different m/z populations can be mass analyzed in several methods. The most common mass analyzer for CIS is time-of-flight (TOF), or TOF-MS.[15–19] Briefly, ions are confined into a small volume structure by means of electric fields and given equal kinetic energy via an instantaneous voltage difference (≈ 500 V). Once kinetically energized, ions drift through a straight tube held at an extremely low ($< 10^{-7}$ Torr) vacuum to minimize stray gas collisions which would perturb ion direction and velocity. Small changes of m/z lead to differing velocities as ions traverse the drift tube, separating ion species of differing m/z in time. A detector is located at the end of the flight path which measures ion current as each packet reaches its destination. Lower m/z ions will arrive at the detector first, and higher m/z later. In some instances, a reflectron can be added post-drift tube to temporally refocus ion packets and extend the flight path for increased resolving power.[20,21] For a mathematical derivation of TOF-MS analysis, see Mamyrin,[22] as it is out of the scope of this thesis.

Figure 1.3 illustrates a Computer Assisted Drawing (CAD) of currently used TOF-MS in the Garand lab for CIS data acquisition. The cryogenic ion trap (CIT, red box in figure) both accumulates ions and provides a structure for cryogenic cooling of ions generated upstream (not shown). By means of an instantaneous voltage difference between the two red electrodes, the CIT also acts as the starting location of the TOF-MS. Post excitation, ions are radially focused into a beam by means of an Einzel lens[23], which helps correct stray ion velocity vectors. A zoom-in of the post-CIT Einzel lens can be shown in the grey box. Mass selection occurs at the mass gate (orange), also in the grey box, via a precisely timed voltage drop. At this stage, initial m/z separation has occurred. By applying a dramatically different voltage at a precise time and for a precise duration, the never-tagged ion population can be given a terminal velocity vector, thus achieving mass filtration. Post-filtration laser interaction occurs at the denoted region (green circle) in **Figure 1.3**. When the wavelength of light is resonant with some optical transition of the tagged ion species, thermal energy of the ion increases until the spectroscopic tag is dissociated from the ion. Tagged and de-tagged ions will be separated temporally due to now differing masses as they continue through the flight tube. A second Einzel lens again radially focuses into a beam prior to a reflectron chamber. This reflectron, which consists of multiple plates with an applied voltage gradient by means of a resistor network, redirects ion flight paths for additional separation, until they are finally detected by a detector (not shown).

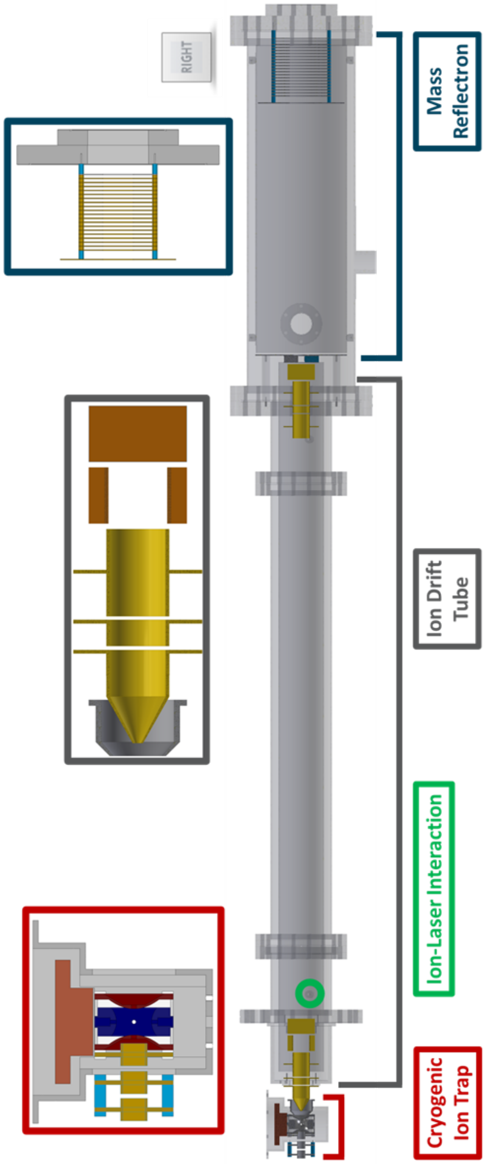

Figure 1.3 CAD of TOF-MS-IR used for current CIS experiments.

There are notable benefits of TOF-MS based mass analyzers with regards to CIS data collection. For example, TOF-MS offers resolving power for +4 change of mass that occurs from the common spectroscopic tag D_2, even for multiply charged species where the change in m/z is reduced[24]. In addition, the mass gate provides a simple, yet easy “guess-and-check” method for the necessary pre-laser mass filtration. Using commercial equipment (Jordan TOF), it is possible to operate the cryogenic ion trap as both an accumulation stage and provide the high voltage difference to needed for adequate kinetic energizing.

Drawbacks and practical limitations to TOF-MS do exist, however. First, the drift tube and reflectron structures require large, cumbersome vacuum components, making additional instrumentation costly and limiting the number of dedicated instruments a research lab can house. Second, extremely low-pressure regions are required for both drift tube and reflectron stages, necessitating high throughput vacuum solutions which again can be costly for future lab expansions. Third, several deflector optics, reflector plates, and Einzel lens voltages make ion beam alignment and optimization tedious when changing to new mass ranges. Precise timing is needed to accurately mass filter differences of +4 amu needed for pre-laser interactions. This is further complicated by the fact that mass filtration occurring during mass analysis, near the beginning of ion flight time where separation of masses is minimal. Orienting the mass gate delay and duration too close to the tagged species can induce some degradation of temporal resolving power due to ions observing the change of voltage. Laser alignment itself can be arduous as ion flight paths can be imperfectly aligned and visual inspection of ion-laser alignment is not possible. Monitoring beam width, alignment, power, etc. can be difficult to optimize due to the focal point of the laser being inside the vacuum chamber.

Most pertinent to the work presented, however, is the lack of control of ions present while inside the CIT, and a desire for an ion manipulation prior to mass analysis, instead during mass analysis. If this mass filtration were accomplished upstream in the CIS instrumentation, complex reaction chemistry prior to the laser interaction would be achievable. By performing the mass filtration during ion flight time, no modifications can be made to filtered ion populations prior to detection. There is a growing need for multi-staged gas phase reaction chemistry studies to probe further catalytic reaction intermediates and to observe complex solvation environments in the gas phase. These studies are not possible due to location of the mass separation stage. Recently, by expanding instrumentation to house more CITs,[25] some complex ions systems of interest, including the preliminary ion solvation and catalytic intermediate studies mentioned above, have been achieved. However, the functionality required for future complex systems would require an unrealistic number of CITs. If instead the manipulation of ion species present in individual CITs could be tailored by mass filtration, further instrument expansion would not be necessary. This desire for in-trap ion manipulation, as well as a need for future compact instrumentation has led to studies into alternative mass analyzers capable of replicating cryogenic cooling, mass filtration, and facilitating ion-laser interactions needed for CIS in a single ion trap.

Section 1.4 Radial Ejection Linear Quadrupole Mass Spectrometry

In addition to TOF-MS, several mass analyzer solutions exist. For the sake of brevity, this thesis will be limited to quadrupole ion trap (QIT) mass analyzers. For an overview of other types of mass analyzers, see Haag.[9] The primary difference between QIT-MS and TOF-MS can be distilled to size and separation mechanism. Rather than cumbersome flight tube and reflectron housings, QIT-MS instead relies on housing ions in a single small volume (< 300 cm^3) ion trap. Both periodic (AC) and static (DC) voltages are used to coerce ions into a stable equilibrium of motion within the trap. Manipulating AC and DC voltages can incrementally excite ions of differing m/z until the excitation force is greater than the confining force of the QIT, leading to ion displacement from the trap at a predefined exit hole. A more detailed explanation for ion motion in a QIT-MS will be given in **Chapter 2**.

There are, broadly speaking, two types of quadrupole shapes available for mass selective QIT-MS: cylindrical and linear. The cylindrical ion trap, or Paul Trap, originally invented by Wolfgang Paul,[26] is comprised of one central ring electrode and two endcap electrodes, as shown in **Figure 1.4**. The overall shape of the device is a cylinder, where the ring electrode confines ions in the radial direction and the endcap electrodes confine ions in the height, or axial, direction. Small diameter holes are present in both endcap electrodes, serving as the ion introduction and departure sites. By manipulating the electric fields present in both the ring and endcaps, it is possible to sequentially eject ions from the exit hole to then strike a detector.

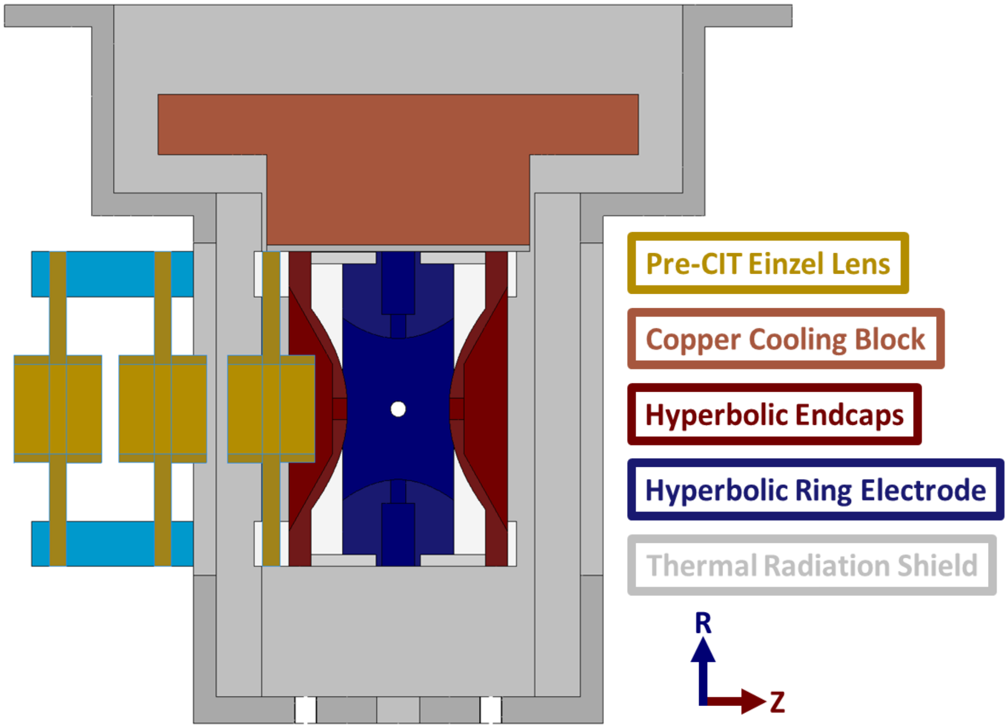

Figure 1.4 CAD of currently used cylindrical ion trap for CIS.

Though not mass selective, this structure already exists in current CIS instrumentation (see **Figure 1.3**, cryogenic ion trap section). The problem with this design, with respect to CIS, arises from low trapping efficiencies and low ion storage capability.[27] These storage inefficiencies are solved by linear quadrupole ion traps (LQITs). By extruding the hyperbolic profile along the Z-axis, the internal volume can be changed from a spherical shape to a cylindrical shape, thus increasing the trapping and storage capacity tenfold, as reported by Schwartz, Senko and Syka.[28] Both cylindrical and linear QITs utilize hyperbolic cross sections to produce quadrupolar electric fields needed for ion confinement. In LQITs, the hyperbolic profile is extruded the entire length of the ion trap, as originally described by Church in 1969.[29] As ions enter the LQIT, two oppositely phased AC signals are applied to each electrode pair (X-axis and Y-axis) which act to repel ions from the current pair, then attract them to the adjacent electrode pair. As ions travel from one electrode to another, the magnitude of the AC signal is switched, causing deflection to the original ion direction. This periodic repulsion and attraction cause an equilibrium of motion which radially confines ions. Axial confinement is achieved by means of two metal endcaps are located at both ends of the LQIT. **Figure 1.5** shows two CADs of the LQIT used throughout this thesis. The planar endcaps are omitted for the sake of visualization, and the red/blue coloration represented the two phases of AC signal applied. A small rectangular slit was milled out of one horizontal electrode so that as the kinetic energy of ions in the X-axis exceeds the confining forces generated by the electrostatic fields, radial ejection occurs during AC and DC manipulation. A more detailed account of the dimensions, hyperbolic curve, and other properties can be found in **Chapter 3**.

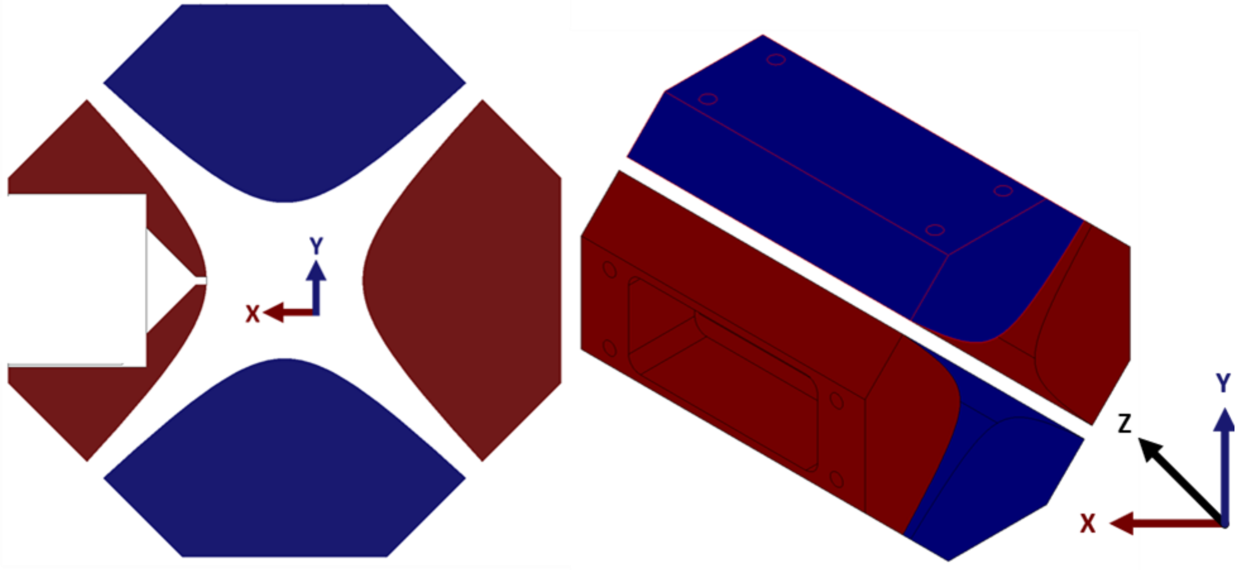

Figure 1.5 CAD of LQIT used throughout this thesis.

LQIT are not without complications, however. Compared to TOF and other modern mass analyzers, radial ejection LQITs tend to have lower resolution, especially for small m/z (< 10,000 m/z).[30] To keep ions continually confined for extended periods of time, hundreds of milliseconds, a comparatively high amount of gas pressure is needed (> 10^{-5} Torr). The instrument cycle, or time between completed mass spectra, is significantly longer than TOF (hundreds of milliseconds vs. hundreds of microseconds). Large amplitude (up to 10 kV), high frequency (1 MHz) AC fields are needed to confine ions within an LQIT's electrodes, which can be costly and dangerous to generate. Finally, due to the need for an external laser system, commercial instrumentation would prove difficult to modify. To this end, a homebuilt instrument utilizing LQIT-MS instrument was planned to assess the viability of this mass analyzers for CIS integration.

Section 1.5 Digitally Driven Quadrupoles

Alternative means of confining ions were explored to address the cost of generating the AC waveform needed to operate a LQIT-MS. As alluded to many times previously, ions require three components to be enclosed in an LQIT for an extended duration: gas, static DC fields, and periodic AC fields. Gas acts as a medium in which kinetic energy is absorbed by means of inelastic collisions. In LQIT-MS, new gas is constantly introduced, while kinetically energized gas becomes evacuated by means of a vacuum pump, thus creating a steady state ion velocity within the ion trap. DC fields axially trap ions entering the LQIT by means of two endcaps which provide a potential well whose depth exerts a force greater than the average kinetic energy of ions in the trap. AC fields keep ions in a stable equilibrium of motion as they move back and forth between electrode pairs as previously discussed.

Originally proposed in 1868 by Émile Mathieu,[31] the mathematical equations that describe ion motion in a periodic field are complex, and an overview of the equations can be found in **Chapter 2**. It was assumed that only sinusoidal waveforms were capable of producing stable ion motion in a QIT. However, throughout the 1970's, several researchers, including Sheretov and Terent'ev,[32] and Richards *et al,*[33] proved stable ion motion in a QIT utilizing any periodic field was possible. Most are largely impractical, but a common alternative to sinusoidal waves are rectangular, or square waves. These consist of two voltage states, HIGH and LOW, that are switched periodically. For a visual reference to each waveform, see **Figure 1.6**.

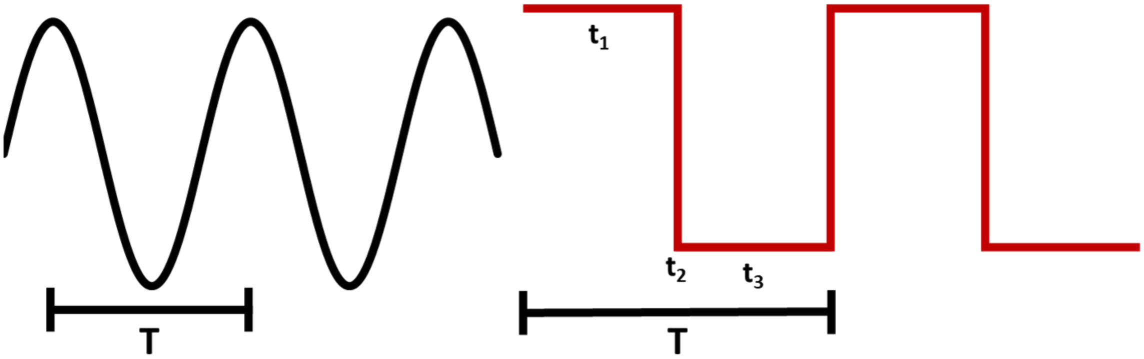

Figure 1.6 Visual representation of sine and square waves.

A distillation of square waves to two voltages and two timings also made their relationship to ion motion much easier to derive and understand. Additionally, square waves offer a user control in both the period, T, and duty cycle, t_1/T, that was not present in existing sine wave operation of QITs, which involve a fixed frequency variable amplitude method for mass analysis. The main impediment to wide-scale implementation of square wave QIT operation in the 1970s was a lack of means for large amplitude square wave generation. Through current Metal Oxide Field Effect Transistors (MOSFETs) and Direct Digital Synthesis (DDS) modules, as well as emerging Field Programmable Gate Arrays (FPGAs) technologies, the ease for the generation and amplification of square waves has re-ignited an interest in square wave based digitally driven quadrupole technology and the ability to use this technology as an alternative waveform to perform QIT mass analysis. In 2004, Ding *et al*[34] demonstrated mass analysis in a "digital" cylindrical ion trap operated solely by square waves. Since then, a few researchers have shown success in digital ion traps and digital ion guides as mass filtration devices.[30,35–38] It was not until very recently that LQIT-MS operating with rectangular fields, termed linear digital ion trap (LDIT) mass spectrometry, was reported.[39,40] How these squares are used to operate an LDIT-MS instrument as both a mass analyzer and provide the mass filtration needed for the complex CIS experiments planned will be outlined in the rest of this thesis.

Section 1.6 Conclusion

With respect to the Garand group and CIS community at large, LDITs offer the promise of affordable LDIT operation and complex methodologies for ion manipulation schemes inside a trap capable radially ejection mass analysis, drastically simplifying existing and future instrumentation machinery and increasing the sample complexity of gas phase ion reaction chemistry. CIS innovations made possible by the work presented in this thesis can be condensed into three areas. The first is the prospect of instrumental miniaturization. By condensing ion mass accumulation, storage, manipulation, and analysis into one structure that occupies less than 300 cm^3, the prospect of multiple instruments performing CIS on varied fields of research becomes significantly more obtainable. Second, the radial ejection nature of LDIT-MS leads to a regime where the laser beam path is parallel instead of perpendicular with ion beams, facilitating an estimated four-fold increase in ion-laser overlap. **Figure 1.7** depicts a top-down CAD schematic of the proposed ion-laser overlap. Note that vertical Y-axis electrodes have be omitted for clarity. Finally, the third major rationale for the work presented is the development of an ion manipulation toolset within a mass selective ion trap. By altering the square waves, their amplitude, shape, and complexity, ion species control within an ion trap can be further expanded from simple mass filtration to dedicated multi-stepped ion manipulation stages. These advances are the building blocks for breakthroughs in complex ion clustering and reaction chemistry, as well as the prospect of a higher throughput spectroscopic data collection workflow.

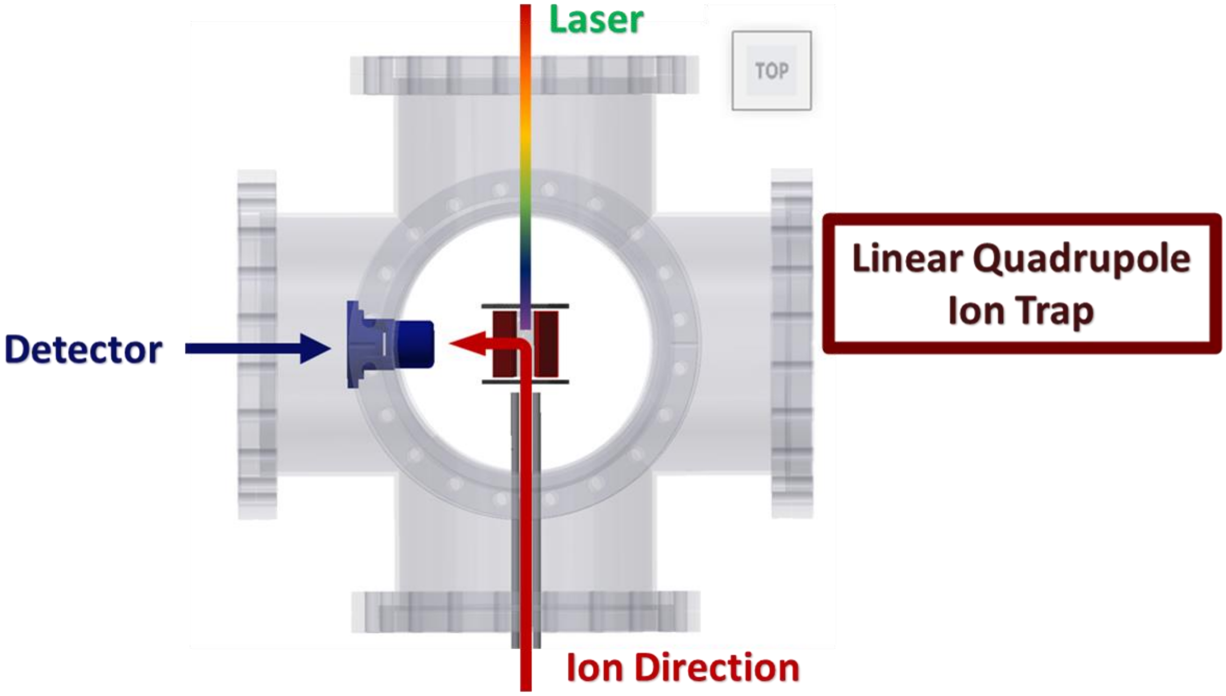

Figure 1.7 CAD of LDIT with laser introduction for CIS.

Section 1.7 References

(1) Han, Y.; Zhang, Y.; Xu, C.; Hsu, C. S. Molecular Characterization of Sulfur-Containing Compounds in Petroleum. *Fuel*. Elsevier Ltd June 1, 2018, pp 144–158. https://doi.org/10.1016/j.fuel.2018.02.110.

(2) Barros-García, F. J.; Bernalte-García, Á.; Cumbrera, F. L.; Lozano-Vila, A. M.; Luna-Giles, F.; Meléndez-Martínez, J. J.; Ortiz, Á. L. Synthesis, Molecular Characterization by Infrared Spectroscopy, and Crystal Structure Determination by X-Ray Powder Diffractometry of [ZnCl 2(TdTz)] [TdTz = 2-(3,4-Dichlorophenyl)Imino-N-(2-Thiazin-2-Yl) Thiazolidine]. *Polyhedron* **2005**, *24* (15), 1975–1982. https://doi.org/10.1016/j.poly.2005.06.003.

(3) Hunt, D. F.; Yates Iii, J. R.; Shabanowitz, J.; Winston, S.; Hauer, C. R. *Protein Sequencing by Tandem*

Mass Spectrometry (Collision-Activated Dissociation/Liquid Secondary-Ion Mass Spectrometry/Apolipoprotein B); 1986; Vol. 83.

(4) Gabelica, V.; Marklund, E. Fundamentals of Ion Mobility Spectrometry. *Current Opinion in Chemical Biology*. Elsevier Ltd February 1, 2018, pp 51–59. https://doi.org/10.1016/j.cbpa.2017.10.022.

(5) Voss, J. M.; Duffy, E. M.; Marsh, B. M.; Garand, E. Mass Spectrometric and Vibrational Characterization of Reaction Intermediates in [Ru(Bpy)(Tpy)(H2O)]2+ Catalyzed Water Oxidation. *Chempluschem* **2017**, *82* (5), 691–694. https://doi.org/10.1002/cplu.201700085.

(6) Fischer, K. C.; Voss, J. M.; Zhou, J.; Garand, E. Probing Solvation-Induced Structural Changes in Conformationally Flexible Peptides: IR Spectroscopy of Gly3H+·(H2O). *J. Phys. Chem. A* **2018**, *122* (41), 8213–8221. https://doi.org/10.1021/acs.jpca.8b07546.

(7) Kreinbihl, J. J.; Frederiks, N. C.; Waller, S. E.; Yang, Y.; Johnson, C. J. Establishing the Structural Motifs Present in Small Ammonium and Aminium Bisulfate Clusters of Relevance to Atmospheric New Particle Formation. *J. Chem. Phys.* **2020**, *153* (3), 034307. https://doi.org/10.1063/5.0015094.

(8) Wolk, A. B.; Leavitt, C. M.; Garand, E.; Johnson, M. A. Cryogenic Ion Chemistry and Spectroscopy. *Acc. Chem. Res.* **2014**, *47* (1), 202–210. https://doi.org/10.1021/ar400125a.

(9) Haag, A. M. Mass Analyzers and Mass Spectrometers. In *Advances in Experimental Medicine and Biology*; Springer New York LLC, 2016; Vol. 919, pp 157–169. https://doi.org/10.1007/978-3-319-41448-5_7.

(10) Ke, M.; Shen, H.; Wang, L.; Luo, S.; Lin, L.; Yang, J.; Tian, R. *Sample Preparation, Analysis and Practical Applications for Mass Spectrometry-Based Proteomics*; 2016; Vol. 919.

(11) Kalli, A.; Smith, G. T.; Sweredoski, M. J.; Hess, S. Evaluation and Optimization of Mass Spectrometric Settings during Data-Dependent Acquisition Mode: Focus on LTQ-Orbitrap Mass Analyzers. **2013**. https://doi.org/10.1021/pr3011588.

(12) Soler, C.; Hamilton, B.; Furey, A.; James, K. J.; Mañes, J.; Picó, Y. Comparison of Four Mass Analyzers for Determining Carbosulfan and Its Metabolites in Citrus by Liquid Chromatography/Mass Spectrometry. *Rapid Commun. Mass Spectrom.* **2006**, *20* (14), 2151–2164. https://doi.org/10.1002/rcm.2561.

(13) Wang, L.; Xu, F.; Ding, C. F. Performance and Geometry Optimization of the Ceramic-Based Rectilinear Ion Traps. *Rapid Commun. Mass Spectrom.* **2012**, *26* (17), 2068–2074. https://doi.org/10.1002/rcm.6308.

(14) Garand, E. Spectroscopy of Reactive Complexes and Solvated Clusters: A Bottom-Up Approach Using Cryogenic Ion Traps. *J. Phys. Chem. A* **2018**, *122* (32), 6479–6490. https://doi.org/10.1021/acs.jpca.8b05712.

(15) Polfer, N. C.; Oomens, J. Vibrational Spectroscopy of Bare and Solvated Ionic Complexes of Biological Relevance. *Mass Spectrom. Rev.* **2009**, *28* (3), 468–494. https://doi.org/10.1002/mas.20215.

(16) Schwarz, H.; Smis, A. A.; Martin, D. Identificationo FActive Sitesa Nd Structural Characterization of Reactive Ionic Intermediates by Cryogenic Ion Trap Vibrational Spectroscopy. **2019**, *25*, 2112–2126. https://doi.org/10.1002/chem.201805836.

(17) Headrick, J. M.; Diken, E. G.; Walters, R. S.; Hammer, N. I.; Christie, R. A.; Cui, J.; Myshakin, E. M.; Duncan, M. A.; Johnson, M. A.; Jordan, K. D. Chemistry: Spectral Signatures of Hydrated Proton

Vibrations in Water Clusters. *Science (80-.).* **2005**, *308* (5729), 1765–1769. https://doi.org/10.1126/science.1113094.

(18) Johnson, C. J.; Wolk, A. B.; Fournier, J. A.; Sullivan, E. N.; Weddle, G. H.; Johnson, M. A. Communication: He-Tagged Vibrational Spectra of the SarGlyH+ and H+(H2O)2,3 Ions: Quantifying Tag Effects in Cryogenic Ion Vibrational Predissociation (CIVP) Spectroscopy. *J. Chem. Phys.* **2014**, *140* (22), 221101. https://doi.org/10.1063/1.4880475.

(19) Johnson, C. J.; Fournier, J. A.; Wolke, C. T.; Johnson, M. A. Ionic Liquids from the Bottom up: Local Assembly Motifs in [EMIM][BF 4] through Cryogenic Ion Spectroscopy. *J. Chem. Phys.* **2013**, *139* (22), 224305. https://doi.org/10.1063/1.4838475.

(20) Doroshenko, V. M.; Cotter, R. J. Ideal Velocity Focusing in a Reflectron Time-of-Flight Mass Spectrometer. *J. Am. Soc. Mass Spectrom.* **1999**, *10* (10), 992–999. https://doi.org/10.1016/S1044-0305(99)00067-7.

(21) Mamyrin, B. A.; Karataev, V. I.; Shmikk, D. V; Zagulin, V. A. *The Mass-Reflectron, a New Nonmagnetic Time-of-Flight Mass Spectrometer with High Resolution*; 1973.

(22) Mamyrin, B. A. Time-of-Flight Mass Spectrometry (Concepts, Achievements, and Prospects). *Int. J. Mass Spectrom.* **2001**, *206* (3), 251–266. https://doi.org/10.1016/S1387-3806(00)00392-4.

(23) Nicoll, F. H. The Focusing Properties of the Electrostatic Field between Two Cylinders. *Proc. Phys. Soc.* **1938**, *50* (6), 888–898. https://doi.org/10.1088/0959-5309/50/6/302.

(24) Voss, J. M.; Duffy, E. M.; Marsh, B. M.; Garand, E. Title: Mass Spectrometric and Vibrational Characterization of Intermediate in [Ru(Bpy)(Tpy)(H2O)]2+ Catalyzed Water Oxidation.

https://doi.org/10.1002/cplu.201700085.

(25) Marsh, B. M.; Voss, J. M.; Garand, E. A Dual Cryogenic Ion Trap Spectrometer for the Formation and Characterization of Solvated Ionic Clusters. *J. Chem. Phys.* **2015**, *143* (20). https://doi.org/10.1063/1.4936360.

(26) Paul, W.; Steinwedel, H. Ein Neues Massenspektrometer Ohne Magnetfeld. *Zeitschrift fur Naturforschung - Section A Journal of Physical Sciences*. Verlag der Zeitschrift für Naturforschung July 1, 1953, pp 448–450. https://doi.org/10.1515/zna-1953-0710.

(27) Douglas, D. J.; Frank, A. J.; Mao, D. Linear Ion Traps in Mass Spectrometry. *Mass Spectrom. Rev.* **2005**, *24* (1), 1–29. https://doi.org/10.1002/mas.20004.

(28) Schwartz, J. C.; Senko, M. W.; Syka, J. E. P. *FOCUS: QUADRUPOLE ION TRAPS A Two-Dimensional Quadrupole Ion Trap Mass Spectrometer*; 2002.

(29) Church, D. A. Storage-Ring Ion Trap Derived from the Linear Quadrupole Radio-Frequency Mass Filter. **1969**. https://doi.org/10.1063/1.1658153.

(30) Hoffman, N. M.; Gotlib, Z. P.; Opačić, B.; Huntley, A. P.; Moon, A. M.; Donahoe, K. E. G.; Brabeck, G. F.; Reilly, P. T. A. Digital Waveform Technology and the Next Generation of Mass Spectrometers. *J. Am. Soc. Mass Spectrom.* **2018**, *29* (2), 331–341. https://doi.org/10.1007/s13361-017-1807-8.

(31) Mathieu, É. Mémoire Sur Le Mouvement Vibratoire d'une Membrane de Forme Elliptique. *J. Math. Pures Appl.* **1868**, *13*, 137–203.

(32) Sheretov, E. P.; Terent'ev, V. I. Theory of the Pulsed Quadrupole Mass Spectrometer. *Sov. Phys. Tech. Phys.* **1972**, *17*, 755.

(33) Richards, J. A.; Huey, R. M.; Hiller, J. A New Operating Mode for the Quadrupole Mass Filter. *Int. J. Mass Spectrom. Ion Phys.* **1973**, *12* (4), 317–339. https://doi.org/10.1016/0020-7381(73)80102-0.

(34) Ding, L.; Sudakov, M.; Brancia, F. L.; Giles, R.; Kumashiro, S. A Digital Ion Trap Mass Spectrometer Coupled with Atmospheric Pressure Ion Sources. *J. Mass Spectrom.* **2004**, *39* (5), 471–484. https://doi.org/10.1002/jms.637.

(35) Xue, B.; Sun, L.; Huang, Z.; Gao, W.; Fan, R.; Cheng, P.; Ding, L.; Ma, L.; Zhou, Z. A Hand-Portable Digital Linear Ion Trap Mass Spectrometer. *Analyst* **2016**, *141* (19), 5535–5542. https://doi.org/10.1039/c6an01118g.

(36) Brabeck, G. F.; Chen, H.; Hoffman, N. M.; Wang, L.; Reilly, P. T. A. Development of MSn in Digitally Operated Linear Ion Guides. *Anal. Chem.* **2014**, *86* (15), 7757–7763. https://doi.org/10.1021/ac501685v.

(37) Brancia, F. L.; McCullough, B.; Entwistle, A.; Grossmann, J. G.; Ding, L. Digital Asymmetric Waveform Isolation (DAWI) in a Digital Linear Ion Trap. *J. Am. Soc. Mass Spectrom.* **2010**, *21* (9), 1530–1533. https://doi.org/10.1016/j.jasms.2010.05.003.

(38) Xu, F.; Wang, L.; Dai, X.; Fang, X.; Ding, C. F. Resonance Activation and Collision-Induced-Dissociation of Ions Using Rectangular Wave Dipolar Potentials in a Digital Ion Trap Mass Spectrometer. *J. Am. Soc. Mass Spectrom.* **2014**, *25* (4), 556–562. https://doi.org/10.1007/s13361-013-0804-9.

(39) Sun, L.; Xue, B.; Huang, Z.; Cheng, P.; Ma, L.; Ding, L.; Zhou, Z. Chemical Mass Shifts in a Digital Linear Ion Trap as Analytical Identity of O-, m-, and p-Xylene. *J. Am. Soc. Mass Spectrom.* **2018**, *29* (7), 1386–1393. https://doi.org/10.1007/s13361-018-1963-5.

(40) Reece, M. E.; Huntley, A. P.; Moon, A. M.; Reilly, P. T. A. Digital Mass Analysis in a Linear Ion Trap without Auxiliary Waveforms. *J. Am. Soc. Mass Spectrom.* **2020**, *31* (1), 103–108. https://doi.org/10.1021/jasms.9b00012.

Chapter 2 Principles of Operation

This purpose of this chapter is to introduce terms and concepts necessary for understanding ion motion in linear quadrupole ion traps (LQITs) by means of periodic and static electric fields. A general overview of the axial and radial stabilization of ions will be demonstrated, and critical mathematical equations deriving those fields will be discussed. Differences between sinusoidal and rectangular (square) waves will also be illustrated. Finally, perturbations to stable ion motion will be demonstrated for LQITs containing multiple ion populations of different m/z. For the sake of brevity and clarifications, in-depth mathematical derivations will be minimized in favor of visual illustrations.

Section 2.1 Ion Motion in a Quadrupolar Field

Before diving heavily into the nuances of linear quadrupole mass spectrometry, a brief generalization is presented below to show the methods in which ions are confined by static and periodic electric fields. A more detailed description of the exact waveforms and how a stable ion equilibrium is established will be given in following sections. For the remainder of this thesis, the extrusion of the hyperbolic profile which spans the length of an LQIT will be considered the axial, or Z-axis. The four hyperbolic electrodes will be divided into two electrode pairs, one comprising the X-axis and the other comprising the Y-axis. Mathematically, the X-axis and Y-axis coordinates are interchangeable, such that when appropriate, these axes may be referred to as the radial direction. In reality, one or both of these electrode pairs will have some hole present at the apex of the hyperbolic profile which will allow for ion extraction and eventual detection.

2.1.1 Axial Trapping by Static Electric Fields

Typically, an LQIT is housed in a structure containing two endcaps that serve to axially confine ions. This is accomplished by applying static electric fields on the endcaps where the magnitude of the field is higher than the average potential applied two electrode pairs of an LQIT. An example of this can be shown in **Figure 2.1**. The left portion of this figure represents a 3D potential energy view (PEV) in green of two endcaps (yellow in the bottom portion) in an example LQIT. Simulations are generated in SIMION 8.1. As can be seen from the figure, a potential well is formed along the LQIT length by the voltage difference between the two endcaps and the DC offset, or average potential applied to the LQIT electrode pairs. This potential well, along with a collisional buffer gas, is used to prevent ions with high kinetic energy from escaping the ion trap structure through the holes present in the endcaps.

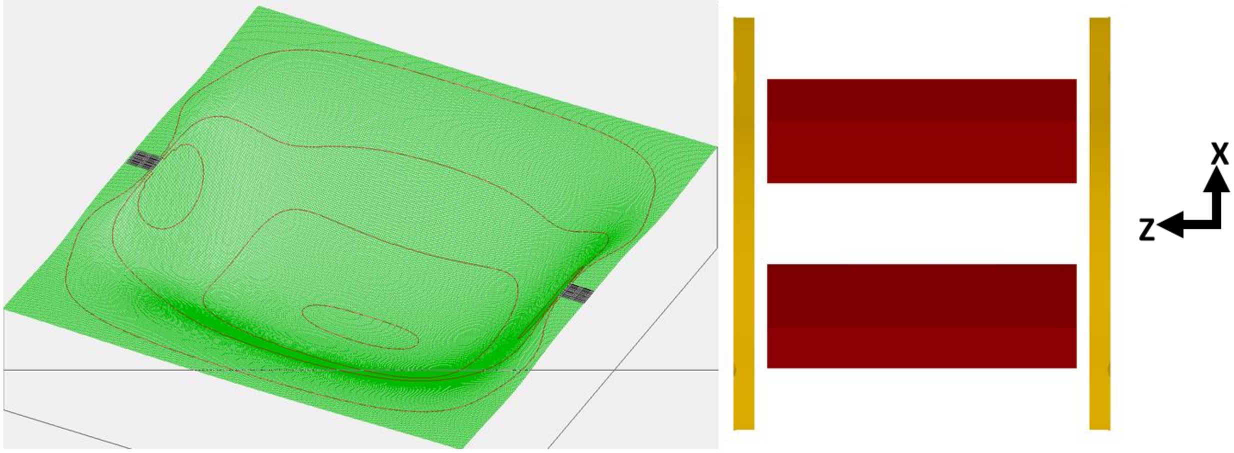

Figure 2.1 3D PEV of the axial confinement (left).LQIT CAD for reference(right).

2.1.2 Radial Trapping by Periodic Electric Fields

Conversely to axial trapping, radial stability is a bit more complex. Due to Earnshaw's Theorem, which states that an ion (or any charged particle) cannot to be confined using only static electric fields,[1] a time-dependent periodic electric potential must be utilized to provide ions in an LQIT with stable motion by alternating repulsive and attractive forces as ions move in 3D space. This motion is called the secular frequency and will be covered in later sections. Visualizing these electric fields pictorially is difficult due to the time dependent nature of the waveform. Rather, two snapshots of the radial electric fields generated by two oppositely phased sine waves applied to the LQIT electrode pairs are given below in **Figure 2.2**. Also generated in SIMION 8.1. The PEV (green) shows two snapshots representing the maxima and minima of the applied sine waves on each electrode pair. If an ion were to be placed in the middle of the “saddle” which forms from the instantaneous potential difference between the electrode pairs, the ion would move from the higher horizontal potential to the low vertical potential in the left-hand PEV. Before the ion reaches the Y-axis electrode pair, the magnitude of the two periodic potentials has flipped, causing an inversion of the saddle, now vertically oriented. Such inversion causes ion motion back toward the X-axis, where the process is repeated, generating radial trapping.

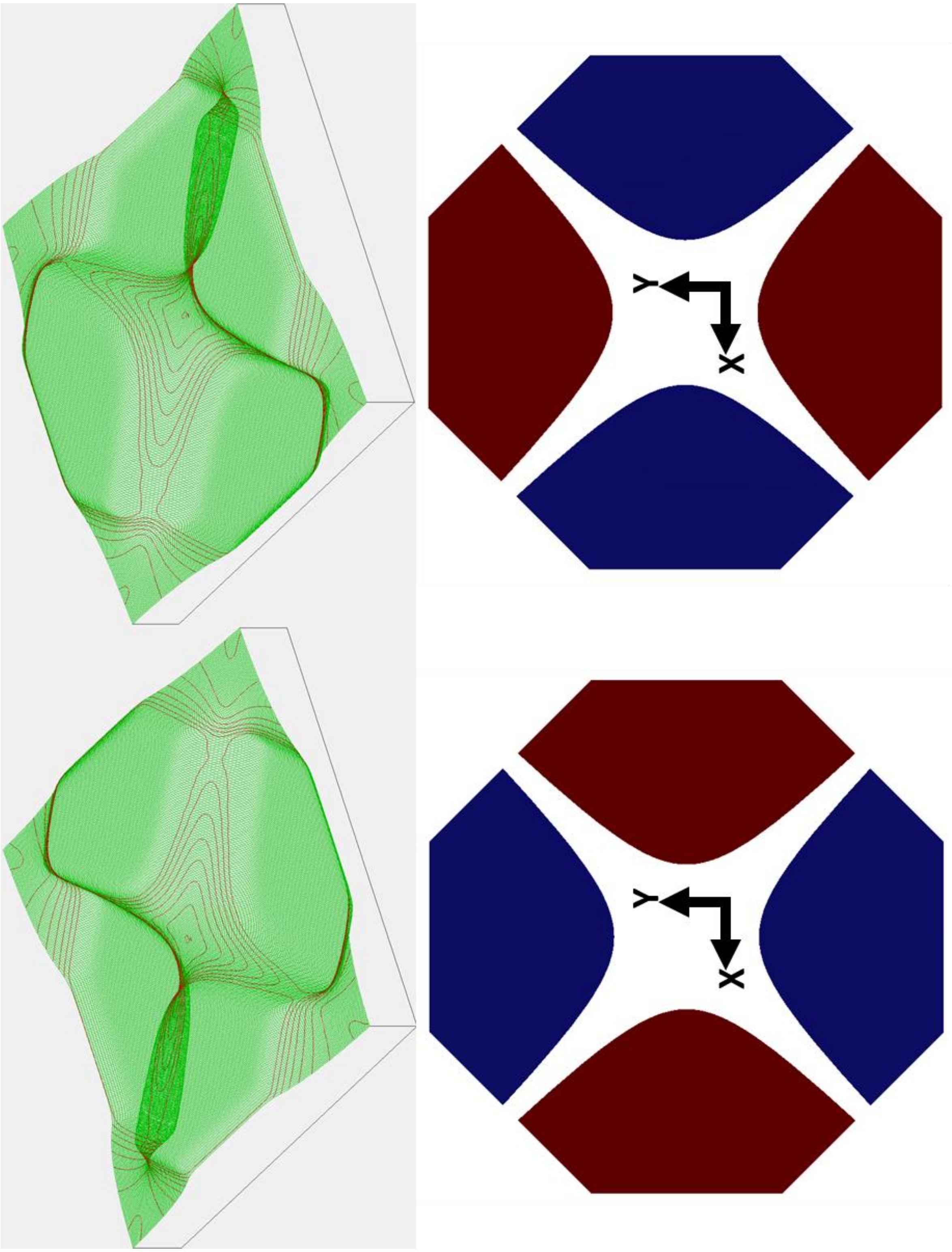

Figure 2.2 3D PEV of X-axis and Y-axis electrodes of an LQIT (left).

Section 2.2 Ion Motion in a Sinusoidal Field

Confinement of ions in an LQIT requires the use of time dependent periodic electric fields. The most commonly used electric field is a sinusoidal waveform, an example of which was illustrated in **Chapter 1**. The following subsections will describe how the stable equilibrium of a singular ion of mass, *m*, is obtained, how an LQIT containing multiple ion populations with differing masses can be manipulated to isolate one specie, and finally how sequential separation masses by their mass-to-charge ratio (m/z) is achieved. The following derivation is paraphrased from Douglas,[2] and March.[3,4]

2.2.1 Stable Motion

Each of the electrode pairs of an LQIT has two oppositely phased sine waves applied to them. The magnitude of the potential at an electrode at any time can be given from the following equation.

$$\Psi(\mathrm{t}) = \pm(U - V\cos\Omega t) \qquad \textit{Eq. 1}$$

Where *U* is the DC potential difference between the electrode pairs, *V* is the zero-to-peak (V_{0p}) magnitude of the AC field and *Ω* is the angular frequency of the applied waveform. As the distance from the electrode increases, the effective potential decreases. A Cartesian coordinate system for the pure quadrupolar field can be assigned to the internal volume of the LQIT such that,

$$\phi(\mathrm{x},\mathrm{y}) = \frac{x^2 - y^2}{r_0^2}\,\Psi \qquad \textit{Eq. 2}$$

where ϕ is the effective potential, *x* and *y* are the Cartesian coordinates, and r_0 is the effective radius of the electrode pairs. By incorporating *Eq. 1* into *Eq. 2*, the magnitude of the electric field anywhere in the interval volume of the LQIT can be defined by *Eq 3*.

$$\Phi(\mathrm{x,y,t}) = \frac{x^2 - y^2}{r_0^2}(U - V\cos\Omega t) \qquad \textit{Eq. 3}$$

Determining the exact position of an ion in this Cartesian coordinate system involves the use the second order linear differential Mathieu equation, given below.

$$\frac{\mathrm{d}^2u}{d\xi^2} + (a_u - 2q_u\cos 2\xi)u = 0;\ \ \xi = \frac{\Omega t}{2} \qquad \textit{Eq. 4}$$

Where *u* represents the Cartesian direction of interest (*x* or *y*), and both a_u and q_u are dimensionless parameters that relate to ion stability. Substituting *Ωt/2* for *ξ*, multiplying both sides by *m* and rearranging *Eq. 4* yields

$$m\frac{d^2u}{dt^2} = -\frac{m\Omega^2}{4}(a_u - 2q_u\, cos\, \Omega t)u \qquad \textit{Eq. 5}$$

The left-hand side of the previous equation can be used to define the force exerted on an ion with mass, *m*, that is based on the dimensionless trapping parameters, a_u and q_u, and the frequency, *Ω*, of the sine wave applied to the LQIT in a single axis. The resulting force can be considered in each axis, independently. The remaining derivation will only consider the *u* = *x*-direction, but the same steps can be followed for the *y*-direction.

By means of Newton's 2nd law, the acceleration of an ion in an electric field can be described as

$$F_x = ma = m\frac{d^2x}{dt^2} = -e\frac{\partial\phi}{\partial x} \qquad \textit{Eq. 6}$$

where *a* is the acceleration, *e* is the elementary charge, and ϕ is the potential from *Eq. 3* at any given point along the *x*-axis of the Cartesian space. Thus, by differentiating ϕ with respect to *x* we obtain:

$$\frac{\partial \phi}{\partial x} = \frac{2x}{r_0^2}(U + V \cos \Omega t)x \qquad \textit{Eq. 7}$$

Substituting *Eq. 7* into *Eq. 6* yields

$$m\frac{d^2x}{dt^2} = \frac{-2e}{r_0^2}(U + V \cos \Omega t)x \qquad \textit{Eq. 8}$$

Equalizing *Eq.8* with *Eq.5* when *u* = *x* allows for the definition of the Mathieu a_x and q_x terms in the equations below.

$$a_x = \frac{8eU}{mr_0^2\Omega^2}; \quad q_x = -\frac{4eV}{mr_0^2\Omega^2} \qquad \textit{Eq. 9}$$

These two dimensionless parameters allow for solutions to the Mathieu equation to solved for a given ion in terms of stable and unstable equilibrium of motion while contained in an LQIT for the *x*-direction and *y*-direction, separately. These solutions are out of the scope of this thesis as several assumptions must be made in order to solve the many integral orders of the Mathieu functions. For in-depth approaches to Matrix-based solutions of the Mathieu equation for sine waves, see Pipes,[5] or Konenkov *et al*.[6] The product of these researchers work is the production of the Mathieu stability diagram, which correlates the a_u and q_u parameters as a function of *x* and *y* stability in an LQIT. The areas in which stable motion is achieved for both directions are referred to as stability regions. Future discussion in this thesis will be limited to the 1st stability region, which is shown in **Figure 2.3** taken from Douglas[2].

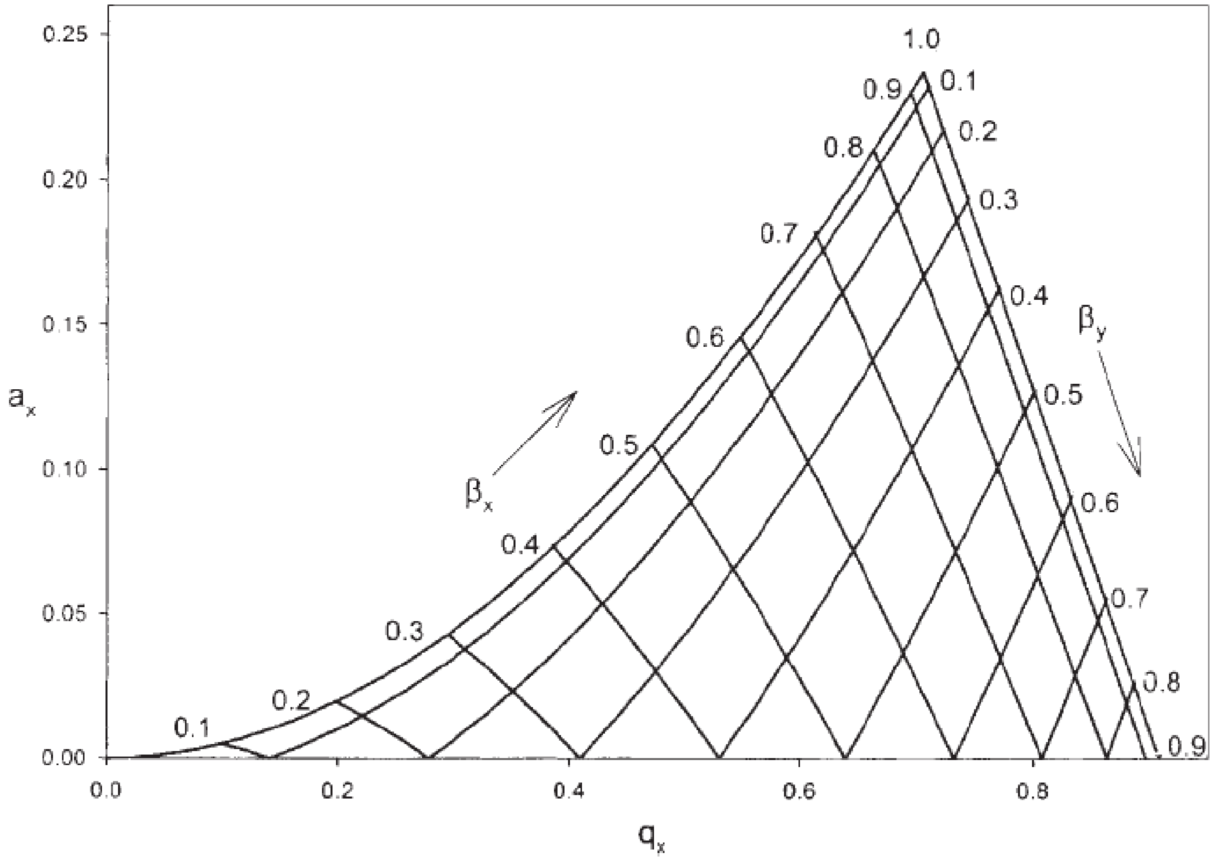

Figure 2.3 Mathieu 1st stability region.

In the figure above, anything to the left of the stability region is considered to be stable in only the *x*-direction. Anything to the right of the stability region is considered to be stable in only the *y*-direction. The region itself is comprised of all values of *a* and *q* which are correlated to stable ion motion in a sine wave operated LQIT. Cross-sectional lines present in the stability region correspond to the β_x and β_y dimensionless trapping parameters, which range from 0.0 to 1.0 where anything past 1.0 is considered unstable in the respective direction. This β_u parameter is a complex function comprised of a continued fraction of a_u and q_u but can be approximated for small values for q_x and q_y (i.e., $q_x < 0.2$ and $q_z < 0.4$) such that

$$\beta_u \approx \sqrt{a_u + \frac{q_u^2}{2}} \qquad \textit{Eq. 10}$$

The effect of relating the stability of ions in both *x* and *y* directions with the Mathieu *a* and *q* parameters allows for a fundamental understanding of how LQITs are operated for various ion manipulation functions. By defining the effective radius, r_0, of an LQIT and the sine wave applied to it by the magnitude of the sine wave, *V*, the DC potential difference between electrodes, *U*, and the frequency, *Ω*, assigning a Mathieu *a-q* coordinate for a generic ion with mass, *m*, and charge state, *z*e*, is possible. If this coordinate falls within the stability region of the figure above, the ion will move throughout the LQIT with a stable equilibrium of motion, indefinitely. By altering any of the characteristics of the sine waveform applied, the coordinate in *a-q* space can be moved within the stability region without consequence. If this movement ever causes the ion's coordinate to leave the stability region, either termination of the ion by striking the electrode, or ejection by moving through a pre-fabricated hole in the electrode will be achieved.

2.2.2 Mass Isolation

Now that a method of correlating experimental waveform parameters to the stability of a singular ion has been obtained, this definition can be expanded for an LQIT containing multiple ion species, all with differing masses. If, for example, an LQIT contains five ion species of differing masses, such that $m_1 > m_2 > m_3 > m_4 > m_5$. According to *Eq. 9*, each of these masses will have a unique *a-q* coordinate. Due to the nature of *a* and *q*, heavier ions (e.g., m_1) will have a smaller magnitude *a-q* coordinate, whereas lighter ions (e.g., m_5) will have a higher magnitude *a-q* coordinate. In the given example we will assume initially there is no DC potential between the two rod pairs, thus making $a = 0$, which aligns all five masses along the *q*-axis. An example of this is shown in **Figure 2.4**.

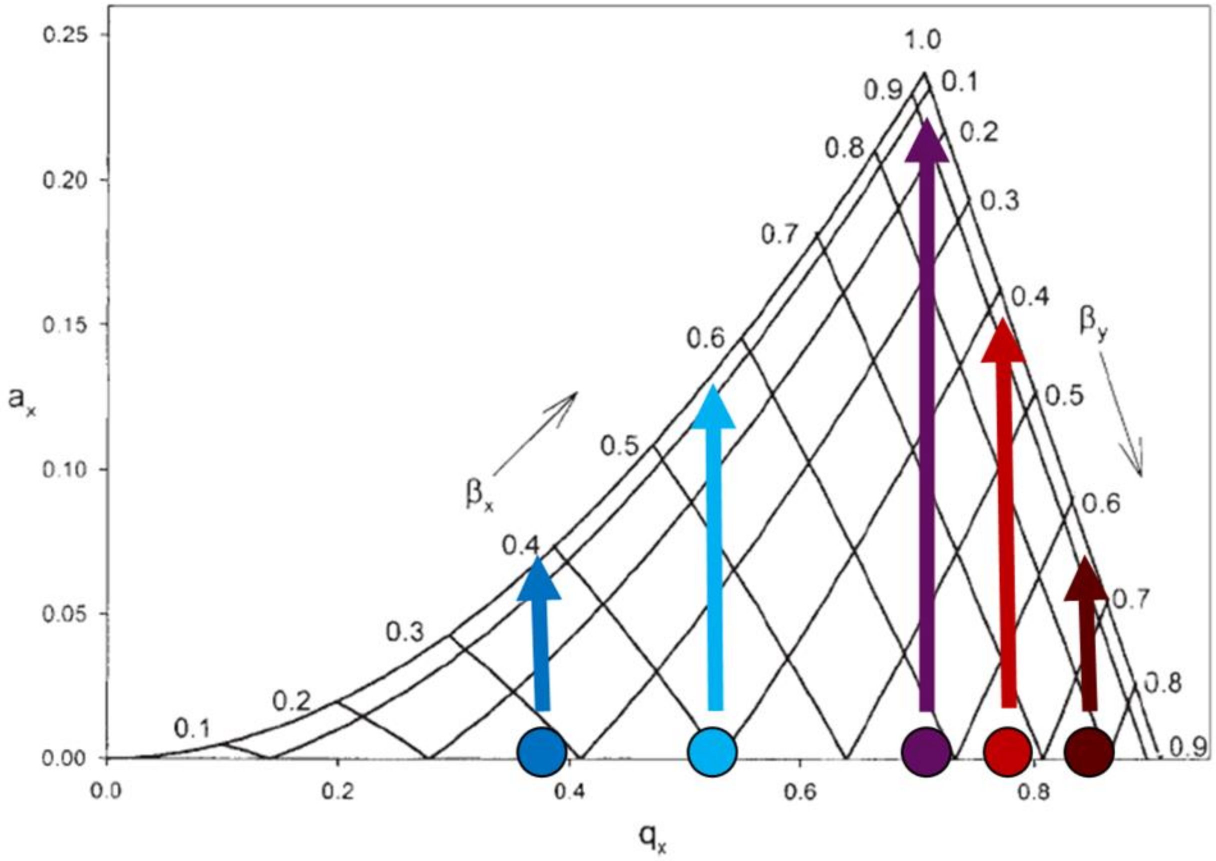

Figure 2.4 Stability region with five masses. Arrows represent *a* direction movement.

Once trapped and stable motion is achieved, any of the experimental parameters (i.e., *U*, *V*, or *Ω*) can be used to simultaneously move all five of the ions throughout *a*-*q* space. If, in this hypothetical, the *U* parameter was scaled linearly, the net result be an increase in the *a* parameter for each mass, shown in the figure as colored arrows. Eventually, the lighter and heavier ions would become radially unstable, resulting in termination from the trap. As the remaining ions move closer to the apex of the stability region, eventually only one ion would remain. Fundamentally, this is the purpose of a mass isolation stage.

Most dedicated linear quadrupoles concerned with mass isolation are referred to as quadrupole mass filters (QMF).[7] These devices are not ion traps, but rather ion transport devices used between ion generation and detection. Rather than scanning just the *U* parameter, both *U* and *V* are scanned at an adjustable rate due to the fixed frequency nature of sine wave generation. This allows for the experimental determination of the applied waveform which best isolates the singular ion of interest from a collection of ions. It is possible to perform mass isolation in an LQIT[8] but doing so typically requires the use of complex sine waveforms, which will be covered in later sections.

2.2.3 Mass Analysis

QMFs are useful for filtering impure sample solutions, isolating precursors and/or product ions for tandem MS,[9] and as mass analyzers in continuous ion generation instrumentation.[10] When the prolonged confinement of ions is required, LQITs are used instead. Once a collection of ions is present in the ion trap, ejection is necessary for mass analysis. There are several methods for LQIT based mass analysis[11] but presented below is the most simplistic and commercially available.

The same example in the previous section is used such that five ions of differing masses experience stable motion in an LQIT. No U component is applied to the electrode pairs so that all ion a-q coordinates reside along the q-axis. Instead, only the V parameter is scanned by gradually increasing the zero-to-peak voltage of the applied sine wave. This, in turn, increases the magnitude of q component while maintaining no change in the a value. Eventually, the lightest ion reaches the stability boundary and becomes radially unstable. From lightest to heaviest, the next four masses are ejected in the same manner. This is referred to as a mass instability scan,[12] and can be seen in **Figure 2.5**. Other methods of LQIT mass analysis are available,[13] but require complex sine waveforms and will be covered in a later section.

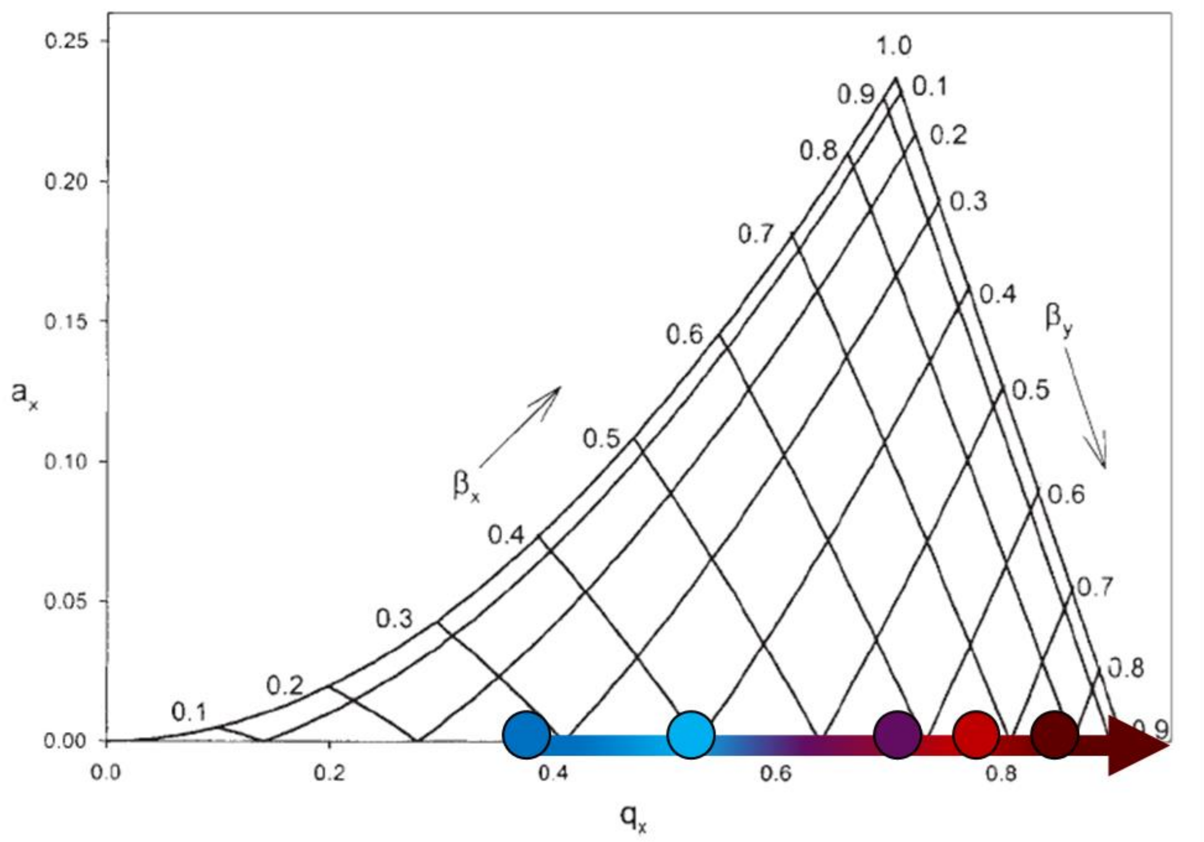

Figure 2.5 Stability region with five masses. Multi-colored arrow represents mass instability scan.

2.2.4 Limitations of Sinusoidal Waveforms

As mentioned in previous sections, sinusoidal waveforms are commonly used for a variety of applications. There are, however, several limitations to sine wave operation. The circuitry used to generate sine waves produce a fixed frequency, variable amplitude waveform.[14] A DC potential between electrode pairs can be added to circuitry trivially. Typically, sine wave-based LQITs operate at a nominal frequency of 1 MHz, from V_{0p} ranges of 0 kV up to 10 kV, requiring specialized electrical wiring and equipment to operate. Due to the nature of the frequency generation, only a static frequency is achievable, preventing it from become a scannable parameter. The function of the LQIT is typically pre-determined as either scanning *U/V* or just *V* as sole *U* scanning is not common. Finally, many of the modern functionalities require the use of complex sine waveforms which further complicate mass calibration.

Section 2.3 Ion Motion in a Rectangular Field

Quintessentially, a lack of waveform modularity and frequency control have led others, such as Sheretov and Terent'ev,[15] and Richards *etal*[16] to investigate the use of alternative waveforms to operate QITs with different waveforms. One of the promising waveform alternatives is rectangular, or square waves. An example of a square waveform was provided in **Chapter 1**. The simplicity of the square waves is very appealing both in terms of understanding the forces applied to ions in a rectangular field and due to the waveform tailoring that could be utilized by modulations to both the frequency and duty cycle. This functionality is not possible with sine waves. To highlight how these new changeable parameters are used, the following discussions revisit mass isolation and analysis using square waves.

2.3.1 Stable Motion

In a previous section a derivation was described using the second order linear differential Mathieu equation. This equation is a sine wave-specific case of a broader second order linear differential equation, called the Hill equation.[17] Rather than specified to a sinusoidal waveform, the Hill equation describes the stable or unstable ion motion of any periodic field, including square waves. Both Mathieu and Hill equations utilize the same a, q, and β dimensionless parameters to describe the stability or instability of ions in a given square wave. Unlike the continuous voltage changing sine waves, the square wave applied to each electrode pair of a linear "digital" ion trap (LDIT) can be defined by two voltage states, HIGH or LOW which are switched between at a period, T. These voltages are held constant, but the force applied to an ion anywhere in the original Cartesian coordinates for a pure quadrupolar field can still defined by *Eq. 3*. The manner in which ion stability is determined is provided below, paraphrased by Brabeck *et al*.[17]

The net potential difference between the *x* and *y* electrode pairs are defined for a given period by three time segments, so that T = $t_1 + t_2 + t_3$, corresponding to positive quadrupolar fields, no quadrupolar field, and negative quadrupolar field in the *u* direction, respectively. The matrix for each time segments is given below.

$$V(f_n, t_n) = \begin{bmatrix} cos\left(\tau_n\sqrt{f_n}\right) & \frac{1}{\sqrt{f_n}} sin\left(\tau_n\sqrt{f_n}\right) \\ -\sqrt{f_n}\, sin\left(\tau_n\sqrt{f_n}\right) & cos\left(\tau_n\sqrt{f_n}\right) \end{bmatrix} \quad \text{if f > 0} \qquad \textit{Eq. 11}$$

or

$$V(f_n, t_n) = \begin{bmatrix} cosh\left(\tau_n\sqrt{-f_n}\right) & \frac{1}{\sqrt{-f_n}} sinh\left(\tau_n\sqrt{-f_n}\right) \\ -\sqrt{-f_n}\, sinh\left(\tau_n\sqrt{-f_n}\right) & cosh\left(\tau_n\sqrt{-f_n}\right) \end{bmatrix} \quad \text{if f < 0} \qquad \textit{Eq. 12}$$

where $\tau_n = \pi t_n/T$, $f_n = a + mq$, m = 2, 0, or -2 during the t_1, t_2, or t_3 time segments, respectively. By solving the above matrices for each of the three separate voltage states, the products can be multiplied together to determine the transfer matrix over one period, such that

$$M = V(f_1, t_1) \times V(f_2, t_2) \times V(f_3, t_3) \times \ldots \times V(f_n, t_n) \qquad \textit{Eq. 13}$$

In the simplest case of $n = 3$, the trace of the above transfer function can be used to determined stable or unstable motion in a rectangular field. When the trace of the transfer function is less than 2, a stable equilibrium of motion is achieved for a given *a*-*q* coordinate. A value greater than 2 yields unstable motion in the *u* coordinate. For a more detailed description of this matrix solution to the Hill equation, see Konenkov *et al*[6].

Functionally, the above derivation allows for a straightforward calculation of the 1st stability region for square waves. For every value of *a* and *q* value, f_n can be calculated. Each of the three time segments, t_1, t_2, and t_3 can be correlated to a static voltage state of the applied LDIT electrode pairs. The voltage state where the direction of interest's electrode pair is HIGH is defined as t_1. Thus, by inputting the magnitude, V, of the square wave, and any potential difference between electrode pairs, U, values of τ_n and f_n are easily calculated. Generating the transfer function for the $n = 3$ case and determining the trace of the transfer function generates a numeric value to determine stable or unstable ion motion at the given square wave parameters. Extrapolating this for a range of a and q values produces the stability diagram shown in **Figure 2.6**, generated from Brabeck and Reilly.[17]

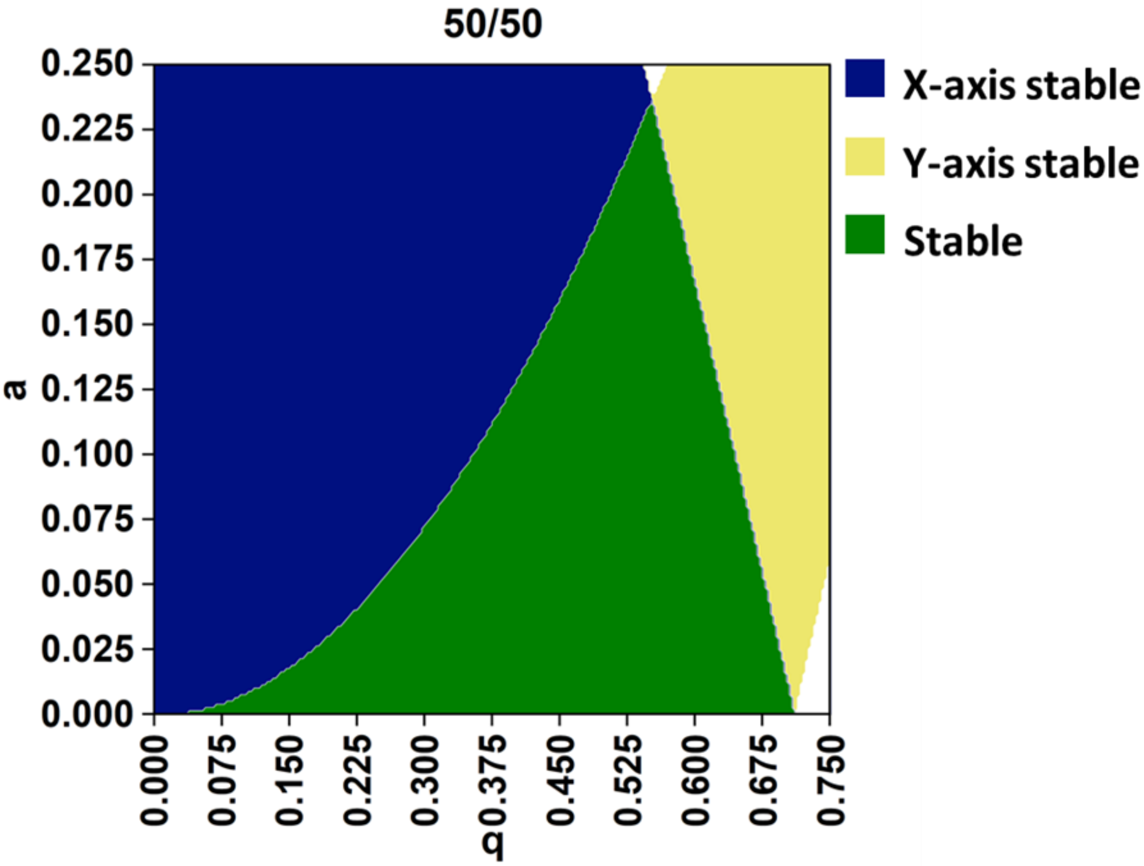

Figure 2.6 Mathieu (Hill) 1st stability region of LDITs.

The overall shape of the stability region is largely unchanged when the duty cycle of the square waves applied are maintained at 50% on the X-axis and 50% on the Y-axis (hereafter 50/50). Differences between sine wave and square wave stability regions manifest as the *a-q* coordinates of the right-hand and upper apexes. The right hand apex of a sine wave is defined to be (0, 0.908) whereas the same boundary condition occurs at (0, 0.7125) for square waves. The upper apex of the stability regions also differ, from (0.237, 0.706)[2] for sine waves and (0.236, 0.550)[17] for square waves. Functionally, this would manifest as smaller mass range and a higher low mass cutoff in an LDIT compared to a sine wave-based LQIT. This assumption would only be true if the same *U*, *V*, and *Ω* parameters would be used on each of the devices, which is seldomly the case, as will be showcased in the following sections.

2.3.2 Mass Isolation

Using the example of five ions with differing masses such that $m_1 > m_2 > m_3 > m_4 > m_5$, an explanation of how mass isolation occurring in both LDITs and digital mass filters (DMFs) can be illustrated. The major advantage of digital generated waveforms is the ability to tailor both the period, *T*, and duty cycle, t_n/T, in addition to the pre-existing *U* and *V* parameters. This tailoring has led to numerous studies about the ability to isolate mass ranges using square waves via frequency and duty cycle alterations.[17–20] Rather than scaling *U/V* as seen with sine waves, the operational parameters of DITs and DMFs are instantaneous changes to the frequency and duty cycle. Modern waveform generators can produce variable frequency and variable duty cycle square waves trivially. Additionally, several generators include a “burst” mode which allows for an instantaneous switching to a secondary frequency and duty cycle for either a set duration or a set number of periods. From an *a-q* space perspective, this allows for rapid changes to the underlying experimental parameters of the Mathieu *a* and *q* trapping parameters.

Recall from previous sections that once an ion’s *a-q* coordinate is brought outside of the stability region, the ion becomes unstable. This instability causes a non-zero amount of ion displacement along the relevant axis, eventually striking an electrode pair. Terminal displacement can occur in as little as 10 periods,[21] which translates to < 10 µs for frequencies ranging in the mid to high kilohertz range. For DITs, incorporating the waveform burst mode mentioned above would allow the example's five ions to be trapped under the 50/50 stability region in the figure above, then a secondary burst frequency and duty cycle will be applied to perform the mass isolation.

An example of this mass isolation is given in **Figure 2.7**, which illustrates a phenomenon unique to square waves, compared to sine waves. In the five masses example, *a-q* coordinates are assigned to each of the ion species prior to isolation. These coordinates are determined by the *a* and *q* dimensionless trapping parameters, which in turn scale with *U, V* and *Ω*. The period, *T*, of the square waves is considered in *Ω* term, such that $\Omega = 2\pi/T$, but the duty cycle is not. Changing the duty cycle of the square wave applied to the LDIT changes the relative weight of each of the time segments, t_1, t_2, and t_3. For the 50/50 stability region, $t_1 = t_3$, and $t_2 = 0$. For any other duty cycle pairing an inequality of time segments is present. This in turn affects which *a-q* coordinates correspond to stable and unstable ion motion, therefore changing the shape of the stability region. This distortion occurs while still maintaining the *a-q* coordinates of the five masses. By manipulating the stability diagram, not the ion's coordinates, mass isolation is achieved. One of the key advantages of using square waves for mass isolation in an LDIT is that once isolated, the square wave can be returned to the 50/50 duty cycle, allowing for any future ion introduction, by either gas phase ion chemical reactions,[22] or tandem-MS studies to occur, all in one ion trap. This modular isolation is not possible in sine waves due to the nature of sine wave generation and the fact that sine waves by definition have no duty cycle control.

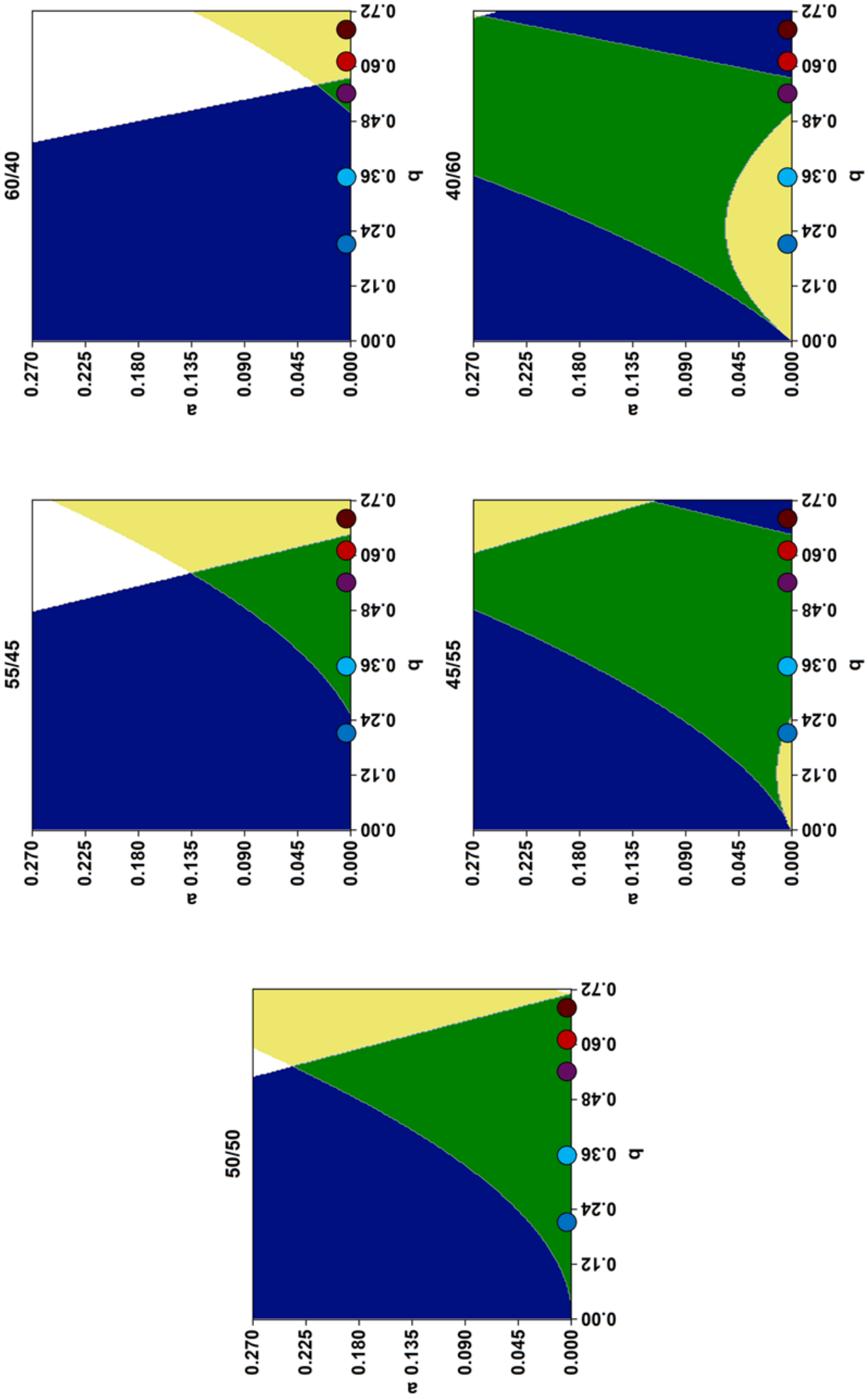

Figure 2.7 Square wave stability region changes as a function of the duty cycle applied.

2.3.3 Mass Analysis

Recall that sine wave-based LQIT mass analysis is achieved by means of scanning the V parameter when $a = 0$, thus performing a mass instability scan. Technically speaking, a square wave amplitude scan is possible and would generate the same mass instability scan as the sine wave counterpart, but this has yet to be reported. The primary reason for this is how square wave amplification is achieved, which will be detailed in **Chapter 3**. Instead, square wave-based LDIT mass analysis involves scanning the Ω parameter, which is present in both a and q equations. Due to the ease in which the frequency of a square wave can be changed by modern arbitrary waveform generators, this is a preferrable parameter to scan. There are two complications which arise from this frequency scan, however.

The first is how the square wave stability diagram is constructed at a 50/50 duty cycle pairing. When $t_1 = t_3$, the area past right-hand apex of the stability region represents no ion stability, instead of only Y-axis stability. If scanning along the q-axis when $a = 0$, ions transitioning from stable to unstable would terminate at a point somewhere between the X-axis and Y-axis electrode pairs, thus making detection impossible. A small change to the duty cycle such that $t_1 > t_3$ (e.g., 50.5/49.5) is used to solve this problem. An illustration of the effect this has can be shown in **Figure 2.8**. The consequence of asymmetric time segments is that $a \neq 0$, making the determination of the exact q_{eject} difficult to predict. This is largely a non-issues at very small duty cycle pairing differences but can make theoretical calibration of mass spectra tedious.

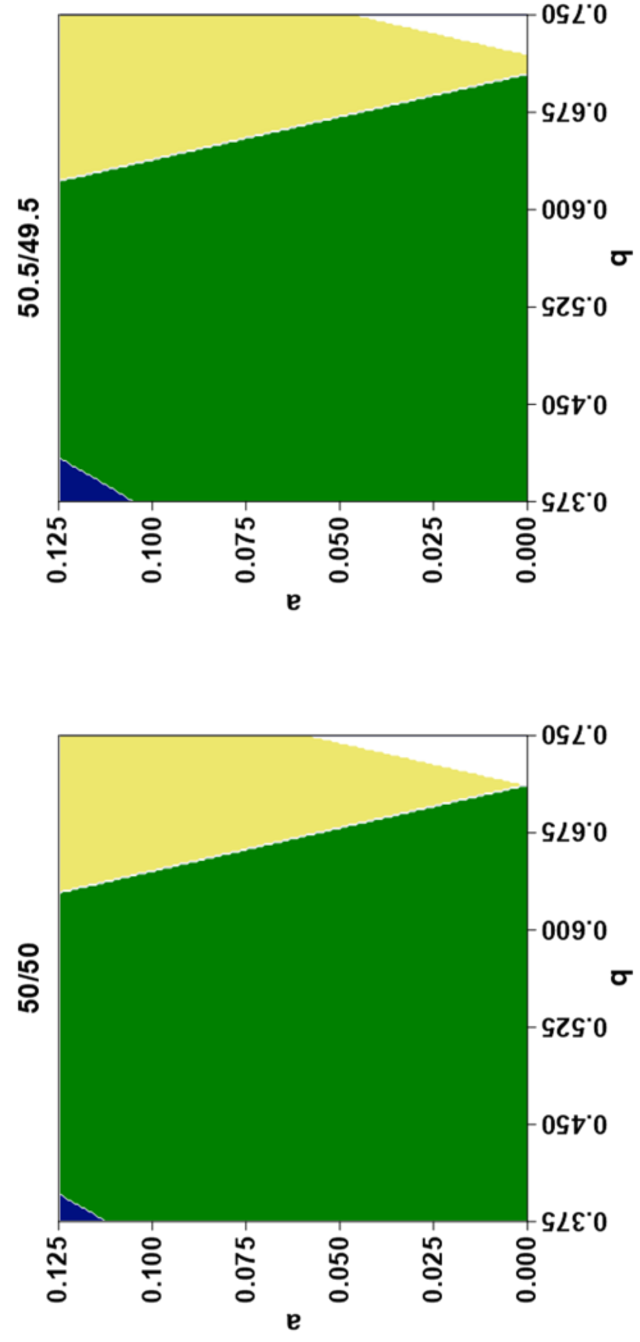

Figure 2.8 Zoom-in of stability regions at different duty cycle pairings.

The second major complication arising from frequency based mass scanning is the fact that $a \propto 1/\Omega^2$ and $q \propto 1/\Omega^2$. Regardless of which point along the Y-axis boundary line the ions are radially ejected from the LDIT, there is a lack of linearity between the scanning parameter, Ω, and the detection parameter, m/z. If a linear sweep between two frequencies (e.g., 600 kHz to 200 kHz) were to be employed, ions of increasing mass would be presented in a non-linear fashion, thus making experimental mass calibration difficult.

To alleviate this, a downward stepped frequency scan has been utilized successfully.[21,23] Rather than a linear sweep between two frequencies, a list of frequencies can be generated prior to mass analysis. This frequency list is then iteratively stepped from higher frequency to lower frequency. Each frequency step has been previously calculated for a particular m/z step utilizing an expected *a*-*q* ejection coordinate based on the experimental parameters *U*, *V*, and the duty cycle. The effect is a non-linear sweep of the frequencies, but a linear detection of m/z, which is preferred for mass calibration. An example of a stepped frequency sweep, and the corresponding m/z vs. ejection frequency can be shown in **Figure 2.9**. Thus, by defining the experimental parameters of the applied square wave for LDIT-MS, it is possible to produce a linear mass spectrum of ions contained in the LDIT.

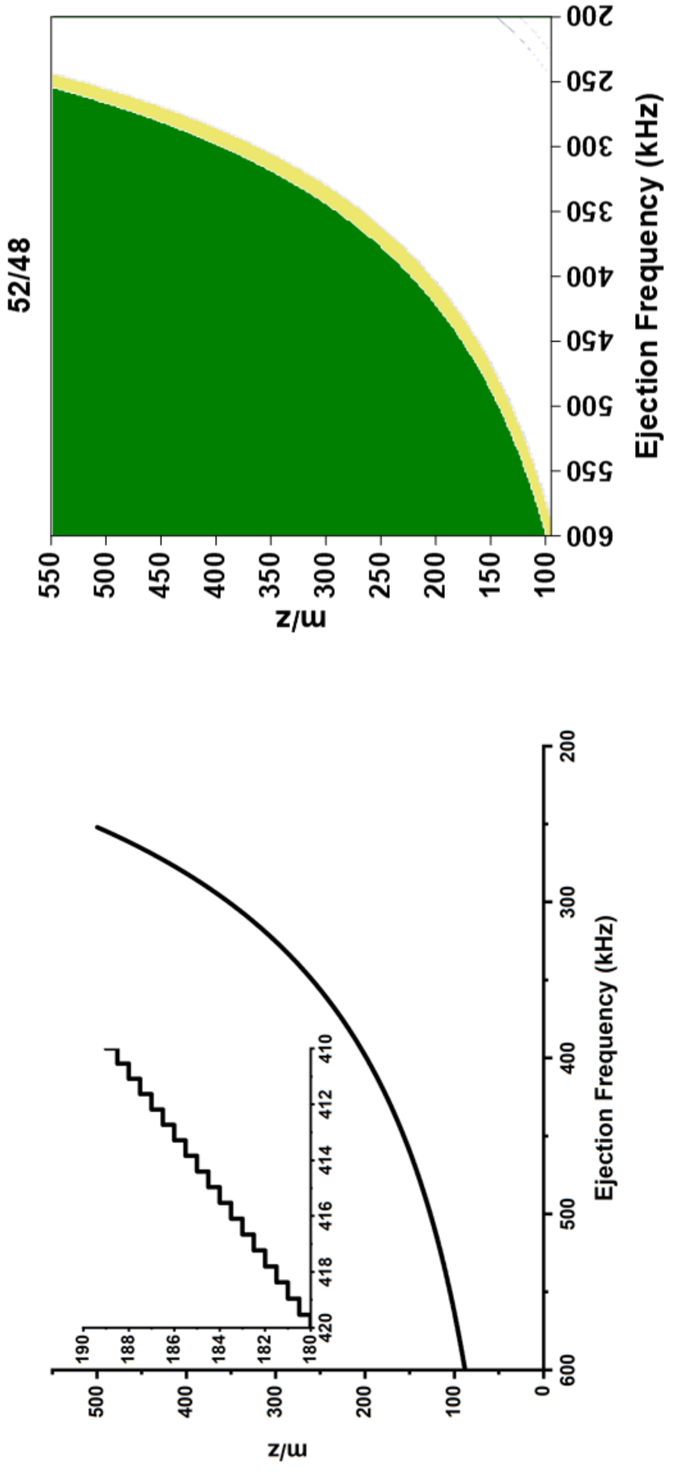

Figure 2.9 Stepped frequency sweep representations.

Section 2.4 Ion Motion in Complex Periodic Fields

The preceding sections established how ions can be collected, stored, and manipulated in both sine wave-based LQITs and square wave-based LDITs. Multiple sections have alluded to increased functionality of LQITs through the use of complex waveforms, which will be covered here. To clarify nomenclature that will be used throughout this thesis, a complex waveform consists of two individual waveforms superimposed atop one another. An example of this is shown in **Figure 2.10**. Future references will refer to the two components as a base frequency and an auxiliary frequency. Base frequencies are comprised of the higher frequency and higher amplitude component of the complex waveform, whereas auxiliary frequencies are the lower frequency, lower amplitude waveforms. Complex waveforms involving two square wave frequencies are broken into two sub-categories: phase coherent and phase incoherent. Phase coherent complex square waves dictate that the auxiliary frequency be an integer multiple of the base frequency, such that $f_{base} = f_{aux}/N$, where $N = 2, 3, 4, \ldots, N$. Phase incoherent complex square waves are any frequency combinations in which the above is not true.

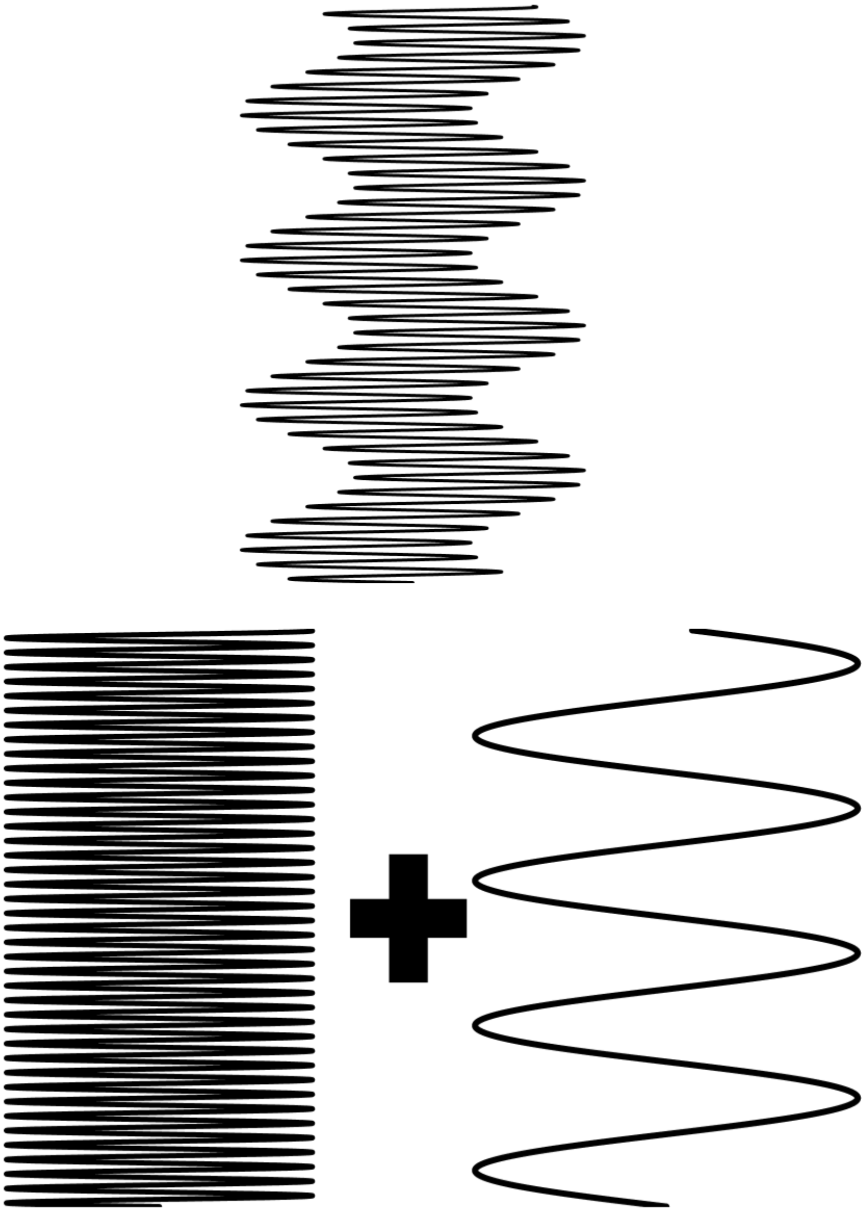

Figure 2.10 Base and auxiliary sine waves combining to make a complex waveform (right).

Alluded to in a previous section, ions do not stay still when confined in an LQIT. Instead, a stable equilibrium of motion is present for each ion whose *a-q* coordinates dictate stable motion. This motion is mass dependent and is as complex to describe as the forces applied to ions in an LIQT. The primary contributing frequency in which an ion oscillates along the central Z-axis is referred to as the fundamental or secular frequency,[13] and can be defined as:

$$\omega_{u,n} = \frac{(2n + \beta_u)\Omega}{2}; \quad -\infty < n < \infty \qquad \textit{Eq. 14}$$

where again *u* is the axis of interest (*x* or *y*), β is the dimensionless parameter from above and *n* is an integer. Also recall from earlier that β is a complex continued fraction dependent on *a* and *q*, which in turn, are dependent on the mass of an ion. Secular frequencies of ions contained in an LQIT are both m/z dependent and dependent on the experimental parameters of the applied waveform (*U, V,* and *Ω*).

Through the use of complex waveforms, it is possible for the auxiliary waveform to match a secular frequency of ion populations in the LQIT. Cooks and coworkers,[13,24,25] as well as McLuckey and coworkers[26] have shown generating an auxiliary frequency creates a "hole" in *a-q* space in which ions falling through can be radially ejected. Doing so provides a method for ion manipulation in an LQIT by means of resonant ejection, in which the applied auxiliary waveform interacts with the secular frequency of a specific m/z, causing ejection from the trap that does not occur at one of the boundary lines.

There are two ion manipulations schemes which illustrate the use of auxiliary waveforms. The first involved increasing the m/z range of a given LQIT. Recall that typically mass instability scan involves the use of 1 MHz sine waves scaled to amplitudes up to 10 kHz. Available circuitry limits the maximum frequency and amplitude which are achievable, thus limiting the upper m/z range. As the need for larger m/z mass analysis grows, the need for increasing high mass cutoffs also grows. By applying an auxiliary frequency which generates an *a*-*q* hole along the *q*-axis, an extension of the high mass cutoff occurs by lower the *q* needed for radial ejection. A schematic for this is shown in **Figure 2.11**.

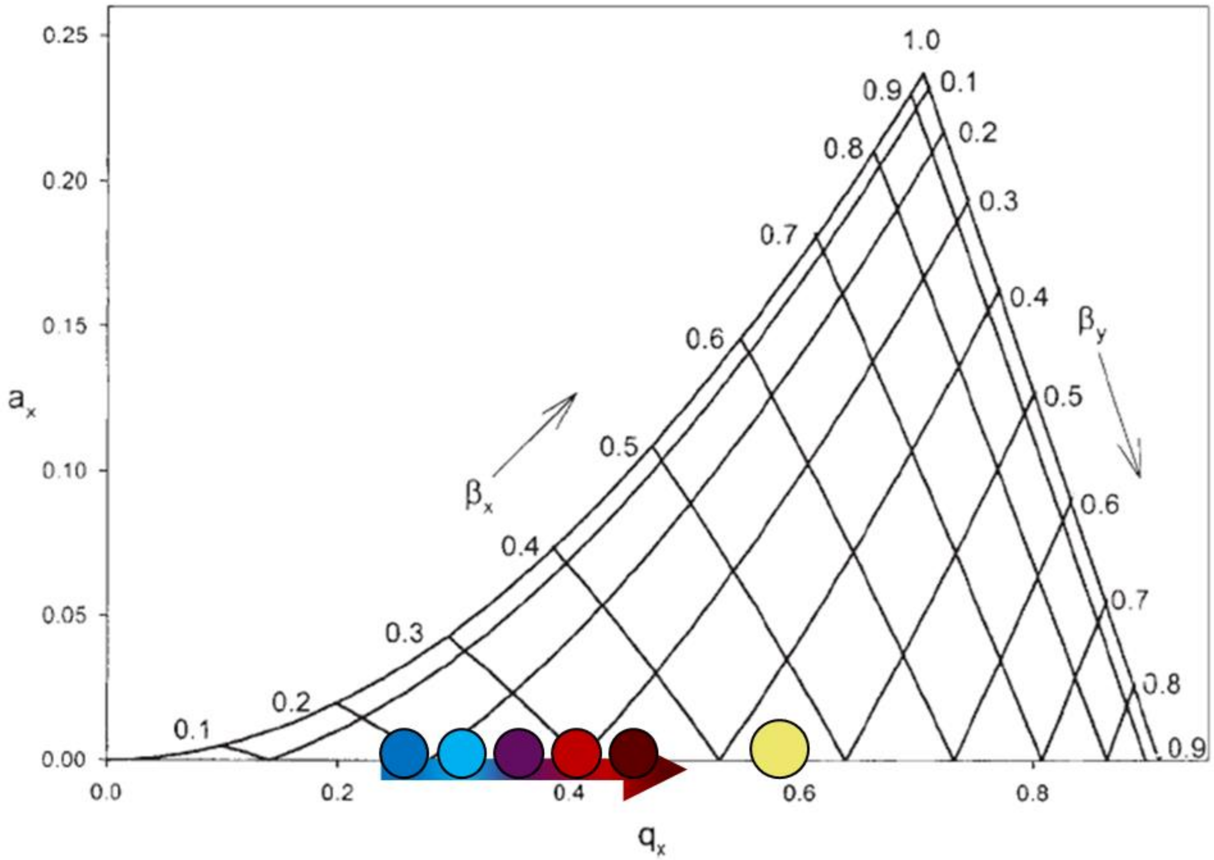

Figure 2.11 Mass instability schematic which utilizes complex waveforms. Yellow circle represents *a*-*q* hole.

The second method which involves complex waveforms is as follows. A static base freuqncy keeps a population of different m/z spcies stable. The frequency scan of the auxiliary frequency generates moving *a*-*q* hole. This moving hole created by the auxiliary waveform allows for an alternative mass analysis and mass isolation. Although there are a few methods of operation,[2] the schematic in **Figure 2.12** highlights the scanning of the auxiliary frequency to sequentially eject low m/z ions. This functionality can be expanded by using a band-stop frequency scan in which the secular frequency of the ion of interest is passed over, thus creating a similar effect to QMFs.

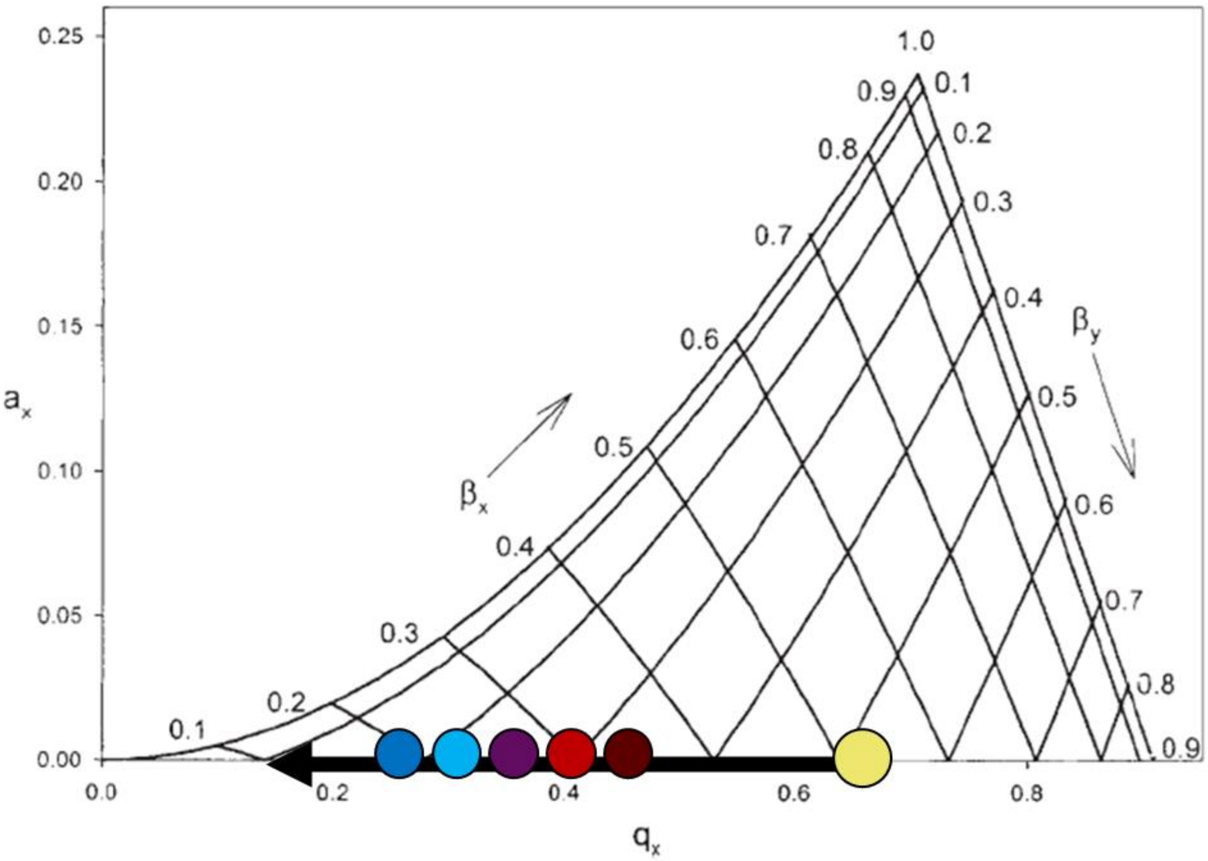

Figure 2.12 Auxiliary frequency scan to sequentially remove lower m/z ions.

Functionally, the presence of an auxiliary waveform applied to LQITs allows for ion manipulation that is m/z dependent. By changing the frequency of the auxiliary waveform, a hole can be generated in *a*-*q* space at the researcher's convenience for any use they may need. All of the above have involved the use of complex sine waves as the use of complex square wave operation of LDITs have been scarcely reported. A more in-depth explanation for how complex square waves can be generated and some of the limitations which have previously prevented such generation will be discussed in **Chapter 3**. By accomplishing complex square wave generation, the possibilities to eject any ion present in any cryogenic ion trap during any of the ion chemical reactions occurring in a cryogenic ion spectroscopy instrument facilitates future complex reaction schemes, by ejecting particular reagent and product ions from the CITs.

Section 2.5 Conclusion

This chapter has served as the foundation in which future discussions relating to LQIT operation will be built upon. By deriving stable ion motion in periodic electric fields, explaining the generation and uses of the Mathieu 1st stability region, an understanding of how LQITs can be used as a viable mass analyzer alternative to TOF-MS. Addressing the limitations of current sine wave-based LQIT-MS operation has led to the examination of a square wave based LDIT-MS. Differences between the two waveforms as they pertain to LQITs have been conveyed. Finally, the introduction of complex waveforms and the ability to manipulation individual ion species present in an LQIT have been introduced and will be expanded upon further in future chapters.

Section 2.6 Chapter 2 References

(1) Griffiths, D. J.; Inglefield, C. Introduction to Electrodynamics. *Cit. Am. J. Phys.* **2005**, *73*, 574. https://doi.org/10.1119/1.4766311.

(2) Douglas, D. J.; Frank, A. J.; Mao, D. Linear Ion Traps in Mass Spectrometry. *Mass Spectrom. Rev.* **2005**, *24* (1), 1–29. https://doi.org/10.1002/mas.20004.

(3) March, R. E. An Introduction to Quadrupole Ion Trap Mass Spectrometry. *J. Mass Spectrom.* **1997**, *32* (4), 351–369. https://doi.org/10.1002/(SICI)1096-9888(199704)32:4<351::AID-JMS512>3.0.CO;2-Y.

(4) March, R. E. Quadrupole Ion Traps. *Mass Spectrom. Rev.* **2009**, *28* (6), 961–989.

https://doi.org/10.1002/mas.20250.

(5) Pipes, L. A. Matrix Solution of Equations of the Mathieu-Hill Type. *J. Appl. Phys.* **1953**, *24* (7), 902–910. https://doi.org/10.1063/1.1721400.

(6) Konenkov, N. V.; Sudakov, M.; Douglas, D. J. Matrix Methods for the Calculation of Stability Diagrams in Quadrupole Mass Spectrometry. *J. Am. Soc. Mass Spectrom.* **2002**, *13* (6), 597–613. https://doi.org/10.1016/S1044-0305(02)00365-3.

(7) Miller, P. E.; Bonner Denton, M. *The Quadrupole Mass Filter: Basic Operating Concepts*; UTC, 1986; Vol. 63.

(8) Douglas, D. J.; Konenkov, N. V. Mass Selectivity of Dipolar Resonant Excitation in a Linear Quadrupole Ion Trap. *Rapid Commun. Mass Spectrom.* **2014**, *28* (5), 430–438. https://doi.org/10.1002/rcm.6795.

(9) Steen, H.; Kuster, B.; Fernandez, M.; Pandey, A.; Mann, M. Detection of Tyrosine Phosphorylated Peptides by Precursor Ion Scanning Quadrupole TOF Mass Spectrometry in Positive Ion Mode. *Anal. Chem.* **2001**, *73* (7), 1440–1448. https://doi.org/10.1021/ac001318c.

(10) Miller, P. E.; Denton, M. B. The Transmission Properties of an RF-Only Quadrupole Mass Filter. *Int. J. Mass Spectrom. Ion Process.* **1986**, *72* (3), 223–238. https://doi.org/10.1016/0168-1176(86)80021-0.

(11) Haag, A. M. Mass Analyzers and Mass Spectrometers. In *Advances in Experimental Medicine and Biology*; Springer New York LLC, 2016; Vol. 919, pp 157–169. https://doi.org/10.1007/978-3-319-41448-5_7.

(12) Hopfgartner, G.; Varesio, E.; Tschäppät, V.; Grivet, C.; Bourgogne, E.; Leuthold, L. A. Triple Quadrupole Linear Ion Trap Mass Spectrometer for the Analysis of Small Molecules and Macromolecules. *J. Mass Spectrom.* **2004**, *39* (8), 845–855. https://doi.org/10.1002/jms.659.

(13) Snyder, D. T.; Pulliam, C. J.; Wiley, J. S.; Duncan, J.; Cooks, R. G. Experimental Characterization of Secular Frequency Scanning in Ion Trap Mass Spectrometers. *J. Am. Soc. Mass Spectrom.* **2016**, *27* (7), 1243–1255. https://doi.org/10.1007/s13361-016-1377-1.

(14) Mathur, R.; O'Connor, P. B. Design and Implementation of a High Power Rf Oscillator on a Printed Circuit Board for Multipole Ion Guides. *Rev. Sci. Instrum.* **2006**, *77* (11), 114101. https://doi.org/10.1063/1.2387881.

(15) Sheretov, E. P.; Terent'ev, V. I. Theory of the Pulsed Quadrupole Mass Spectrometer. *Sov. Phys. Tech. Phys.* **1972**, *17*, 755.

(16) Richards, J. A.; Huey, R. M.; Hiller, J. A New Operating Mode for the Quadrupole Mass Filter. *Int. J. Mass Spectrom. Ion Phys.* **1973**, *12* (4), 317–339. https://doi.org/10.1016/0020-7381(73)80102-0.

(17) Brabeck, G. F.; Reilly, P. T. A. Mapping Ion Stability in Digitally Driven Ion Traps and Guides. *Int. J. Mass Spectrom.* **2014**, *364* (1), 1–8. https://doi.org/10.1016/j.ijms.2014.03.008.

(18) Brabeck, G. F.; Chen, H.; Hoffman, N. M.; Wang, L.; Reilly, P. T. A. Development of MSn in Digitally Operated Linear Ion Guides. *Anal. Chem.* **2014**, *86* (15), 7757–7763. https://doi.org/10.1021/ac501685v.

(19) Huntley, A. P.; Brabeck, G. F.; Reilly, P. T. A. Influence of the RF Drive Potential on the Acceptance Behavior of Pure Quadrupole Mass Filters Operated in Stability Zones A and B. *Int. J. Mass*

Spectrom. **2020**, *450*, 116303. https://doi.org/10.1016/j.ijms.2020.116303.

(20) Brabeck, G. F.; Koizumi, H.; Koizumi, E.; Reilly, P. T. A. Characterization of Quadrupole Mass Filters Operated with Frequency-Asymmetric and Amplitude-Asymmetric Waveforms. *Int. J. Mass Spectrom.* **2016**, *404*, 8–13. https://doi.org/10.1016/j.ijms.2016.04.002.

(21) Reece, M. E.; Huntley, A. P.; Moon, A. M.; Reilly, P. T. A. Digital Mass Analysis in a Linear Ion Trap without Auxiliary Waveforms. *J. Am. Soc. Mass Spectrom.* **2020**, *31* (1), 103–108. https://doi.org/10.1021/jasms.9b00012.

(22) Marsh, B. M.; Voss, J. M.; Garand, E. A Dual Cryogenic Ion Trap Spectrometer for the Formation and Characterization of Solvated Ionic Clusters. *J. Chem. Phys.* **2015**, *143* (20). https://doi.org/10.1063/1.4936360.

(23) Ding, L.; Sudakov, M.; Brancia, F. L.; Giles, R.; Kumashiro, S. A Digital Ion Trap Mass Spectrometer Coupled with Atmospheric Pressure Ion Sources. *J. Mass Spectrom.* **2004**, *39* (5), 471–484. https://doi.org/10.1002/jms.637.

(24) Snyder, D. T.; Pulliam, C. J.; Cooks, R. G. Single Analyzer Precursor Scans Using an Ion Trap. *Rapid Commun. Mass Spectrom.* **2016**, *30* (7), 800–804. https://doi.org/10.1002/rcm.7500.

(25) Snyder, D. T.; Peng, W. P.; Cooks, R. G. Resonance Methods in Quadrupole Ion Traps. *Chem. Phys. Lett.* **2017**, *668*, 69–89. https://doi.org/10.1016/j.cplett.2016.11.011.

(26) Lee, K. W.; Eakins, G. S.; Carlsen, M. S.; McLuckey, S. A. Ion Trap Operational Modes for Ion/Ion Reactions Yielding High Mass-to-Charge Product Ions. *Int. J. Mass Spectrom.* **2020**, *451*, 116313. https://doi.org/10.1016/j.ijms.2020.116313.

Chapter 3 Experimental Design and Operation

The purpose of this chapter is to explore the current iteration of the linear digital ion trap (LDIT) mass spectrometer, affectionately nicknamed “QTPI” for its comparatively compact size. A more detailed description of the instrumentation will be explained in this chapter, accompanied by several CADs. The operation of ion skimmers, apertures, and hexapole ion guides, will be mentioned briefly but will not be covered in extreme detail. Instead, much of this chapter is meant to explain how the LDIT itself functions, an overview of the circuitry needed for LDIT operation and how the raw data is converted to a usable mass spectrum. The mathematical theory was covered in **Chapter 2**; this chapter will provide an overview of the hardware and software development that was completed to perform radial ejection mass analysis needed for future CIS experiments, of which a large majority of instrument development time was spent. Note that the software and circuitry presented in this chapter will be approached from an overview perspective, instead of line-by-line software breakdown or exact component values. Details including explanations and screenshots of critical software code, KiCAD PCB structures, bill of materials, etc. will be covered in the **Appendix**. Finally, throughout this chapter there are several author’s notes that are intended to be helpful for anyone working on this or similar instrumentation in the Garand group.

Section 3.1 Instrumental Overview

A top-view CAD rendering of the entire instrumentation as of 4-7-2021 is shown in **Figure 3.1**. A brief overview of the experimental procedure is summarized below. The following subsections will cover each vacuum pump stage in detail as well as an unfinished study into an ion skimmer alternative. Objects colored yellow (capillary, skimmer, LDIT endcaps, and exit optics) have only static DC voltages applied to them throughout instrument operation. Green electrodes (hexapole ion guide one and two) are operated in radiofrequency (rf) only mode, consisting of a large amplitude (300 V_{pp}) high frequency (1 MHz) sine wave with no DC potential between rod pairs. A singular orange small diameter aperture is pulsed between two voltage states to break continuity of the ESI source. X-axis LDIT electrodes are shown in red, Y-axis electrodes are omitted for visual clarity. A section detailing the LDIT can be found in Subsection 3.1.3 . Finally, the continuous electron multiplier (CEM) detector housing is colored in blue. All electrodes have some static DC voltage that is applied to them, causing a general voltage gradient from the front of the instrument (capillary) to the back of the instrument (LDIT back endcap) that facilitates ion transport. When AC signal is present (hexapole ion guides and LDIT square waves), it is superimposed atop a DC voltage such that both phases of AC signals are floated equally. This causes no Mathieu *a* component for hexapole ion guides, nor does it contribute to any already present Mathieu *a* component in LDIT operation. Static DC voltages are supplied by multi-output ±100 V adjustable voltage power supplies which are located on an adjacent 19-inch electronics rack (not shown). Sine wave generation is accomplished by circuitry adapted from O'Connor *et al*[1]. Square wave generation and amplification circuits are adapted from Reilly *et al*[2,3].

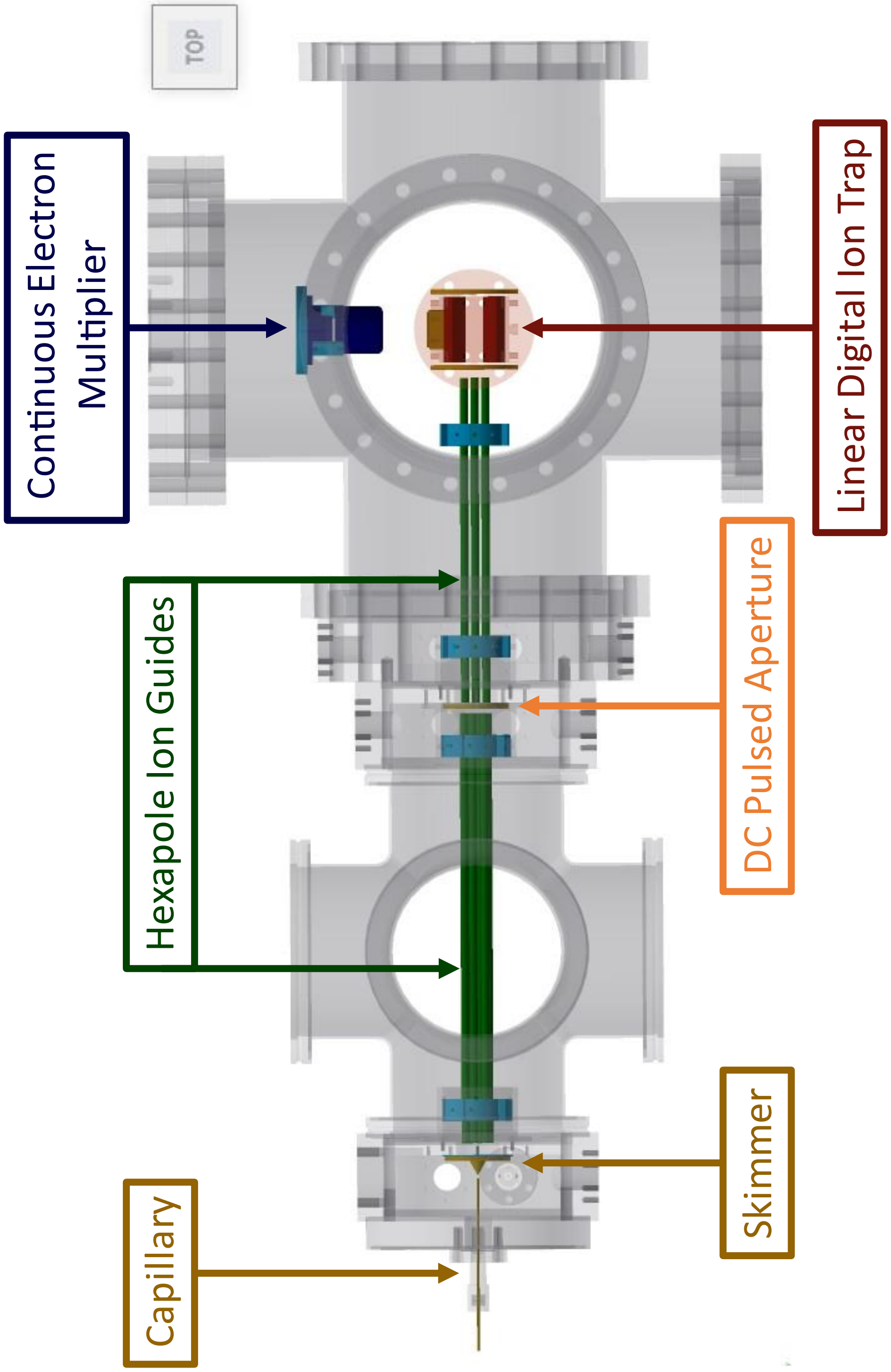

Figure 3.1 Top-down CAD QTPI instrumentation.

Ions are generated by means of a 2 kV ESI source consisting of a 30 µm silica tip (New Objective PicoTip) pumped at rate 2.0 uL/min (not shown). A steel capillary inlet (I.D. = 0.3 mm) coupled with a brass skimmer (I.D. = 0.381 mm) transports ions into differentially pumped vacuum regions. Ion transport is achieved by two rf-only hexapole ion guides operating nominally at 1 MHz 300 V_{pp} intersected by a small diameter aperture (I.D. = 1.27 mm). A pulsed DC voltage is applied to the aperture to convert continuous ion generation to temporally short (<25 µs) packets for mass analysis. Helium buffer gas is introduced directly into the LQIT housing by a precision leak valve (Granville Philips 203) to quench axial motion of ions entering the LDIT. Pressure is held at roughly 5 x 10^{-5} Torr throughout mass analysis in the final vacuum chamber containing both LDIT and CEM detector. Ions enter the LDIT by means of a planar endcap held at a static DC voltage and are prevented from exiting by means of a second endcap held at a slightly higher DC voltage. Upon collisionally cooling for a variable time (from 100 ms to 500 ms), ions are sequentially ejected via a downward stepped frequency sweep, where lightest m/z ions are radially ejected from a 0.5 mm by 17.75 mm exit slit milled into the one X-axis LDIT electrode. Once ejected, ions are guided by DC deflectors, then strike a CEM detector, whose signal is amplified by a transimpedance amplifier (Philips Scientific 6931), digitized for software collection by means of a USB oscilloscope (PicoScope 5243A) and interpolated by custom LabView software.

3.1.1 Ion Skimmer and Ion Funnel Region

This region is held at roughly 4 Torr by a 11.33 L/s rotary vane mechanical pump (Varian SD-700). Newly generated ions are shuttled from atmosphere to the first vacuum region via a narrow capillary held at high (100 V to 500 V) voltage. Early into QTPI development, a prototype ion funnel was designed and fabricated with the intention of replacing the commonplace ion skimmer setup. Poor ion transmission through a skimmer[4] was the primary motivator for this project. The design was very heavily based off Shaffer *et al.*[4,5] The ion funnel contains a series of thin (0.254 cm) brass electrodes fabricated with inner diameters starting from 22.15 mm, reducing to 0.4 mm in size over a total of 22 electrodes. A DC gradient pushes ions from the capillary to the last electrode and is applied to each of the electrodes by means of a resistor network wired in series. A potential energy view is shown in **Figure 3.2** to illustrate this. Two oppositely phased 1 MHz 300 Vpp rf fields radially confine ions as they travel through the device. Adjacent electrodes receive oppositely phased rf. Separately, each rf phase is applied to corresponding electrodes by means of several capacitors wired in parallel at intervals between resistors in the network. A photograph of the ion funnel prototype containing the resistor and capacitor components is shown in **Figure 3.2**. The final electrode receives no rf signal but instead is held at a much lower (> 25 V difference from plate #21) voltage to funnel ions into the next vacuum stage. A CAD of the entire vacuum stage can also be found in **Figure 3.2**.

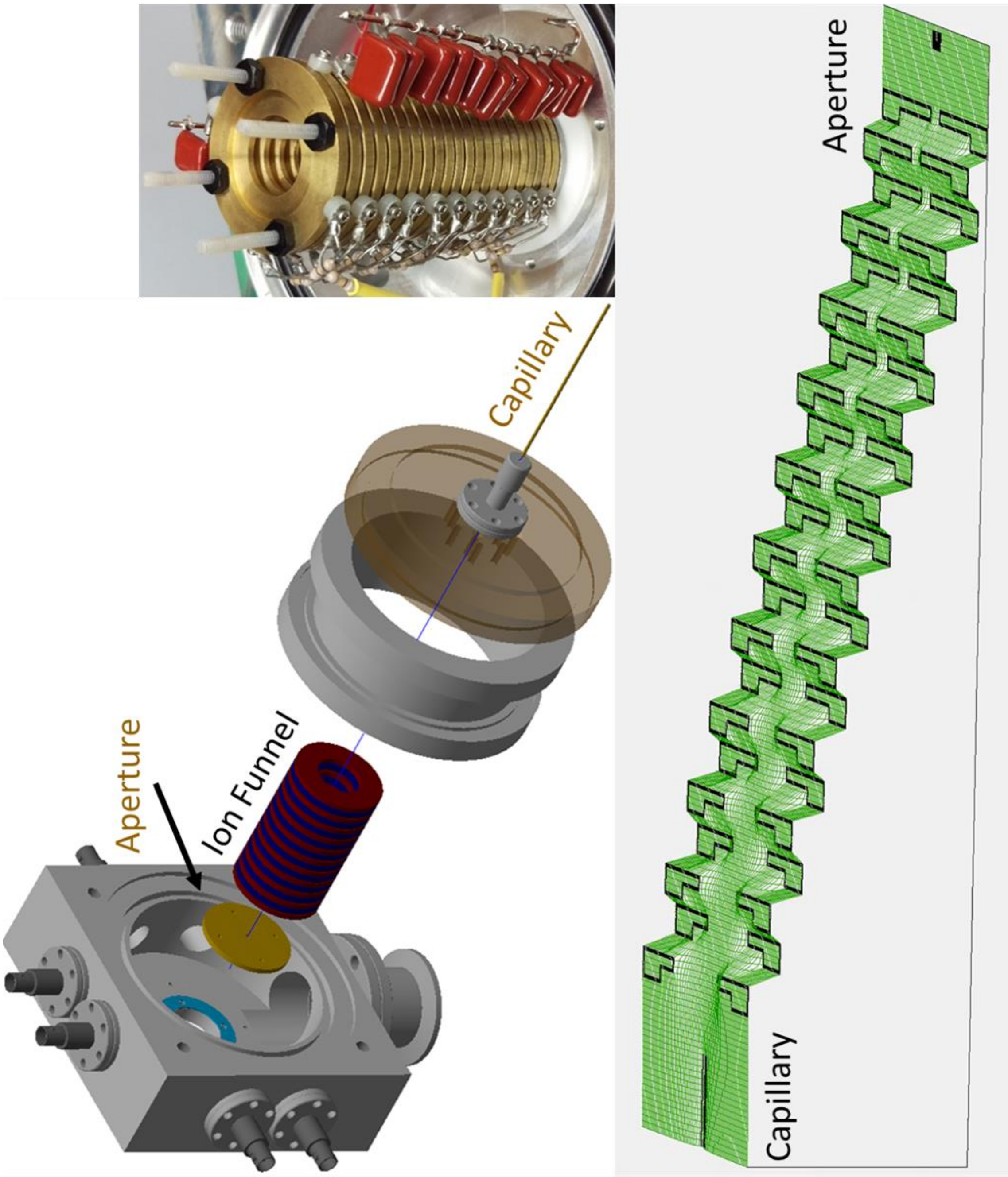

Figure 3.2 CAD of ion funnel block (top left), photograph of prototype (top right), and PEV (bottom).

Overall, this project showed promise and the prototype that was developed did facilitate ion transfer from capillary to eventual mass analysis stage. The primary reason no further designs were iterated and tested was due to a lack of means to do so. Direct comparisons were needed between total ion abundance and mass-calibrated quantification for ion funnel and skimmer blocks, as well as ion fragmentation occurring in the two devices. Both studies required a functioning, mass-calibrated mass analyzer. Unfortunately for this project, QTPI was not well-enough characterized to provide a detection method for those studies. Eventually, after a prolonged diagnostic session when QTPI was non-operational, the decision was made to replace the ion funnel for an already-fabricated ion skimmer to minimize points of failure on the instrument. The project was never revived once operational status of QTPI was achieved due to a time constraint for LDIT-based studies. Author's note: Ion funnels and ion carpets[6] are the next major instrument evolution for any kind of gas phase ion transport. With modern PCB printing techniques, designing flat, complicated devices that can have necessary circuitry built into the device would be a drastically improvement over traditional skimmer designs.

The Ion funnel block was swapped to a typical ion skimmer setup to simplify non-LDIT operation during exploratory phases. Capillary voltage is generally held above skimmer voltage and has been kept as high as 500 V relative to ground. Skimmer voltage is generally the highest voltage of the ±100 V DC supplies across all the axial dc gradient voltages. Ions exit the capillary in a plume, the voltage differential causes some of them to have favorable vectors to the skimmer's hole, thus letting roughly 1%[4] of ions through. Exploded and cross-sectional CAD views of the capillary plus ion skimmer section can be found in **Figure 3.3**, where again yellow electrodes are represented as static DC voltages applied. Author's note: the distance between the vacuum side tip of the capillary and the cone of the skimmer will dictate the maximum pressure not only in this region, but of both subsequent vacuum regions, therefore monitor all pressure gauges while adjusting this distance is paramount to proper operation.

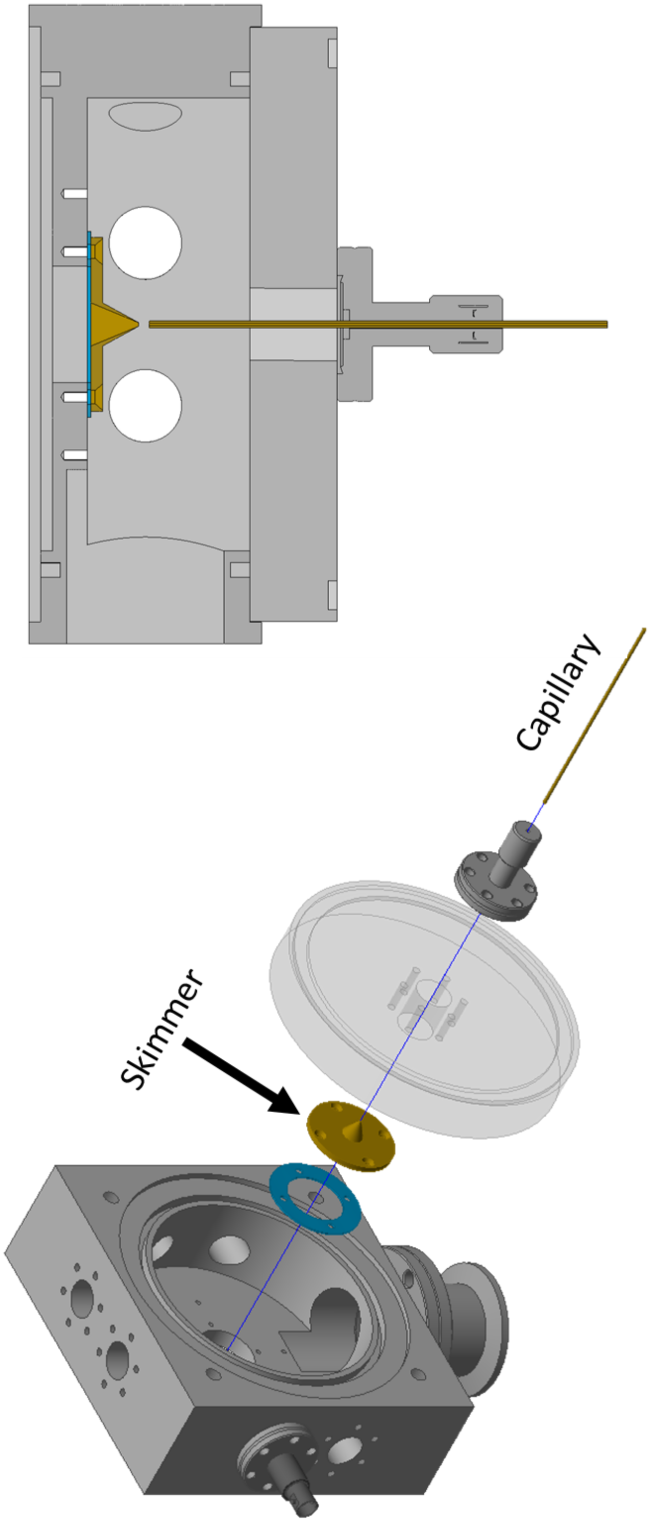

Figure 3.3 CADs of capillary skimmer setup.

3.1.2 Ion Guide and Pulsed Aperture Stage

Past the skimmer, ions enter a chamber whose pressure is roughly 3 to 5 mTorr by means of a 230 L/s turbomolecular pump (Balzers TPU 240), and travel through a 25 cm hexapole ion guide. This ion guide and the one in the next section are operating by two ≈300 V_{pp} 1 MHz sine waves oriented in opposite phases across two electrode pairs comprised of three straight circular stainless-steel rods. No DC voltage is applied between the electrode pairs, though the entire device is floated to a voltage control from the ± 100 V adjustable voltage supply on the electronics rack. A small diameter aperture acts to constrict the flow of air from this chamber to the 3rd vacuum stage and is pulsed between a HIGH and LOW voltage state. The timing for this is dictated by a delay generator (Stanford Research DG535), usually at the very beginning of the instrument cycle. Ion acceptance window into the 3rd stage can range from 25 µs to tens of ms. These voltage states are manifested by means of a commercial DC pulser (Willamette High Voltage PHVSW-005V) and the magnitude of them is dictated by two ±100 V adjustable voltage supplies. Author's note: if a second mechanical pump stage has yet to be installed prior to this chamber, both the pressure of the chamber and bias of the ion guide largely dictate the amount of non-ESI fragmentation that occurs. Adjustment of these voltages and the capillary-skimmer distance early in the diagnostic process may prove helpful as this distance dictates this chamber's pressure.

3.1.3 Linear Digital Ion Trap and Detection Stage

The ion guide present in this chamber is functionally the same as previously described. A pressure of roughly 5 x 10^{-5} Torr is maintained by a 360 L/s turbomolecular pump (Leybold Turbovac 360CSV). Post ion guide the planar endcap directs ions into the LDIT apparatus. Two planar endcaps act to axially confine ions once entering the trap. Radial confinement is achieved by four hyperbolic electrode that roughly follow the following equation:

$$y = \sqrt{x^2 - 0.5}$$

Where the 0.5 dictates the radius between electrodes in cm. One X-axis electrode has a 0.5 mm by 17.75 mm square hole milled into the apex of the hyperbola to use as ion extraction for radial ejection. **Figure 3.4** shows an exploded view CAD of the LDIT used in this thesis, with a cross-section of the trap present to illustrate the radial ejection slit. As above, yellow electrodes are kept at static DC voltages, and red and blue electrodes have both AC and DC components where adjacent AC components are 180° out of phase of one another. For the overwhelming majority of experiments the amplitude of the AC component was locked to either 150 V_{pp} by means of an adjustable 500 V DC supply (Advanced Energy 1/2C24-NP250) or 100 V_{pp} by means of a 100 V 4 A DC supply (Acopian A100HT400). The LDIT electrodes, and housing unit are made of copper to facilitate future CIS experiments require cryogenic cooling (see **Chapter 6**).

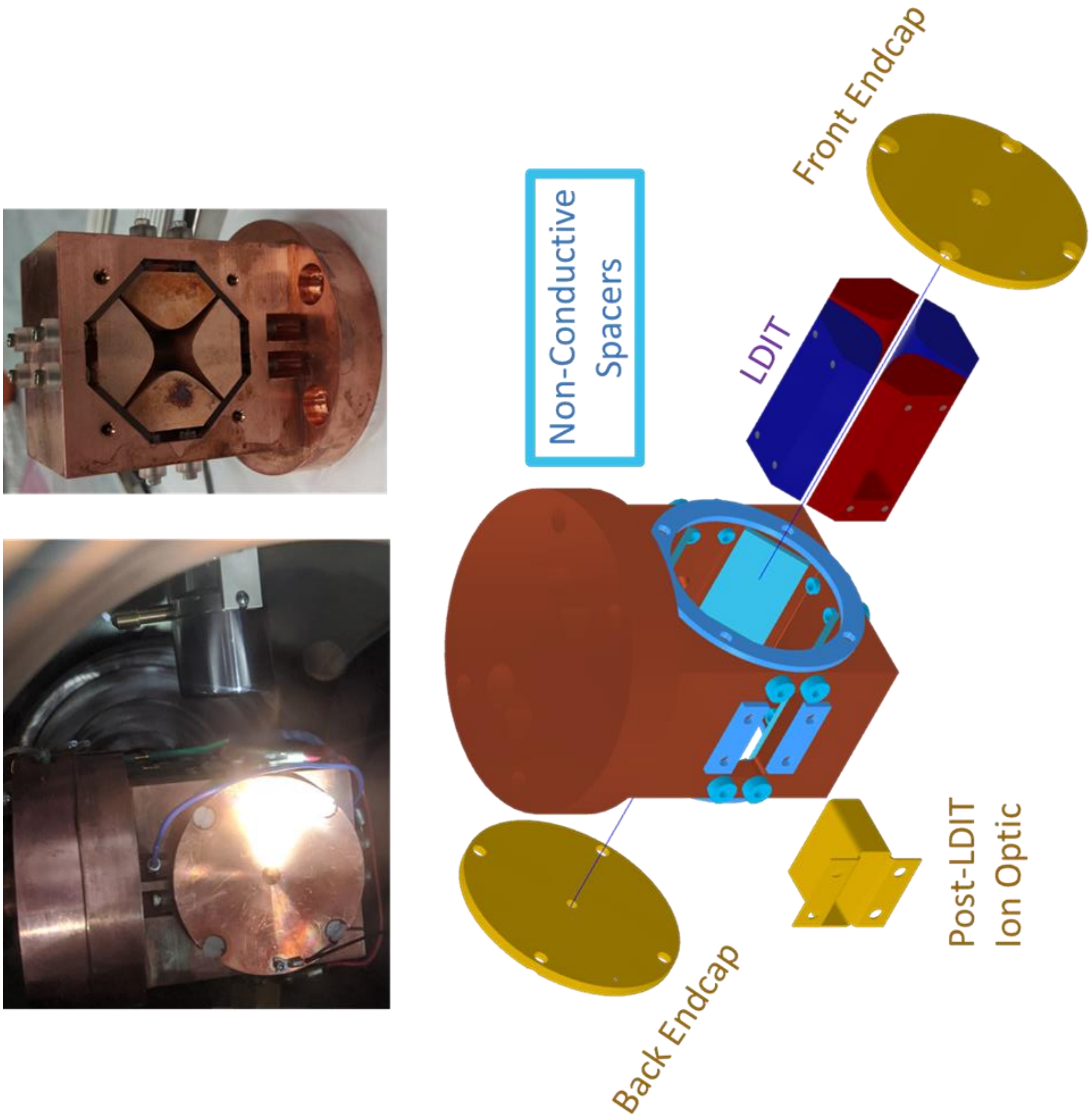

Figure 3.4 CAD of LDIT used in QTPI with pictures.

Post-LDIT ions are focused by DC deflectors and accelerated through roughly 10 cm of empty space then detected by a CEM detector held at -4 kV. Several voltages have been experimented with for the post-LDIT optics, but generally -300 V to -1200 V were used. Originally, a microchannel plate was used for detection, but the need for pressures above the recommended operation led to CEM incorporation. **Figure 3.5** shows an exploded CAD view of current CEM implementation. A big thanks to Dr. Lloyd Smith for providing a retired Thermo LCQ-MS instrument which was disassembled to harvest the CEM detector, and a big thanks to Dr. Martha Vestling for donating a retired Bruker TOF-MS instrument to obtain the microchannel plate detector.

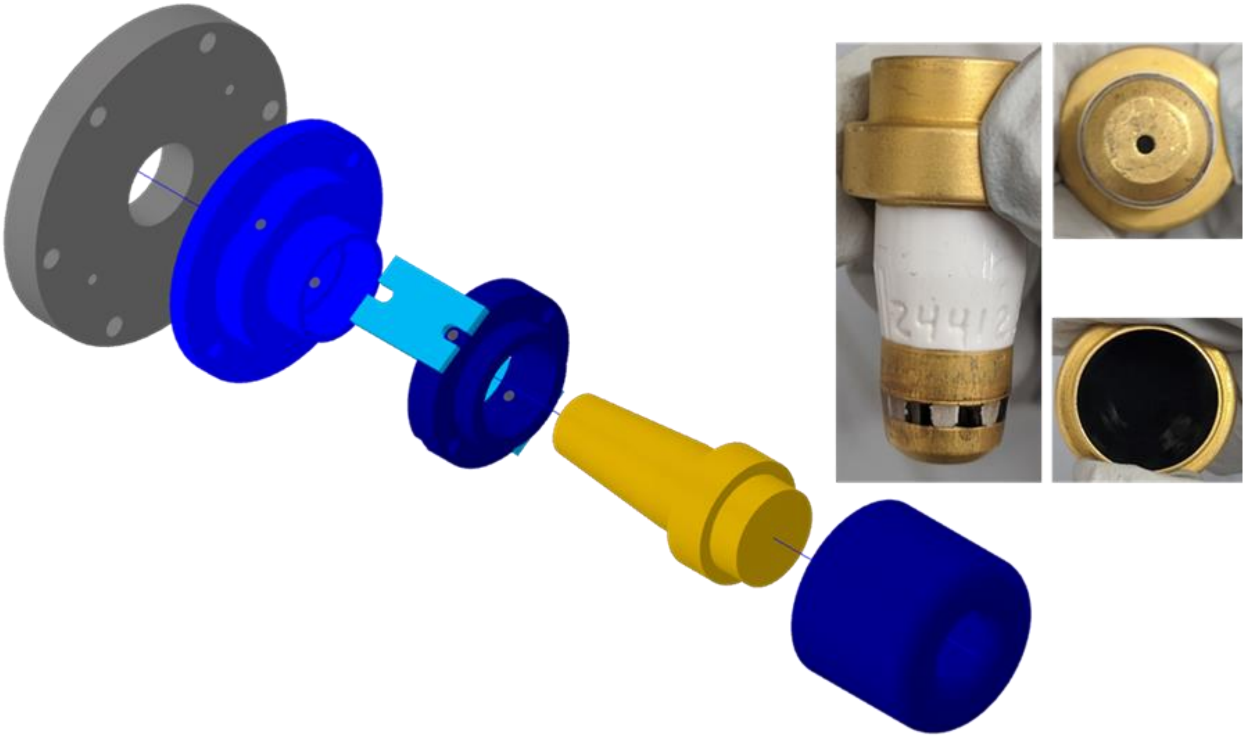

Figure 3.5 CAD of CEM detector with photographs.

Section 3.2 Linear Digital Ion Trap Instrument Cycle

Before detailing software and circuitry developed for successful LDIT operation, clarifying frequency and duty cycle waveform intervals and their functions will make the proceeding sections significantly easier to digest. Upon entering the LDIT, ions experience four distinct intervals before radial ejection: trapping, mass filtration, selective species exclusion (SSE), and mass analysis. These intervals are constantly looped by means of the waveform generator firmware. Circuitry developed to generate these square waveforms and their amplification will be covered in Section 3.4 . It is important to note the nomenclature for square waves before detailing the intervals. Unless otherwise noted, the same frequency but opposite phases are applied to the X-axis and Y-axis separately. Independent duty cycle control is achievable for the X-axis and Y-axis separately. These are represented as the percentage of the HIGH duration relative to the entire period. An example configuration would be 700 kHz with 55/47 duty cycle pairing on the X and Y axes, respectively. Finally, the amplitude of the square wave is denoted in peak-to-peak voltage, or V_{PP}, and is locked to 100 V_{pp} unless specified. **Figure 3.6** shows a block diagram of how these intervals are arranged to perform a single LDIT instrument cycle.

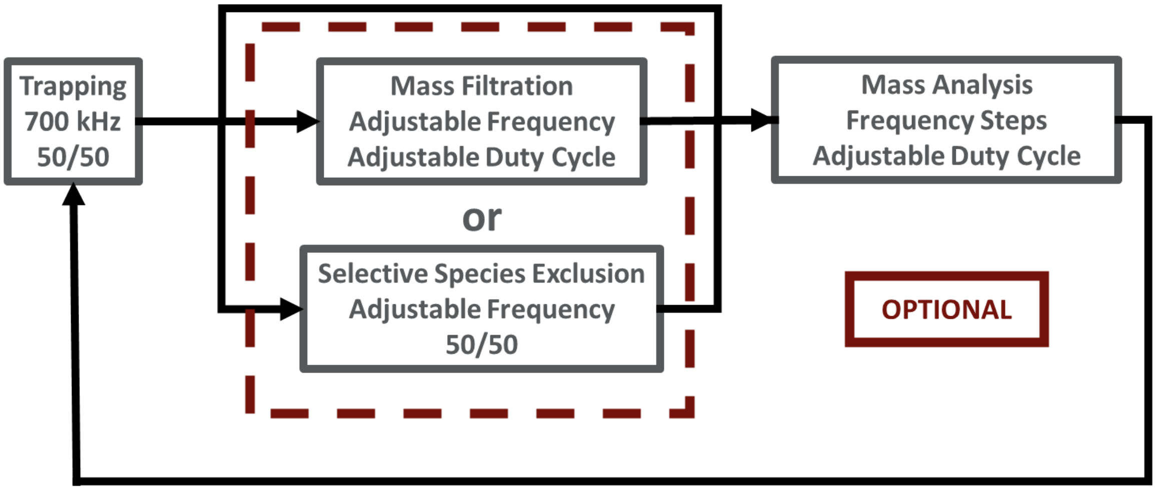

Figure 3.6 Block overview of LDIT instrument cycle.

3.2.1 LDIT Trapping Interval

Immediately upon entering the LDIT, ions are greeted with 700 kHz 50/50 square waves. This corresponds to the maximum frequency attainable by current square wave amplification circuitry, dictating an experimentally determined low mass cutoff of ≈75 m/z. Functionally, this interval is designed to collect the broadest mass range possible and allow them to collide with collisional cooling buffer gas (He) for 100 ms to 500 ms. As the duration of this trapping period is increased, a better signal response of all ions is observed (data not shown). With trapping durations lasting 500 ms and mass analysis taking anywhere from 20 to 150 ms, the maximum time between new mass spectra is close to 700 ms. With a rolling average of 10 MS for adequate noise averaging, this results in a genuinely new averaged MS every 7 seconds. Such long trapping durations should only be used when necessary, as most mass analysis will not require this long of instrument cycles.

3.2.2 LDIT Mass Filtration and Selective Species Exclusion Intervals

Once adequate collision cooling has occurred, two optional intervals can be incorporated by means of user control in the waveform generator's firmware. The difference between these two intervals are the roles they provide. The mass filtration interval is used to isolate of a single m/z species from a sample containing several different m/z species, functionally similar to mass gating in current TOF-MS CIS instrumentation. This is accomplished through instantaneously changing of the frequency and duty cycle pairing from the previous 700 kHz 50/50 to a frequency and duty cycle which brings the ion of interest to the apex of the Mathieu stability region, roughly a = 0.236 and q = 0.550. The theory of mass isolation in a quadrupole ion trap was covered more in **Chapter 2**. The minimum duration of this interval is roughly 10 µs. This duration limitation is solely based on the time it takes to update the frequency on the waveform generator. Current user control only allows for direct frequency and duty cycle control, requiring optimal frequency and duty cycle settings for mass isolation to be determined experimentally.

Results pertaining to the inception of this interval can be found in **Chapter 5** and the immediate uses of this interval can be found in **Chapter 6**.

The function of the SSE interval is to selectively exclude individual m/z species of disinterest. This interval requires the use of complex square waveforms, whose generation are covered in later sections. As with the trapping interval, 700 kHz 50/50 square waves are applied to both X-axis and Y-axis. On only the X-axis, a small amplitude (0.1 to 10 V_{pp}) adjustable frequency square wave is superimposed atop the base 700 kHz frequency. At the time of writing both the base waveform duty cycle and the superimposed duty cycle are locked to 50%. Presently the user interface is functionally identical to the mass filtration interval where a single adjustable auxiliary frequency is selected, also requiring experimental determination of per-application frequency. Author's note: if complex waveform generation becomes prominent in Garand group instrumentation , FPGAs will make generating a dynamic number of SSE frequencies and duty cycles significantly easier. The same can be said for dipolar mass analysis as well.

Switching between these two intervals is done via variable control on the Arduino interface. Additionally, both intervals can be bypassed if not needed. At the time of writing only mass filtration or SSE intervals are possible, not both. Both intervals could easily be implemented in existing waveform firmware by simply adding them into the interval loop sequentially. At the time of writing, these intervals serve no function for improving mass analyzer performance, which was the primary research objective. These techniques were developed solely with the intention of future CIS experiments, which have yet to be explored. Examples of how they can be used for CIS will be covered in **Chapter 5 and Chapter 6**.

3.2.3 Mass Analysis Interval

When the aperture voltage is brought LOW, ions are accumulated in the LDIT by the trapping interval, then optionally manipulated by mass filtration or SSE intervals, and finally are subjugated to a downward stepped frequency sweep. Rather than choosing a start, stop and Δfrequency, the user designates which start, stop and Δm/z the mass scan will be performed over. The waveform generator then dynamically calculates the applied frequency at each m/z step by means of the Mathieu *q* equation given below, rearranged to solve for m/z.

$$\frac{m}{z} = \frac{eV}{q r_0^2 \pi^2 f^2}$$

Where V, q and r_0 are the zero-to-peak voltage, q_{eject} and effective radius of the LDIT, respectively. These variables serve as calibration parameters which mimic experimental parameters such that V = 50 V_{0p}, and r_0 = 0.005 meters. There are two unintuitive aspects about this on-the-fly frequency calculation. The first that is the value of q is never known. Usually, when the duty cycle pairing is 50/50, the LDIT should be operating in a mass instability mass scan,[8] such that a = 0 and changes in frequency cause ions to be scanned across the Mathieu q-axis, eventually ejecting at q = 0.7125.[9] The LDIT is never operated in this manner. By moving the duty pair away from 50/50, (i.e., one electrode pair is above 50%, the other below 50%) significantly better resolving power can be attained due to a shift in the pseudopotential wells for the X-axis and Y-axis, favoring the detection axis. Functionally, this is similar to adding a DC bias between electrode pairs in sine wave LQIT operation. As such, the Mathieu a component is almost never equal to zero, making the position along the Mathieu stability region boundary line difficult to calculate. Instead, the user controller calibration q parameter from the equation serves as an arbitrary calibration constant.

The second unintuitive aspect of this calibration equation is that although the theoretical *V* and r_0 are known, through circuit inefficiencies and mechanical construction imperfections, these values differ from the theoretical values. At the end of the day, this on-the-fly frequency calculation is used as an initial guess for calibration purposes until external calibrant are used for final calibration. A full description of the calibration workflow is given in **Chapter 4**.

Additional to the frequency calculation, there is also a user input for determining how many periods the frequency scan will stay at a given step. This is also done by a user-controlled variable in the waveform generator's firmware and is usually only changed when the Δm/z is changed. Every time a new frequency is reached after the designated number of periods, an external channel on the waveform generator provides a temporally dynamic pulse, which is also recorded by the analog-to-digital converter (ADC) and is used for later data processing (see Section 3.3). Once the mass scan is complete, the entire interval loop is restarted with the trapping interval and an external channel on the waveform generation sends a signal to the delay generator, which begins a new instrument cycle. A sample stepped frequency scan can be seen in **Figure 3.7**.

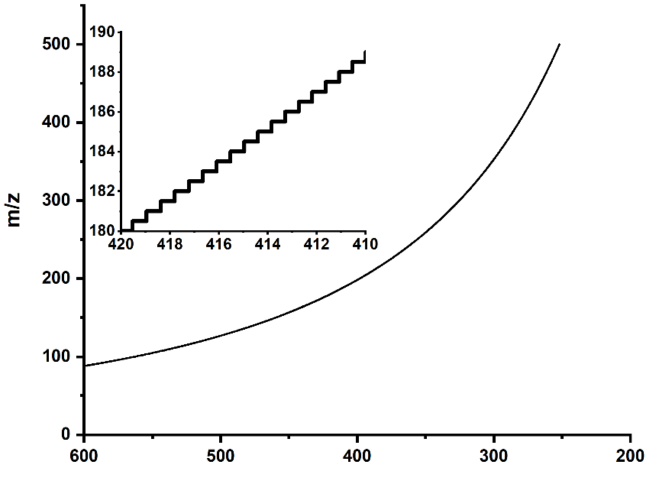

Figure 3.7 Downward stepped frequency curve for LDIT mass analysis.

Section 3.3 Data Acquisition and Processing

Once ions reach the CEM detector, a 100 MHz bipolar transimpedance amplifier converts the resulting current to a voltage readable by a USB-oscilloscope acting as an analog-to-digital converter (ADC). The ADC streams data to a PC, which is interpolated by a LabView program for post-processing, averaging, and display. **Error! Reference source not found.** summarizes the events that lead to real-time display and acquisition.

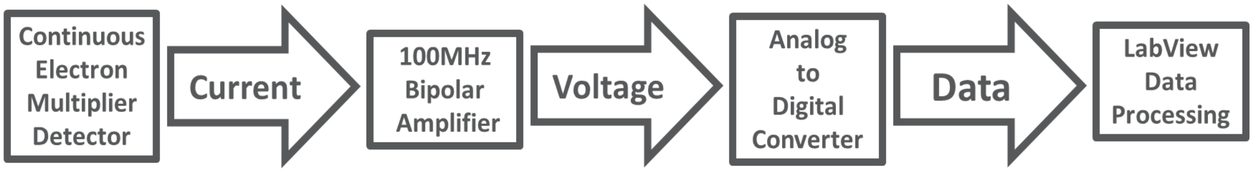

Figure 3.8 Block diagram navigating data collection from post detector to Labview display.

While functional, the transimpedance amplifier and ADC are both not well suited for this instrument and replacements should be found in continued development. Both devices were initially purchased with TOF-MS applications in mind, i.e., low nanosecond data acquisition rate and less than 250 microseconds data acquisition windows. High amplifier response rate is useful, but problems arise from the significantly longer mass scan times, i.e., tens to hundreds of milliseconds. To compensate for this, data is constantly streamed from the ADC to the PC instead of pre-defined “blocks” of data stored locally on the ADC’s volatile memory. This is problematic because the current ADC was not originally designed for this application, and data transfer to the PC is slower than the instrument cycle. Additionally, the response amplifier itself is designed to detect spikes of current lasting ones to tens of nanoseconds, but LDIT ion packets are ones to tens of microseconds in length. Thus, tens of ion packets are detected per frequency step. A pulse counting amplifier would be better suited for this application.[10] Performance development of the LDIT system was prioritized over finding adequate replacements for both devices. Additional LabView programming was developed to help mitigate these inefficiencies.

The Low Voltage Waveform Generator (LVWFG) is responsible for the generation of square waves throughout the entire instrument cycle, covered in Section 3.2 . This device also outputs two 0 V to 5 V time-to-live (TTL) pulses which are collected by the ADC. The first is the SCAN channel, which stays LOW until the mass scan has started and remains HIGH until the end of the last mass scan step. The rising edge of this channel informs LabView when to start polling data from the ADC stream. The falling edge is used to dictate the global start time (t = 0 ms) for the next instrument cycle. The second channel, TRIGGER, sends a series of variable length pulses throughout the mass scan indicating when a new frequency step has been reached during mass analysis. The duration of the LOW state of this channel is arbitrary and is only used to generate a rising edges for the LabView binning program to recognize. **Figure 3.9** offers a visual representation of these two TTL channels.

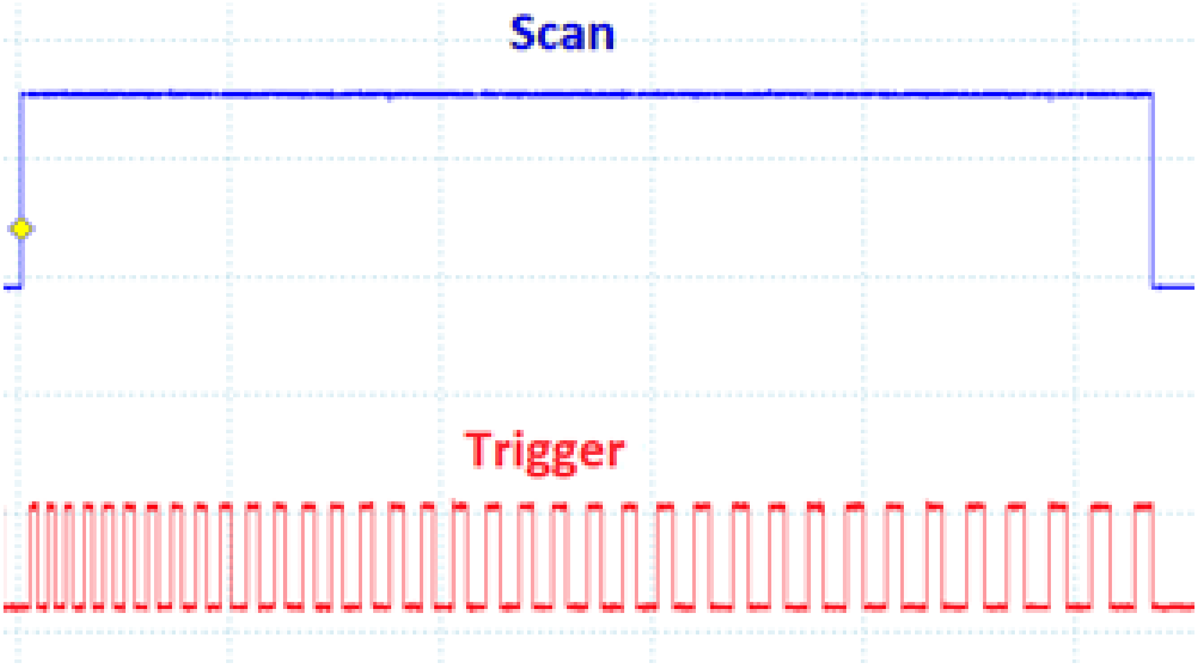

Figure 3.9 SCAN and TRIGGER TTL channels generated from LVWFG.

Due to the temporal length of mass scans and the need to bin the ion current vs. time data, a custom LabView program was developed to act as a dedicated oscilloscope replacement. **Figure 3.10** proves a block diagram overview of this program and more detailed screenshots of critical components can be found in the **Appendix**. Before running the LabView program at the start of a day, the user will input several parameters such as starting m/z, m/z step, various ADC collection parameters (number of samples, time between samples, voltage trigger thresholds, etc.), and others. The overwhelming majority of these settings do not change day-to-day. Some hidden back panel constants are established on program start to correctly interface a connection to the ADC. Once a connection has been opened, data is constantly streamed from the ADC to LabView. Three time domain voltage data sources are inputted into LabView from the Pico: ion response voltage (DATA), TTL mass scan duration (SCAN), and TTL variable length binning windows (TRIGGER). At the rising edge of the SCAN channel, LabView polls the current streaming values from the ADC for a variable amount of datapoints (usually two million). These three 2 million data arrays are then kept in volatile memory on the PC. These data arrays are manipulated by the binning subVi, which will be covered below. Once the three data arrays are converted to one 2D array consisting of ion response vs. m/z step, this array is fed into another subVi where a rolling average of previous instrument cycles have been stored. The number of previous MS which are stored is user controlled. Once averaged, the 2D data array of average ion response vs. m/z step is displayed on the LabView front panel or saved to a .txt file. Aside from initialization parameters, LabView software is run in a continuous cycle by means of a WHILE loop. Upon user input, the WHILE loop stops, which results in closure of the Pico loop and a final 2D data array of averaged ion response vs. m/z step. When this is collected, the 2D array is saved as a .csv filetype. A detailed description of the current binning process is detailed below.

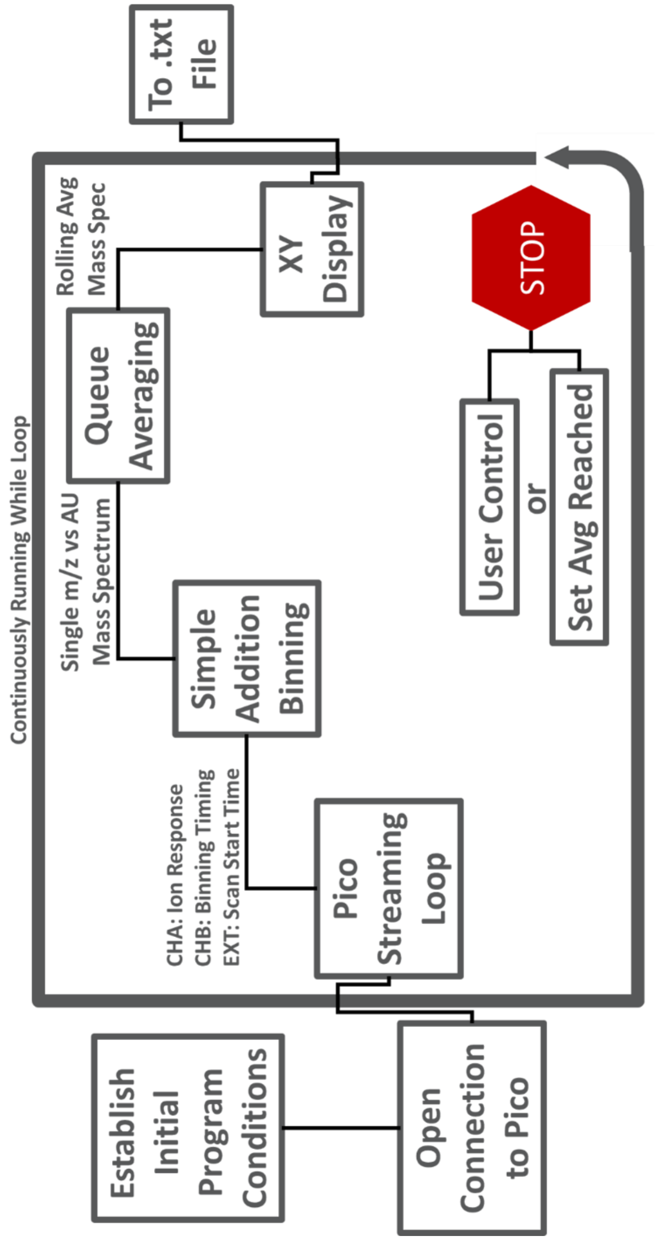

Figure 3.10 Block diagram of custom LabView program for QTPI operation.

During mass analysis, frequencies are stepped from high frequency to low frequency and held at each frequency step for a user-controlled number of periods, N. When a new frequency step is reached, TRIGGER is pulled HIGH and kept HIGH for N number of waveform periods, then returns LOW for a minimal amount of time. A series of pulses with variable temporal windows based on the frequency steps in a mass scan is produced. The purpose for these variable windows is twofold: to ensure the same ion extraction is achieved by all frequency steps and to evenly distribute the MOSFET switching noise present in the DATA channel. Without a variable TRIGGER window size, higher frequency datapoints would suffer from dramatically increased noise and lower frequency steps would not correctly bin all ions from a given frequency.

A description of the binning software is as follows. DATA and TRIGGER arrays (time domain voltage arrays) are loaded into volatile memory. TRIGGER is converted to a 1D Boolean array by means of a simple Y-value comparator to minimize the size of data stored. To avoid inaccurate Boolean assignment, the threshold of the comparator is set very close to the maximum Y-value of TRIGGER, usually 90% of maximum range. Indices for rising and falling edges of TRIGGER are recorded by means of a FOR loop with multiple IF structures which look for when j = TRUE and j-1 = FALSE for rising and j = FALSE and j-1 = TRUE for falling where j is the index of the 1D Boolean TRIGGER array. The indices of the rising and falling edges are compiled into two 1D integer arrays, TRIGGER_RISING and TRIGGER_FALLING, respectively. The large 1D DATA array is then separated into many smaller sub arrays by means of LabView's "Array Subsection" function residing in a FOR loop. The index and length of these smaller arrays are generated by TRIGGER_RISING and (TRIGGER_FALLING – TRIGGER_RISING) respectively. Screenshots of this LabView code can be found in the **Appendix**. The effect is the large 1D DATA array being binned into several smaller 1D arrays which correspond to individual m/z steps during mass analysis, thus creating a binned dataset.

These resulting DATA chunks are then subjected to a noise discrimination portion of the binning subVi. A Y-value threshold comparison is used to minimize noise contributions and the resulting bins are integrated by adding the Y-value of every index in each bin. The final output of this binning subVi is a small 1D array of binned double type values corresponding to the variable binning windows. Separately, another small 1D array of m/z values are generated from end user inputs of the starting m/z and m/z step size based on user input of the waveform generator. The two arrays are combined and converted to a datatype (cluster of arrays) that is required for display in LabView. Several iterations of binning methodologies including voltage discrimination, Fast Fourier Transform (FFT), and software based bandpass filtering have been prototyped, but not fully validated. At the time of writing a software based lowpass filter is prototyped, but not well enough developed to comment on. Author's note: these software solutions are band-aid fixes to help account for the sheer amount of noise that the MOSFETs from square wave amplification circuits produce. Either resolving the noise problem or finding hardware solutions for this binning process would yield significantly better results.

Once a single 2D array of Arbitrary Amplitude (AU) vs. m/z is produced, the data is then stored in a LabView "queue" system where a rolling average of MS scans can be dynamically generated and shown to the end user in real-time. This rolling average involved discarding the oldest 2D array in the queue once the newest 2D array is added to the queue. Per LabView cycle all 2D arrays are averaged before front panel display. Upon user designation (front panel button), an acquisition of a larger number of averaged MS scans (typically 100) can be collected in the same manner as above, then written to file for long term storage and external manipulation.

Section 3.4 Digital Ion Trap Circuitry

A large portion of the development work to get LDIT instrumentation operational was electrical circuit development. Early iterations of square wave generation came from off-the-shelf arbitrary waveform generators (Tektronix WaveStation) in which the frequency was scanned linearly, making mass calibration next to impossible. Additionally, square wave amplification was originally achieved by a singular commercial DC pulser (Willamette High Voltage) whose capabilities were lacking for the comparatively high frequency (700 kHz vs. 10 Hz) required for the targeted mass range (100 to 500 m/z). After extensive literature searches a paper by Hoffman *et al*[2] was found detailing an electrical circuit capable of amplifying square wave frequencies up to 700 kHz at an amplitude of 48 V_{pp}. After prototyping the circuit presented, a collaboration was formed with the principal investigator, Pete Reilly at Washington State University. This led to the modification and fabrication of two separate circuits, a square wave amplifier, nicknamed the High Voltage High Frequency (HVHF) pulser circuit, and a Low Voltage Waveform Generator (LVWFG) that was based on reference 3, also provided by the same collaborator. These circuits' functionality will be detailed in subsections 3.4.1 and 3.4.2 ,respectively.

3.4.1 High Voltage High Frequency Square Wave Amplifier

During initial development of QTPI, target frequencies and amplitudes of square waves were based off a low mass cutoff (LMC) from the following equation.[11]

$$\frac{m}{z}_{LMC} = \frac{V}{q_0 r_0^2 \pi^2} T_{RWF}^2$$

Where V is the zero-to-peak voltage of the AC component, q_0 = 0.7125 corresponds to the a = 0 boundary of the Mathieu stability region for square waves, $r_0 \approx 5$ mm based on the current LDIT electrodes, and $\mathrm{T}_{\mathrm{RWF}}^2$ = 2π/Ω, where is Ω the angular frequency as dictated by the waveform generator. Substituting a target LMC = 75 m/z, we determined a maximum frequency of 700 kHz and an amplitude of 50 V_{0p} at minimum. It was not until many years later that we would realize our mass scan was not operating along the Mathieu $a = 0$ line, thus making this LMC inaccurate. This calculation still provided a good order-of-magnitude for our circuit development. A printed circuit board (PCB) of the published square wave amplifier was fabricated and assembled. A block diagram of the HVHF circuit is shown in **Figure 3.11**. The purpose of the HVHF circuit is to take one square wave TTL input from the LVWFG and amplify it to a peak-to-peak amplitude defined by the V^+ and V^- inputs. This amplitude is typically set so that $V^+ - V^- = 100$ V, though the values of V^+ and V^- are referenced to a common DC voltage from one of the ±100 V adjustable supplied on the electronics rack. In **Figure 3.11**, the horizontal grey line is used to indicate that the top and bottom halves of the circuit are floated atop the V^+ and V^- inputs. The on-board power stage is comprised of the DC-DC converters that generate +15 V, -15 V, and +5 V relative to V^+ or V^- instead of being relative to ground. These DC-DC converters act to power all the MOSFETs and integrated circuits (ICs) on the board. The opto-isolation stage is where the TTL line and return connections are housed. Both sides of the board receive the same TTL input, it is just split for ease of PCB design. The ICPL2631 opto-isolator IC has a built-in light emitting diode (LED) emitter and photo diode receiver used to isolate the ground referenced TTL signal from each common referenced side of the board. The output of this stage is a common to common + 5 V square wave signal that mirrors the original TTL.

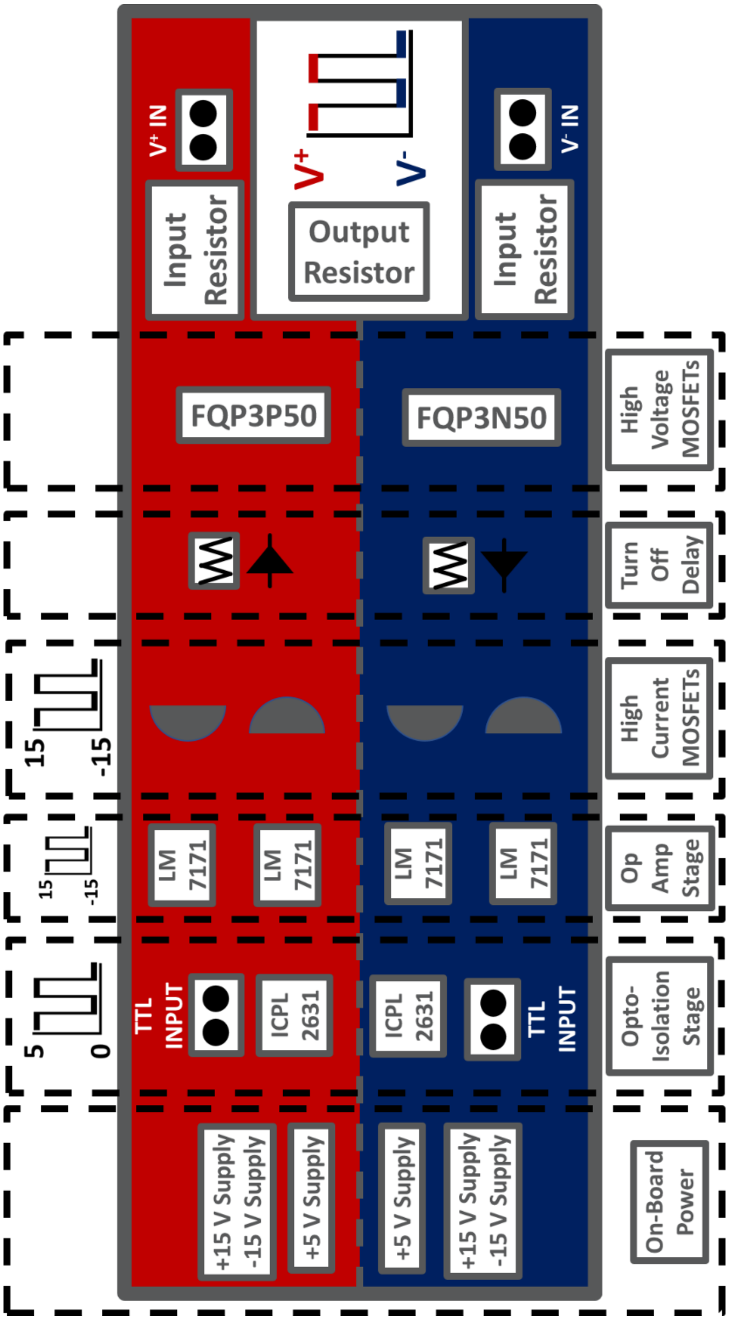

Figure 3.11 HVHF circuit block diagram.

This 5 V_{pp} square wave is then wired into two LM7171 operational amplifiers (hereafter Op Amps), which function as high-speed comparators. The inverting input is wired directly to a voltage reference held at 2.5 V relative to common (not shown). The effect is an amplification from a 5 V_{pp} square wave to a 30 V_{pp} square wave by means of the Op Amp's +15 V and -15 V rail inputs. This 30 V_{pp} square wave is the correct voltage to drive the downstream power MOSFETs but lack enough current to rapidly turn them on and off. Lower voltage, high current MOSFETs are used to amplify the LM7171 outputs at the high current MOSFETs stage. The output is the same 30 V_{pp} square wave but significantly higher current. These smaller MOSFETs have been upgraded through the years as they tend to be failure state of the device when frequencies exceed 700 kHz. Eventually, this 30 V_{pp} high current square wave is fed into the gate of either the FQP3P50 or FQP3N50 power MOSFETs for the V^+ and V^- sides of the board, respectively.

If both power MOSFETs were opened at the same time, the only components separating the V^+ and V^- inputs would be high wattage, 100 Ohm resistors (labeled input resistor on **Figure 3.11**), which would at minimum cause these resistors to explode and at maximum destroy the input voltage supplies! To prevent this, a 3W 5 Ohm resistor and ultra-fast (10 ns) diodes are used to act as turn off delay stage. The power MOSFETS are designed so that one (FQP3P50) is a P-channel MOSFET whose default state is OPEN when no gate voltage is applied, and the other (FQP3N50) is a N-channel MOSFET whose default state is CLOSED to help minimize this. Although the two power MOSFETs chosen are complimentary, the turn on and off delays never match up perfectly, which is why the turn off delay exists. When current flows into the gate of a power MOSFET, it travels through either the resistor or the diode depending on the diode's orientation. For the P-MOSFET, there is a delay to CLOSE the gate, and for the N-MOSFET, there is a delay to OPEN the gate. The effect is that there is a time when both are closed, but not where both are open, due to the diode orientation.

The output of both power MOSFETs are linked so that the output of the circuit is constantly switching between V^+ and V^- at a frequency defined by the original TTL signal from the LVWFG, as shown in **Figure 3.11**. Some example traces of the output can be seen in **Figure 3.12** for the maximum stable frequency (700 kHz) and significantly lower (100 kHz) frequency. As can be seen from the traces, there is a fair amount of ringing that occurs on the output. This is caused primarily by hysteresis of the gate opening and closing processes and by the turn on/off delay mismatch of the complimentary MOSFETs. A fair portion of this ringing can be alleviated by lowpass filtering the circuit output. This is done by an adjustable resistor on the output, which is tuned in accordance with the capacitive load the HVHF is driving (about 180 pF for one LDIT electrode pair). Doing so utilizes the output resistor and the capacitive load to generate an RC constant for lowpass filtering. At maximum frequency, the V^+ voltage state does not fully reach each target voltage until roughly 50% of the half-period. The exact reason for this is unknown, but we have speculated that the switching DC power supplies that have been used cannot provide the instantaneous current required to switch over the course of thousands of waveforms. Anecdotal evidence is given by the fact that if the amplitude of the 700 kHz square wave at the beginning of an instrument cycle is slightly (< 5 V_{pp}) higher than the same 700 kHz square wave at the end of a 500 ms trapping duration (covered in Section 3.2).

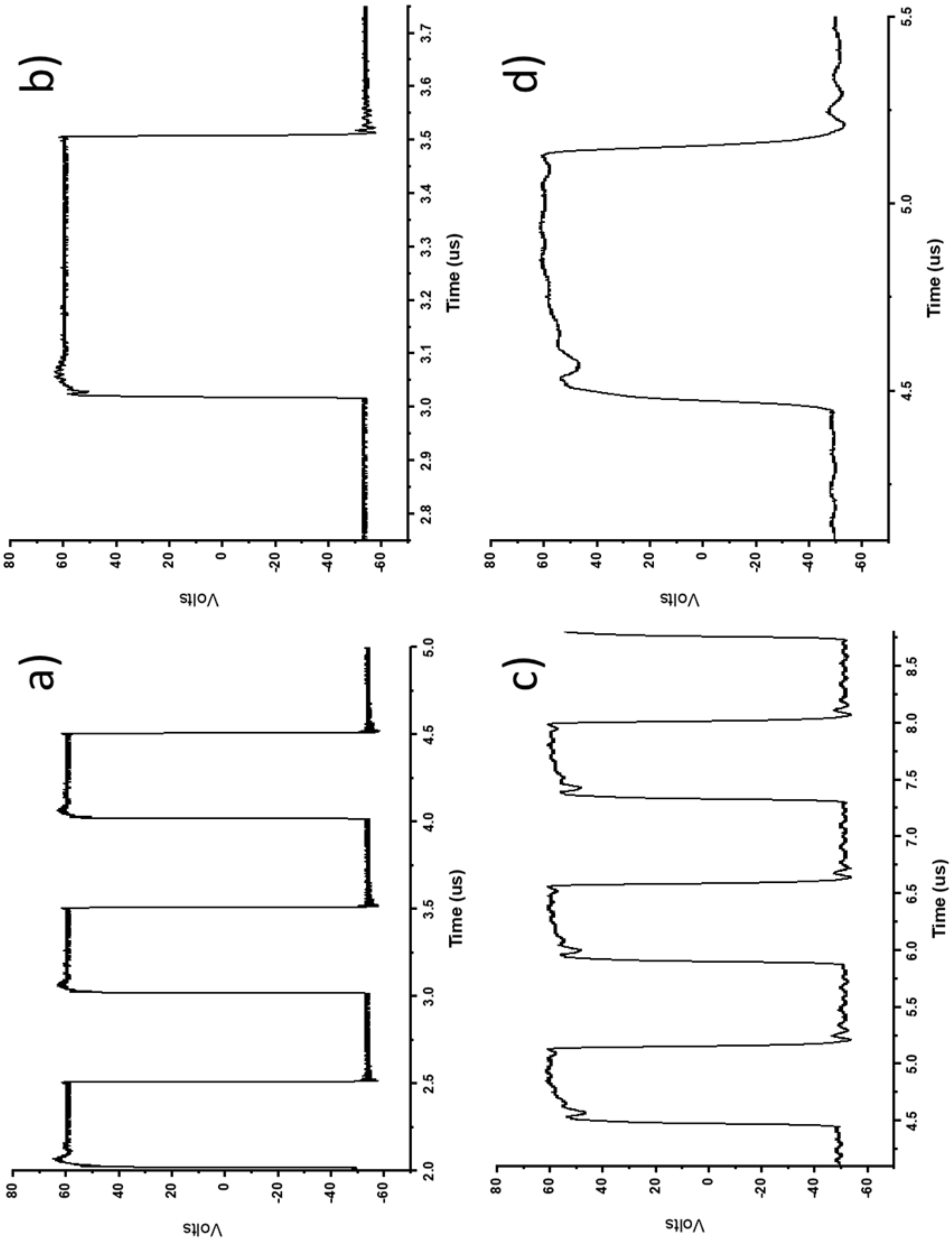

Figure 3.12 Oscilloscope traces of amplified square waves.

3.4.2 Low Voltage Waveform Generator

The original waveform generator that could produce square waves to confine and radially eject ions was woefully inadequate for our application. This was primary due to how it generated square waves. The device would wait for an external trigger from the delay generator, then linearly sweep from two pre-defined frequencies. This was problematic was due to the relationship between m/z and frequency. The relationship between m/z and frequency follows the given proportionality below.

$$\frac{m}{z} \propto \frac{C}{f^2}$$

By scanning frequency linearly with respect to time, when the conversion to m/z occurs, less datapoints per unit m/z were recorded in the beginning of the scan and more datapoints per unit m/z towards the end of the scan. The effect was a mass spectrum with non-uniform m/z spacing, which was not preferred. If instead the frequencies which correspond to each m/z at the desired Δ m/z steps were pre-determined, generating a list of frequencies and stepping between them would yield uniform m/z spacing. This causes a non-linear frequency sweep, but a uniformly spaced mass spectra, which is preferred.

Square waves can be distilled to a minimum of four points per period: the start of HIGH state, the end of HIGH state, the start of LOW state, and the end of LOW state. Some initial investigations were done to determine the viability of arbitrary waveform generators. These would allow a programmatic tailoring of the entire instrument cycle in one list of voltage state vs. time to be used for LDIT operation. Commercial solutions for this, however, proved to be inadequate. The limitation was in the number of datapoints an arbitrary waveform could be comprised of. Upwards of two to ten million voltage states were needed for a full instrument cycle, which commercial options either could not provide or were too expensive.

Around this time, our collaborator Pete Reilly made us aware of a prototype waveform generator his group was developing centered around an inexpensive microcontroller (Arduino) platform. Similar to the HVHF circuit development, PCBs were fabricated, a prototype was made, and some source firmware was provided for basic functionality. The Reilly group, at the time, primarily used this device to operate static frequency, variable duty cycle ion funnels and quadrupole mass filters[12]. A full description of critical software components can be found in **Appendix**. An overview of how the LVWFG hardware produces variable frequency, variable duty cycle square waves is shown in **Figure 3.13**, and a detailed description is given below.

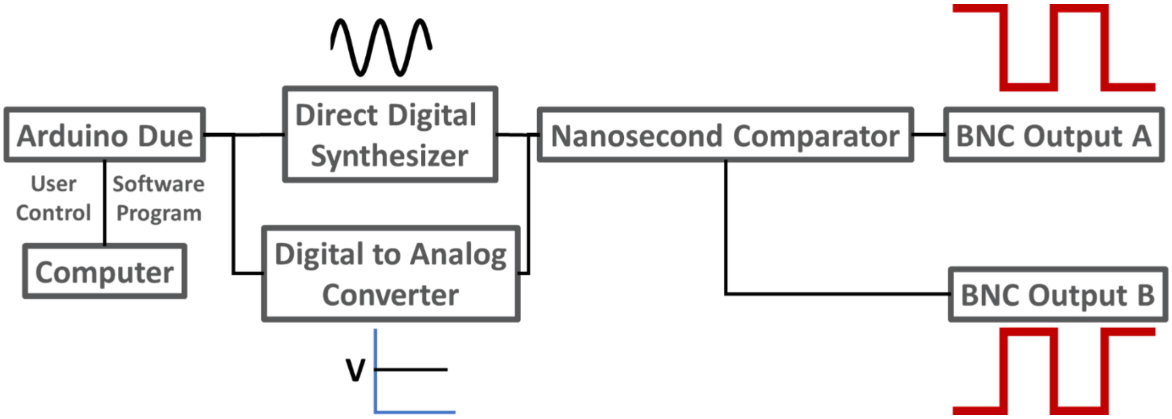

Figure 3.13 Block diagram of LVWFG hardware.

An Arduino Due acts as the Master Clock Unit (MCU) for the LVWFG. Communication between the LVWFG and PC is presently enabled by means of the "Serial Monitor" function of the Arduino IDE software. Text-based inputs are entered to update LDIT operation variables in real-time, not unlike DOS-based instrumentation from years past. A pre-written software using the Arduino's own language (functionally C++) is uploaded before serial communication is established. The three primary functions of text-input commands are: to start the LDIT instrument cycle (covered in Section 3.2) change instrument cycle variables such as start m/z, Δ m/z step, various duty cycles, etc., and finally to put the LVWFG in standby mode when not in use.

Direct Digital Synthesizer (DDS) modules are small form factor frequency synthesizer ICs that can produce a variety of arbitrary waveforms. For this application, simple 0 to 5 V sine waves are produced. The Arduino controls the frequency at any given time via a 32-bit frequency word. Unintuitively, a sine wave output from DDS modules is preferred at this stage, as opposed to square waves. This is because DDS modules can produce frequency differences as low as 1 µHz.[13] Unfortunately, sine waves offer no duty cycle control, which is critical of LDIT operation. Instead, separate Digital to Analog Converters (DACs) are used to generate 18-bit vertical resolution DC voltages ranging from 0 to 5 V, producing minimum voltage differences of $(5\text{-}0)/2^{18} = 19\ \mu\text{V}$. These DACs are also controlled by the Arduino via Serial Peripheral Interfaces (SPIs) communication. The outputs of the two devices are then fed into an ultrafast (< 10 ns) comparator to produce square waves with high frequency resolution and high duty cycle resolution. As the DC voltage is lowered below 2.5 V, more of the sine wave's period is registered as HIGH by the comparator. The inverse is true for raising the DC voltage, thus creating a variable frequency, variable duty cycle square wave output. Multiple DACs and comparators are used to generate output pairs, which are comprised of oppositely phased square wave outputs. There are three output pairs: DDS0, DDS1 and DDS2. Each output pair is comprised of one DDS module, two DACs, and two comparators. This produces two variable frequency variable duty cycle channels which are always oriented to be 180° out of phase.

Author's note: while current LVWFG hardware is robust and offers an intuitive programming interface, there are two areas that could be drastically improved. The first is the computer interfacing of the device. The software code is uploaded to the device non-volatile memory of the Arduino. Every time the device is power cycled, or the connection closed, all the program variables have been altered are re-instated to default upon reconnection. Some of these closes in connections can be from Windows update or computer malfunctions. This can be circumvented by proper LabView integration. A prototype of this was already developed, in that a connection to the Arduino was able to be opened, variables were able to be changed, and diagnostic outputs were able to be read the serial monitor equivalent. Due to a shortage of time, full integrate this functionality was not achieved. If a LabView front panel was established where the user would input the desired variable before the program was ran, these variables could be stored in LabView, which is very easy to establish current values as default in case of unexpected failure. The second improvement that could be made on this system is to completely move past the LVWFG, instead utilizing an FPGA. These devices function very similarly to the Arduino software, but are LabView controlled. Said devices typically have many digital outputs, which would largely make most of the next auxiliary waveform generation, covered in subsection 3.4.3 software based instead of relying on additional hardware circuitry.

3.4.3 Complex Square Waveform Circuitry

Once the upper limit of dipolarless LDIT operation had been achieved (see **Chapter 5**), it was evident that the integration of auxiliary waveforms was needed. With sine waves, this is typically done through a center-tapped transformer where the main high voltage 1 MHz sine wave is wired on one side and the auxiliary frequency is wired through the center tap. The frequency response of the transformer is tuned to the 1 MHz signal as it is unchanged during a dipolar frequency scan.[14] With square waves, this process is doubly complicated. First, transformers act as inductors, impeding massive fluctuations of current. Square waves are largely comprised as static voltages that are switched by means of large fluctuations of current, thus making transformers ineffective for square waves. Second, transformers have an effective frequency range that is often quite narrow. Frequency is the scanned parameter of the mass analysis interval, thus needed a wide dynamic range frequency range, which transformers do not offer. These factors led to investigations towards MOSFET based complex square wave generation based on existing HVHF circuitry. This proved successful with minor modification, consisting of changes to the passive resistor and capacitor values, and the change to the 30 V_{PP} high current MOSFETs noted towards the end of subsection 3.4.1 .

From subsection 3.4.1 , the upper and low halves of the HVHF boards are referenced not to ground, but to separate commons as defined by the V^+ and V^-, respectively. These commons are locked to $V^+ = 50$ V and $V^- = -50$ V under normal operation. If instead the V^+ and V^- commons were dynamically changed at an auxiliary frequency, the resulting downstream square wave amplification would result in a waveform which had frequency components of both the original base (downstream) frequency and the V^+/V^- amplitude modulations from the auxiliary (upstream) frequency. **Figure 3.14** shows a schematic of this complex waveform generation circuitry. The right hand HVHF circuit amplifies the base frequency, but the voltages it switches between is dictated by the current output of the upstream HVHF circuits. Rather than non-complex square wave amplification between V^+ and V^-, instead four voltage states, V^{++}, V^{+-}, V^{-+}, and V^{--}, determine the final amplitude of the complex waveform. Each of these voltages can be independently controlled, but voltage relationship must be maintained such that $V^{++} > V^{+-} > V^{-+} > V^{--}$. Under normal operation these values are locked to +55 V, +50 V, -50 V, and -55 V relative to a common set by one of the ±100 V adjustable DC supplies. This yields the same 100 V_{pp} base square wave, but an auxiliary 10 V_{pp} square wave is superimposed atop this. The example waveforms shown in **Figure 3.14** were designed to illustrate an easy visual understanding of the HVHF outputs. In the figure, the upper HVHF output generates a square wave pulse between V^{+-} and V^{++} for one half of the base frequency. The original base frequency controls the downstream HVHF, one auxiliary TTL input controls the V^{++}/V^{+-} upstream HVHF and the last controls the V^{-+}/V^{--} upstream HVHF.

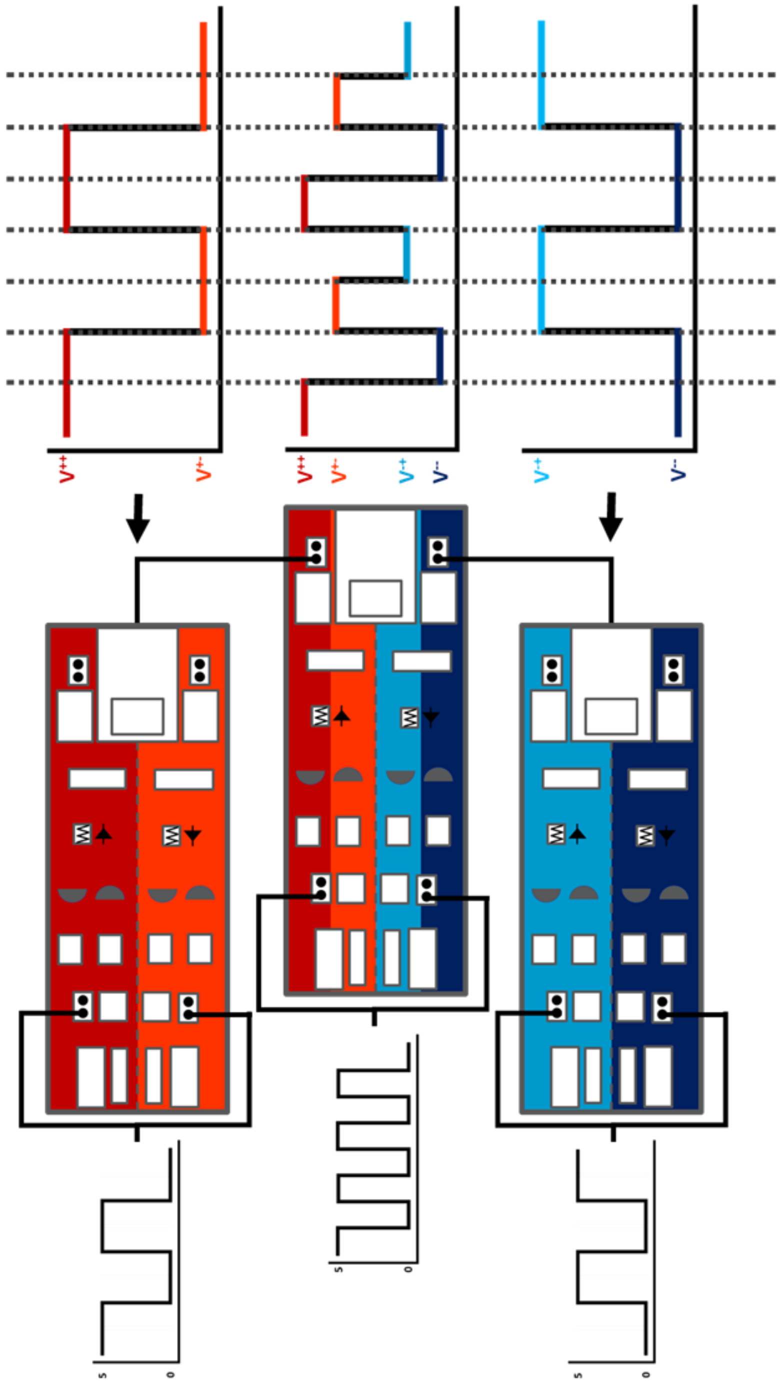

Figure 3.14 Complex waveform amplification circuitry schematic.

When the base frequency and auxiliary frequencies are phase coherent, in that $f_{aux} = f_{base}/N$ where N is an integer greater than one, the complex waveform can be thought of as an amplitude modulation of the base frequency rather than an actual superimposed auxiliary frequency. Extrapolating this amplitude modulation for higher values of N yields exponentially complex waveform design. Each voltage state can be amplitude modulated on a per-period basis, so for example an N = 4 would mean there are eight unique voltage states present in the base frequency, two per period. Each period can either be V^{++} or V^{+-} and V^{+-} or V^{--}, respectively. Additionally, not every period needs to be modulated by the auxiliary frequency. Keeping with the N = 4 example, say only the 1st period would see amplitude modulation. This leads to a mind-numbing amount of complex waveform tailoring that has been initially explored, but only as a proof-of-concept.

For the phase incoherent case, there is no integer division between f_{aux} and f_{base}. This causes the amplitude modulation to occur at any point in the base frequency amplification. The effect is a true superimposition of the auxiliary frequency atop a base frequency, similar to the sine wave example mentioned above. Functionally, the two upstream inputs have the same frequency and a 50/50 duty cycle pairing applied to them. This produces a small amplitude square wave superimposed atop the base frequency. To illustrate the TTL inputs for both f_{base} and f_{aux}, a sample phase incoherent complex waveform is shown in **Figure 3.15**. As can be seen in the figure, for the phase incoherent case, transitions from V^{-+} to V^{++} and $V^{--}$to V^{-+} anywhere in the base frequency, even in the middle of a period. This produces a staggered auxiliary addition to the base amplification. Black and yellow dotted lines are used to represent the base and auxiliary frequencies, respectively.

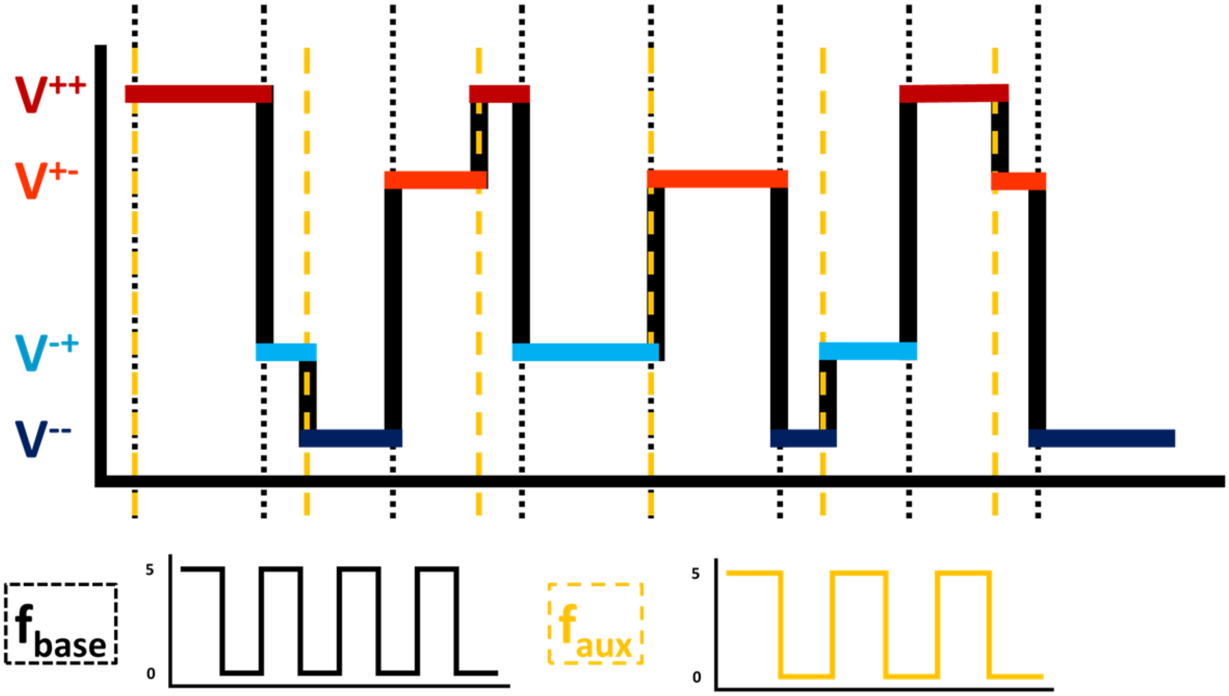

Figure 3.15 Example output of phase incoherent complex waveform generation.

Auxiliary waveform generation is handled in two separate mechanisms. For phase incoherent applications, one of the two remaining LVWFG DDS output pairs is used (see **Figure 3.13**). Only a single phase of this additional LVWFG output is used. Doing so produces no auxiliary waveform on the new DDS output until the SSE interval is initiated. This auxiliary waveform is only present during this interval and the additional LVWFG DDS output is kept LOW and HIGH for the V^+ and V^- inputs of the downstream HVHF circuit for the rest of the instrument cycle. This produces non-complex square waves during the trapping and mass analysis intervals. During the SSE interval, the base frequency is locked at 700 kHz with 50/50 duty cycle and the auxiliary square wave generation is a user-controlled variable frequency. The exact application of phase incoherent complex wave generation will be covered in **Chapter 5**.

The phase coherent complex waveform is only used during the mass analysis interval and will be covered in **Chapter 5**. The LVWFG output controlling the base frequency of the X-axis LDIT electrodes is split and wired into an additional circuitry to generate the auxiliary waveforms that are used during mass analysis. This circuitry was developed with collaboration with Dr. Blaise Thomson, who constructed TTL manipulation circuitry quickly based on minimal input/output information. This circuitry has gone through two iterations. The first was a Divide-By-N (DBN) TTL circuit in which the base frequency (f_{in}) was divided by an integer N, which was controlled by the user following the equation below.

$$f_{aux} = \frac{f_{base}}{N}$$

Such that f_{base} is the base linear frequency from the LVWFG output and f_{aux} is the auxiliary square wave that was wired to both V^{++}/V^{+-} and V^{-+}/V^{--}upstream HVHF circuits. The resulting waveform looked like **Figure 3.16** which most similarly matches the sine wave analog. This was tested on QTPI and while mass analysis still functioned, instrumental performance was not greatly improved (not shown). Instead, further TTL manipulation circuitry was developed to experiment with different complex waveforms and their effect on mass analysis performance. The reason for the lack of success of this complex waveform is unknown. At the time only a static 5 V_{pp} auxiliary amplitude was available, whereas we currently can adjust the amplitude from 0 Vpp to 14 V_{pp}. Further studies into the viability of this waveform need to be attempted in the future.

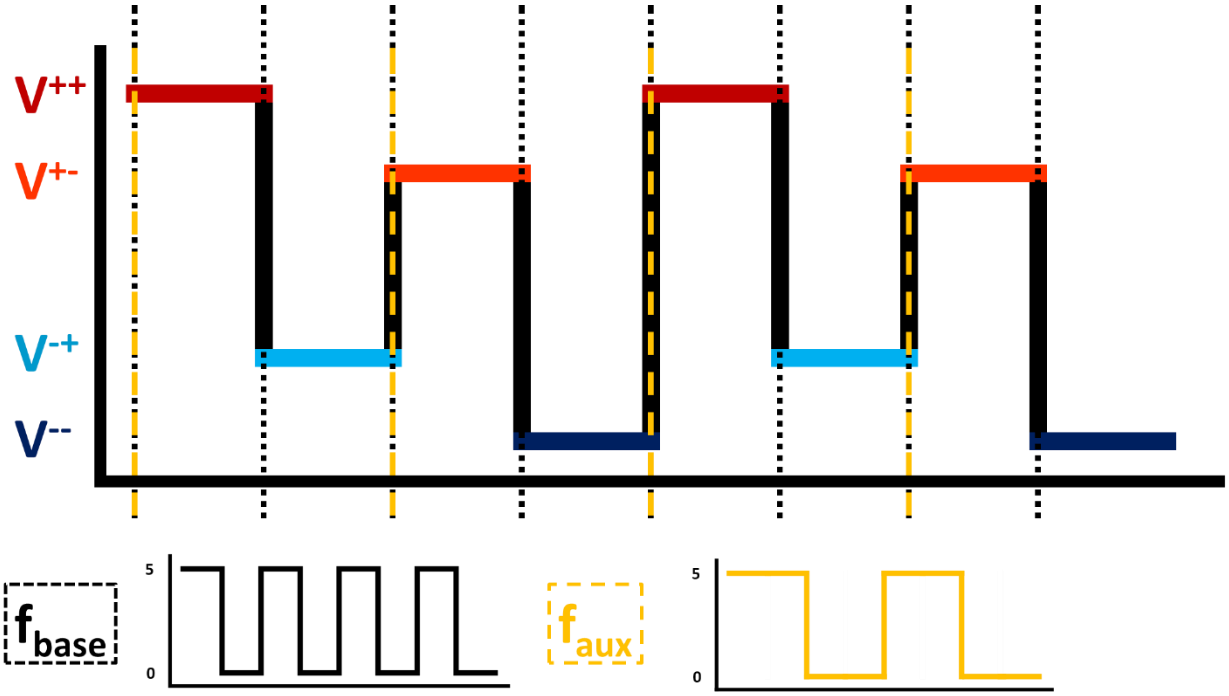

Figure 3.16 Early complex waveform generation using DBN supplemental circuitry.

From the previous design, we next wanted to tailor the complex waveform to have less amplitude modulation periods per value of N. Eventually circuitry was constructed so that only a single period would have amplitude modulation per auxiliary frequency division. This next waveform would have its amplitude modulated from V^{+-} to V^{++} and from V^{-+} to V^{--} as before but would only do so for exactly one period every N number of periods, thus labeling it the one-every-N (OEN) auxiliary waveform. The idea was to chirp ion displacement by amplitude modulation as the native ejection frequency was reached for a given m/z species, providing an extra kick to ions as they approached the exit slit, thus improving extraction efficiency. **Figure 3.17** shows the final circuit design and waveform schematic of the OEN complex waveform. A more detailed discussion of this circuit's success will be given in **Chapter 5**.

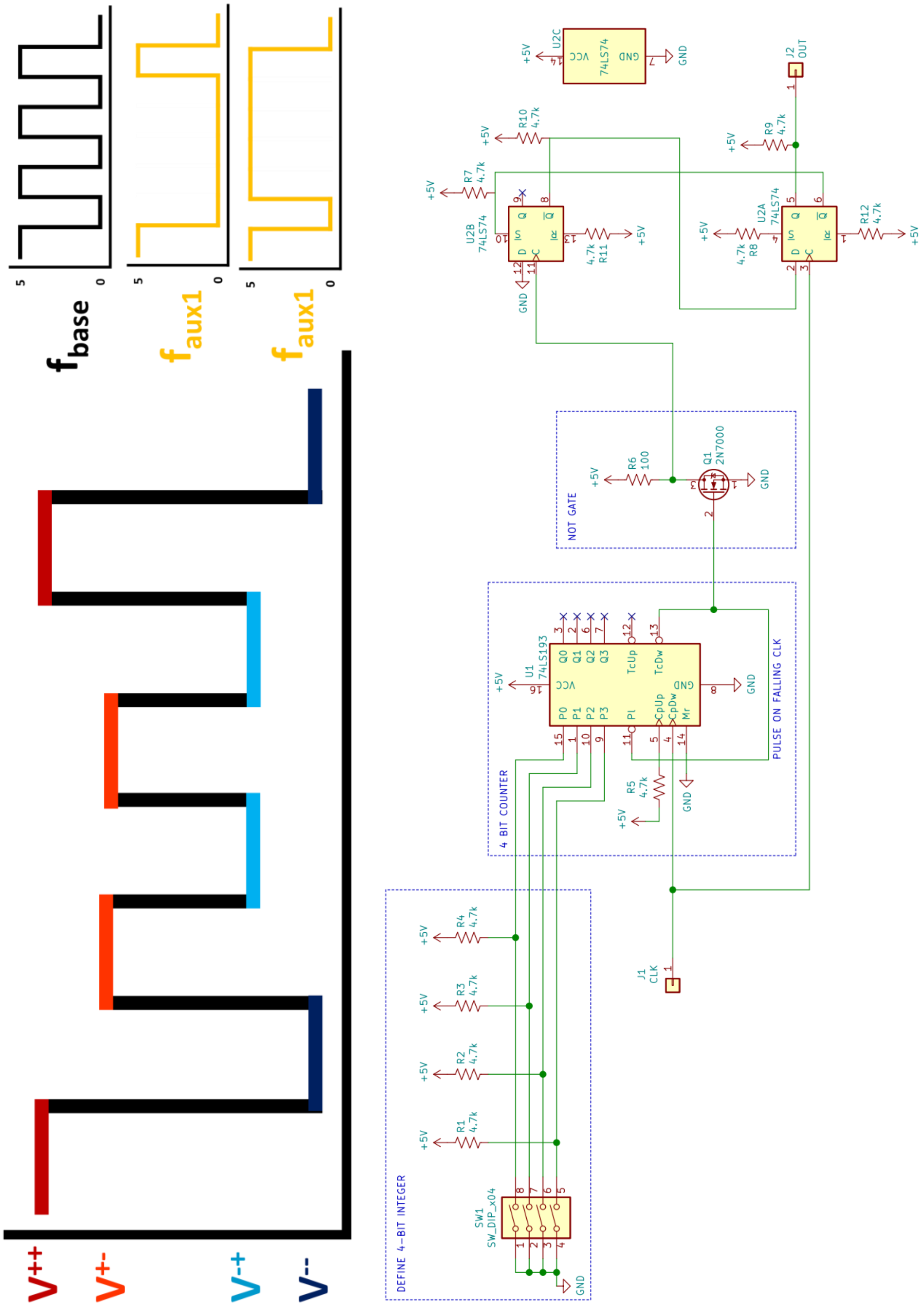

Figure 3.17 Circuit schematic (bottom) and complex waveform example (top) of OEN auxiliary waveform circuitry.

Section 3.5 Conclusion

Presented in this chapter are several facets of the work that went into developing a working LDIT mass spectrometer from scratch. CAD design and fabrication, mechanical engineering, software design and circuit development are areas which the majority development time on this project was spent. For readers non-familiar with the work presented in the rest of the thesis, this chapter will serve as needed visualizations of the instrumentation, the internal components of the instrument, the circuitry required to perform mass analysis, and the software needed to present the data in a meaningful way. For readers familiar with this work, this chapter will serve as a starting point in understanding the instrument with the intention of continuing its development.

Section 3.6 Chapter 3 References

(1) Mathur, R.; O'Connor, P. B. Design and Implementation of a High Power Rf Oscillator on a Printed Circuit Board for Multipole Ion Guides. *Rev. Sci. Instrum.* **2006**, *77* (11), 114101. https://doi.org/10.1063/1.2387881.

(2) Hoffman, N. M.; Opačić, B.; Reilly, P. T. A. Note: An Inexpensive Square Waveform Ion Funnel Driver. *Rev. Sci. Instrum.* **2017**, *88* (1), 1–4. https://doi.org/10.1063/1.4974345.

(3) Hoffman, N. M.; Gotlib, Z. P.; Opačić, B.; Clowers, B. H.; Reilly, P. T. A. A Comparison Based Digital Waveform Generator for High Resolution Duty Cycle. *Rev. Sci. Instrum.* **2018**, *89* (8), 084101. https://doi.org/10.1063/1.5004798.

(4) Shaffer, S. A.; Tang, K.; Anderson, G. A.; Prior, D. C.; Udseth, H. R.; Smith, R. D. A Novel Ion Funnel for Focusing Ions at Elevated Pressure Using Electrospray Ionization Mass Spectrometry. *Rapid Commun. Mass Spectrom.* **1997**, *11* (16), 1813–1817. https://doi.org/10.1002/(SICI)1097-0231(19971030)11:16<1813::AID-RCM87>3.0.CO;2-D.

(5) Shaffer, S. A.; Prior, D. C.; Anderson, G. A.; Udseth, H. R.; Smith, R. D. An Ion Funnel Interface for Improved Ion Focusing and Sensitivity Using Electrospray Ionization Mass Spectrometry. *Anal. Chem.* **1998**, *70* (19), 4111–4119. https://doi.org/10.1021/ac9802170.

(6) Anthony, S. N.; Shinholt, D. L.; Jarrold, M. F. A Simple Electrospray Interface Based on a DC Ion Carpet. *Int. J. Mass Spectrom.* **2014**, *371*, 1–7. https://doi.org/10.1016/j.ijms.2014.06.007.

(7) Brancia, F. L.; McCullough, B.; Entwistle, A.; Grossmann, J. G.; Ding, L. Digital Asymmetric

Waveform Isolation (DAWI) in a Digital Linear Ion Trap. *J. Am. Soc. Mass Spectrom.* **2010**, *21* (9), 1530–1533. https://doi.org/10.1016/j.jasms.2010.05.003.

(8) March, R. E. Quadrupole Ion Traps. *Mass Spectrom. Rev.* **2009**, *28* (6), 961–989. https://doi.org/10.1002/mas.20250.

(9) Ding, L.; Sudakov, M.; Kumashiro, S. A Simulation Study of the Digital Ion Trap Mass Spectrometer. *Int. J. Mass Spectrom.* **2002**, *221* (2), 117–138. https://doi.org/10.1016/S1387-3806(02)00921-1.

(10) De Hoffmann, E.; Stroobant, V. *Mass Spectrometry: Principles and Applications, Third Edition*.

(11) Ding, L.; Sudakov, M.; Brancia, F. L.; Giles, R.; Kumashiro, S. A Digital Ion Trap Mass Spectrometer Coupled with Atmospheric Pressure Ion Sources. *J. Mass Spectrom.* **2004**, *39* (5), 471–484. https://doi.org/10.1002/jms.637.

(12) Brabeck, G. F.; Koizumi, H.; Koizumi, E.; Reilly, P. T. A. Characterization of Quadrupole Mass Filters Operated with Frequency-Asymmetric and Amplitude-Asymmetric Waveforms. *Int. J. Mass Spectrom.* **2016**, *404*, 8–13. https://doi.org/10.1016/j.ijms.2016.04.002.

(13) Hoffman, N. M.; Gotlib, Z. P.; Opačić, B.; Huntley, A. P.; Moon, A. M.; Donahoe, K. E. G.; Brabeck, G. F.; Reilly, P. T. A. Digital Waveform Technology and the Next Generation of Mass Spectrometers. *J. Am. Soc. Mass Spectrom.* **2018**, *29* (2), 331–341. https://doi.org/10.1007/s13361-017-1807-8.

(14) Snyder, D. T.; Pulliam, C. J.; Wiley, J. S.; Duncan, J.; Cooks, R. G. Experimental Characterization of Secular Frequency Scanning in Ion Trap Mass Spectrometers. *J. Am. Soc. Mass Spectrom.* **2016**, *27* (7), 1243–1255. https://doi.org/10.1007/s13361-016-1377-1.

Chapter 4 Intricacies of QTPI Operation

The purpose of this chapter is to detail the non-publishable work that was done to observe, characterize, and solve some of the intricacies present in QTPI's operation. Prior to complex waveform studies, the majority of work done on the instrument involved determining the effect of individual operational parameters to best optimize QTPI performance. This was done with a twofold motivation. The first was to develop the best possible resolution LDIT-MS, determining the limits of scan speed and optimizing duty cycle pairings, pressure, and many other user controller parameters. The second was to develop a methodology which would sacrifice resolving power (Δm) for a faster instrument cycle, from 700 ms at the slowest to 100 ms.

Longer instrument cycles are intended to be used as a high resolution output for exploratory stepwise ion chemistry reactions, such as solvent clustering[1] or probing catalytic intermediates.[2] Shorter instrument cycles are intended to be used when ideal non-LDIT instrument parameters have been determined, allowing for rapid collection spectroscopic data from product of these reactions. Spectroscopic data collection occurs as the integration of ion abundance for a given mass channel, the de-tagged species from **Chapter 1**. On existing TOF-MS this performed by binning a chunk of the ion current vs. time data which correspond to the de-tagged ion's flight time. The output of the LDIT is already binned, making the software for this collection more simplistic. Additionally, by making the mass scan range very small and the Δm/z very high, mass scan should take as little as a few milliseconds.

Resolving power is important in exploratory phases to ensure correct ion species formation but is largely irrelevant for spectroscopic data collection. Coupling fast mass scans with instrument optimizations to minimize needed trap durations, will shortened instrument cycles close to 100 ms, which is the current maximum repetition rate of our lasers. The sacrifices to LDIT resolving power are negligible when the change of mass needed to cryogenic tag species of interest are +18 mass unit apart (water clustering), which will be covered in Chapter 6.

At the request of Dr. Etienne Garand, this chapter also serves to provide a written account of operating procedures necessary for future researchers to work successfully on this instrument. Most of the data shown tells stories interesting to the Garand group, but not the broader scientific community. If a researcher in the Garand lab has decided to work on QTPI or QTPI-like instrumentation, the aim of the proceeding sections is to accelerate familiarity with this system. The sheer amount of user parameters from voltages, pressures, frequencies, duty cycles, and many more can seem overwhelming, but the following sections are intended to break those variables into digestible bites.

Section 4.1 Tips for Successful QTPI Operation

The first recommendation is ensuring progress toward a final goal is the main motivation for optimizations. Whether that objective is maximizing signal, minimizing fragmentation, maximizing Full-Width-Half-Max (FWHM) resolving power, or any future finesses that may be required, always be assessing whether the results are adequate to proceed with the project. Diminishing returns are the main problem a researcher will run into with the sheer number of variables to optimize on this platform. For example, an initial peak of interest has a FWHM of 1.2 m/z at a high scan speed. The time to half that FWHM to 0.6 may only take a week. This can be done concurrently with other optimizations, such as pre-MS mass manipulation parameters and maximum reaction product signal response. However, further reduction of FWHM from 0.6 to 0.3 could take multiple months. If the end goal of the optimization is to have stable signal of a parent ion and several solvent clusters which provide a +18-mass shift, the difference between $\Delta m = 0.6$ and $\Delta m = 0.3$ is negligible, as the mass channel will be integrated during spectroscopic data acquisition. The purpose of this story is to encourage the prioritization of performance adequate for the application instead of performance for performance's sake.

The second recommendation that can be given to researchers working on similar instrumentation is to fully explore a minimal number of user variables at a time for performance optimization. At the time of writing, there are 13 independent DC voltages that are applied to the instrument, two radiofrequency (rf) amplitudes of the two hexapole ion guides, one timing present for the ion acceptance window and many more tunable non-LDIT parameters. LDIT operation itself has well over 20 user-controlled variables that can be changed to impact performance. In other words, when optimizing signal, only ever change one to three parameters at a time. For example, adjusting the relationship between the skimmer, first ion guide bias, and aperture HIGH voltage can cause significant fragmentation when a gentle potential well is not maintained. Always make sure to fully explore the limits of a given parameter before moving to the next one. It is also always preferrable to optimize signal from the front of the instrument towards the back, and to never optimize LDIT and non-LDIT parameters concurrently.

Section 4.2 How QTPI Data is Displayed and Presented

As covered in **Chapter 3**, the final output of QTPI is binned data of ion amplitude vs. m/z. The list of m/z is generated from user start, stop, and Δ m/z inputs. The LVWFG dynamically generates the frequency at each m/z step by means of the Mathieu *q* equation, with experimentally determined calibration constants for V, q, and r_0. Every QTPI mass spectrum presented throughout the rest of this work will be done to reflect the binned nature of the data. This leads to histogram displays as opposed to the normal line graphs. The mass steps generated are less concrete, definitive masses, and more amalgamations of ions radially ejected between mass steps. For example, if a solution containing Cs^+ is mass analyzed with a Δm/z = 1. A peak at nominally 133 will appear. The exact m/z of Cs^+ is 132.90545 but will instead displayed at 133 m/z bin, as it was radially ejected after the 132 m/z bin and before the 134 m/z bin. Exact masses are rounded to the nearest bin during display.

These histograms can be displayed with two X-axes: m/z or frequency. As will be covered following sections, several user parameters can alter the ejection frequency of the same ion species. In the m/z domain, this would manifest as the peak shifting left or right without proper recalibration, which would be confusing. To use the previous example, the same Cs^+ ion would shift from 133 m/z to either 134 m/z or 132 m/z, depending on the parameter. This is not ideal for characterizing the effect of operational parameters. When recording and reporting the effect of these settings, the frequency domain is preferred. One visual oddity is present with frequency domain histograms, however. To display a linear m/z axis, a non-linear frequency list is generated during mass analysis. When the data are displayed in the frequency domain, the spacing is not uniform. Both m/z and frequency histograms of Cs^+ are displayed in **Figure 4.1**. This lack of uniformity in the frequency spectrum (right) can be seen as the spacing at high frequencies (600 to 575 kHz) is further apart than low frequencies (525 to 500 kHz). The only exception to the histogram display is on the front panel of the LabView software, as also seen in **Figure 4.1**. This is because the histogram display for LabView is atrocious, and a line view can be easier for on-the-fly signal optimization.

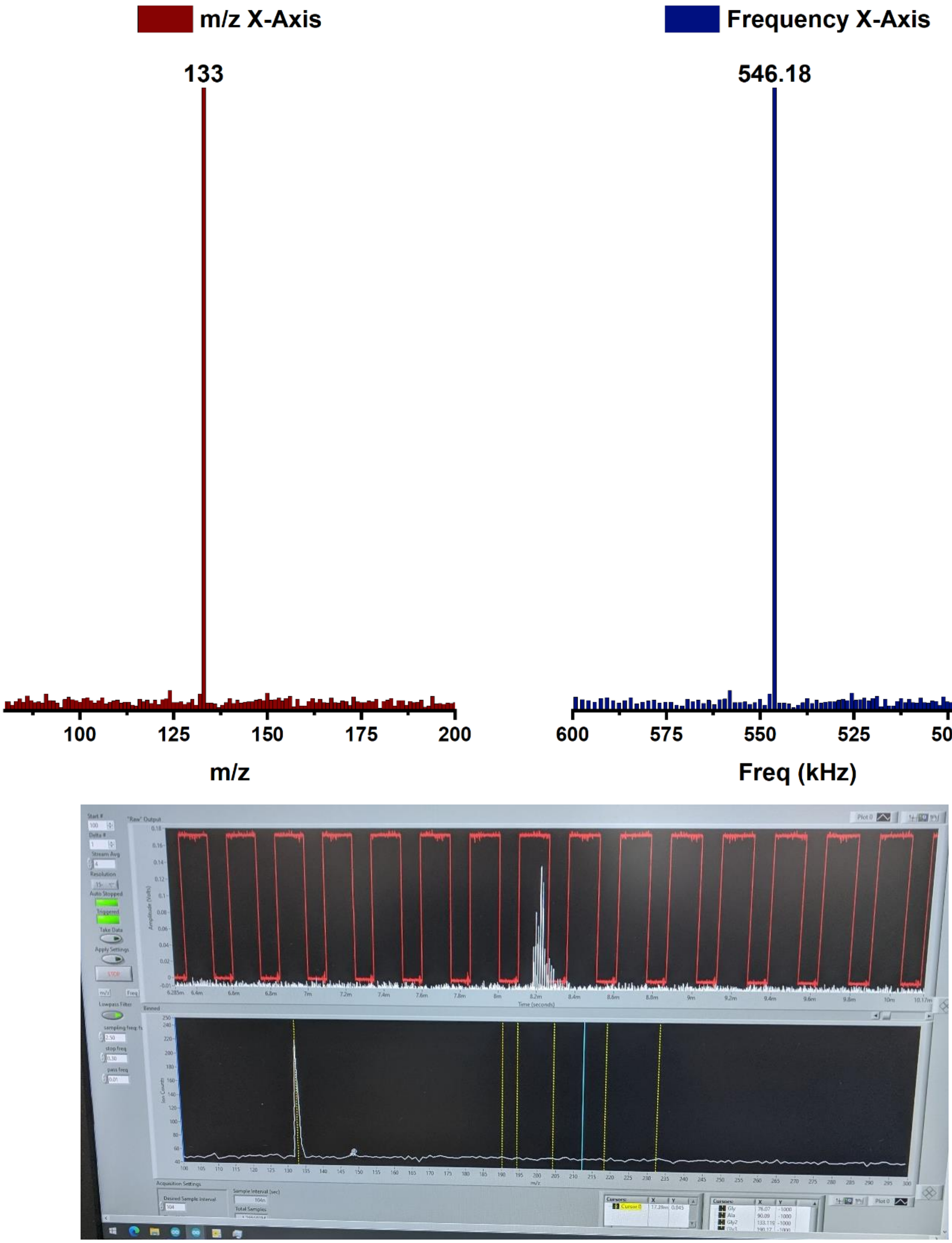

Figure 4.1 Mass spectrum and ejection frequency histograms. Picture of LabView front panel.

During real-time tuning, determining the benefits or detriments of changing user parameters is easy to do, qualitatively. The peak amplitude increases or decreases and/or the FWHM of the peak gets tighter or broader. However, when performance needs to be reported, measuring the signal-to-noise ratio (hereafter S/N) and resolving power is problematic. As can be seen in the above figure, practically all the Cs^+ population is ejected in one bin, so measuring the FWHM is pointless. Another MS example is given below in **Figure 4.2** with a more typical ion distribution. The FWHM resolving power was determined utilizing the peak analyzer function in Origin (OriginLabs). Alternatively, a Gaussian shaped peak could be fit to each individual peak, whose standard deviation could also be correlated to peak resolving power. The latter is much more involved, and unnecessary for most applications. To measure S/N, simply take a section of the mass spectrum that has no ion amplitude, find the mean value, subtract that mean value from the max signal amplitude, then divide that max signal amplitude by the averaged noise. In the example above, this S/N would be ≈ 33. Do note this method is an approximation and a more formal method for determining S/N should be utilized in the future.

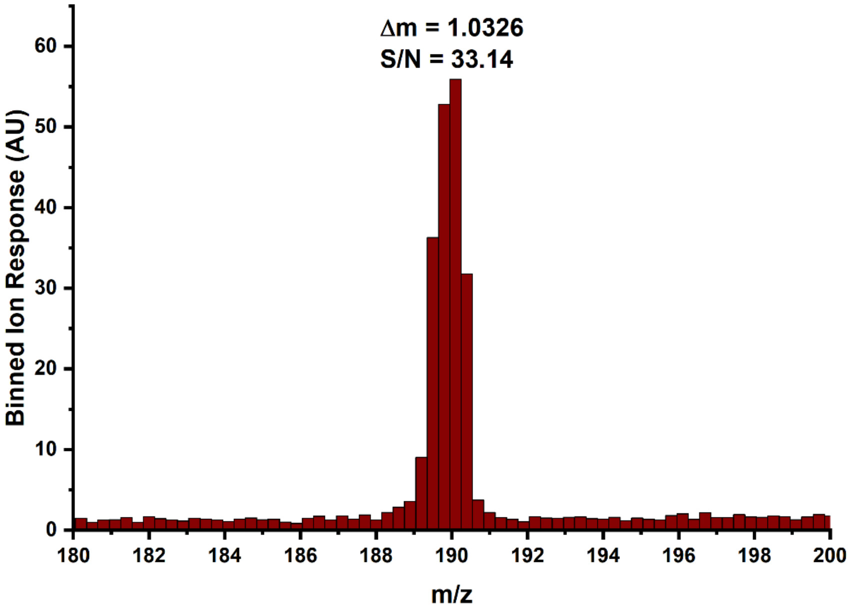

Figure 4.2 Mass spectrum of Gly_3H^+ (m/z = 190) spanning multiple bins.

Section 4.3 Multi-Step Calibration Process

A description of how the list of frequencies that are generated by the LVWFG during a mass scan was covered in **Chapter 3**. To recap, the Mathieu *q* equation is re-arranged to solve for m/z as a function of frequency and user inputted calibration variables for V, q, and r_0. This list of m/z can be plotted in real-time to provide insight into which m/z species are present in the LDIT prior to analysis. In order to do so, calibration is necessary. Theoretical values for these calibration parameters are used as an initial estimate to provide the user with a starting point. These variables are meant to represent the real square wave amplitude, Mathieu *q* boundary coordinate, and the effective radius of the LDIT. Due to circuit inefficiencies and mechanical tolerances, these parameters act only as an initial guess. To better refine the calibration, there is a multi-step methodology developed for a more accurate calibration across a given mass range. This methodology is given below.

Spray Cs^+, with a $\Delta m/z = 1$. Cesium has no vibrational modes nor the possibility to fragment, which makes it the ideal candidate for a single point calibration. If a significantly higher mass range is needed, use a heavier metal that ideally has no high abundance isotopes. Via the LVWFG interface, input the theoretical value of V and r_0. Guess the value of q, typically between 0.65 and 0.7125, pending duty cycle pairings. Methodically, change values of V and q until the single peak reads 133 m/z. Increasing V and decreasing q, separately, will move the peak to a higher reported m/z, and vice versa. Do not change r_0 at this stage. Once Cs^+ is detected in the 133 m/z channel, change solutions to two known mass compounds, currently Gly_2H^+ (133 m/z) and Gly_3H^+ (190 m/z) are used. If using Cs^+ and Gly_2, ensure both species are being reported as 133 m/z. Note the spacing between the reported m/z of the now two most abundant peaks. If this difference is not close to 190-133 = 57 m/z, change the values of r_0 until it is. Doing so will change the spacing between peaks as well as shift the peaks to the left and right, this is normal. Once an appropriate spacing is achieved, re-tune q and V until both species are being reported as 133 m/z and 190 m/z.

If the values of V or r_0 are dramatically different from the theoretical values, revert the calibration variables, return to the Cs^+ solution, redo the single point calibration, then independently spray Gly_2 and Gly_3. If peaks are being reported at dramatically larger spacing (more than 10 m/z) than intended, fragmentation is likely occurring. Adjust entire instrument parameters until this is not the case (i.e., front end DC settings, ESI, etc.). Once Gly_2 and Gly_3 are being reported at nominally correct mass channels, two-point calibration is complete for current LDIT mass scan variables. If scan speed, duty cycles, pressure, trap duration and likely other instrument parameters are changed, this calibration may be invalidated. Correction for usually only involves a minor changes to V and q while monitoring peak spacing, not requiring a full multi-step recalibration.

If data are collected with incorrect calibration, this can be corrected in post-processing, though this should never be done for final data acquisition for publication. This can only be done when two or more known peaks are present in a mass spectrum. Take the MS Y-axis data and load it into an Excel column (column B). In a separate cell (C1), initialize a value of Δm/z based on the original MS Δm/z. In a separate cell (C2) assign an X-offset value at zero. In the column next to the MS Y-axis data (column A), initialize a new start m/z that is the original reported start m/z minus the X-offset, ensuring it is a static variable (e.g., C2). Under the initial start m/z, increment the X value by the separate Δm/z ensuring it is a static variable (e.g., C1). Expand this formula to match the number of rows as the MS-Y data. Plot the data as a bar graph in Excel. Find the row index of the two known peaks. In two separate cells (C3 and C4), display the X-axis value of the two known species' indices. In another separate cell (C5), display the reported X-value difference between the high and lower mass indices. Manipulate the value of Δm/z until the difference cell is the correct spacing (57 for Gly_2H^+ and Gly_3H^+). Change the value of the X-offset so that both row indices read the correct value (133 and 190 in the above example). The mass spectrum has now been recalibrated. Restating for emphasis, this probably should not be used for publication because the current Δm/z is not the original targeted change, and because the original ejection frequencies may not accurately reflect the exact ejection frequencies for a given ion species. This discrepancy can be attributed to the binned nature of the MS collection. **Figure 4.3** shows a screenshot the recalibration process described above. In the future, this could easily be implemented into LabView or Origin for ease of use.

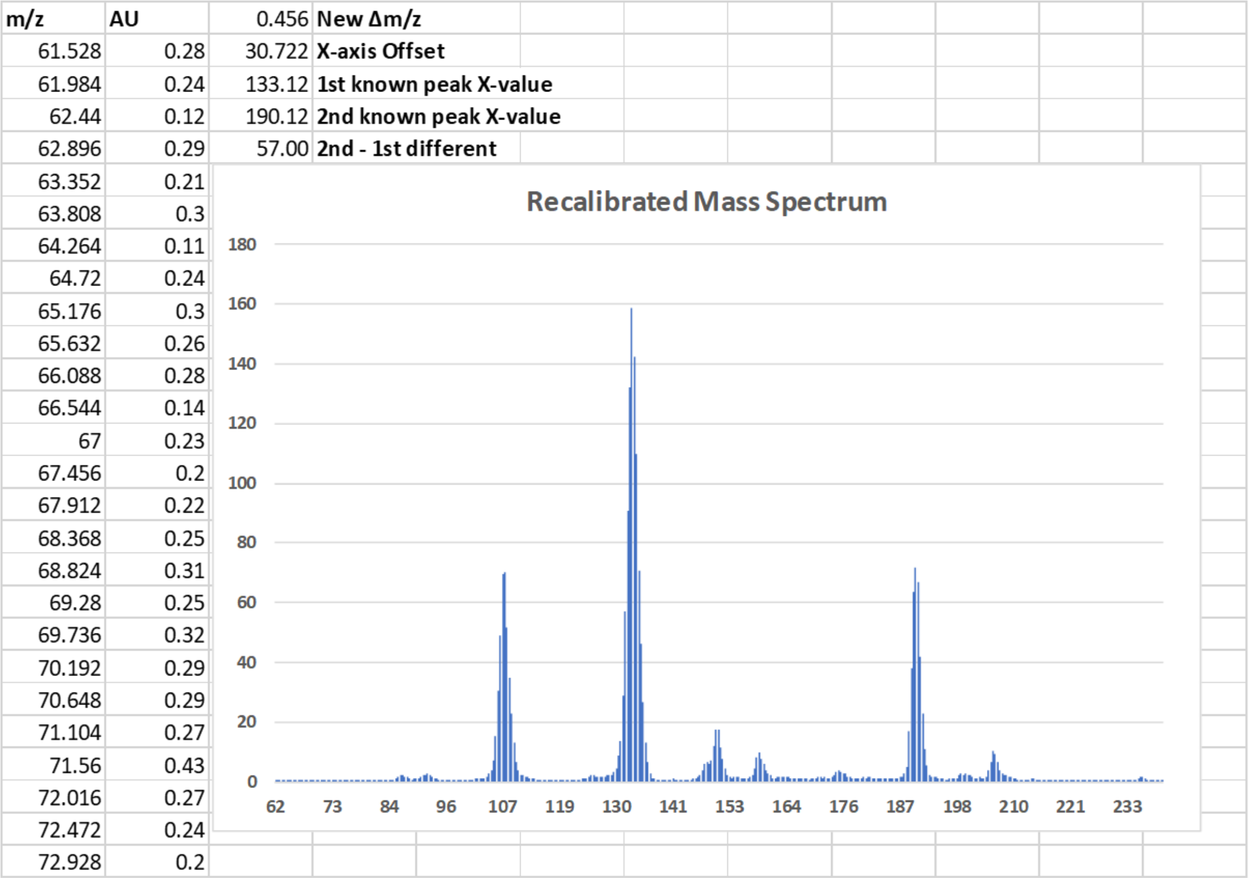

m/z	AU	0.456	New Δm/z
61.528	0.28	30.722	X-axis Offset
61.984	0.24	133.12	1st known peak X-value
62.44	0.12	190.12	2nd known peak X-value
62.896	0.29	57.00	2nd - 1st different
63.352	0.21		
63.808	0.3		
64.264	0.11		
64.72	0.24		
65.176	0.3		
65.632	0.26		
66.088	0.28		
66.544	0.14		
67	0.23		
67.456	0.2		
67.912	0.22		
68.368	0.25		
68.824	0.31		
69.28	0.25		
69.736	0.32		
70.192	0.29		
70.648	0.29		
71.104	0.27		
71.56	0.43		
72.016	0.27		
72.472	0.24		
72.928	0.2		

Figure 4.3 Screenshot of X-axis recalibration done in Excel post-collection.

Section 4.4 MOSFET Noise and Efforts to Minimize It

Although capable of operating the LDIT, being incredibly easy to assemble and robust in functionality, the HVHF circuit generates an incredible amount of noise. Every time one of the power MOSFETs open or close, a ripple effect can be seeing in both the final output waveform and at the output of the transimpedance amplifier. The former is a ripple effect seen in most typical square waves and can be minimized by means of lowpass filtering. The latter is caused by an unknown reason. The transimpedance amplifier is connected to a Faraday cup at the end of the continuous electron multiplier (CEM) detector. Ions strike the detector, causing electron emission, which then re-strike the detector medium, producing more electrons until an eventual gain of roughly 10^7 is produced. These electrons strike the Faraday cup, which is wired directly to the input of the transimpedance amplifier. This amplifier then converts the current response to the voltage domain with a gain of roughly 100.

It is speculated that any open-ended capacitive load (such as the Faraday cup and BNC wiring) acts as an antenna for the power MOSFET switching. Excessive time has been spent minimizing this noise by moving or shielding the transimpedance amplifier. When only a BNC cord is attached to the input of the amplifier, square wave noise is still present, without the connection to the Faraday cup. Even moving the amplifier to a completely separately breaker system, square wave noise could still be seen while detaches from the instrument. The only thing that has eliminated square wave noise from the amplifier was to house the amplifier with a minimal length of BNC cord in a thick-walled metal paint can, acting as a Faraday cage. This was deemed unusable due to not being able to connect to the instrument, as the Faraday cup cannot be enclosed.

Using the binning software, this noise thankfully does not make QTPI inoperable. **Figure 4.1** shows the difference between an area of a mass scan containing no ion response (left) and a large ion response (right). As can be seen from the figure, the timing of the noise spikes match the timing of the square wave switching from HIGH or LOW, or vice versa. This is also why it is imperative that TRIGGER bin windows duration be locked to a discrete number of periods, instead of a static time. For example, two binning windows are both locked at 250 µs, one corresponds to an ejection frequency of 700 kHz, the other to 300 kHz. The former binning window will encapsulate $250*10^{-6}$ / (700,000 * 2) ≈ 350 noise spikes, where the latter will contain ≈ 150 noise spikes.

Three software discriminations packages were developed to help mitigate this. The first was a simple voltage threshold which acted eliminate the $V < 0$ noise. Each individual datapoint was compared against a static DC value, anything below this value was discarded. The second was a bandpass filter approach with the intent of minimizing high frequency components of the noise. LabView has a built-in "SI Lowpass Filter VI" to which each individual bin of ion response vs. time data was passed through and optimal values were determined experimentally in real-time. Finally, a Fast Fourier Transform (FFT) method was attempted with the introduction of the complex waveform mass analysis. The frequency in which ion packets were ejected from the LDIT was dependent on the auxiliary frequency, instead of the base frequency. Noise is generated at the base frequency. Ion response vs. time data was sent into a FFT subVi module and only a lower percentage of the FFT was kept. The FFT was then integrated and reported as binned ion abundance. These systems had some effect on minimizing noise, but all of them are trial-and-error designs and largely unfinished. Additionally, all these methods lead to some exclusion of low amplitude ion signal as well as noise. This has led to a poor limit of detection for the instrument, which is not ideal.

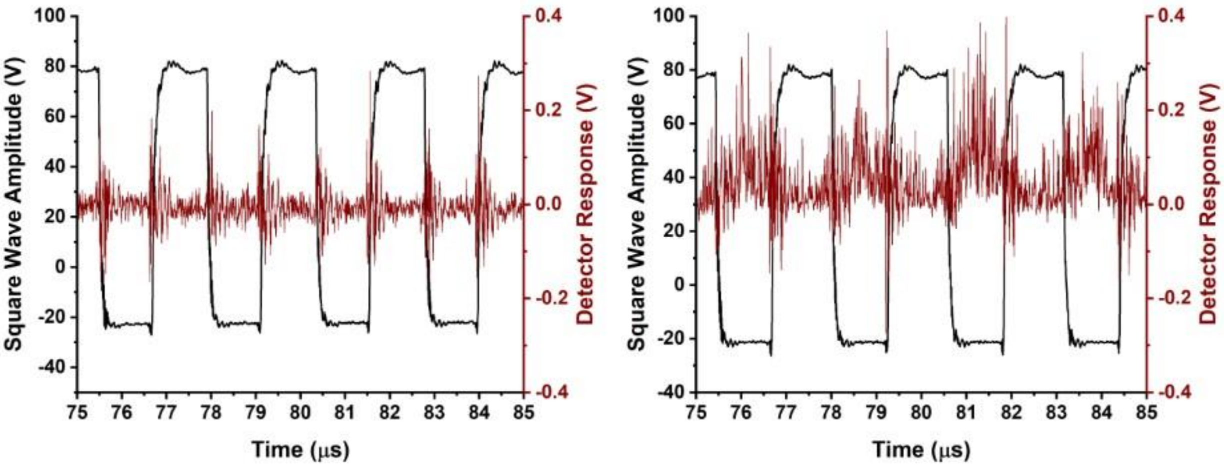

Figure 4.4 Oscilloscope traces of applied square waves (black) and detector response (red).

Section 4.5 Pressure Dependence of QTPI Performance

Originally, a microchannel plate (MCP) detector was implemented during QTPI's initial assembly phase. As functionality grew, it became evident that increasing pressure had a direct positive impact on the S/N and resolving power of mass selected peaks. Unfortunately, the maximum pressure for this MCP was estimated to be 1 x 10^{-5} Torr (exact model unknown). Eventually, the MCP was replaced with a CEM detector capable of handling pressures above 1 x 10^{-4} Torr (exact model unknown). This CEM was extracted from a decommissioned Thermo LCQ, a cylindrical mass analyzer-based instrumentation, making it an ideal replacement for our applications. Scaling the amount of constant gas from 1 x 10^{-5} Torr to 1 x 10^{-4} Torr had a significant impact on the mass analyzer's performance. **Figure 4.5** shows four ejection frequency graphs of the same ion species (PheH$^+$) taken at different collisional gas pressures. Probing the pressure inside the trap is not currently possible, so the presented pressure indicated the entire 3rd vacuum stage chamber pressure gauge (InstruTech CCM501). These data are presented as frequency domain histograms since the PheH$^+$ ejection frequency changes as a function of pressure. As the collision gas pressure is increased, the average ion velocity decreases, thus making the variation inside the pseudopotential well more localized, leading to more concisely extracted ion packets[3]. The effect is that both the total ion response increases, and at higher pressures, ion packet diffusion across multiple bins is decreased. Pressures above 10^{-4} Torr appear to have diminished returns, though higher pressures studies were seldomly performed for risk of detector damage.

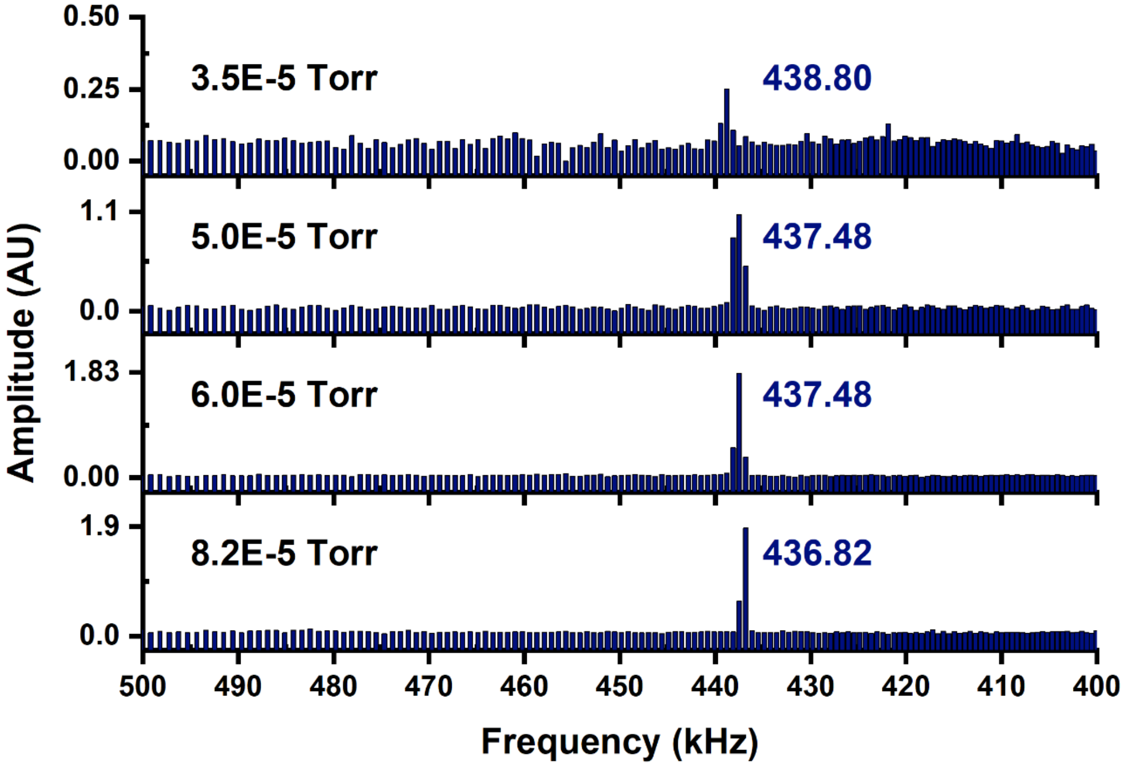

Figure 4.5 Four ejection frequency graphs showing the effect of operational pressure on both ion response and resolving.

Section 4.6 Notable LDIT Operational Observations

The aim of this section is to illustrate two oddities that researchers may observe when optimizing a mass spectrum in real time. These are not the only operational parameters that cause unintended effects, but to catalog all parameters, this document would be five times the current length. The two presented, scan speed and mass analysis duty cycle, are the parameters that are most likely to be changed when refining a mass spectrum.

4.6.1 Scan Speed

To recap, the mass spectrum is comprised of a series of m/z steps, which are generated from a list of frequencies from the LVWFG. Another way of approaching this is that for a given m/z, as the frequency is stepped downwards, the location of the ion's Mathieu *a-q* coordinate is moved toward a boundary line. Each frequency step moves the *a-q* value a particular (non-linear) amount. Eventually, the previous step is still within the 1st stable region and the next step is past the 1st stable region boundary, leading to radial ejection[4]. As the scan speed is decreased, the number of steps between stability and instability increases. Imperfections in the applied waveform, the fact that the LDIT is not infinitely long, and the presence of higher order fields caused by machining tolerances on certain trap parts and the exit slit cause some population of ions to eject before or after their "ideal" ejection frequency.[5]

In addition to this, remember that the presented mass scan is a manually calibrated process. If calibrated at too high of a speed, say Δm/z = 1, there may be some mass inaccuracy as the scan speed is lowered, say to Δm/z = 0.3. This is because the given calibration settings are for the nominal bin in which the ion is detected. As scan speed is slowed, the bin in which the ion most prominently resides in may be between previous bin steps. This can best be seen in **Figure 4.6** where the scan speed of the same ion species (Gly_3H^+) is sequentially slowed, causing a discrepancy for the reported m/z of the peak. This can be corrected by manual recalibration anytime the scan speed is lowered. As can also be noted from the figure, slowing the scan speed down yields more resolved peaks but less overall abundance. This is likely due to increased interaction with the boundary line of the 1st Mathieu stability region. For ions to be detected, they must exit a 0.5 mm by 17.75 mm slit in only one of the X-axis electrodes and then travel through roughly 10 cm of open space. The slower an ion moves in Mathieu *a-q* space toward a boundary line, the more time it interacts with the boundary, causing erratic motion[6]. These erratic motions cause ions to develop velocity vectors that lead to their termination instead of detection.

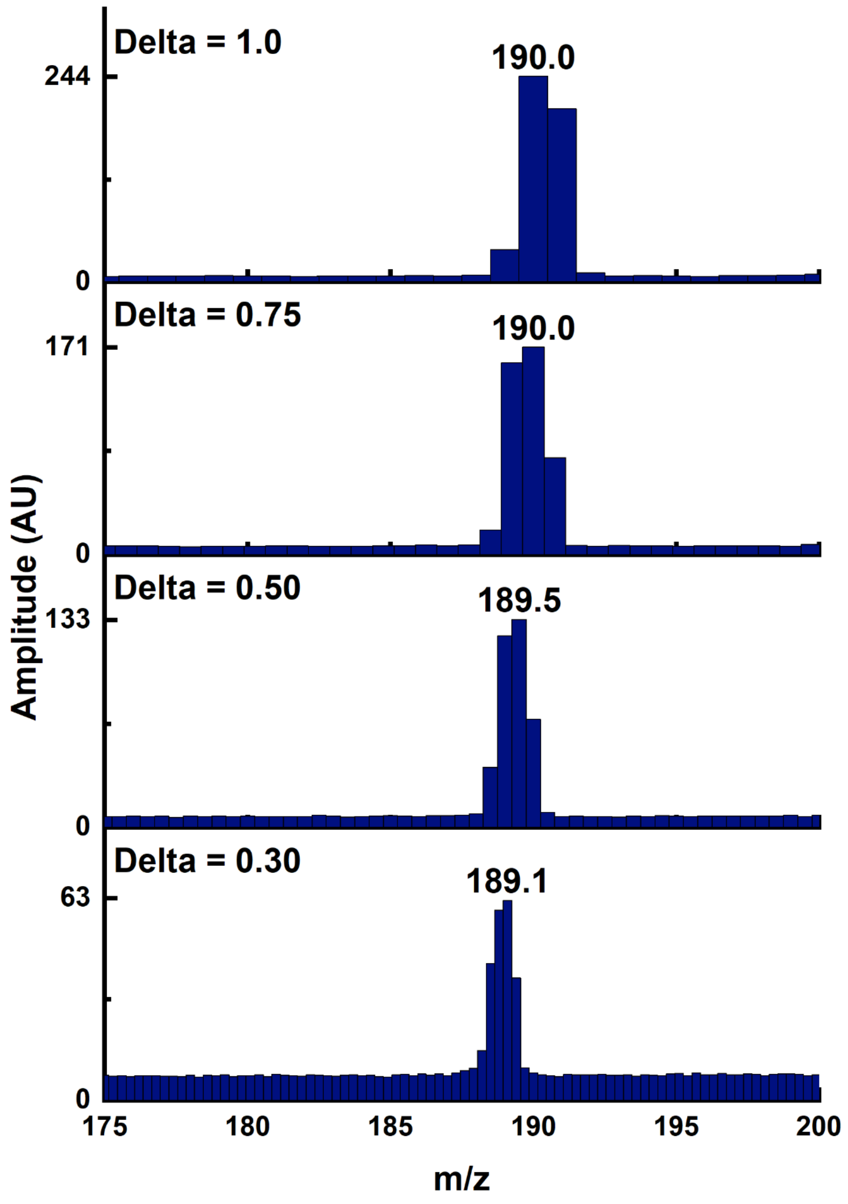

Figure 4.6 Four mass spectra depicting the change in apparent mass as a function of scan speed.

4.6.2 Duty Cycle

Along with changing scan speeds, manipulating the duty cycle on either the X-axis or Y-axis is the other most likely parameter of the LDIT to be changed during mass analysis. Originally, it was thought for best results that these two electrode pairs needed to be changed such that they complement one another (both add to 100%). While this is not a bad approach when initially optimizing the mass analyzer, the two are not required to be locked in this way. The fact is duty cycles on each electrode pair can be manipulated independently of one another and each have a preferred range for optimal performance. Consequently, this makes describing the ideal duty cycle pairing impossible. Generally, the faster the scan speed the further from 50 % either electrode pair duty cycle can be while maintaining adequate ion response and doing so tends in increase high scan speed resolution. Conversely, when scan speed is slowed, duty cycles need to be returned closer to 50%. The magnitude of deviation from 50% is sometimes internally referred to as “softness” or “harshness” of settings, not dissimilar to other Garand instrumentation. Additionally, care should be given when setting duty cycles to be too harsh, as ion fragmentation can occur.

A very frustrating part of mass scan optimization is the fact that changing either electrode pair duty cycles of the applied waveform during mass analysis changes the ejection frequency of all ions present. Similar to pressure and scan speed, this requires proper recalibration once optimal peak performance is achieved. The reason for this is because, unlike sine waves, changing the duty cycle applied to an electrode pair changes the shape of the Mathieu 1st stability region. **Figure 4.7** shows a dramatized warping of the Mathieu 1st stability region at 45 %, 50 % and 55 % from left to right. Given the same list of frequencies from the LVWFG, the same coordinates in Mathieu *a*-*q* space were be calculated, but these coordinates would yield different distances to the nearest boundary line, even passing the boundary in some cases. Despite working on the LDIT for years, an ideal workflow for duty cycle optimization was never found. Some success was found in methodically changing either the X-axis or Y-axis duty cycles until a decrease in ion amplitude was observed. From there, the duty cycle would be scaled back slightly until maximum signal was again observed. This process was repeated on the other electrode pair, until a maximum response and resolving power were determined. More concrete methodologies for signal optimization by means of duty cycle manipulation should be investigated in the future.

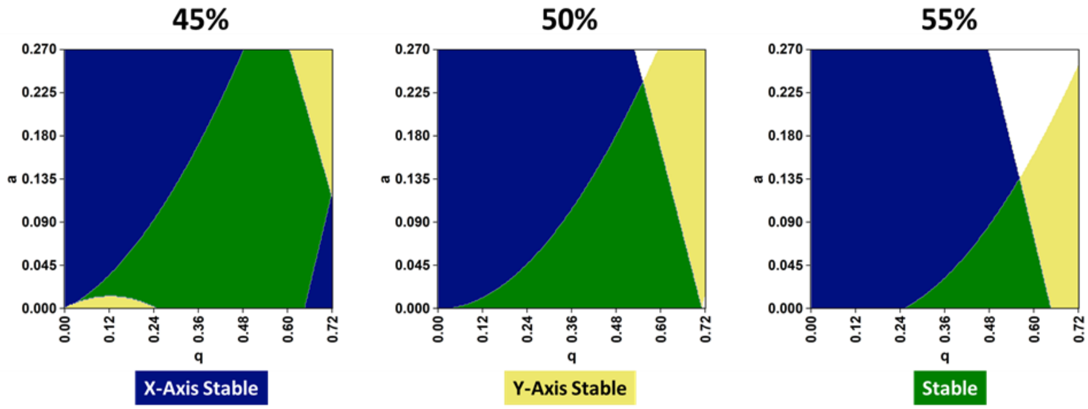

Figure 4.7 Three 1st Mathieu stability region depicting the shift in shape caused by duty cycles

Section 4.7 Conclusion

This chapter was not meant to present novel groundbreaking scientific data. Instead, this chapter serves to help researchers working on QTPI or similar instrumentation when developing their own instrumentation methodologies. By providing a written account of how calibration and display of mass spectra generated by QTPI, the development of standard operating procedures for future binned data instruments that are actively being developed in the Garand group can be initiated. Finally, illustrations of visual oddities with the system for new researchers working on QTPI or similar instrumentation have been presented.

Section 4.8 Chapter 4 References

(1) Marsh, B. M.; Voss, J. M.; Garand, E. A Dual Cryogenic Ion Trap Spectrometer for the Formation and Characterization of Solvated Ionic Clusters. *J. Chem. Phys.* **2015**, *143* (20). https://doi.org/10.1063/1.4936360.

(2) Voss, J. M.; Duffy, E. M.; Marsh, B. M.; Garand, E. Mass Spectrometric and Vibrational Characterization of Reaction Intermediates in [Ru(Bpy)(Tpy)(H2O)]2+ Catalyzed Water Oxidation. *Chempluschem* **2017**, *82* (5), 691–694. https://doi.org/10.1002/cplu.201700085.

(3) Moriwaki, Y.; Tachikawa, M.; Maeno, Y.; Shimizu, T. Collision Cooling of Ions Stored in Quadrupole Radio-Frequency Trap. *Jpn. J. Appl. Phys.* **1992**, *31* (11), L 1640-L 1643. https://doi.org/10.1143/JJAP.31.L1640.

(4) Ding, L.; Sudakov, M.; Kumashiro, S. A Simulation Study of the Digital Ion Trap Mass Spectrometer. *Int. J. Mass Spectrom.* **2002**, *221* (2), 117–138. https://doi.org/10.1016/S1387-3806(02)00921-1.

(5) Douglas, D. J.; Frank, A. J.; Mao, D. Linear Ion Traps in Mass Spectrometry. *Mass Spectrom. Rev.* **2005**, *24* (1), 1–29. https://doi.org/10.1002/mas.20004.

(6) Douglas, D. J.; Konenkov, N. V. Mass Selectivity of Dipolar Resonant Excitation in a Linear Quadrupole Ion Trap. *Rapid Commun. Mass Spectrom.* **2014**, *28* (5), 430–438. https://doi.org/10.1002/rcm.6795.

Chapter 5 QTPI Development Phases and Feature Showcase

This chapter is meant to serve as a catalog of the two instrumentation projects that have been worked on during my tenure in the Garand lab. The first is the construction of a linear digital ion trap Mass Spectrometer (LDIT-MS). Originating as a sine wave operated ion trap, QTPI has become a LDIT-MS whose resolving (Δm) is comparable to existing TOF-MS based instrumentation. Major milestones in functionality and performance will be discussed in this chapter. Eventually, what was deemed the ultimate limit in performance of dipolarless square wave mass analysis was reached. To overcome this restriction, complex square waveform generation was investigated, and early proof-of-concept findings are presented here.

The second instrumentation project was the development of ion manipulation techniques utilizing existing DIT technologies. Both mass isolation and mass exclusion techniques will be demonstrated below. How these techniques are made possible through the movement of ions in Mathieu *a-q* space will be described. Direct Cryogenic Ion Spectroscopy (CIS) applications of these techniques will be overviewed in this chapter and immediate future DIT-based CIS experiments will be covered in **Chapter 6**.These ion manipulation techniques provide the mass filtration required to complete CIS in a LDIT. Additionally, the mass isolation and exclusion will be frame in the context of their application to gas phase ion chemical reactions.

Section 5.1 QTPI as a Dipolarless LDIT-MS

In summer of 2016 construction of basic framing, vacuum chambers, and eventual linear quadrupole ion trap (LQIT) construction had been completed. Ion beam path optimizations were accomplished using a microchannel plate (MCP) detector oriented in the axial direction, after the back planar endcap. During this period, a solenoid pulsed valve was used to introduce gas, allowing ions to be collisionally cooled in the LQIT, before axial ejection by means of a pulsed voltage on the back endcap.

This period allowed for tuning of ion optics, most of which required minimal mechanical alterations. During this stage, sine waves were applied to both X-axis and Y-axis at a static frequency of 1 MHz and an amplitude of approximately 300 V_{pp}. No presentable data was produced during this stage.

Once basic functionality was obtained, a waveform generator (LeCroy WaveStation) provided a low voltage variable frequency square wave, which was wired to a commercial high voltage DC pulser (Willamette High Voltage) operating at roughly 100 V_{pp} to 150 V_{PP}. This variable frequency high voltage square wave was applied to the Y-axis electrode pair. A second output from the waveform generator produced a 20 V_{pp} variable frequency square wave and was utilized on the X-axis. The instrument cycle during this period consisted of a trapping cycle (500 kHz 50/50), then mass analysis by means of a linear frequency sweep between 500 kHz and 100 kHz. This caused radial ejection of ions in a non-linear fashion with respect to the m/z domain, making calibration difficult. The low amplitude on the X-axis coupled with the linear frequency sweep generated very poorly resolved mass spectrum, an example of which is shown in **Figure 5.1**. A well-characterized catalyst ($[Ru(Bpy)(tpy)]^{2+}$) was ionized by means of electrospray ionization (ESI) and the relative populations of the base $[Ru(bpy)(tpy)]^{2+}$, water complex $[Ru(bpy)(tpy)(H_2O)]^{2+}$, and nitrogen adduct $[Ru(bpy)(tpy)(N_2)]^{2+}$ were confirmed by means of existing TOF-MS mass analysis (data not shown). The ability to radially eject ions in a mass selective manner yielded a proof-of-concept to justify further studies into the use of square waves to operate the LQIT. This work was completed through the 2016-2017 academic calendar.

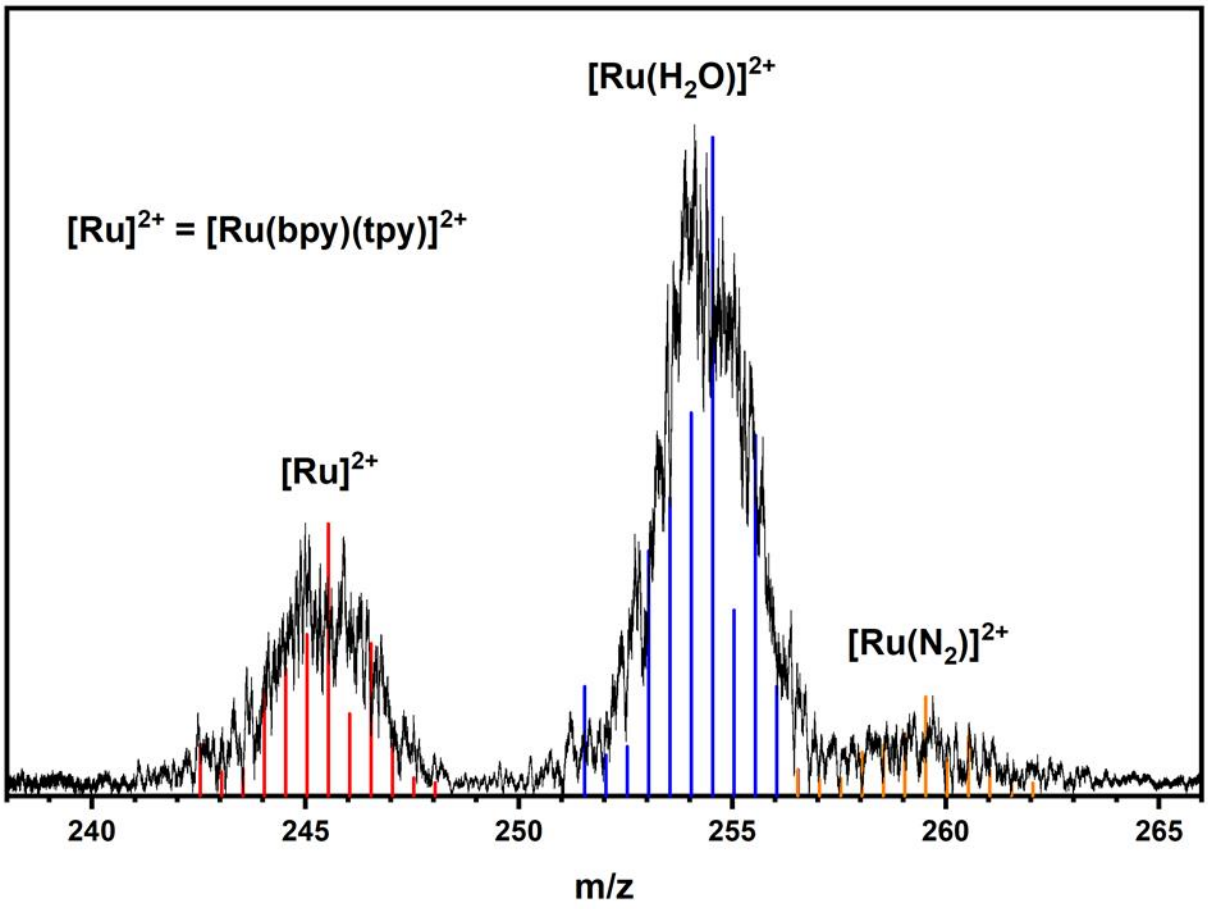

Figure 5.1 Mass spectrum of $[Ru(bpy)(tpy)]^{2+}$ showing the prevalence of both water and nitrogen adduct formation.

Based on existing DIT publications,[1–5] immediate discrepancies between experimental and reported square waveforms used in analysis became evident. Electrical circuit developments were attempted to raise maximum stable frequencies, from roughly 500 kHz to 700 kHz for the commercial DC pulser to little success. An initial prototype involving power MOSFETs based square wave amplification was attempted, but no stable design was finalized. Eventual collaboration with Dr. Pete Reilly at Washington State University led to the fabrication of two High Voltage High Frequency (HVHF) square wave amplifiers, each capable of driving the roughly 180 pF capacitive load of a single LQIT electrode pair at 700 kHz 150 V_{pp} based on Hoffman *et al.*[6] These circuits, in addition to the fabrication of an Arduino based Low Voltage Waveform Generator (LVWFG) circuit based on Hoffman *et al*[7] eventually led to the successful radial ejection of Cs^+ with significantly higher resolving power. A mass spectrum of early Cs^+ and a solution containing Gly_2H^+ and Gly_3H^+ are separately shown in **Figure 5.2**. The Y-axis of all presented mass spectra are in arbitrary units (AU).

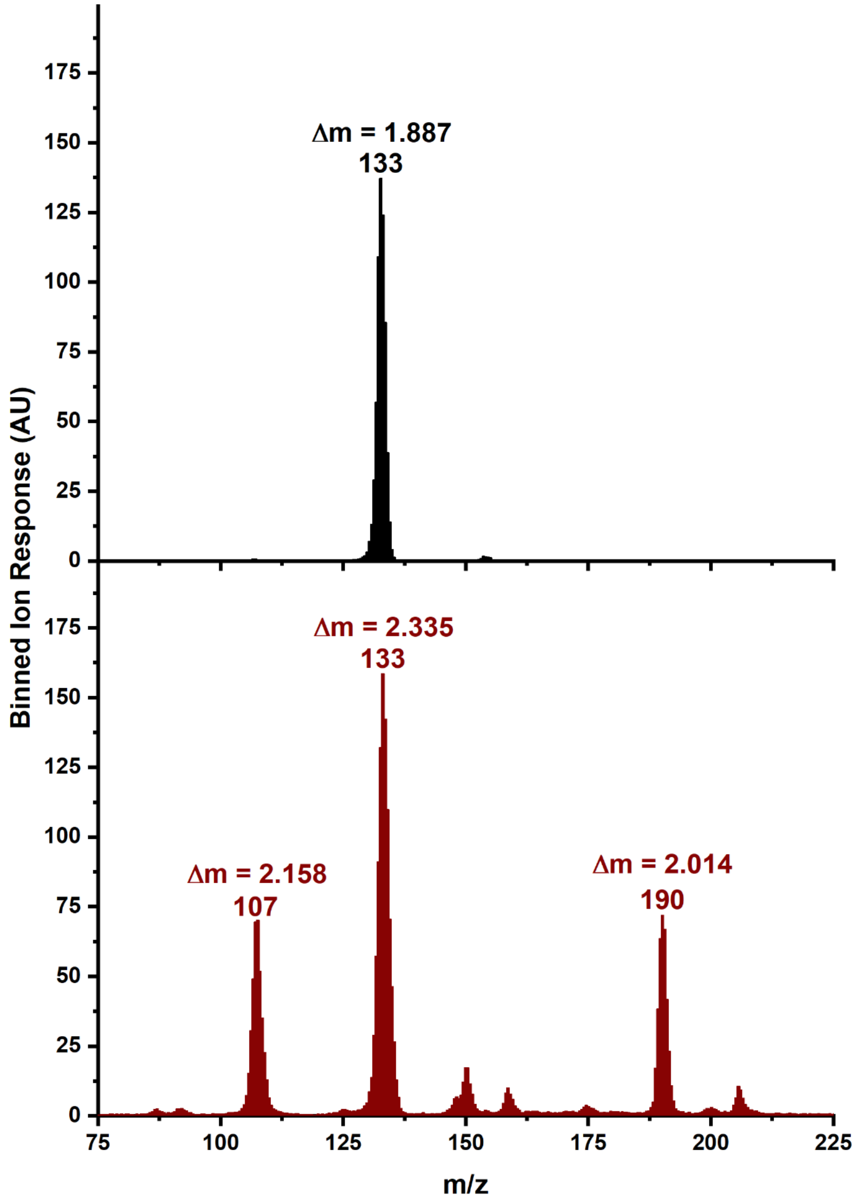

Figure 5.2 Kangaroo based mass spectra of Cs^+ (top) and Gly_2H^+ + Gly_3H^+ (bottom).

Mass spectra above were produced by means of a “Kangaroo” mass scan. During each m/z step, the applied square wave would “jump” between two frequencies. The first frequency corresponded to a location in *a*-*q* space where the current to-be-ejected m/z was deep within the stability region (q_{deep}). The second frequency corresponded to a point significantly closer to the Y-axis boundary line of the stability region (q_{cliff}). Each new m/z step was returned to a different q_{deep} value which was closer to the boundary line than the last. The hope was that when not actively ejecting an ion, the remaining ion population in the LDIT could be returned to an *a*-*q* coordinate which provided less displacement along the X-axis. A visualization of this jumping can be seen in **Figure 5.3**. This figure only shows a single ion (red circle) traversing through *a*-*q* space in six m/z steps, each comprising two individual frequency changes (red arrows). When the sixth m/z step reaches the q_{cliff}, radial ejection occurs. In theory, by jumping deeper in the stability region during each m/z step, better ion cooling and more concisely extracted ion packets would be achieved. This was not the case. This method led to erratic ion behavior at slower scan speeds, likely due to the q_{deep} prior to mass ejection located too close to the boundary line. Eventually, this method was replaced with a downward stepwise frequency scan consistent with other published work, which was covered in **Chapter 2** and **Chapter 3**.[8]

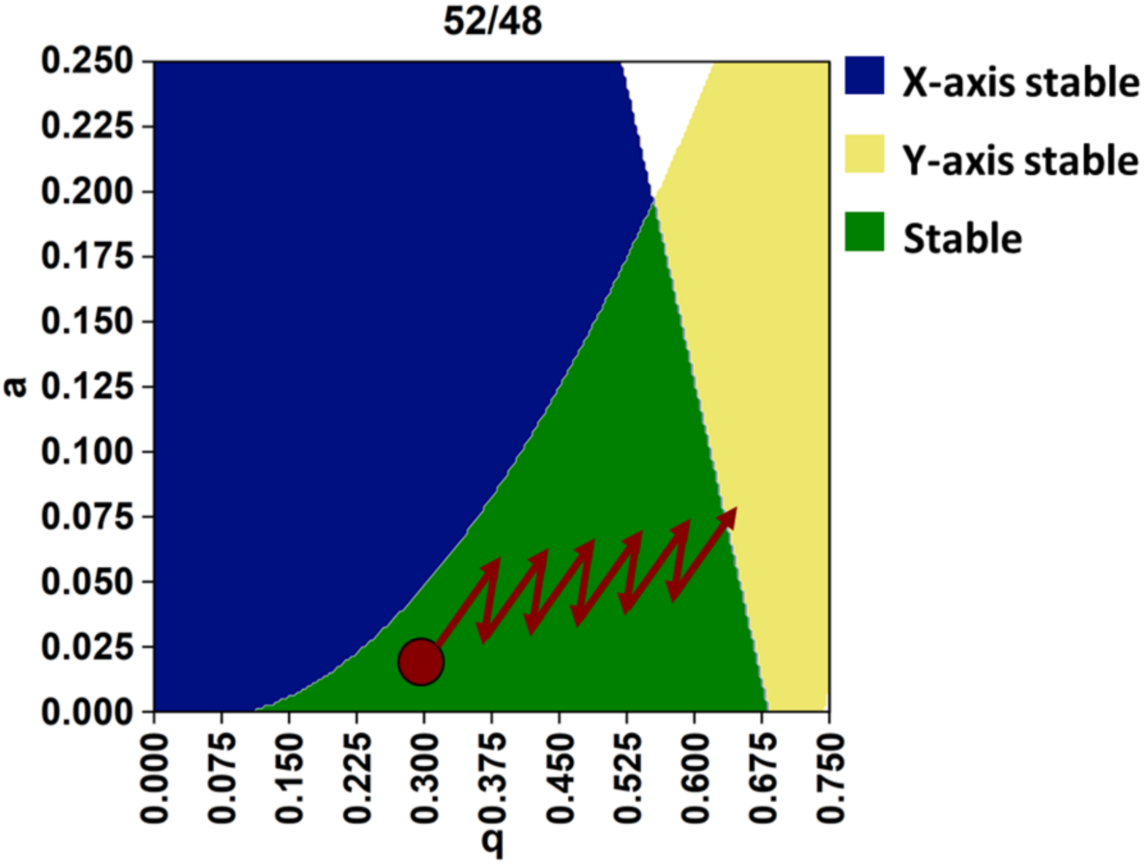

Figure 5.3 Mathieu stability region displaying kangaroo mass scan.

At this point QTPI was a functioning radial ejection LDIT, but resolving power was lackluster. Over the course of several months, incremental improvements were made in performance optimizations including software design for LVWFG and accompanying LabView binning and noise discrimination software. Circuit development to minimize overshoot and ripple of applied square waves was developed, and further beam path optimizations were made. At the time, an adjustable 0 to 500 V DC to DC amplifier (Advanced Energy) was used to generate 150 V_{pp}, variable frequency square wave for both X-axis and Y-axis electrodes. This dictated a low mass cutoff (≈87 m/z) higher than what was desired (< 75 m/z), eventually leading to the reduction of the applied waveform to 100 V_{PP}. This single DC-DC converter only generated 0.125 amps of current for each V+ and V^- inputs of the two HVHF circuits, which proved to be inadequate at higher frequencies (700 kHz). An additional DC-DC amplifier was purchased and implemented leading to a doubling of the raw ion response, as shown in **Figure 5.4**.

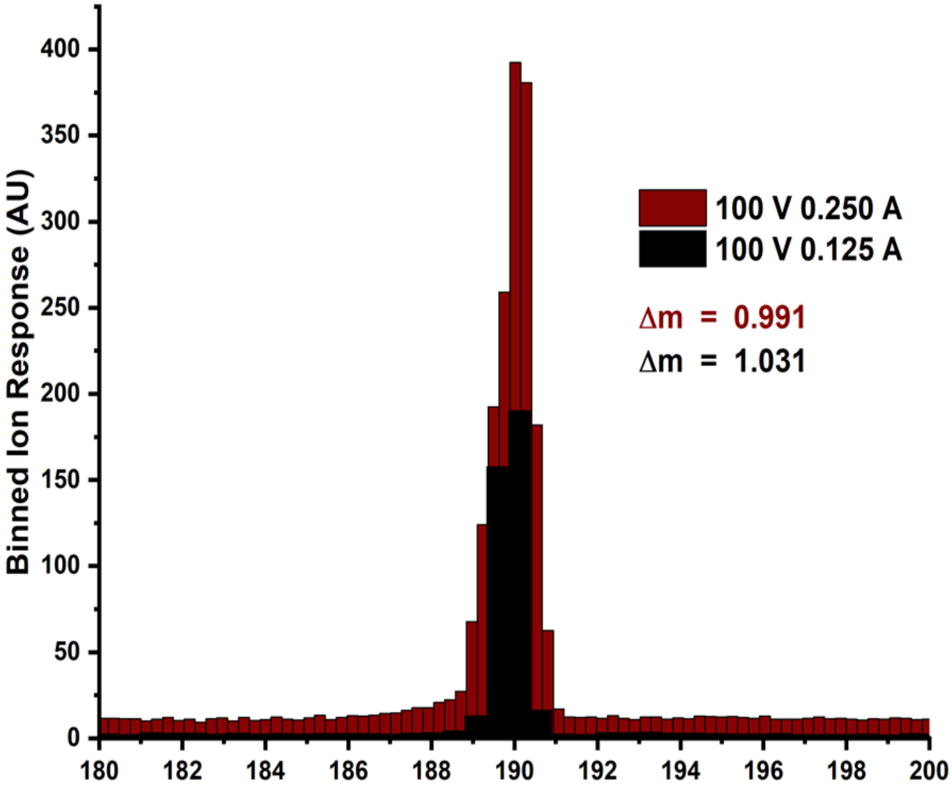

Figure 5.4 Mass spectra of one vs. two DC-DC supplies.

Throughout the instrument cycle, the singular DC supply would not be able to maintain the 100 V_{pp} amplitude, leading to a drop in voltage by the end of the high frequency (700 kHz) trapping interval. As the frequency decreased throughout the mass scan, the power requirement decreased, leading to an increase in square wave V_{pp} by the end of the mass analysis interval. This mismatch between applied waveform amplitudes is believed to have led to the significant performance loss. Previous fluctuations were minimized by the additional DC supply, allowing for a slower scan speed while maintaining adequate resolving power, from 0.5 Δm/z to 0.25 Δm/z.

With a resolving power barely below Δm = 1.0, QTPI was still not performing well enough to be warrant CIS integration. Again, over months additional changes were made to instrumentation design, ion optic alignments, and mass analysis variables provided by the LVWFG were explored in detail. MCP based detection was replaced with a Continuous Electron Multiplier (CEM) allowing for higher operational pressures. Continuous collisional gas introduction by means of a precision leak valve was introduced to accommodate the higher-pressure limit. Duration in which ions were held at maximum frequency and neutral duty cycle (700 kHz 50/50 trapping interval) was dramatically increased from < 100 ms to upwards of 500 ms, based on similar instrumentation from Cooks *et al.*[9] Extensive studies into the effect mass analysis duty cycles had on resolving power as a function of scan speed were explored. These changes led to incremental gains, but no major improvement to resolving power. Eventually, a non-adjustable 100 V 4 A DC power supply was purchased to confirm if earlier square wave amplitude fluctuations were still the current limitation or whether further circuit development was needed. This change drastically improved the desired resolution. Along with resolving power improvements, a new scan speed limit, from 0.25 Δm/z to 0.15 Δm/z was achieved. These mass spectral gains can be seen in **Figure 5.5**.

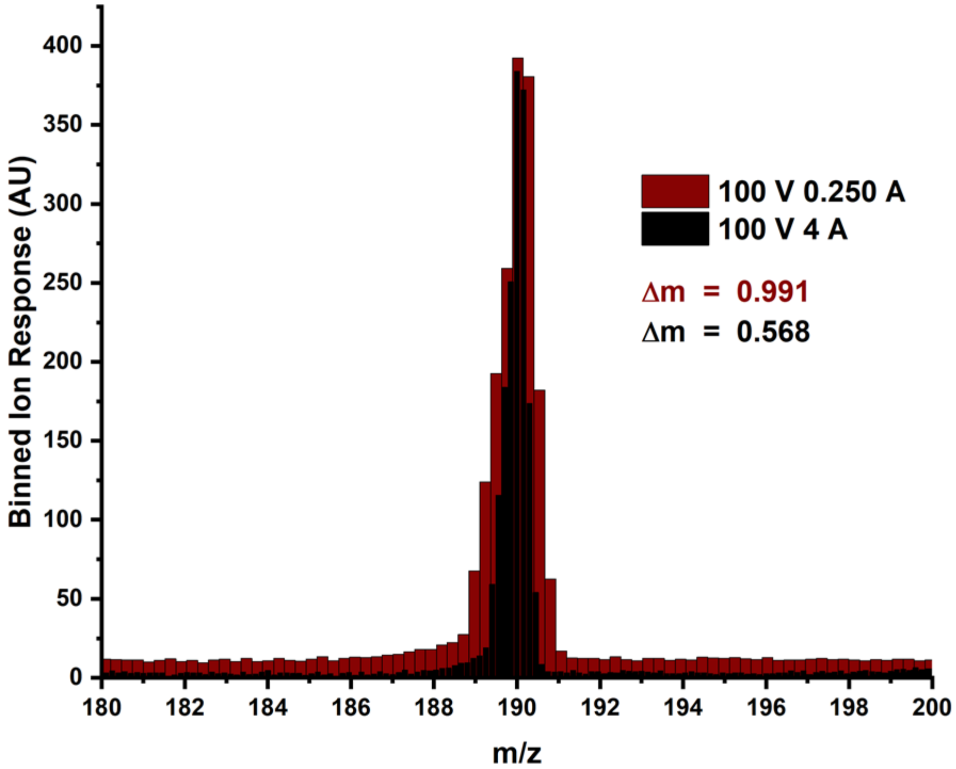

Figure 5.5 Mass spectra illustrating difference between 0.25 A and 4 A DC supplies.

Finally, with Δm close to 0.5 m/z, the viability of the square wave based LDIT as a mass analyzer for future CIS implementation proved promising. After minor adjustments to operational conditions, a final resolving power of Δm ≈ 0.4 and a final scan speed of Δm/z = 0.1 was achieved. This resolving power was directly compared to current CIS capable TOF-MS instrumentation and is shown in **Figure 5.6**. Despite roughly half the signal-to-noise (hereafter S/N) and double the Δm of the TOF-MS, we felt comfortable in determining this adequate performance for CIS integration.

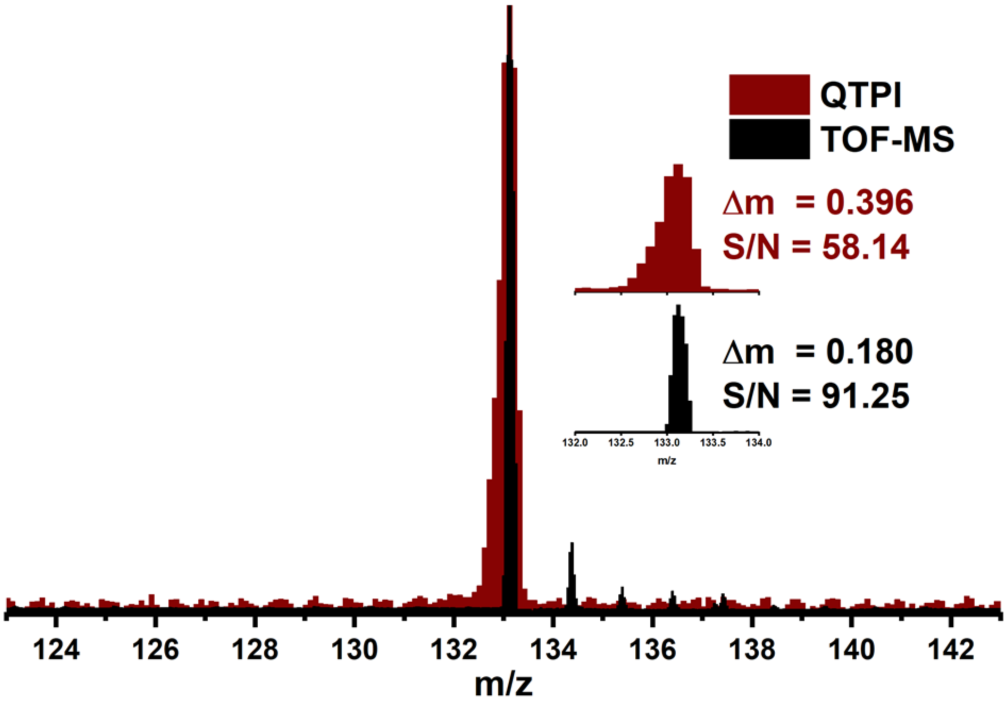

Figure 5.6 Mass spectra illustrating QTPI vs. current TOF-MS instrumentation.

Section 5.2 Complex Square Wave Integration

During the development of QTPI, the use of complex waveforms during mass analysis was being concurrently reported on by Cook *et al*[9,10] and McLuckey *et al*.[11] These reports led additional development efforts into incorporating complex square waves to the LDIT for further performance gains and increased ion manipulation functionality. Once there was an understanding of how auxiliary waveforms could be introduced to a QIT-based mass analyzer, circuitry was developed to attempt incorporation on QTPI. This work was done to further improve LDIT-MS performance to be identical to existing TOF-MS mass analyzers. The function of complex (dipolar) waveforms is as follows. At a given applied base frequency, each m/z population present in an ion trap will move throughout its confines with different rates. The period of this motion is referred to as the secular frequency, and is m/z dependent.[12] If a small auxiliary waveform is applied to the QIT, the amplitude of motion for a specific m/z's secular frequency can be excited. Eventually this excitation force can overcome the confining force of the QIT, leading to ejection from the trap. Several research group have reported success with the use of dipolar waveforms during mass analysis.[4,9,10,13,14] In cylindrical ion traps, the dipolar waveform is applied to the hyperbolic endcaps and the auxiliary frequency is scanned while maintaining static frequency trapping waveform on the ring electrode. When the applied frequency matches a secular frequency of an ion population in the QIT, resonant axial ejection occurs.

In LQITs however, the dipolar frequency is superimposed atop already existing trapping waveforms. Either the dipolar frequency is scanned while the base frequency is held constant, or both dipolar and base frequency are scanned such that the dipolar frequency is an integer division of the base frequency. This superimposed dipolar frequency is applied only to electrode pairs containing an exit slit (i.e., the X-axis for QTPI). Unlike cylindrical ion traps, the generation of this dipolar frequency is more involved.

For sine wave operation, this dipolar superimposition is accomplished by means of a centered-tapped transformer. These transformers act as inductors who impede the large fluctuation of current. Sine waves which are a continually changing voltage do not possess large current fluctuations. Square waves consist of two DC voltage states which are switched between rapidly. Switching between the two voltage states requires large fluctuations of electrical current. Due to the inductance of transformers and the current driven nature of square waves, this is an inefficient process. Instead, additional circuitry involving multiple square wave amplifiers was developed and was covered in **Chapter 3**. A prototype capable of generating dipolar square waveforms was started in the summer of 2019 and a stable working circuit was completed in November of 2019. For dipolar mass analysis, the downstream high frequency component was comprised of the stepped frequency mass scan as also described in **Chapter 3**. Upstream dipolar frequencies consisted of specifically designed waveforms to generate a final complex waveform whose V_{pp} amplitude was modulated for one period every N number of periods. Amplitude modulation was locked at 10 V_{pp} and a N value of 7 was chosen for the work presented below. The goal of this design was to explore dipolar mass analysis and the potential gains to resolution on existing QTPI methodology. Detector responses for both dipolarless and dipolar LDIT operation can be shown in **Figure 5.7**. An example of the final complex dipolar frequency can also be seen in the bottom portion of this figure where small increases (+5 V) or decreases (-5 V) can be seen every seven periods.

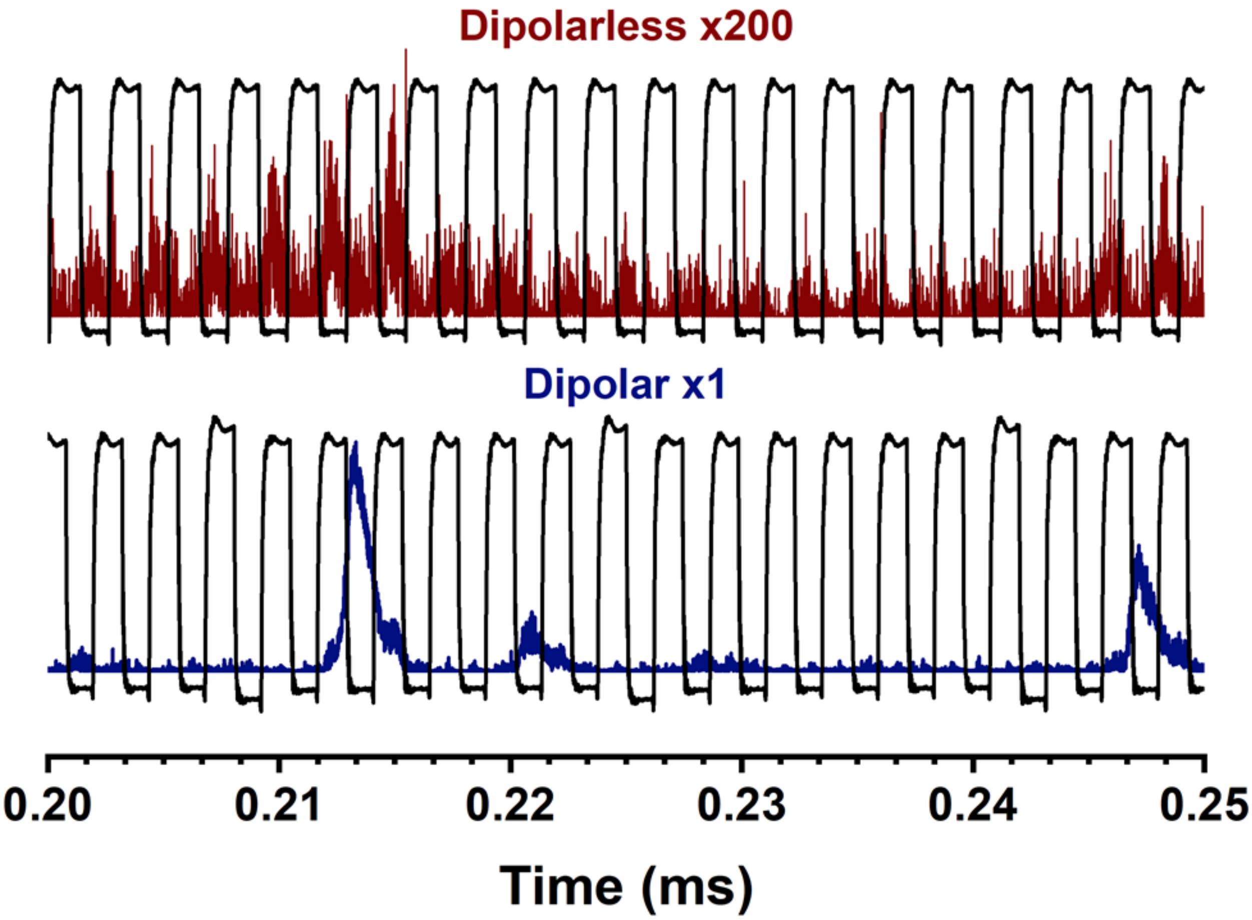

Figure 5.7 Ion responses of dipolarless (red) and dipolar (blue) mass analysis with accompanying applied waveforms (black).

An artificial magnification of 200 times the dipolarless ion response was required to properly see comparisons between the two detection bins, indicating the significant impact dipolar mass analysis had. In the dipolarless case, packets of ions were being radially ejected as the square wave switches from HIGH to LOW states. When the frequency step for a given m/z reaches the boundary line of the Mathieu stability region, large enough ion displacement in the detection axis (X-axis) occurs, causing ejection from the LDIT and subsequent detection. Only a small population of the given m/z ions is displaced per period, requiring several periods for complete ejection. In the dipolar case, a given m/z ion population resides deeper in the Mathieu stability region. Amplitude modulation seen by the ions act to instantaneously move the Mathieu *q* coordinate for a single period toward the boundary line. Eventually, a frequency step is oriented such that the *q* "jump" pushes past the boundary line for a single period. This *q* jumping provides a swift exit from the boundary region into the radially unstable zone, circumventing prolonged interaction with imperfect electric fields present at the exit slit. An exaggeration of this effect can be seen in **Figure 5.8**. Rather than differing m/z species, the respective red and blue circles represent individual ions present in the LDIT. In the dipolarless case (left), variance between the kinetic energy of ion populations cause some dots to be closer to the boundary line and some to be further away. When the frequency change occurs (red arrows), complete red ion ejection does not occur. In the dipolar case, the ions are deeper in the stability region, leading to less variance in their *a*-*q* coordinates. When the frequency change occurs, the additional amplitude modulation causes a larger displacement in *a*-*q* space past the boundary line. Significantly more ions per period of the auxiliary frequency enter the radial displacement region, causing more concise extraction, which can be seen from the above figure.

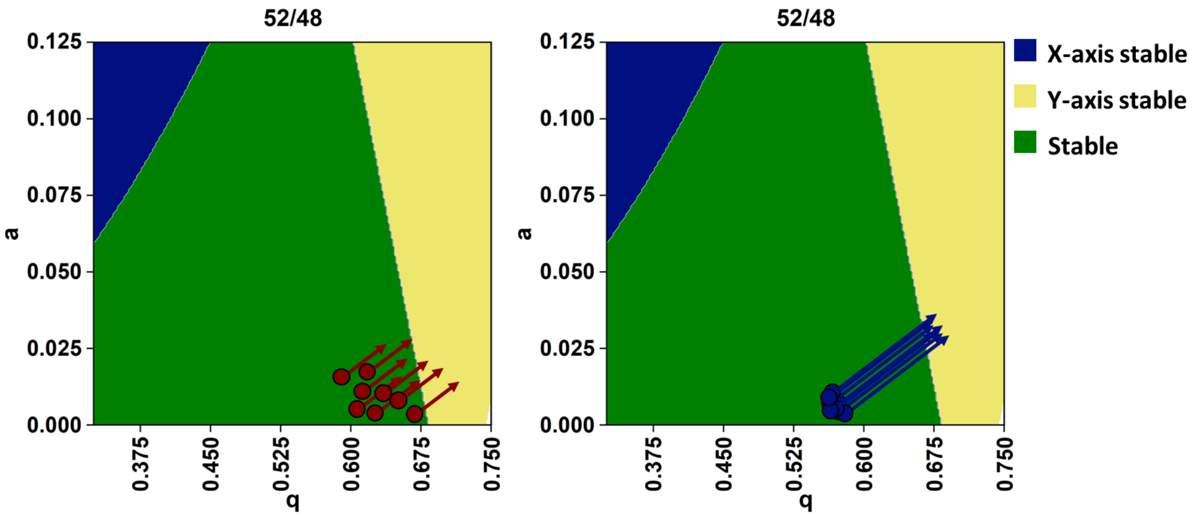

Figure 5.8 Mathieu stability diagram showing the dipolarless (left) and dipolar (right) ion extraction.

This lack of kinetic energy variance and conciseness of boundary ejection leads to significant increases to resolution during mass analysis. Normalized mass scans of both dipolarless and dipolar waveforms can be found in **Figure 5.9**. By means of dipolar mass analysis, a new resolving power of Δm = 0.278 was achieved. This increase in resolving power did come at a major degradation to the S/N observed. Likely this is due to the additional MOSFET switching noise, which was mentioned in **Chapter 4**, and not an actual degradation of the ion response. Dipolarless operation involved the use of four power MOSFETs across two HVHF boards. Circuitry required for dipolar incorporation doubles that amount to eight power MOSFETs, each generating individual noise spikes every time a MOSFET is opened or closed. Originally, we thought this noise contribution would be minimized due to the phase coherence of the applied waveform, but as evident from the figure above, this was not the case. Future circuitry development will be performed to minimize this MOSFET switching noise.

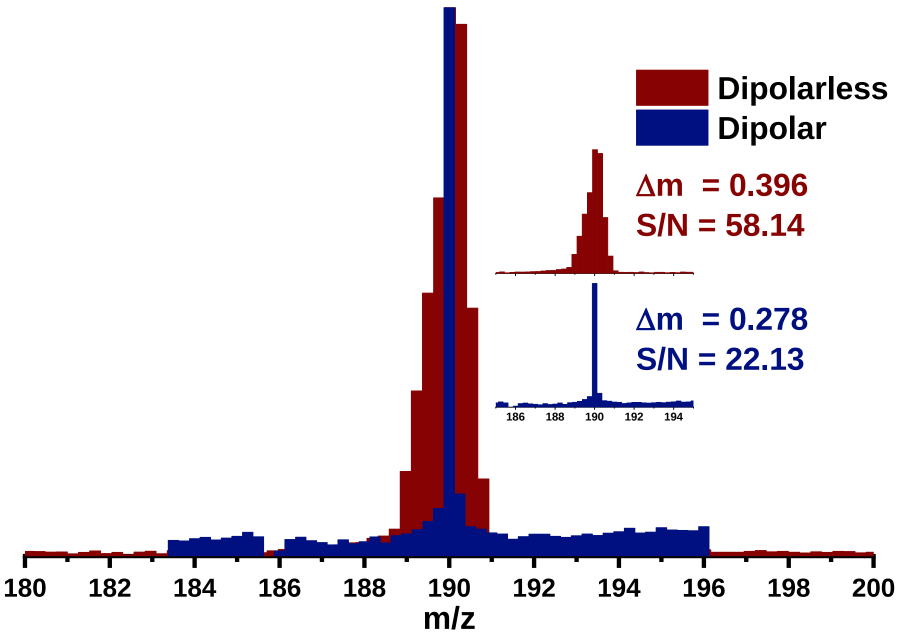

Figure 5.9 Mass spectra of Gly$_3$H$^+$ utilizing dipolarless (red) and OEN dipolar waveforms (blue).

The complex waveform study provided above was an extremely early proof-of-concept. Original development of dipolar mass analysis was not successfully implemented until November 2019. Between November 2019 and March 2020, exploratory studies into different possible waveform constructions were investigated, leading to the one-every-N (OEN) circuitry that was used to obtain the data above. In March of 2020, a major global pandemic (COVID-19) required the prolonged shutdown of research facilities. Upon returning to the lab, significant mechanical problems with QTPI were found, diagnosed, and mostly fixed. Some additional work has been done to better characterize ideal OEN dipolar mass analysis, but a complete story has yet to be finalized.

The major problem with characterizing this design is the sheer number of variables that are needed to be explored to determine optimal waveform design. For each square wave period, a HIGH and LOW state is present. The amplitude of these voltage states can be modulated on a per-period basis. The V$_{pp}$ amplitude of the auxiliary waveform can also be modulated. Finally, the frequency in which this modulation occurs can be reduced by any integer value of N. As the number of N increases, the number of possibilities for waveform tailoring becomes mind-numbingly high. It is my hope that this work will be continued by future researchers in an attempt to finalize adequate square wave dipolar mass analysis settings.

Section 5.3 Digital Ion Trap Applications for Cryogenic Ion Spectroscopy

Separate to the need for radial ejection mass analysis and its replacement of existing TOF-MS, the other motivation for investigations into square wave-based digital ion traps has been the mass selectivity these DITs can offer while holding or transporting ions. Recall from **Chapter 1** that in order to perform CIS the ion of interest must be cooled to 10 K by means of inelastic collisions with 10 K buffer gas seeded with a spectroscopic tag (D_2). Some ion population never reaches the required temperature for tag condensation. This never-tagged species must be evacuated prior to the laser interaction. Currently this is done via mass gating during the ion flight path. Through ion manipulation techniques covered below, an alternative method of accomplishing this has been achieved.

Additionally, 80K cryogenic reaction ion traps (RITs) have been developed and reported.[15] These RITs are most commonly used for gas phase ion chemical reactions prior to 10 K spectroscopic tagging. Current RITs are comprised of short length, round rod quadrupoles or octopoles operating with 1 MHz 300 V_{pp} sine waves with no DC potential differences between electrode pairs. These static frequency, high amplitude sine waves make ion storage across a wide mass range possible but offer nothing in terms of mass manipulation. Due to this lack of mass selectivity, the complexity of ion chemistry reactions is limited to single molecule ion clustering experiments and single stage ion chemical reactions. Incorporating mass selectivity to one or more RITs would allow for complex ion solvation systems and multi-step ion chemical reactions.

By providing a variable temperature range from 300 to 80 K, several gas molecules can be non-covalently adhered to ions of interest. Most commonly water is used to mimic solution phase solvation effects[16] and to determine structural changes of the parent ion as water solvation shell size increases.[17] These studies are able to be completed with one RIT and one CIT, both of which are not mass selective. If instead, however, two DITs were implemented before the CIT, studies involving multi-solvent species would be attainable. These multi-solvent species could be comprised of either two separate solvents (e.g., water and methanol) or two isotopes of the same solvent (e.g., H_2O and D_2O). The former would provide insight to structural changes of biologically relevant ions where solvent environments are complex systems. The latter would exploit the differences in the spring constants of O-H vs. O-D bonds to selectively probe individual solvent molecules in large cluster sizes.[18]

Current instrumentation involving only one RIT and one CIT makes these studies impossible, as little success has been found with pulsing multiple solvent molecule types into one RIT. Instead, the use of two RITs would allow for solvent A to be clustered in RIT A and solvent B to be clustered RIT B. Without the per-trap mass filtration of DITs, near overlapping masses (< 4 m/z) between 18 amu (water), 20 amu (D_2O) and 32 amu (MeOH) cluster molecules coupled additional 4 amu spectroscopic tag (D_2) is likely. Through the use of duty cycle based mass filtration, it is possible to isolate only a single cluster size, per-trap, to minimize these overlapping masses.

Additional to solvation experiments, a RIT has also been used to probe key catalytic intermediates in a Ruthenium based water oxidation catalysis cycle.[19–21] Most of these catalytic intermediates were generated during or previous to ion generation, and the resulting products were solvated to investigate the catalytic pathway. To date only the first few steps of this catalytic cycle has been thoroughly examined. One of the primary reasons for this is the small change of mass which occurs shortly in this pathway, from $[Ru(OH)]^{2+}$ to $[Ru(O)]^{2+}$ where $[Ru]^{2+}$ is $[Ru(bpy)(tpy)]^{2+}$. This change of mass is further complicated by the

7 stable isotopes of Ruthenium, making each $[Ru]^{2+}$ span a 3.5 m/z range. These two factors have made further studies into the catalytic cycle impossible.

If instead of a singular non-mass selective RIT, two mass selective digital ion reaction traps (DIRTs) were used, further reaction steps into this water oxidation pathway could be determined by generating the first intermediate in the first DIRT, mass isolating it to minimize isotopic overlap, then transporting this intermediate into the second DIRT, where the $[Ru(O)]^{2+}$ could be properly probed. This ion reactions scheme requires the use of per-trap mass filtration to be accomplished and is also well suited for the mass isolation detailed below.

5.3.1 Dipolarless Mass Filtration

While originally reported by Li Ding and coworkers[14] as an alternative method for mass analysis, a large body of work has been presented about the capability for DITs to be used as in-line mass filters.[3,22–25] With regard to sine waves, this is accomplished by scaling the DC and AC potential, but for square waveforms, this is accomplished through manipulation of the applied frequency and duty cycle. Altering the duty cycle both perturbs the shape of the Mathieu stability region and provides a non-zero Mathieu a component for m/z in the LDIT. Manipulating the applied frequency, Ω, changes both Mathieu a and q parameters such that $a \propto 1/\Omega^2$ and $q \propto 1/\Omega^2$, respectively. Thus, decreasing the value of Ω will move both Mathieu a and q parameters. The warping of the region's shape and a-q movement produces a similar mass isolation functionally to sine waves. This can best be visualized by **Figure 5.10**.

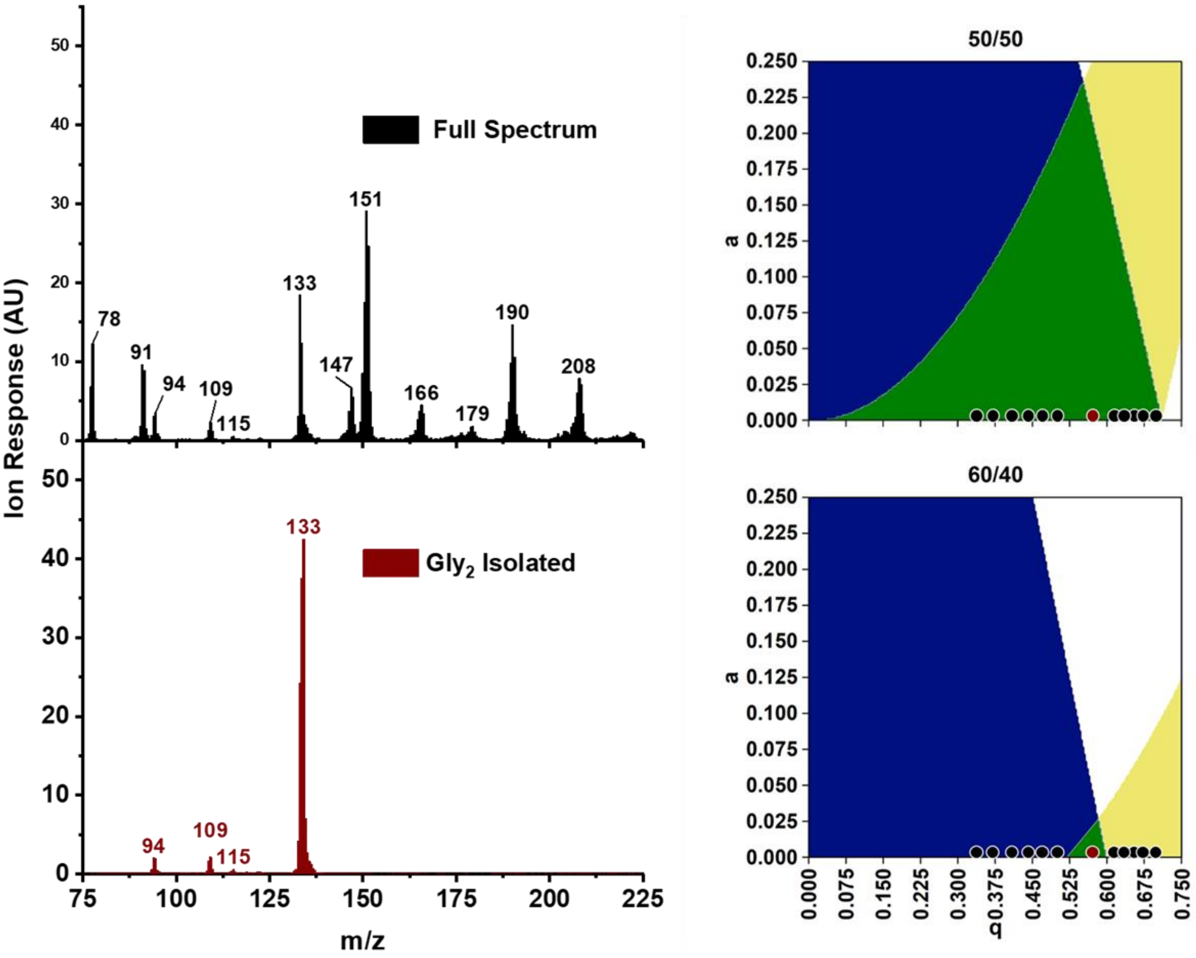

Figure 5.10 Pre-MS mass isolation of Gly_2H^+ by frequency and duty cycle manipulations.

A solution containing a heavily degraded combination of Gly_2H^+ and Gly_3H^+ was sprayed and mass analyzed. Electrospray and ion optic voltages were intentionally manipulated to perform maximum fragmentation while still maintaining adequate parent peak abundance. Prior to mass analysis, a 100 V_{pp} 525 kHz square wave with 60% duty cycle on the X-axis and 40% duty cycle on Y-axis was applied for approximately 10 µs. The resulting isolated ion population was then analyzed using identical mass scan settings as the spectrum in black. As can be seen from the figure above, prior termination of almost all previous ion species was accomplished. The appearance of the 94 m/z, 109 m/z, and 115 m/z peaks can be attributes to minor fragmentation occurring from the filtration process itself. Bringing the 133 m/z ions too close to boundary lines likely caused minor boundary activated collision induced dissociation to occur.

A visualization of the narrow stability band provided by these waveform settings can be found in **Figure 5.11**, generated from determining ion stability in accordance with matrix solution of the Hill equation, as outlined by Reilly and coworkers.[26] Both figures illustrate the ability of DITs to provide pre-MS mass filtration needed to perform CIS in QTPI and to perform per-trap mass isolation for the above outline complex ion chemical reactions.

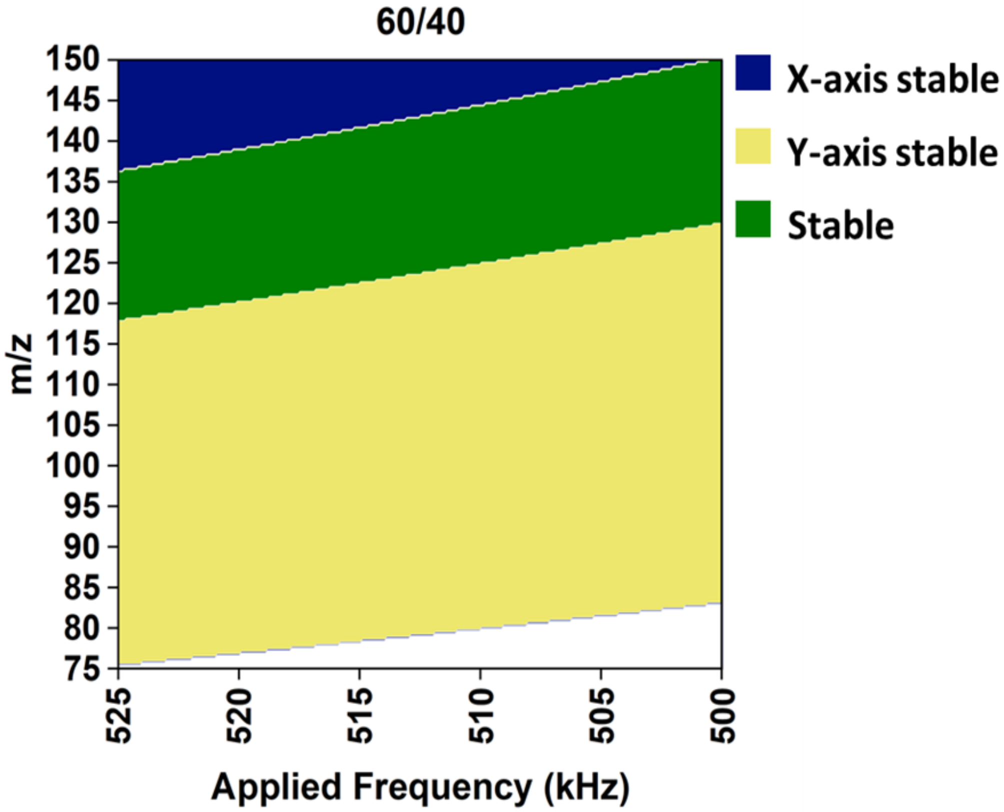

Figure 5.11 m/z vs. Frequency graph of the pre-MS mass isolation technique.

Section 5.4 Selective Species Exclusion and Its uses in Cryogenic Ion Spectroscopy

Although dipolar mass analysis was certainly an area of interest for complex waveform generation, the main motivation for circuit development was the secular frequency matching capability of auxiliary waveforms in static QIT operating conditions. The presence of an auxiliary waveform can be thought of as a small hole of instability that is generated in Mathieu *a-q* space. Typically, these holes are oriented such that while scanning across the Mathieu *q*-axis, where $a = 0$, ejection will occur deeper in the stability region before an ion traverses *a-q* space towards a boundary line. Cooks *et al*[9] described this as a "black hole" that is generated by auxiliary waves. If the black hole is placed such that an ion population present in a QIT would fall within it, this ion would be ejected from the trap prior to mass analysis. While future developments into auxiliary waveforms during mass analysis are planned, the primary appeal of complex square waves is the ability to selective exclude multiple ion species present in a RIT.

With existing complex waveform generation circuitry already developed, a technique involving the use of auxiliary waveforms was created to exclude ions of disinterest prior to mass analysis. The only modification needed to existing complex waveform circuitry was a de-coupling of the phase coherence for the upstream HVHF components, see **Chapter 3** for more details. Instead of splitting the downstream frequency input into an external TTL manipulation circuit, an additional channel of the LVWFG was directly wired to upstream HVHF circuits. This allows variable frequency control of the auxiliary waveform during this exclusion interval and normal dipolarless mass analysis on the LDIT. Prior to the analysis interval, a complex waveform with a base frequency of 700 kHz at 50/50 was applied to both electrode pairs. On only the X-axis, a 10 V_{pp} variable frequency square wave was superimposed atop the base trapping frequency. This waveform is difficult to capture due to the phase incoherence, but an oscilloscope trace of a similar output waveform can be found in **Figure 5.12**. The yellow waveform represents the variable frequency which is controlled by the second output of the LVWFG. With a roughly 200 ns delay, the same frequency see can be seen an as amplitude modulation on the teal waveform, represented the complex square wave applied to the X-axis.

CH2 High 64.00V
CH2 Low -5.000V
CH1 2.00V
CH2 10.0V
400ns
5.35200µs
500MS/s
20M points
CH1 2.20V
300kHz

Figure 5.12 Oscilloscope traces of auxiliary waveform component (yellow) and final complex waveform (teal).

By changing the frequency that is applied during this selective species exclusion (SSE) interval, ions of disinterest can be individually terminated prior to mass analysis. The auxiliary frequency that is applied matches the secular frequency of ions trapped in the static 700 kHz 50/50 confining waveform. At the time of writing, these frequencies are experimentally determined through a guess-and-check system. In the future, a method for determining secular frequency matching will likely be developed.

Pre-MS expulsion of individual m/z species in a complex sample is shown in **Figure 5.13**. In all mass spectrum presented, the exact same MS settings were used, the only difference was the addition of the auxiliary waveform for 10 µs prior to mass analysis (frequencies shown in figure). Mathieu stability diagrams are shown to the right of each MS, denoting a whole (white circle) in *a*-*q* space. No duty cycle manipulations were done to the auxiliary waveform during this period and as mentioned above, secular frequencies were determined experimentally. It is unclear whether the applied frequencies are matching the fundamental secular frequency or higher ordered harmonics of the secular frequency. Also of interest is the change in amplitude of the remaining two peaks when one is excluded. The exact reason for this is unknown, but early speculation points towards space charge effects being the culprit, as other space charge effects have caused problems in the LDIT before.

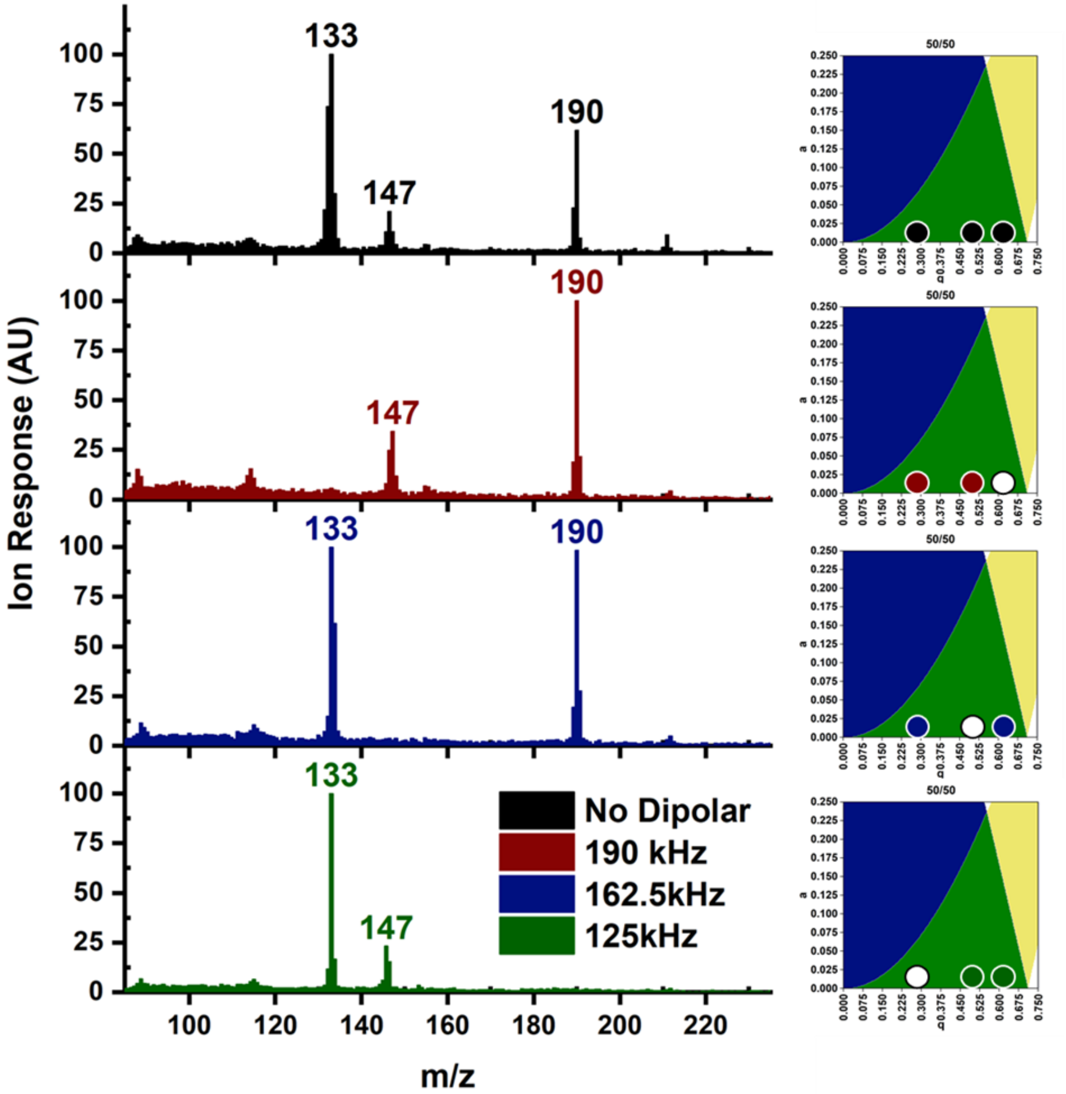

Figure 5.13 Mass spectra showing the effect of selective species exclusion.

The implications of this technique are directly useful to CIS instrumentation. Not only is this mass exclusion interval able to function as a mass isolation stage by means of a band-stop frequency sweep. But additional complex ion reaction schemes are possible. Upon cryostat integrations, CIS capability will immediately be possible on QTPI. By tailoring this instrument to be focused on ion solvation studies, spectroscopic tags significantly greater than the resolving power of QTPI can be used (e.g., +18 amu water). Upon generating a distribution of water clusters, SSE can be implemented to eject either odd or even water cluster sizes. These removed populations can be re-populated by means of a laser interaction with the remaining water clusters. If an optical transition is present in any of the cluster sizes at a given wavelength, re-population of the previously excludes mass channels is possible. The effect would be the collection of multiple IR datasets concurrently. A detailed instrument cycle which involved the use of SSE, a prototype liquid nitrogen cryostat, and existing laser infrastructure is detailed in **Chapter 6**, with a visual aid of this process.

Section 5.5 Conclusion

Through years of development QTPI has become a functioning LDIT-MS whose performance is finally comparable to existing TOF-MS instrument. The capability of providing pre-MS mass isolation and exclusion will allow for future CIS studies to be performed on QTPI with the integration of a cryostat and tunable wavelength laser. Additional to this, two techniques utilizing square wave-based DITs have been shown to provide both mass isolation and mass exclusion. Future complex CIS experiments were speculated upon using these techniques.

Section 5.6 Chapter 5 References

(1) Ding, L.; Sudakov, M.; Kumashiro, S. A Simulation Study of the Digital Ion Trap Mass Spectrometer. *Int. J. Mass Spectrom.* **2002**, *221* (2), 117–138. https://doi.org/10.1016/S1387-3806(02)00921-1.

(2) Singh, R.; Jayaram, V.; Reilly, P. T. A. Duty Cycle-Based Isolation in Linear Quadrupole Ion Traps. *Int. J. Mass Spectrom.* **2013**, *343–344*, 45–49. https://doi.org/10.1016/j.ijms.2013.02.012.

(3) Brancia, F. L.; McCullough, B.; Entwistle, A.; Grossmann, J. G.; Ding, L. Digital Asymmetric Waveform Isolation (DAWI) in a Digital Linear Ion Trap. *J. Am. Soc. Mass Spectrom.* **2010**, *21* (9), 1530–1533. https://doi.org/10.1016/j.jasms.2010.05.003.

(4) Wang, L.; Xu, F.; Ding, C. F. Dipolar Direct Current Driven Collision-Induced Dissociation in a Digital Ceramic-Based Rectilinear Ion Trap Mass Spectrometer. *Anal. Chem.* **2013**, *85* (3), 1271–1275. https://doi.org/10.1021/ac3031256.

(5) Berton, A.; Traldi, P.; Ding, L.; Brancia, F. L. Mapping the Stability Diagram of a Digital Ion Trap (DIT) Mass Spectrometer Varying the Duty Cycle of the Trapping Rectangular Waveform. *J. Am. Soc. Mass Spectrom.* **2008**, *19* (4), 620–625. https://doi.org/10.1016/j.jasms.2007.12.012.

(6) Hoffman, N. M.; Opačić, B.; Reilly, P. T. A. Note: An Inexpensive Square Waveform Ion Funnel Driver. *Rev. Sci. Instrum.* **2017**, *88* (1), 1–4. https://doi.org/10.1063/1.4974345.

(7) Hoffman, N. M.; Gotlib, Z. P.; Opačić, B.; Clowers, B. H.; Reilly, P. T. A. A Comparison Based Digital Waveform Generator for High Resolution Duty Cycle. *Rev. Sci. Instrum.* **2018**, *89* (8), 084101. https://doi.org/10.1063/1.5004798.

(8) Shinholt, D. L.; Anthony, S. N.; Alexander, A. W.; Draper, B. E.; Jarrold, M. F. A Frequency and Amplitude Scanned Quadrupole Mass Filter for the Analysis of High m / z Ions. *Rev. Sci. Instrum.* **2014**, *85* (11), 113109. https://doi.org/10.1063/1.4900627.

(9) Snyder, D. T.; Pulliam, C. J.; Wiley, J. S.; Duncan, J.; Cooks, R. G. Experimental Characterization of Secular Frequency Scanning in Ion Trap Mass Spectrometers. *J. Am. Soc. Mass Spectrom.* **2016**, *27* (7), 1243–1255. https://doi.org/10.1007/s13361-016-1377-1.

(10) Snyder, D. T.; Peng, W. P.; Cooks, R. G. Resonance Methods in Quadrupole Ion Traps. *Chem. Phys. Lett.* **2017**, *668*, 69–89. https://doi.org/10.1016/j.cplett.2016.11.011.

(11) Lee, K. W.; Eakins, G. S.; Carlsen, M. S.; McLuckey, S. A. Ion Trap Operational Modes for Ion/Ion Reactions Yielding High Mass-to-Charge Product Ions. *Int. J. Mass Spectrom.* **2020**, *451*, 116313. https://doi.org/10.1016/j.ijms.2020.116313.

(12) Ding, L.; Kumashiro, S. Ion Motion in the Rectangular Wave Quadrupole Field and Digital Operation Mode of a Quadrupole Ion Trap Mass Spectrometer. *Rapid Commun. Mass Spectrom.* **2006**, *20* (1), 3–8. https://doi.org/10.1002/rcm.2253.

(13) Xu, F.; Wang, L.; Dai, X.; Fang, X.; Ding, C. F. Resonance Activation and Collision-Induced-Dissociation of Ions Using Rectangular Wave Dipolar Potentials in a Digital Ion Trap Mass Spectrometer. *J. Am. Soc. Mass Spectrom.* **2014**, *25* (4), 556–562. https://doi.org/10.1007/s13361-013-0804-9.

(14) Ding, L.; Sudakov, M.; Brancia, F. L.; Giles, R.; Kumashiro, S. A Digital Ion Trap Mass Spectrometer Coupled with Atmospheric Pressure Ion Sources. *J. Mass Spectrom.* **2004**, *39* (5), 471–484. https://doi.org/10.1002/jms.637.

(15) Marsh, B. M.; Voss, J. M.; Garand, E. A Dual Cryogenic Ion Trap Spectrometer for the Formation and Characterization of Solvated Ionic Clusters. *J. Chem. Phys.* **2015**, *143* (20). https://doi.org/10.1063/1.4936360.

(16) Fischer, K. C.; Voss, J. M.; Zhou, J.; Garand, E. Probing Solvation-Induced Structural Changes in Conformationally Flexible Peptides: IR Spectroscopy of Gly3H+·(H2O). *J. Phys. Chem. A* **2018**, *122* (41), 8213–8221. https://doi.org/10.1021/acs.jpca.8b07546.

(17) Fischer, K. C.; Sherman, S. L.; Garand, E. Competition between Solvation and Intramolecular Hydrogen-Bonding in Microsolvated Protonated Glycine and β-Alanine. *J. Phys. Chem* **2020**, *2020*, 1593–1602. https://doi.org/10.1021/acs.jpca.9b11977.

(18) Fournier, J. A.; Wolke, C. T.; Johnson, C. J.; Johnson, M. A.; Heine, N.; Gewinner, S.; Schöllkopf, W.; Esser, T. K.; Fagiani, M. R.; Knorke, H.; Asmis, K. R. Site-Specific Vibrational Spectral Signatures of Water Molecules in the Magic H 3 O + (H 2 O) 20 and Cs + (H 2 O) 20 Clusters. https://doi.org/10.1073/pnas.1420734111.

(19) Duffy, E. M.; Voss, J. M.; Garand, E. Vibrational Characterization of Microsolvated Electrocatalytic Water Oxidation Intermediate: [Ru(Tpy)(Bpy)(OH)]2+(H2O)0-4. *J. Phys. Chem. A* **2017**, *121* (29), 5468–5474. https://doi.org/10.1021/acs.jpca.7b05255.

(20) Duffy, E. M.; Marsh, B. M.; Voss, J. M.; Garand, E. Characterization of the Oxygen Binding Motif in a Ruthenium Water Oxidation Catalyst by Vibrational Spectroscopy. *Angew. Chemie* **2016**, *128* (12), 4147–4150. https://doi.org/10.1002/ange.201600350.

(21) Voss, J. M.; Duffy, E. M.; Marsh, B. M.; Garand, E. Mass Spectrometric and Vibrational Characterization of Reaction Intermediates in [Ru(Bpy)(Tpy)(H2O)]2+ Catalyzed Water Oxidation. *Chempluschem* **2017**, *82* (5), 691–694. https://doi.org/10.1002/cplu.201700085.

(22) Brabeck, G. F.; Koizumi, H.; Koizumi, E.; Reilly, P. T. A. Characterization of Quadrupole Mass Filters Operated with Frequency-Asymmetric and Amplitude-Asymmetric Waveforms. *Int. J. Mass Spectrom.* **2016**, *404*, 8–13. https://doi.org/10.1016/j.ijms.2016.04.002.

(23) Richards, J. A.; Huey, R. M.; Hiller, J. A New Operating Mode for the Quadrupole Mass Filter. *Int. J. Mass Spectrom. Ion Phys.* **1973**, *12* (4), 317–339. https://doi.org/10.1016/0020-7381(73)80102-0.

(24) Richards, J. A.; Huey, R. M.; Hiller, J. Waveform Parameter Tolerances for the Quadrupole Mass Filter with Rectangular Excitation. *Int. J. Mass Spectrom. Ion Phys.* **1974**, *15* (4), 417–428.

https://doi.org/10.1016/0020-7381(74)80039-2.

(25) Hoffman, N. M.; Gotlib, Z. P.; Opačić, B.; Huntley, A. P.; Moon, A. M.; Donahoe, K. E. G.; Brabeck, G. F.; Reilly, P. T. A. Digital Waveform Technology and the Next Generation of Mass Spectrometers. *J. Am. Soc. Mass Spectrom.* **2018**, *29* (2), 331–341. https://doi.org/10.1007/s13361-017-1807-8.

(26) Brabeck, G. F.; Chen, H.; Hoffman, N. M.; Wang, L.; Reilly, P. T. A. Development of MSn in Digitally Operated Linear Ion Guides. *Anal. Chem.* **2014**, *86* (15), 7757–7763. https://doi.org/10.1021/ac501685v.

Chapter 6 Future Directions

The purpose of this chapter is threefold. The first is to catalog the partial progress of converting QTPI to a Cryogenic Ion Spectroscopy (CIS) capable instrument. This includes detailing a prototype cryostat that is ready for installation and detailing immediate future plans for laser introduction. The second is to discuss how mass isolation and exclusion manipulation techniques will be used in current CIS instrumentation for immediate complex reaction schemes. Finally, a methodology for simultaneous spectroscopic data collection utilizing complex waveforms on QTPI will be outlined.

Section 6.1 Preliminary Work: QTPI Water Clustering Spectroscopy

Current cryogenic ion traps (CITs) required the use of liquid Helium cryostats to achieve metal electrode temperatures of 10 K. The cost of these cryostats can range from \$50,000 to \$100,000. QTPI has never received direct funding, making the acquisition of a Helium cryostat an impossibility. Pursuing other, more cost-efficient means of cooling were necessary. To that end, in 2015, the Garand group had successfully used a commercial 80 K liquid Nitrogen (hereafter LN_2) cryostat for the purpose of solvating ions of interest prior to the 10 K CIT.[1] This LN_2 cryostat (Janis Research) was significantly more affordable at around \$5,000 to \$8,000. Roughly a year later, Voss *et al*[2] were able to use the solvation molecules (water) as both a clustering agent and a spectroscopic tag. The temperature difference between 80 K and 10 K yields less resolved spectroscopic data but was still more than adequate for a large number of chemical systems. The decision was made to implement a LN_2 cryostat onto QTPI once performance was at an acceptable level. This cryostat would be used to provide QTPI a means to perform ion solvation and eventual 80 K spectroscopic data collection at a much lower cost than using a 10 K CIT.

6.1.1 Liquid Nitrogen Cryostat Integration

These LN_2 cryostats are effectively just reservoirs for LN_2. The bottom of the reservoir has an extrusion which interfaces with a copper cold head by means of an interference or press fit connection. A copper ion trap housing is constructed whose top is constrained to the cryostat's cold head via bolt and thread connections. Appropriate thermally conductive material, such as Indium foil (Sigma Aldrich) or cryogenic vacuum grease (Apiezon) is applied between these two connections for proper thermal conductivity. On either the cold head or trap housing, holes of appropriate diameter are milled to allow for the placement of both thermal probes (thermocouple or resistance temperature detector) and heating devices (cartridge heater or heating tape). The on-off control for the heating device and the display for thermal probe are connected to an external temperature controller, allowing for precise temperature management.

With the help of Steve Meyers, the Instrument Shop Supervisor, a method for developing a vacuum compatible weld enabled the construction of a home-built LN_2 cryostat. This cryostat was successfully tested on a proof-of-concept instrument and was shown capable of performing near 80 K solvation experiments. This original design was adapted to fit on the larger volume linear digital ion trap (LDIT) housing of QTPI. A major design change from the interference fit design to a matching chamfer pair between the LN_2 reservoir and cold head was implemented to aide in ease of fabrication. A CAD of the QTPI specific LN_2 cryostat is shown in **Figure 6.1**. This device was submitted in November 2019 and was completed in August of 2020. Since August, work has been done to test the vacuum capable weld, the new chamfered cold head design, and a method of providing electric wiring and pre-cooled continuous gas to the LDIT. The mechanical problems that plagued QTPI since returning from the COVID-19 shutdown shelved implementation of this cryostat, favoring extended studies into the dipolar mass analysis project, which is still incomplete.

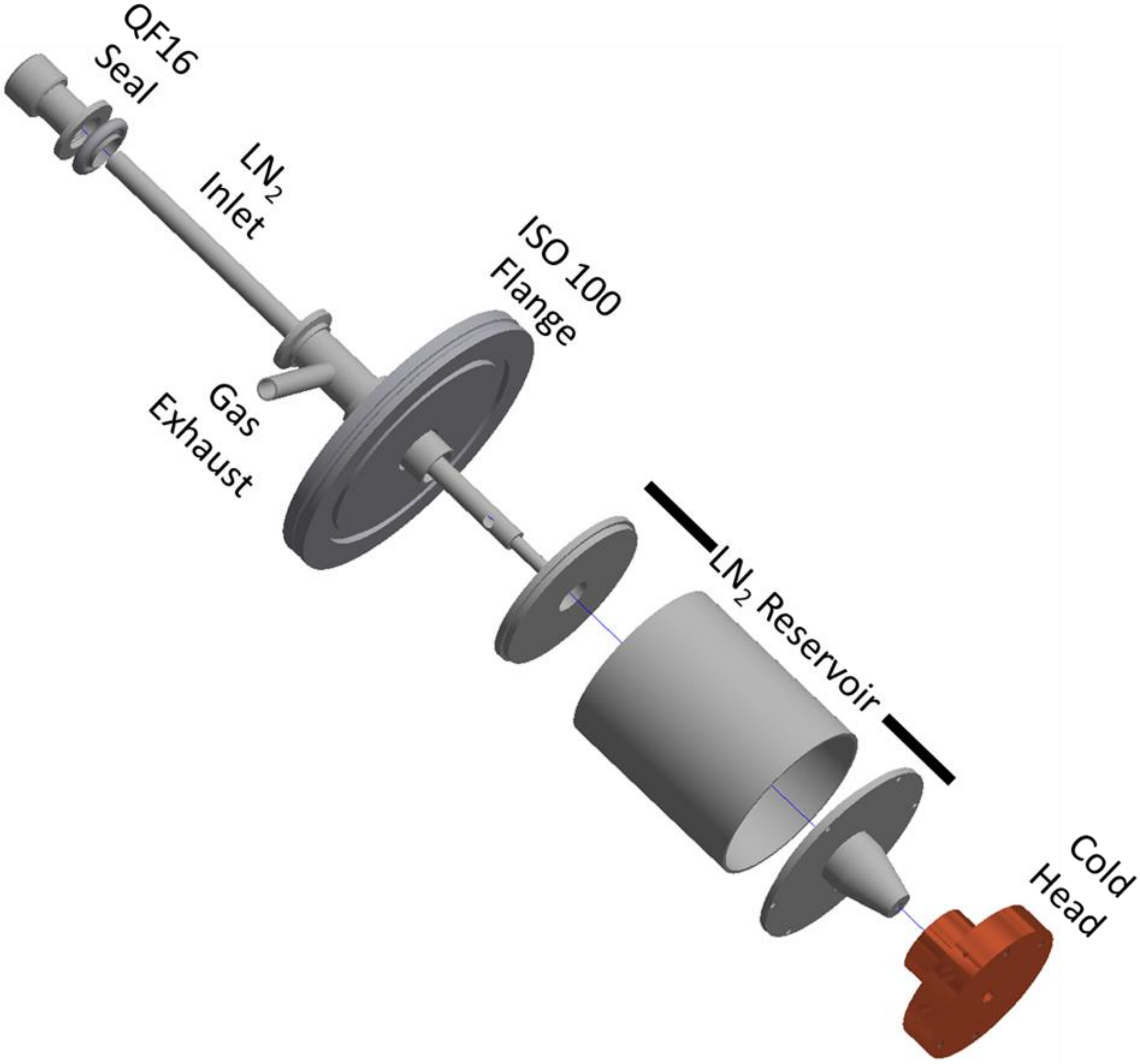

Figure 6.1 CAD and exploded view of prototype LN_2 cryostat.

At the time of writing, this cryostat has been put into QTPI with the LDIT in place and successfully cooled close enough to 80 K to determine that there were no mechanical malfunctions with the vacuum tight weld. However, two major problems were discovered. First, in the haste to get this project submitted, considerations for electrical wiring to the LDIT were neglected. Previous to the cryostat, electrical power was wired from the top facing ConFlat 8-inch vacuum flange, and gas was introduced from the non-detection X-axis side of the LDIT housing. To solve the electrical problems, a new wiring system was utilized using a Mil-Spec multi-pin vacuum flange, which now resides on the non-detection X-axis ConFlat 8-inch vacuum flange.

The second problem involves the current gas introduction system. The LDIT needs a constant flow of gas by means of a precision leak valve during operation. Normally on CIT, a short pulse of gas is introduced into the system. This gas collides with the cold metal electrodes and is in turn cooled itself. This is not likely to happen with a constant flow of gas. To solve this problem, a long length of 1/8 inch OD copper tubing was coiled around the LN_2 reservoir before being introduced into the LDIT housing. A CAD figure of this can be seen in **Figure 6.2**. This 1/8-inch copper tubing was used to maximize the number of turns and because the normal 1/4-inch tubing proved too difficult to tightly wind around the device. One plastic zip-tie was used to adhere the inlet and outlet of the tubing in place. A removable interface to the gas manifold through the non-detection X-axis of the instrument is attached to the coil inlet (not shown). The cooling effectiveness of this copper coil cannot be determined without water clustering ions.

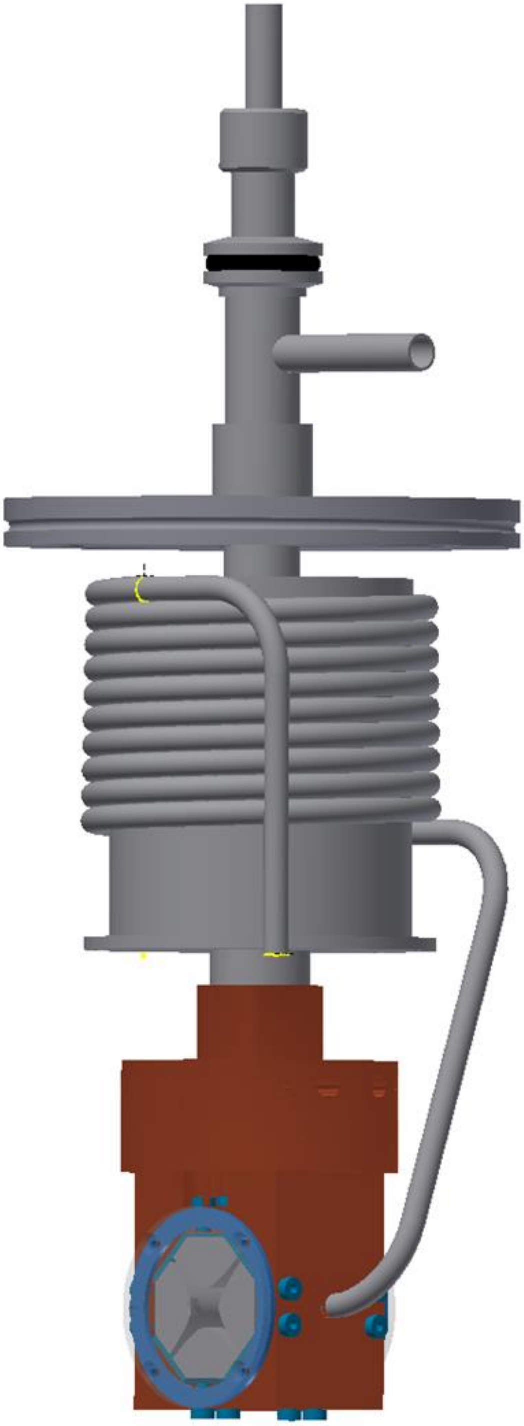

Figure 6.2 CAD figure of the new LN_2 cryostat for QTPI with copper tubing wrapped around the LN_2 reservoir.

A collage showing various angles of the LN_2 cryostat introduction is shown in **Figure 6.3**. Later success was found in using as many removable connectors as possible (green heat shrink). A support pillar was needed to stabilize the multi-core wire as many of the individual wires were prone to breaking under any kind of mechanical stress. In the future, adding an additional interlocking connector (an example shown in the figure) closer to the LDIT housing would yield a significantly easier time removing the cryostat-LDIT combination from the vacuum chamber. By bending the gas inlet toward the bottom of the LDIT, the inlet and outlet to the copper coil can be mechanically constrained, leading to over-coiling of the copper line, which seemed to provide adequate contact surface with the LN_2 reservoir. Keeping this in place with a zip-tie seemed to work fine for initial testing, but the copper tubing may prove too cold when LN_2 is present. How this LN_2 cryostat will be implemented along with currently developed ion manipulation techniques will be covered in later sections.

Figure 6.3 Collage of LN_2 cryostat prototyping on QTPI's LDIT.

6.1.2 Tunable Infrared Laser Integration

QTPI is placed directly next to a 20 foot laser table housing two Continuum Powerlite neodymium: yttrium aluminum garnet (Nd:YAG) lasers and two LaserVision optical parametric oscillator and optical parametric amplifier (OPO/OPA) tunable IR laser optics. The Nd:YAG laser pumps 1064 nm light at up to 10 Hz into the OPO/OPA, which generates IR light tunable from 600 cm^{-1} to 4500 cm^{-1}. These laser systems are being used concurrently for another CIS instrument. As a proof-of-concept, a flipping mirror will redirect the beam of a single laser system into a to-be-made laser enclosure containing laser optics. These optics will align the laser into the rear of QTPI, which has been intentionally left free of equipment during development. An appropriate vacuum flange laser window will be mounted to the ConFlat 8-inch vacuum chamber where a pre-existing hole on the back planar endcap of the LDIT already exists. The existing delay generator (Stanford Research) has enough unused connections to allow for direct laser control. Additions to the custom LabView program will be made to integrate a range of m/z bins and correlate them to the laser wavelength. A very similar LabView program already exists on other CIS instrumentation, so adaptation should be trivial. For proof-of-concept purposes a manual scan can be performed through the LaserVision software to ensure water cluster depletion is occurring.

Section 6.2 QTPI as A Solvation Focused Cryogenic Ion Spectroscopy Instrument

Assuming the LN_2 cryostat functions with little modification and laser integration goes smoothly, QTPI will have finally evolved into a CIS capable instrument. Using the existing instrument cycle with a mass filtration interval to remove the never-tagged ion species before mass analysis, it will be possible to collect 80 K spectroscopic data. Functionally, this will look identical to the CIS workflow figure in **Chapter 1** except for the substitution of D_2 for H_2O. This has always been the planned development pathway for QTPI since radial ejection mass selection occurred back in October 2017. A previously published system, such as the 1-butyl-3-methylimidazolium[2] ($[BMIM]^+$) or more recently tri-glycine[3] (Gly_3H^+) would be the best starting point for method development and benchmarking. From there, a diverse area of study is available for future researchers working on this project. Unfortunately, the development of the mass spectrometer took too long to be able to attempt any of these experiments, but every design choice during development was made with future CIS implementation in mind.

Section 6.3 Digital Ion Traps as Cryogenic Ion Spectroscopy Toolsets

Previous chapters have served to introduce square wave based digital ion traps, the software and hardware requirements for their operations, and the advancements needed to make them a viable toolset in CIS. Through developments presented in this thesis, DITs have become a digital "toolbox" of ion manipulation techniques crucial to future, complex CIS studies. Presented in the following sections are some immediate applications that are planned.

6.3.1 Mass Filtration Applications

To recap, post cryogenic cooling and spectroscopic tag adherence, there is always some population of species which possess unfavorable energetics for tag adherences. For background-free spectroscopic data collection this species needs to be removed prior to the laser interaction. As shown in **Chapter 5**, this mass filtration is achievable in DITs by means of frequency and duty cycle changes to the applied square waveforms. The change from this filtration occurring during mass analysis (i.e., mass gating at the very beginning TOF-MS) to filtration occurring in any DIT present in the instrument drastically increases the capabilities of any CIS instrumentation containing one or more DITs. Presently, an addition to one of the CIS TOF-MS instruments is being prototyped which will include two 80 K short length, round rod linear quadrupole ion traps operated with square waves. The to-be-implemented digital ion reaction traps (DIRTs) operate with the same 100 V_{pp} variable frequency square waves as QTPI, with a LVWFG waveform generator capable of operating a similar instrument cycle and without the mass analysis interval. These DIRTs will be used for two applications by utilizing in-trap mass filtration.

The first application involves gas phase ion chemistry systems that require non-isotopically pure metal containing compounds. One of the more detailed investigations the Garand group has done over the years is investigating the $[Ru(bpy)(tpy)]^{2+}$ (hereafter $[Ru]^{2+}$) catalytic intermediates of the water oxidation cycle.[4–7] A major hurdle to the analysis of this chemical system has been the convolution of isotopes present in this compound and its intermediates. The Ruthenium complex has 11 peaks separated by 0.5 m/z spanning a total m/z range of 5.5 m/z (seven stable isotopes of Ru and four unique isotopes combinations resulting from C_{13} peaks). Molecular Deuterium (D_2) has a change of mass of +4 amu, therefore only 1.5 m/z of the 5.5 m/z range will not overlap between tagged and not tagged $[Ru]^{2+}$ populations. A simulated mass spectrum of the base $[Ru]^{2+}$ complex and the $[Ru]^{2+}\cdot D_2$ with a FWHM similar to existing CIS instrumentation ($\Delta m = 0.2$) is shown in **Figure 6.4**. As can be seen from the figure, only the first three peaks of the $[Ru]^{2+}$ complex are independent of the D_2 adduct. Therefore, to obtain background free spectroscopy, only a small portion of the total ion abundance is able to be integrated. Prior to DIT integration, the only way to solve this problem is to use isotopically pure Ruthenium, which is estimated to be \$6,000 to \$11,000 for 30 micrograms of the starting reagent.

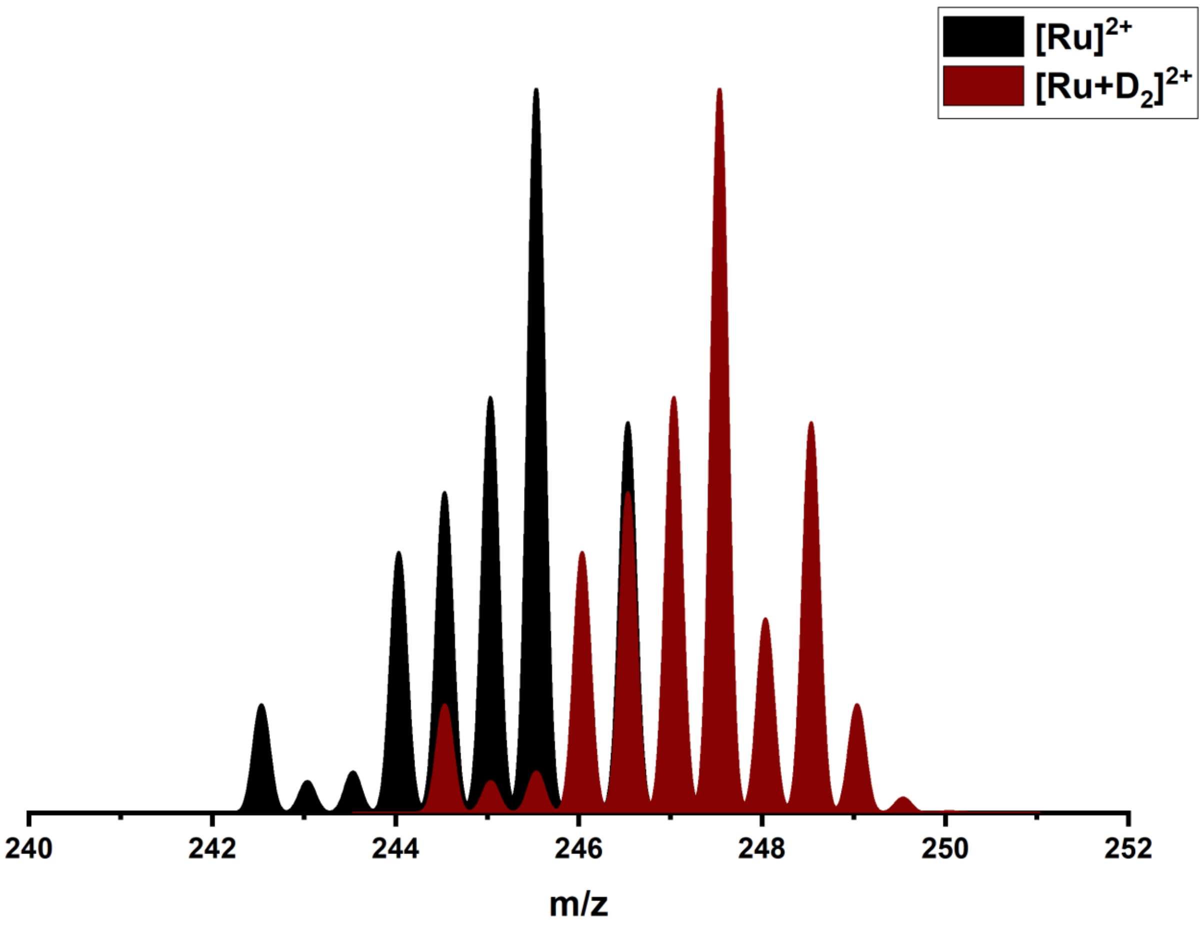

Figure 6.4 Simulated MS of [Ru]$^{2+}$ and [Ru·D$_2$]$^{2+}$.

By utilizing square wave based mass filtration prior to D_2 adherence, the minor isotopes that have overlapping m/z could be removed. This would lead to significantly more ion populations which can be integrated during spectroscopic data collection. An example of this is shown in **Figure 6.5**. This is not possible with current TOF-MS based mass gating because this filtration has to be done prior to the CIT where D_2 adherence occurs. The future instrumentation project involving the addition of two cryogenic DRTs would certainly be able to attain this isolation.

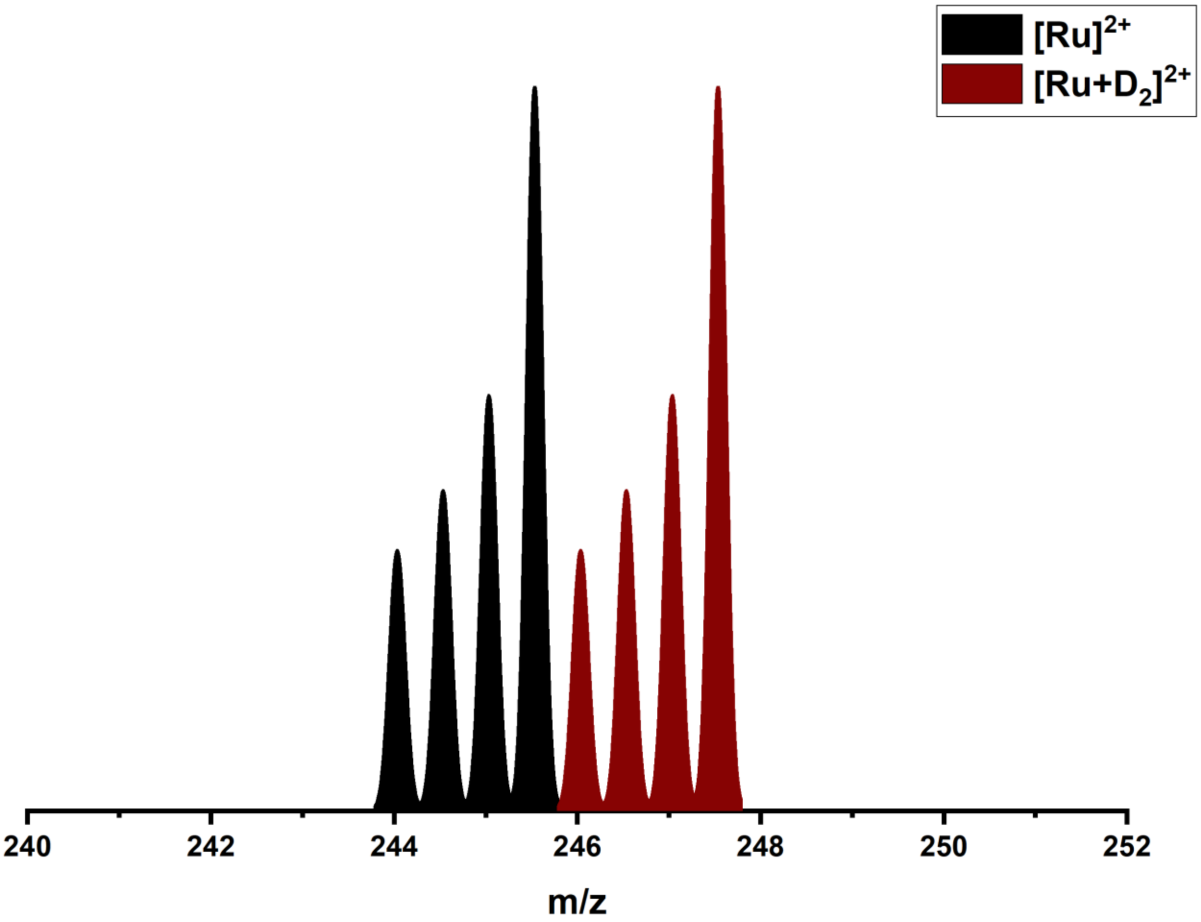

Figure 6.5 Simulated MS of [Ru]2+ and [Ru·D2]2+ after pre-MS mass filtration.

The second application of this technique is the isolation of single solvent cluster sizes per DIRT. When gas containing a solvent like water or methanol is pulsed into a CIT, a distribution of clusters is generated. An area of interest is how the presence of two different solvent molecules on an ion perturb its structure. By pulsing different solvents into each DIRT, studies into these complex cluster environments would be achievable. Insights from these studies could then be correlated to the complex environment of liquid phase solutions. The problem with this experiment is the sheer number of combinations that can occur between the two DIRTs. To help minimize this, mass filtration will be implemented on each of the ion traps.

In the first DIRT, water is pulsed to generate some number of water clusters. This ion population is then mass filtered for only a single water cluster size, it is transported to the second DIRT. Methanol is pulsed in this trap and mass filtered for an individual complex cluster size. The effect is an ion cluster with two different solvent molecules present. The amount of both can be controlled by means of per-trap mass filtration. This work is still very much a work in progress, but some initial data collected by Gina Roesch can be shown in **Figure 6.6**. In the figure, a solution containing Gly_2H^+ was sprayed via ESI. Water was introduced in the first DIRT. From there, a short duration interval was initiated whose frequency and duty cycles resulted in the lowpass, highpass, and finally mass isolation of $Gly_2H^+ \cdot (H_2O)_2$.

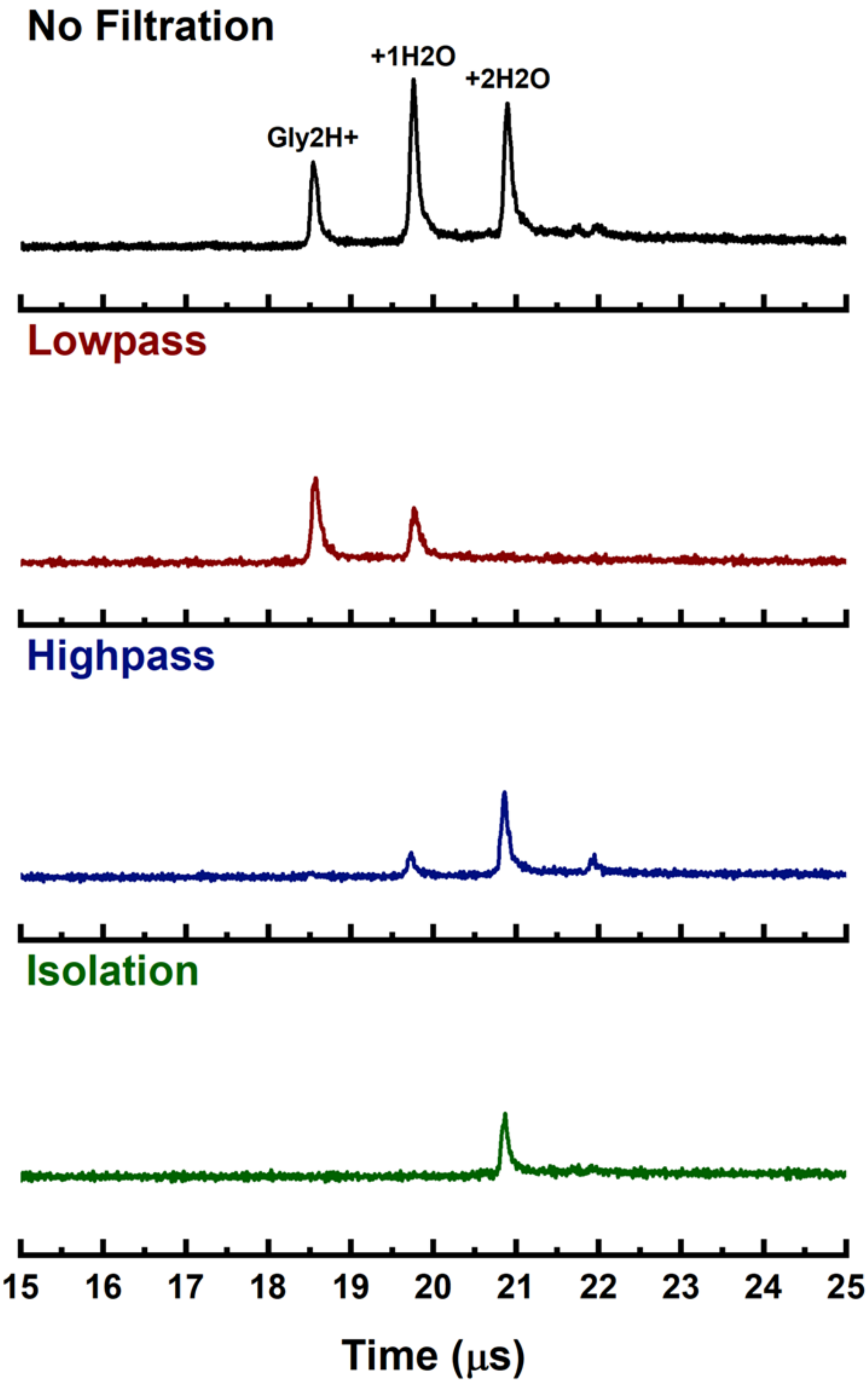

Figure 6.6 Mass spectra showing the lowpass, highpass, and isolation mass filtration.

There has been some difficulty maintaining adequate ion amplitude while applying square waves to the DIRTs in this prototype instrument, but these issues will likely be resolved with future developments. In future studies, the mass isolated $Gly_2H^+{\cdot}(H_2O)_2$ would then be sent to a second DIRT where methanol would be pulsed generating $Gly_2H^+{\cdot}(H_2O)_2(MeOH)_N$, where N is a variable methanol cluster size. This complex cluster will then enter the 10 K CIT, have a D_2 tag adhered, then proceed to the TOF-MS where the never-tagged complex cluster would be filtered by mass gating and a resulting IR spectrum of the complex cluster would be collected.

6.3.2 Selective Species Exclusion

Functionally, the complex waveform based selective species exclusion (SSE) interval can be used interchangeably used with a normal duty cycle-based mass isolation. Programming this would be slightly tedious as it would involve generating a bandstop-like frequency list, where the excluded frequency correlates to isolated ion’s secular frequency. This is not very difficult to do, but additional LVWFG software development would be required.

This methodology may be attractive to future researchers as the small amplitude auxiliary frequency may prove a “softer” isolation methodology compared to the current duty cycle based approach. This is because, in the duty cycle mass filtration technique, as the applied frequency and duty cycle are changed, the ion distribution is being brought toward the apex of the Mathieu stability region. Getting too close to the apex may induce pseudo boundary activated collision induced dissociation,[8] which would cause a degradation of the ion of interest. Auxiliary based mass isolation sequentially ejects everything but the ion of interest, which remains deep in the stability region. The reason this has not been done on the prototype DIRTs is a lack of a finalized design for the complex waveform circuitry. Future circuitry optimizations need to be made, then a new PCB needs to be designed such that all three HVHF sub-circuits are combined into one board.

Section 6.4 QTPI as A Simultaneous IR Collection Device

Additional to softer mass isolation the following is the planned progression of QTPI as a water cluster focused CIS instrument utilizing complex waveforms. The immediate future work for complex waveforms on QTPI is a characterization of the improvements to mass analysis that the one-every-N (OEN) or similar amplitude modulation based dipolar mass analysis can provide. That being said, the primary motivation for complex square wave generation was always to use this SSE interval to fully control of any and every ion population in a CIT. The applications of this are numerous but presented below is the most immediate project that incorporates not only the already functional SSE interval, but also the existing preliminary work that has been done to turn QTPI into a water cluster focused LN_2 CIS capable instrument.

There are some instances in which a solvation clustering molecule, such as water, is used for both ion clustering and as a spectroscopic tag.[9,10] In these experiments, an ion of interest is generated and cooled to 80 K. Collision gas-containing water is introduced, generating a distribution of cluster sizes present in the ion trap. In current TOF-MS based CIS instrumentation, each water would be spectroscopically interrogated, sequentially. If, for example, a total cluster distribution of up to 30 water molecules were present, this would require 30 total spectroscopic datasets to be collected. At the time of writing, with optimal performance, one publication grade set of high-resolution IR spectroscopic data takes about eight continuous hours of data collection. Assuming normal work hours, the minimum amount of time this dataset could be complete is roughly one month.

Assuming the successful implementation of the pre-existing LN_2 cryostat, and full enclosed laser optic setup is used to provide a tunable IR laser beam inside QTPI's trap, this water cluster experiment could easily be performed by QTPI. At the end of the trapping interval, the duty cycle-based mass isolation will be used to highpass filter the N-1 water cluster out of the LDIT, where N is the current water cluster being studied (e.g., 1, 2, 3… 30). At the very start of the mass scan, the tunable laser would shoot into the LDIT ion trap, causing a dissociation of the N water cluster to N-1, thus acting as the de-tagged species needed for CIS. The N-1 mass channel will be integrated as a function of laser wavelength, thus providing 80 K spectroscopic data of the N sized water cluster. The effect is the same month-long spectroscopic study into the solvation effect of the ion of interest.

If SSE were to be used instead of the duty cycle mass filtration technique, it is feasible that multiple IR spectrums could be collected in tandem. The instrument cycle would be similar to the previously described, the only substitution being the auxiliary waveform-based SSE interval instead of the duty cycle based mass isolation. Recall that by applying a small auxiliary waveform during the SSE interval, individual ion species can be excluded prior to the laser interaction. This is because each of the 30 water clusters present in the ion trap are all co-existing in the LDIT. Each has their own secular frequency in which they are oscillating within the LDIT. The auxiliary frequency generated during the SSE interval can match any secular frequencies of ions present in the LDIT.

Currently, this SSE interval only provides one auxiliary frequency, but this can easily be expanded to produce several auxiliary square waves. Changing the auxiliary frequency happens instantaneously, not by scanning from one frequency to another. This sequential changing allows for true selective species exclusion by ejecting multiple water cluster sizes in the SSE interval (e.g., even N cluster sizes) but leaves others (e.g., odd N cluster sizes) intact in the LDIT. When the laser interaction occurs, all of the even N water cluster sizes will be re-populated, based on laser absorption of the remaining odd N water cluster sizes. By separately integrated each of re-populated de-tagged species, simultaneous IR spectra could be collected. A sample schematic of what this CIS experiment might look like is provided in **Figure 6.7**, adapted from Marsh *et al*.[1]

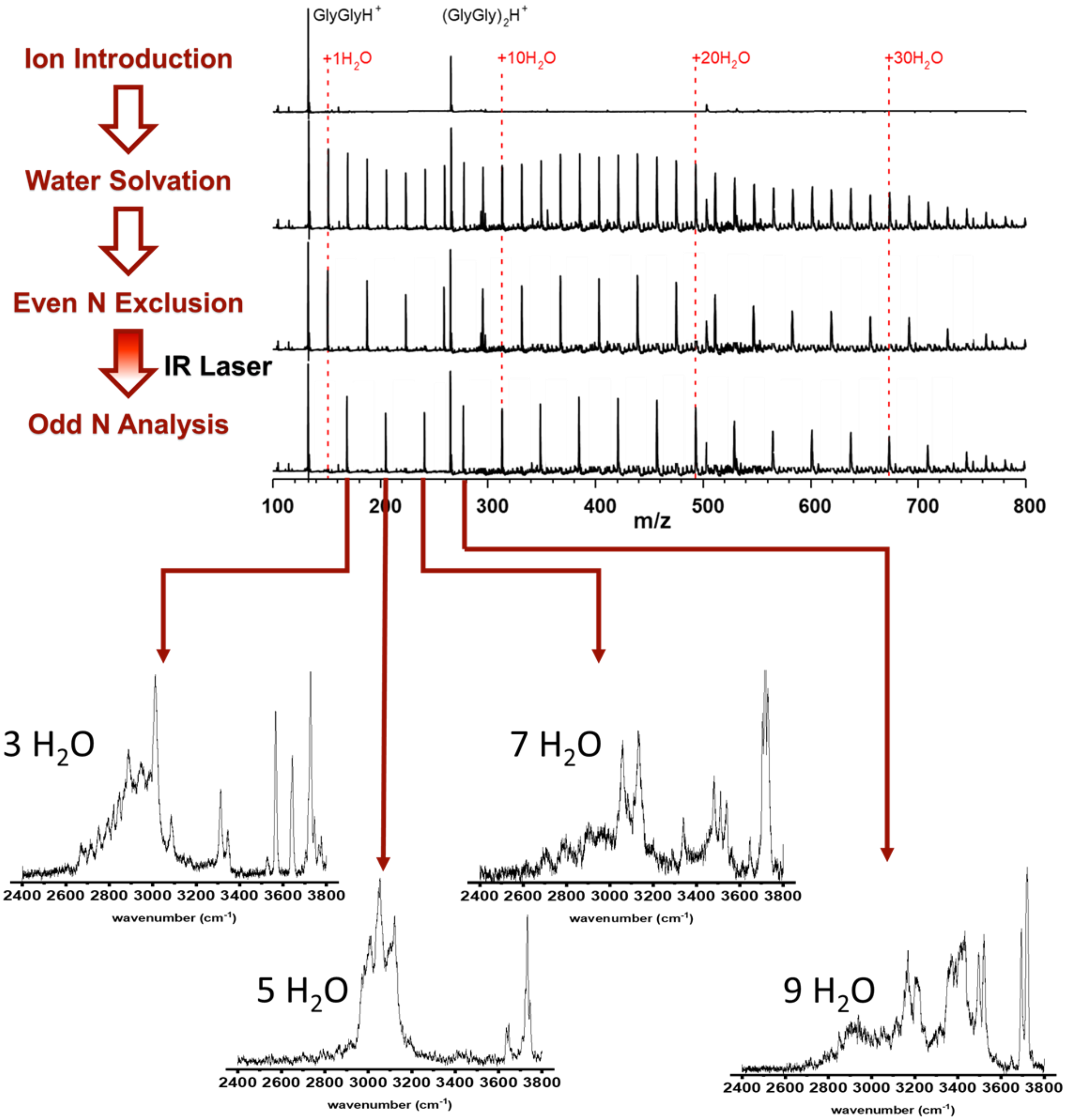

Figure 6.7 Hypothetical schematic detailing the multi-plexed IR collection.

In the figure above, Gly_2H^+ is generated via ESI. During the trapping interval of the LDIT in QTPI, water is pulsed into the trap by means of a pulsed valve additional to the constant He stream supplied by the precision leak valve. After some time, a distribution of water clusters from N = 1 to N = 30 is formed. A series of auxiliary square waveforms are applied via the SSE interval. This interval is comprised of up to

15 separate auxiliary frequencies, each corresponding to a different even N water cluster size (N = 2, 4 ,6… 28). Each frequency of the auxiliary waveform is applied for roughly 10 µs for a total of up to 150 µs. These frequencies will be determined experimentally prior to IR collection. Just before mass analysis occurs, an external TTL signal is sent to a nearby Nd:YAG OPO/OPA tunable IR laser system. The beam travels through newly made laser optics until reaching the axial axis of the LDIT by means of a pre-existing hole in the back planar endcap. The current wavelength of light will cause a single water solvent to be dissociated from some of the remaining up to 15 water cluster sizes. These dissociated species will repopulate the previously excluded even N water cluster size mass channels. The amount of repopulation is proportional to the absorption intensity of the laser wavelength on the N+1 water cluster size. All even N water cluster size mass channels are monitored, and their amplitudes are recorded as a function of laser wavelength. At the end of a singular laser scan, up to 15 simultaneous IR spectra datasets have been collected. Once adequate averaging of these IR spectra is obtained, the same procedure is replicated, save ejecting the odd N water cluster sizes, and performing CIS on the even N sizes. A complete collection of the 30 water cluster system has been performed. Even if the hypothetical CIS experiment above works for only two or three or four water cluster sizes at a time, that still yields a two or three or four factor increase in the IR spectra throughput of this CIS instrumentation.

The above experiment has always been the endgame for all of the work done building QTPI, getting the mass spectral resolving power to an adequate enough level, developing the circuitry required not only to operate the LQIT with square waves, but also to introduce the complex waveform generation. This multi-plexed spectroscopy collection scheme is impossible without auxiliary waveforms. If this collection method works in any facet, significantly more solvation studies are available. Under this hypothetical, QTPI will never be a 10 K high resolution CIS instrument which rivals current TOF-MS instrumentation. QTPI instead will be a high throughput, lower resolution instrument capable of providing information about which cluster sizes are structure defining. These structurally defining cluster sizes can then be generated in the 10 K, high resolution, slow IR data acquisition instrument. The effect is an overall higher throughput analysis of ion solvation systems, which would allow future Garand group researchers to produce more data, and a more guided study into which solvation sizes are worth extreme scrutiny and which cluster sizes largely provide no functional or structural relevance.

Section 6.5 Thesis Conclusion

QTPI started as summer project to make a make a low-resolution mass spectrometer for the purpose of checking synthesis products before putting them on real CIS instrumentation. Through years of instrumental development, performance is finally comparable enough to TOF-MS based CIS instrumentation, propelling it past a one-off project and into a platform for technique development. With the addition of an already fabricated LN_2 cryostat, water clustering experiments will be easily accomplished. Through the use of auxiliary waveforms for selectively excluding particular m/z, everything is already set in place to perform spectroscopy inside QTPI. With future exploratory studies into how best to incorporate complex waveforms both during and before mass analysis, QTPI may prove to be the first instance of multi-plexed CIS data collection. If so, this instrument will be capable of high throughput spectroscopy that is still better than room temperature commercial solutions. With continued work this instrument could eventually be brought to cryogenic temperatures similar to current CIS instrumentation, drastically increasing the ability to approach and solve ever increasing complex experimental needs.

Separate to the instrumentation that was developed, the software and hardware tools developed along the way have proved to be valuable assets for the entire Garand group. The $300 HVHF circuitry has replaced thousand dollar DC pulsers for ion transport. The low-cost Arduino LVWFG is currently providing the square wave generation on a prototype addition to current CIS instrumentation involving two DIRTs capable of performing per-trap mass filtration. Existing Labview and Arduino firmware will serve as a foundation for a future triple DIT instrument with the goal of continuous cryogenic IR collection. Finally, these square wave-based toolsets will be published and made available to other CIS based research groups in the hope to further this field of research.

Section 6.6 Chapter 6 References

(1) Marsh, B. M.; Voss, J. M.; Garand, E. A Dual Cryogenic Ion Trap Spectrometer for the Formation and Characterization of Solvated Ionic Clusters. *J. Chem. Phys.* **2015**, *143* (20). https://doi.org/10.1063/1.4936360.

(2) Voss, J. M.; Marsh, B. M.; Zhou, J.; Garand, E. Interaction between Ionic Liquid Cation and Water: Infrared Predissociation Study of [Bmim]+·(H2O)N Clusters. *Phys. Chem. Chem. Phys.* **2016**, *18* (28), 18905–18913. https://doi.org/10.1039/c6cp02730j.

(3) Fischer, K. C.; Voss, J. M.; Zhou, J.; Garand, E. Probing Solvation-Induced Structural Changes in Conformationally Flexible Peptides: IR Spectroscopy of Gly3H+·(H2O). *J. Phys. Chem. A* **2018**, *122* (41), 8213–8221. https://doi.org/10.1021/acs.jpca.8b07546.

(4) Duffy, E. M.; Marsh, B. M.; Garand, E. Probing the Hydrogen-Bonded Water Network at the Active Site of a Water Oxidation Catalyst: [Ru(Bpy)(Tpy)(H2O)]2+·(H2O)0-4. *J. Phys. Chem. A* **2015**, *119* (24), 6326–6332. https://doi.org/10.1021/acs.jpca.5b04778.

(5) Duffy, E. M.; Marsh, B. M.; Voss, J. M.; Garand, E. Characterization of the Oxygen Binding Motif in a Ruthenium Water Oxidation Catalyst by Vibrational Spectroscopy. *Angew. Chemie* **2016**, *128* (12), 4147–4150. https://doi.org/10.1002/ange.201600350.

(6) Voss, J. M.; Duffy, E. M.; Marsh, B. M.; Garand, E. Mass Spectrometric and Vibrational

Characterization of Reaction Intermediates in [Ru(Bpy)(Tpy)(H2O)]2+ Catalyzed Water Oxidation. *Chempluschem* **2017**, *82* (5), 691–694. https://doi.org/10.1002/cplu.201700085.

(7) Duffy, E. M.; Voss, J. M.; Garand, E. Vibrational Characterization of Microsolvated Electrocatalytic Water Oxidation Intermediate: [Ru(Tpy)(Bpy)(OH)]2+(H2O)0-4. *J. Phys. Chem. A* **2017**, *121* (29), 5468–5474. https://doi.org/10.1021/acs.jpca.7b05255.

(8) Vachet, R. W.; Glish, G. L. *Boundary-Activated Dissociation of Peptide Ions in a Quadrupole Ion Trap*; 1986; Vol. 83.

(9) Fischer, K. C.; Sherman, S. L.; Garand, E. Competition between Solvation and Intramolecular Hydrogen-Bonding in Microsolvated Protonated Glycine and β-Alanine. *J. Phys. Chem* **2020**, *2020*, 1593–1602. https://doi.org/10.1021/acs.jpca.9b11977.

(10) Fischer, K. C.; Sherman, S. L.; Voss, J. M.; Zhou, J.; Garand, E. Microsolvation Structures of Protonated Glycine and l -Alanine. *J. Phys. Chem. A* **2019**, *123* (15), 3355–3366. https://doi.org/10.1021/acs.jpca.9b01578.

Appendix

The following appendix is meant to provide visual representation of critical components of both the QTPI LabView instrument firmware, and the LVWFG firmware. The nature of both LabView and the Arduino interface makes presenting the entire code impossible. Instead, some sections are highlighted with a brief overview of their functions. Limited HVHF and LVWFG hardware details will also be displayed. Relevant personnel will be pointed out for current circuitry related details, as the initial work completed constructing these circuits is no longer close enough to current hardware iterations for the HVHF circuitry to accurately present.

Section 7.1 LabView Software

LabView is a pictorial programming language that involves "wiring" functional subsections to one another. This programming language has a front panel which acts as a GUI and a back panel where the actual code resides. Additional to this, it is common for individual functions, such as the binning software, to exist as a subVi which is represented as a small square with wire inputs and outputs. Detailing the inputs and outputs of every single function and subVi would make this thesis three times in length. Instead, subsections will be used to describe functional sections of code. The full firmware can be found on the QTPI computer's desktop under the QPTPI/LabView Code folder.

7.1.1 LabView Front Panel

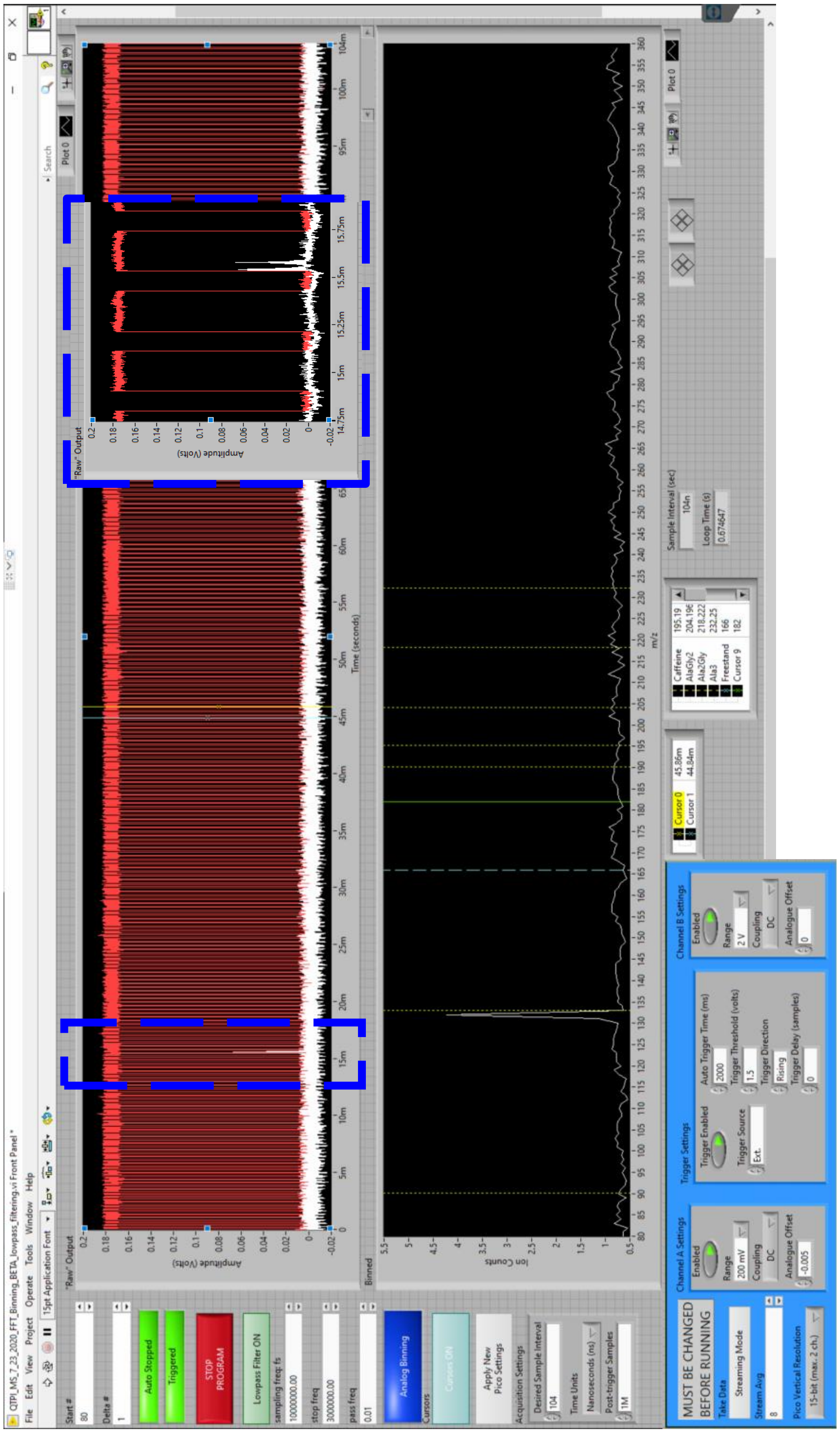

Start # 80

Delta # 1

sampling freq: fs 10000000.00

stop freq 3000000.00

pass freq 0.01

Acquisition Settings
Desired Sample Interval 104
Time Units Nanoseconds (ns)
Post-trigger Samples 1M

MUST BE CHANGED BEFORE RUNNING
Take Data Streaming Mode
Stream Avg 8
Pico Vertical Resolution 15-bit (max. 2 ch.)

Channel A Settings
Enabled
Range 200 mV
Coupling DC
Analogue Offset -0.005

Trigger Settings
Trigger Enabled
Trigger Source Ext.
Auto Trigger Time (ms) 2000
Trigger Threshold (volts) 1.5
Trigger Direction Rising
Trigger Delay (samples) 0

Channel B Settings
Enabled
Range 2 V
Coupling DC
Analogue Offset 0

Cursor 0	45.86m
Cursor 1	44.84m

Caffeine	195.19
AlaGly2	204.196
Ala2Gly	218.222
Ala3	232.25
Freestand	166
Cursor 9	182

Sample Interval (sec) 104n

Loop Time (s) 0.674647

Figure 7.1 LabView front panel.

Figure 7.1 shows the current version of the LabView front panel. The left-hand column allows for user input of values like start m/z, Δm/z, lowpass noise mitigation settings, current analog binning, or prototype FFT binning, cursor visibility, and others. The "Apply New Pico Settings" and resulting box underneath dictate at what interval (in nanoseconds) and for how many samples the acquisition window from the PicoScope ADC collects. The area in light blue are user controls that can only be changed when the program is not running. A boolean button is used to determine whether the LabView code is ran in streaming mode, where the program runs continuously with a rolling average set by "Stream Avg" or in a static 100 MS mode. The Channel A, Channel B, and Trigger Settings are all standard oscilloscope settings used to dictate how the PicoScope collects data. Cursor displays for both the "Raw Output" and "Binned" output are provided next to the blue box. Some diagnostic displays are given to indicate the current sample interval and total loop time. Finally, the two XY graphs display the current mass spectrum raw mass spectrum and a binned average mass spectrum. The top graph displays real time single MS data in the form of detector response (white) and LVFG TRIGGER (red). The lower display shows a line graph of the rolling average MS spectra.

7.1.2 LabView Back Panel

The back panel is too large to display in one figure. As such, the left, middle and right sections of the code will be displayed and discussed separately. **Figure 7.2** shows the left-most portion of the LabView back panel. Various user inputs are instated prior to the WHILE loop (see front panel). A nested case structure is used to check the boolean value of the "Take Data" button on the front panel. Section **a** is used to set the queue system as the streaming value (default 8) or a static 100 MS acquisition. The first time the inner case structure is ran, a counter is initialized, where the program is auto-stopped after 100 MS.

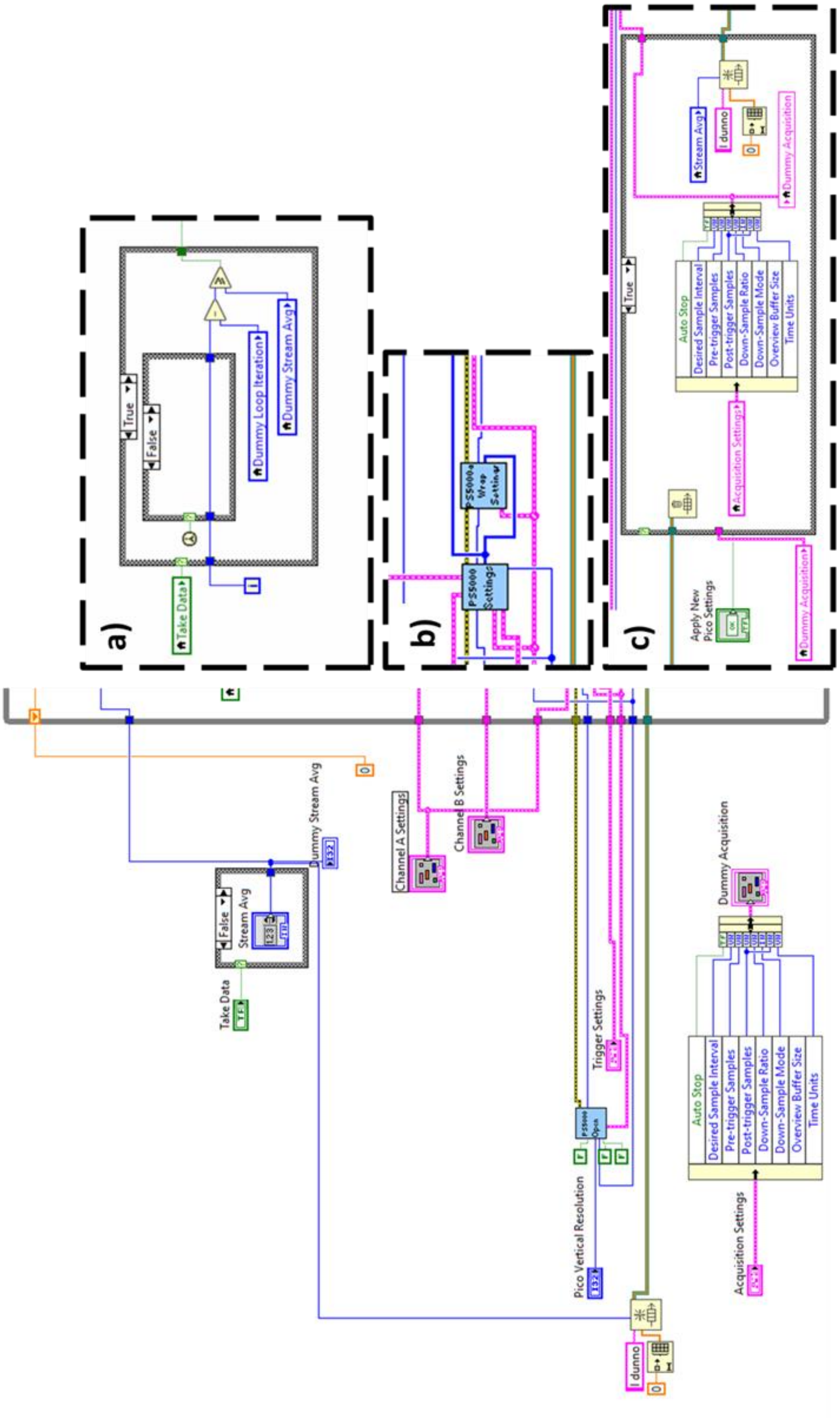

Figure 7.2 Left-hand LabView back panel left most section.

The PicoScope has pre-made LabView subVis and example LabView code available through their website (**b** in the figure). Any subVi that is colored light blue with black text is made by them. There is not a good description of these subVis, how they work, or what the required data types are. For future development of a PicoScope system, use a pre-existing example LabView program and modify it to fit the functionality required. Finally, the initial PicoScope streaming acquisition window can be set by the "Acquisition Settings" cluster of elements left of the WHILE loop. Almost none of these were ever changed. A dummy cluster was generated and is referenced as a local variable inside the WHILE loop to update the acquisition window, determined by the time between points (default 104 ns) and number of points (default 1 million points). The update structure is trigged by the front panel button and is shown in section **c**.

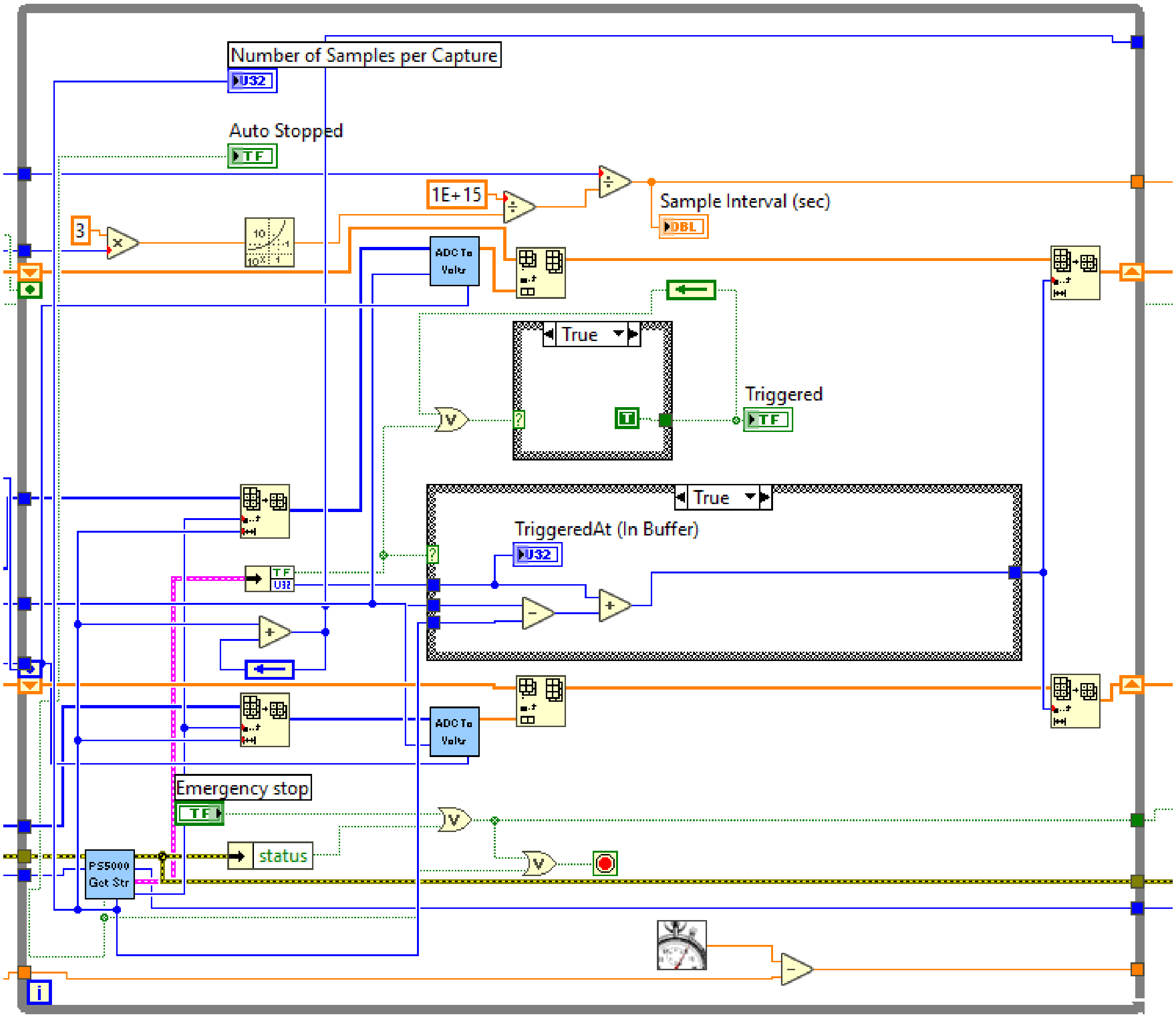

Figure 7.3 PicoScope "Get Streaming Data" portion of the LabView firmware.

Figure 7.3 is the middle section of the LabView firmware. Originally, a “block” method was used to send packets of data which were stored on the PicoScope’s internal volatile memory. The long (50 to 200 ms) acquisition windows needed to QTPI provide too much for the PicoScope, which tended to crash. Communication with PicoScope support led to them sending over the above figure. The provided streaming example from PicoScope’s website did not work, and this was a hotfix for it. Never touch this portion of the code until a complete rewrite of the firmware is necessary. If improvements need to be made, see if an update to the provided LabView example from PicoScope actually runs first. The two orange outputs with up arrows on the right-hand side are the two data outputs of this WHILE loop. One being the ion response data, the other being the LVWFG TRIGGER data.

Figure 7.4 shows the final right-hand portion of the LabView back panel. The current lowpass filter system is shown at section **a**. This is still very much of a work-in-progress that should be explored in the future. Section **b** contains a boolean switch between voltage based analog binning process and work-in-progress FFT binning process when using complex waveforms for mass analysis (not shown). Sections **c** and **f** “bundle” the X and Y double type data into a cluster of 1D arrays needed for the XY graphs on the front panel. Section **d** is the PicoScope status and error handle subVis which are supposed to mitigate errors the PicoScope receives, preventing a crash to desktop. Finally, **e** shows the stop function of the WHILE loop. Multiple OR gates corresponding to errors or user input stop the WHILE loop. LabView’s “enqueue” and “get queue” sections are housed in this section as well.

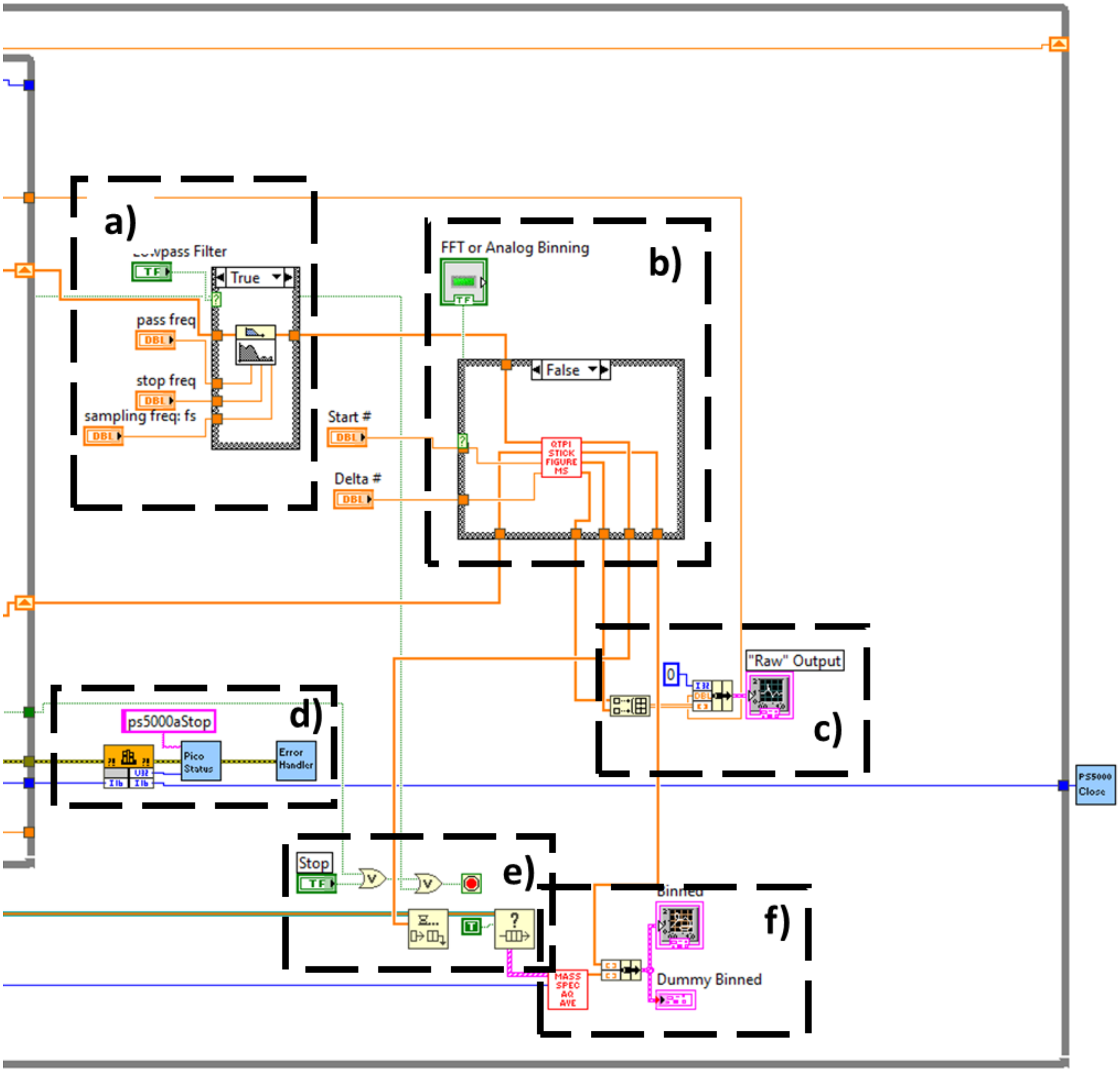

Figure 7.4 Right-hand LabView back panel.

7.1.3 Analog Binning Sub-Vi

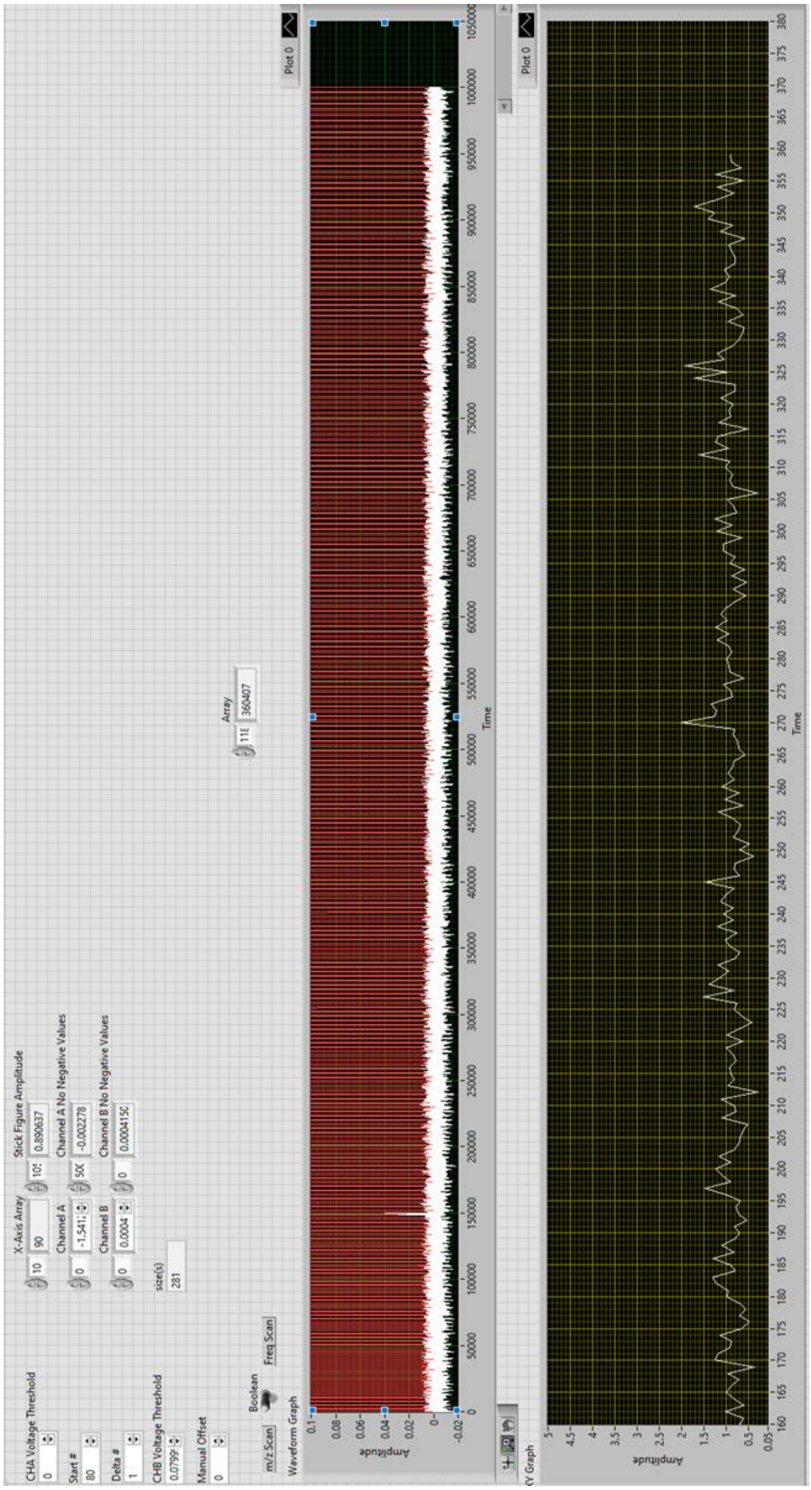

CHA Voltage Threshold 0

Start # 80

Delta # 1

CHB Voltage Threshold 0.0799

Manual Offset 0

X-Axis Array 10 90

Stick Figure Amplitude 10: 0.890637

Channel A 0 -1.541:

Channel A No Negative Values 50(-0.002278

Channel B 0 0.0004

Channel B No Negative Values 0 0.0004150

size(s) 281

Array 11E 360407

Figure 7.5 Front panel of the analog binning sub-Vi

Figure 7.5 shows the front panel of the analog binning sub-Vi. To be honest, this is almost never used, and this front panel largely only exists for diagnostic purposes. Of note, the “CHA Voltage Threshold” and “CHB Voltage Threshold” are used to designate the Y value (in Volts) of the PicoScope Channel A and Channel B used in the binning process, respectively. CHA Voltage Threshold is used to reject and V < 0 noise from the detector. CHB Voltage Threshold is used to determine where the TRIGGER_RISING edges are in the array of data to generate the bins. A long time ago a linear frequency sweep interval was designed for diagnostic purposes but is no longer used, but the boolean switch is still on the front panel.

Figure 7.6 provides the back panel view of the analog binning sub-VI. Section **a** utilizes a FOR loop with four case structures which act as IF structures. These IF structures look at the current index of the entire data array and anytime the previous index was FALSE, if the current index if TRUE, the index location is marked as a rising edge. Similarly, anywhere the previous index is TRUE, and the current index is FALSE is marked as a falling edge. At the time of writing only the rising edges are considered, and the length of the subsequent sub-array is determined by TRIGGER_RISING[j+1] – TRIGGER_RISING[j], such that each subarray starts at TRIGGER_RISING[j] for a length of TRIGGER_RISING[j+1] – TRIGGER_RISING[j]. Section **b** takes each sub-array which now corresponds to when the LVWFG TRIGGER channel is HIGH, and sequentially adds all of the Y values together. The resulting size of the 1D binned array is equal to the number of m/z steps presented by the PicoScope acquisition window. It is possible to have this window smaller than the full mass scan. Finally, section **c** initializes and iterates a 1D array whose initial value is the start m/z from the main LabView front panel and iterates it by an amount set by the Δm/z values on the same front panel. This makes the displayed XY graph of the binned mass scan only as long as the acquisition window in case of mass scan truncation.

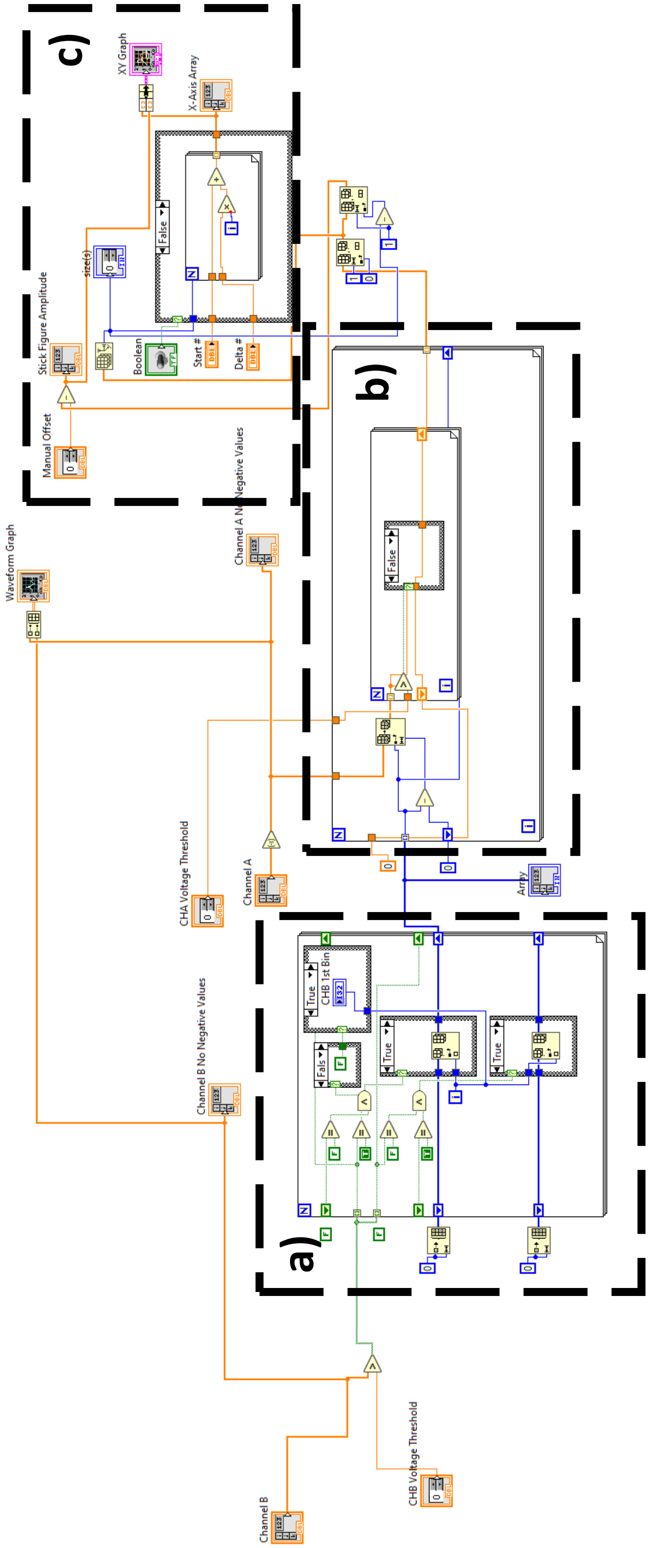

Figure 7.6 Back panel of the analog binning sub-Vi.

Section 7.2 Arduino Programming

Generally, the Arduino program is broken into three sections. The first is an initialization of all of the necessary Arduino pin states, SPI communication channel, and frequency word initialization, and default variables for any user control inputs (not shown). The second sections is a lengthy series of functions which correlate to how user input variable control is handled. Generally, each variable is assigned a one character command (e.g., ~, !, @, #, $, etc.) to save space on the Arduino EEPROM memory. Finally, the third section is the void loop() function which consists of several intervals, which are then later defined as the instrument cycle intervals. For a detail look into the initialization and user input sections, see the Arduino code on QTPI's computer under "Desktop/QTPI/Arduino Code."

7.2.1 Serial Communication commands

Figure 7.7 shows a mostly complete list of the one-character commands. The only commands not shown are for the mass isolation and exclusion intervals as the current firmware version has those sections commented out (covered below). A brief description of the what the one character commands do are given by both the variable name and the commented description on the right. Some commands are single variable changes, e.g., R700000 will set the "maxFrequency" variable to 700,000 Hz. Some commands change multiple variable, e.g., W0:500 and W1:10 will set the "trapDuration" and "crapDuration" interval, respectively. There an Excel document in the same folder as the Arduino code is a more in-depth breakdown of what each commonly used command does and how it should be formatted. To determine which variables are controlled by which commands, simply find via Ctrl+F, the variable, find where it is updated in the middle serial communication section of the overall code, then find which command changes it.

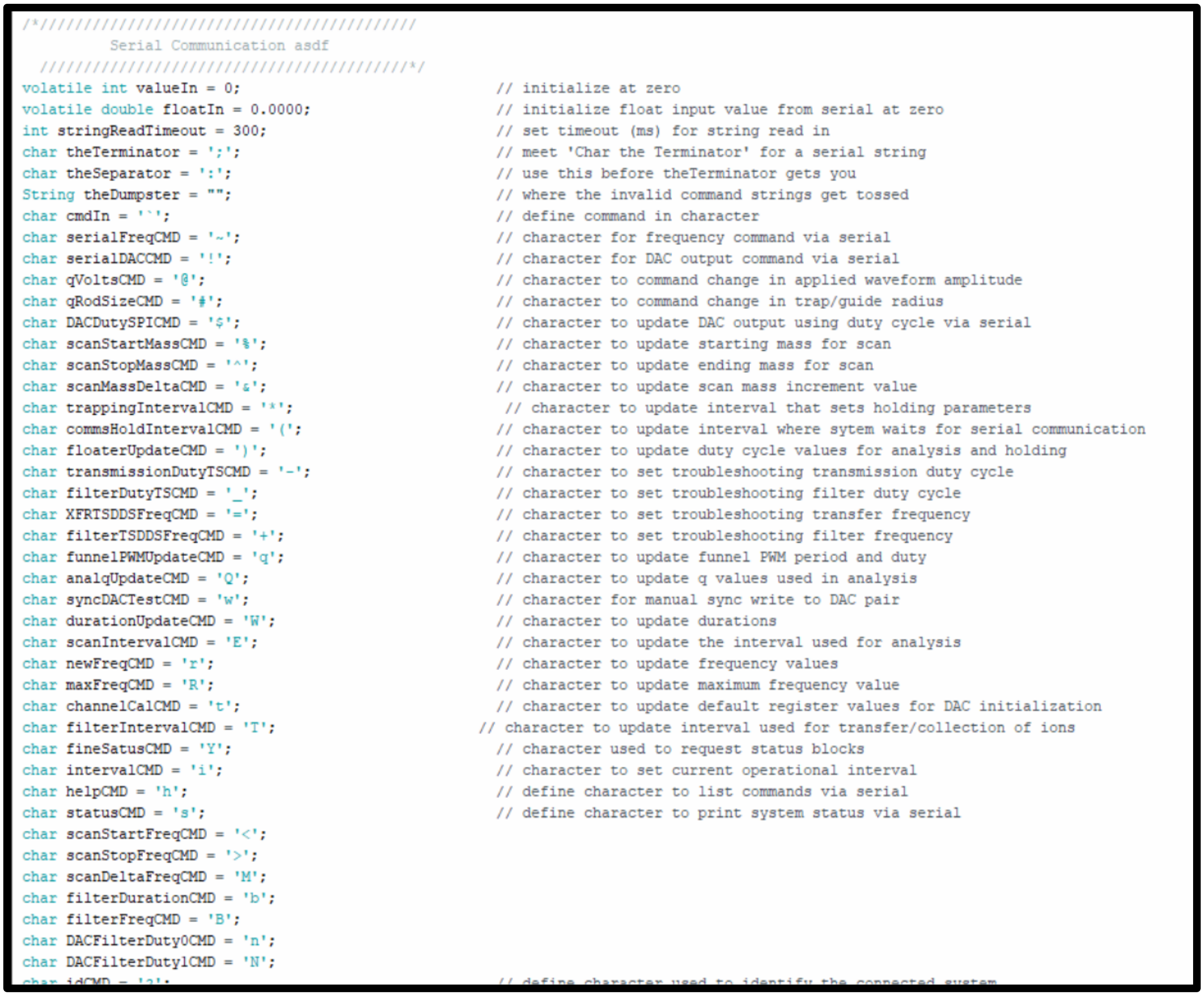

```
/*///////////////////////////////////////////
          Serial Communication asdf
  //////////////////////////////////////////*/
volatile int valueIn = 0;                             // initialize at zero
volatile double floatIn = 0.0000;                     // initialize float input value from serial at zero
int stringReadTimeout = 300;                          // set timeout (ms) for string read in
char theTerminator = ';';                             // meet 'Char the Terminator' for a serial string
char theSeparator = ':';                              // use this before theTerminator gets you
String theDumpster = "";                              // where the invalid command strings get tossed
char cmdIn = '`';                                     // define command in character
char serialFreqCMD = '~';                             // character for frequency command via serial
char serialDACCMD = '!';                              // character for DAC output command via serial
char qVoltsCMD = '@';                                 // character to command change in applied waveform amplitude
char qRodSizeCMD = '#';                               // character to command change in trap/guide radius
char DACDutySPICMD = '$';                             // character to update DAC output using duty cycle via serial
char scanStartMassCMD = '%';                          // character to update starting mass for scan
char scanStopMassCMD = '^';                           // character to update ending mass for scan
char scanMassDeltaCMD = '&';                          // character to update scan mass increment value
char trappingIntervalCMD = '*';                        // character to update interval that sets holding parameters
char commsHoldIntervalCMD = '(';                      // character to update interval where sytem waits for serial communication
char floaterUpdateCMD = ')';                          // character to update duty cycle values for analysis and holding
char transmissionDutyTSCMD = '-';                     // character to set troubleshooting transmission duty cycle
char filterDutyTSCMD = '_';                           // character to set troubleshooting filter duty cycle
char XFRTSDDSFreqCMD = '=';                           // character to set troubleshooting transfer frequency
char filterTSDDSFreqCMD = '+';                        // character to set troubleshooting filter frequency
char funnelPWMUpdateCMD = 'q';                        // character to update funnel PWM period and duty
char analqUpdateCMD = 'Q';                            // character to update q values used in analysis
char syncDACTestCMD = 'w';                            // character for manual sync write to DAC pair
char durationUpdateCMD = 'W';                         // character to update durations
char scanIntervalCMD = 'E';                           // character to update the interval used for analysis
char newFreqCMD = 'r';                                // character to update frequency values
char maxFreqCMD = 'R';                                // character to update maximum frequency value
char channelCalCMD = 't';                             // character to update default register values for DAC initialization
char filterIntervalCMD = 'T';                       // character to update interval used for transfer/collection of ions
char fineSatusCMD = 'Y';                              // character used to request status blocks
char intervalCMD = 'i';                               // character to set current operational interval
char helpCMD = 'h';                                   // define character to list commands via serial
char statusCMD = 's';                                 // define character to print system status via serial
char scanStartFreqCMD = '<';
char scanStopFreqCMD = '>';
char scanDeltaFreqCMD = 'M';
char filterDurationCMD = 'b';
char filterFreqCMD = 'B';
char DACFilterDuty0CMD = 'n';
char DACFilterDuty1CMD = 'N';
char idCMD = '?';                                     // define character used to identify the connected system
```

Figure 7.7 Mostly complete list of one character commands and their intended function.

7.2.2 Instrument Interval Section

As mentioned above, the main looping function, void loop(), cycles through several functions which correspond to the instrument interval cycles (trapping, isolation/exclusion, analysis, crapping, etc.). Not all of the intervals are used, and the last line of each interval points to then next in the cycle by means of pre-defined variables (e.g., scanInterval = 4). A description of each interval's function currently used will be given below.

```
void loop()
{
  if (interval == 0)
  {
    interval0();
  }

  else if (interval == 1)
  {
    interval1();
  }

  else if (interval == 2)
  {
    interval2();
  }

  else if (interval == 3)
  {
    interval3();
  }

  else if (interval == 4)
  {
    interval4();
  }

  else if (interval == 5)
  {
    interval5();
  }

  else if (interval == 6)
  {
    interval6();
  }

  else if (interval == 7)
  {
    interval7();
  }
}
```

```
/*/////////////////////////////////////////
  INTERVAL CODE
  ////////////////////////////////////////....

void interval0()  //Exit Loop Interval
{
  digitalWrite(visual0, HIGH);
  if (Serial.available() > 0)
  {
    readSerialData();
  }
  digitalWrite(visual0, LOW);
}

void interval1()  //Enter Loop Interval
{
  digitalWrite(visual0, HIGH);
  if (Serial.available() > 0)
  {
    readSerialData();
  }
  else if (interval != 0)
  {
    interval = trappingInterval;
  }
  digitalWrite(visual0, LOW);
}
```

```
void interval2() //Mass Collection Trapping Interval
{
  Serial.print("Trapping for ");
  Serial.print((trapDuration));
  Serial.print("ms at ");
  Serial.print(trapFreq / 1000);
  Serial.print("kHz with ");
  Serial.print(DACTrapDuty2 * 100);
  Serial.print("%/");
  Serial.print(DACTrapDuty3 * 100);
  Serial.println("% Duty Cycle");
  volatile int trapDurationDummy = trapDuration * 1000;   /

  DACCMD2 = DACcalcVari(calAmp2, calCor2, DACTrapDuty2, 2);
  DACCMD3 = DACcalcVari(calAmp3, calCor3, DACTrapDuty3, 1);
  commandSyncFreqChange(trapFreq, DDSAND1);
  syncUpdateDDS(xfrFltDDSmask);
  cmdDACSyncOut(DACXFROutputCMD, DACCS2, DACCMD2);
  cmdDACSyncOut(DACXFROutputCMD, DACCS3, DACCMD3);
  latchFilterDACs();
  //digitalWrite(signal42, HIGH);
  microsDelay(trapDurationDummy);
  interval = scanInterval;

}
```

Figure 7.8 a) void loop() function, b) interval 0, and c) interval 1 code.

Figure 7.8 section **a** display the main void loop() interval, which checks the current value of the "interval" variable and runs the corresponding function. Important to note that Arduino, and by extension C++, software code is compiled all at once meaning that the interval functions are called in void loop() but are not defined until the end of the overall code. Section **b** shows the exit loop interval. The "i" one character command is used to override the current value of the "interval" variable, thus jumping to particular intervals. Every interval used in the instrument cycle, point toward another interval, thus the previous interval will lead to another interval being executed. The effect is an endless loop of intervals (e.g., 2 → 3 → 4 → 5 → 2, etc.). At any point via user input (i.e., "i0" command), the interval variable is overwritten to 0, thus breaking the instrument cycle. Interval 1 is also shown in section **b** which is the start loop interval, such that inputting the "i1" command will return the instrument cycle to operation. Section **c** shows the trapping interval, which consists of taking the main LVWFG output to the trapping square wave (i.e., 700 kHz 50/50 duty cycle).

Figure 7.9 shows the third interval, which houses the optional mass isolation or mass exclusion intervals. Originally, these two functionalities, mass isolation and exclusion, were separated into two separate interval functions. Once the proof-of-concept for both ion manipulation techniques were proved, these functions were never used. Both isolation and exclusion are never used in conjunction because in the current instrument regime they are unused. Instead, both functionalities were thrown into one interval to save space. Switching between the two, at the time of writing, involved commenting out, via "//", either the middle section (mass isolation) or bottom section (exclusion). In the future these techniques should be re-separated into different functions and given proper variable designations.

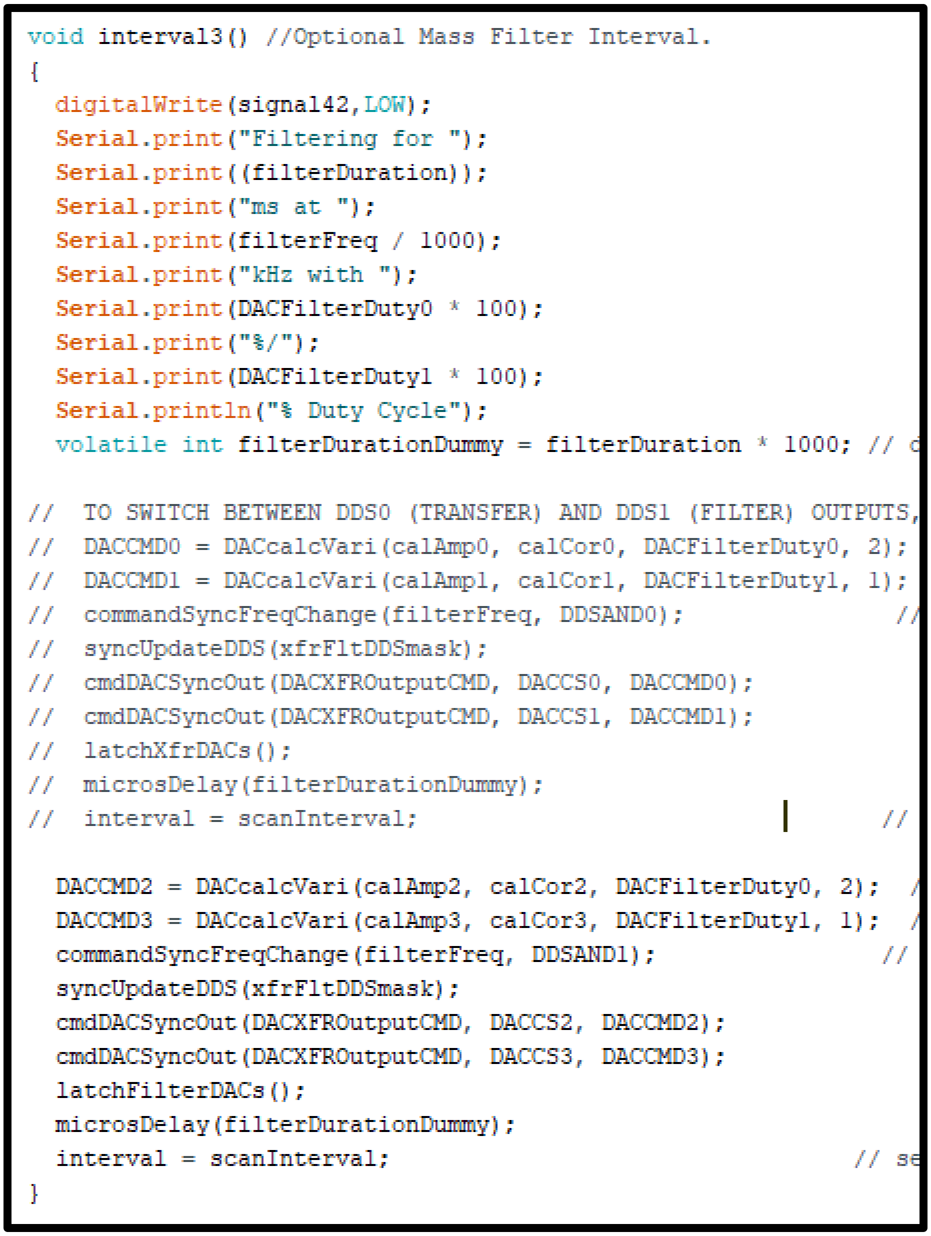

```
void interval3() //Optional Mass Filter Interval.
{
  digitalWrite(signal42,LOW);
  Serial.print("Filtering for ");
  Serial.print((filterDuration));
  Serial.print("ms at ");
  Serial.print(filterFreq / 1000);
  Serial.print("kHz with ");
  Serial.print(DACFilterDuty0 * 100);
  Serial.print("%/");
  Serial.print(DACFilterDuty1 * 100);
  Serial.println("% Duty Cycle");
  volatile int filterDurationDummy = filterDuration * 1000; // c

//  TO SWITCH BETWEEN DDS0 (TRANSFER) AND DDS1 (FILTER) OUTPUTS,
//  DACCMD0 = DACcalcVari(calAmp0, calCor0, DACFilterDuty0, 2);
//  DACCMD1 = DACcalcVari(calAmp1, calCor1, DACFilterDuty1, 1);
//  commandSyncFreqChange(filterFreq, DDSAND0);               //
//  syncUpdateDDS(xfrFltDDSmask);
//  cmdDACSyncOut(DACXFROutputCMD, DACCS0, DACCMD0);
//  cmdDACSyncOut(DACXFROutputCMD, DACCS1, DACCMD1);
//  latchXfrDACs();
//  microsDelay(filterDurationDummy);
//  interval = scanInterval;                                 //

  DACCMD2 = DACcalcVari(calAmp2, calCor2, DACFilterDuty0, 2);  /
  DACCMD3 = DACcalcVari(calAmp3, calCor3, DACFilterDuty1, 1);  /
  commandSyncFreqChange(filterFreq, DDSAND1);                //
  syncUpdateDDS(xfrFltDDSmask);
  cmdDACSyncOut(DACXFROutputCMD, DACCS2, DACCMD2);
  cmdDACSyncOut(DACXFROutputCMD, DACCS3, DACCMD3);
  latchFilterDACs();
  microsDelay(filterDurationDummy);
  interval = scanInterval;                                 // se
}
```

Figure 7.9 Arduino Interval 3 function containing the mass isolation or mass exclusion.

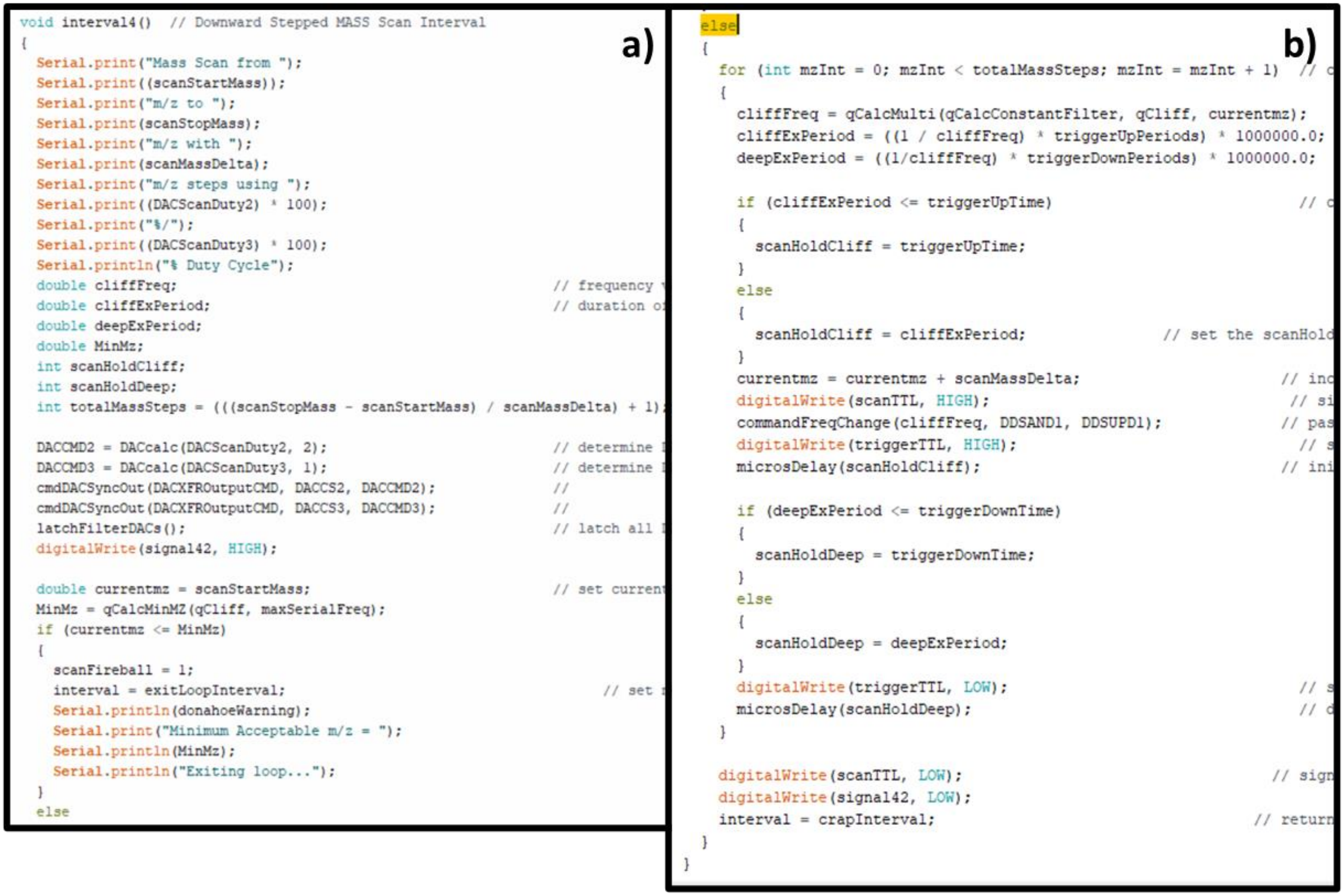

```
void interval4()  // Downward Stepped MASS Scan Interval
{
  Serial.print("Mass Scan from ");
  Serial.print((scanStartMass));
  Serial.print("m/z to ");
  Serial.print(scanStopMass);
  Serial.print("m/z with ");
  Serial.print(scanMassDelta);
  Serial.print("m/z steps using ");
  Serial.print((DACScanDuty2) * 100);
  Serial.print("%/");
  Serial.print((DACScanDuty3) * 100);
  Serial.println("% Duty Cycle");
  double cliffFreq;                                          // frequency
  double cliffExPeriod;                                      // duration o
  double deepExPeriod;
  double MinMz;
  int scanHoldCliff;
  int scanHoldDeep;
  int totalMassSteps = (((scanStopMass - scanStartMass) / scanMassDelta) + 1)

  DACCMD2 = DACcalc(DACScanDuty2, 2);                        // determine
  DACCMD3 = DACcalc(DACScanDuty3, 1);                        // determine
  cmdDACSyncOut(DACXFROutputCMD, DACCS2, DACCMD2);           //
  cmdDACSyncOut(DACXFROutputCMD, DACCS3, DACCMD3);           //
  latchFilterDACs();                                         // latch all
  digitalWrite(signal42, HIGH);

  double currentmz = scanStartMass;                          // set curren
  MinMz = qCalcMinMZ(qCliff, maxSerialFreq);
  if (currentmz <= MinMz)
  {
    scanFireball = 1;
    interval = exitLoopInterval;                                // set
    Serial.println(donahoeWarning);
    Serial.print("Minimum Acceptable m/z = ");
    Serial.println(MinMz);
    Serial.println("Exiting loop...");
  }
  else
```

```
  else
  {
    for (int mzInt = 0; mzInt < totalMassSteps; mzInt = mzInt + 1)  //
    {
      cliffFreq = qCalcMulti(qCalcConstantFilter, qCliff, currentmz);
      cliffExPeriod = ((1 / cliffFreq) * triggerUpPeriods) * 1000000.0;
      deepExPeriod = ((1/cliffFreq) * triggerDownPeriods) * 1000000.0;

      if (cliffExPeriod <= triggerUpTime)                            //
      {
        scanHoldCliff = triggerUpTime;
      }
      else
      {
        scanHoldCliff = cliffExPeriod;                 // set the scanHold
      }
      currentmz = currentmz + scanMassDelta;                         // inc
      digitalWrite(scanTTL, HIGH);                                    // si
      commandFreqChange(cliffFreq, DDSAND1, DDSUPD1);                // pas
      digitalWrite(triggerTTL, HIGH);                                 // s
      microsDelay(scanHoldCliff);                                    // ini

      if (deepExPeriod <= triggerDownTime)
      {
        scanHoldDeep = triggerDownTime;
      }
      else
      {
        scanHoldDeep = deepExPeriod;
      }
      digitalWrite(triggerTTL, LOW);                                  // s
      microsDelay(scanHoldDeep);                                      // d
    }

    digitalWrite(scanTTL, LOW);                                     // sign
    digitalWrite(signal42, LOW);
    interval = crapInterval;                                       // return
  }
}
```

Figure 7.10 Arduino interval 4 function containing stepwise mass analysis functionality.

Both sections **a** and **b** of **Figure 7.10** showcase the downward stepped frequency mass analysis interval. The “else” line at the end of section **a** is continued at the top of section **b**. This interval initialized some local variables, calculates the total number of m/z steps, sets the duty cycle values of the X-axis and Y-axis outputs, then via a FOR loop, sequentially changes the frequency based on the current m/z step. The MinMz is a (not shown) function which calculated the minimum start m/z value based on the “maxFrequency” variable to ensure no damage to the HVHF circuit occurs. The “cliffFreq” runs a function which is the re-arrangement of the Mathieu *q* equation solving for frequency as a function of m/z. Next the frequency is changed, and a wait period dependent on the number of periods is accomplished via the “microsDelay” function, set by user input command, is used to keep the frequency at the current value. This process is repeated until no more m/z steps are present. The “crapInterval” is not shown, but it is identical to interval 2, except the frequency and duty cycle are set to a very low frequency and very high duty cycles to clear the ion trap between instrument cycles.

Figure 7.11 visualizes what the user input commands look like while operating the LDIT. Via Arduino’s “Serial Monitor” functionality, a dialog box-based GUI allows for various variable controls of the LVWFG firmware. A list of these functions was given above. Section **a** displays the command, “i1”, to enter the instrument cycle. A cycling display of various interval parameters, such as trap duration, start m/z, interval specific duty cycles, and more are shown. Section **b** provides an example of the frequency information diagnostic interval. This interval is identical to the mass analysis interval, except it outputs exactly which frequencies the LVWFG is outputting each m/z step, along with some the calibration variables. This interval is not in the instrument cycle and is self-terminating (i.e., returns to interval 0). Section **c** shows the “s” command which prints the current value of various variables used in operation and example command formatting for how to change variables.

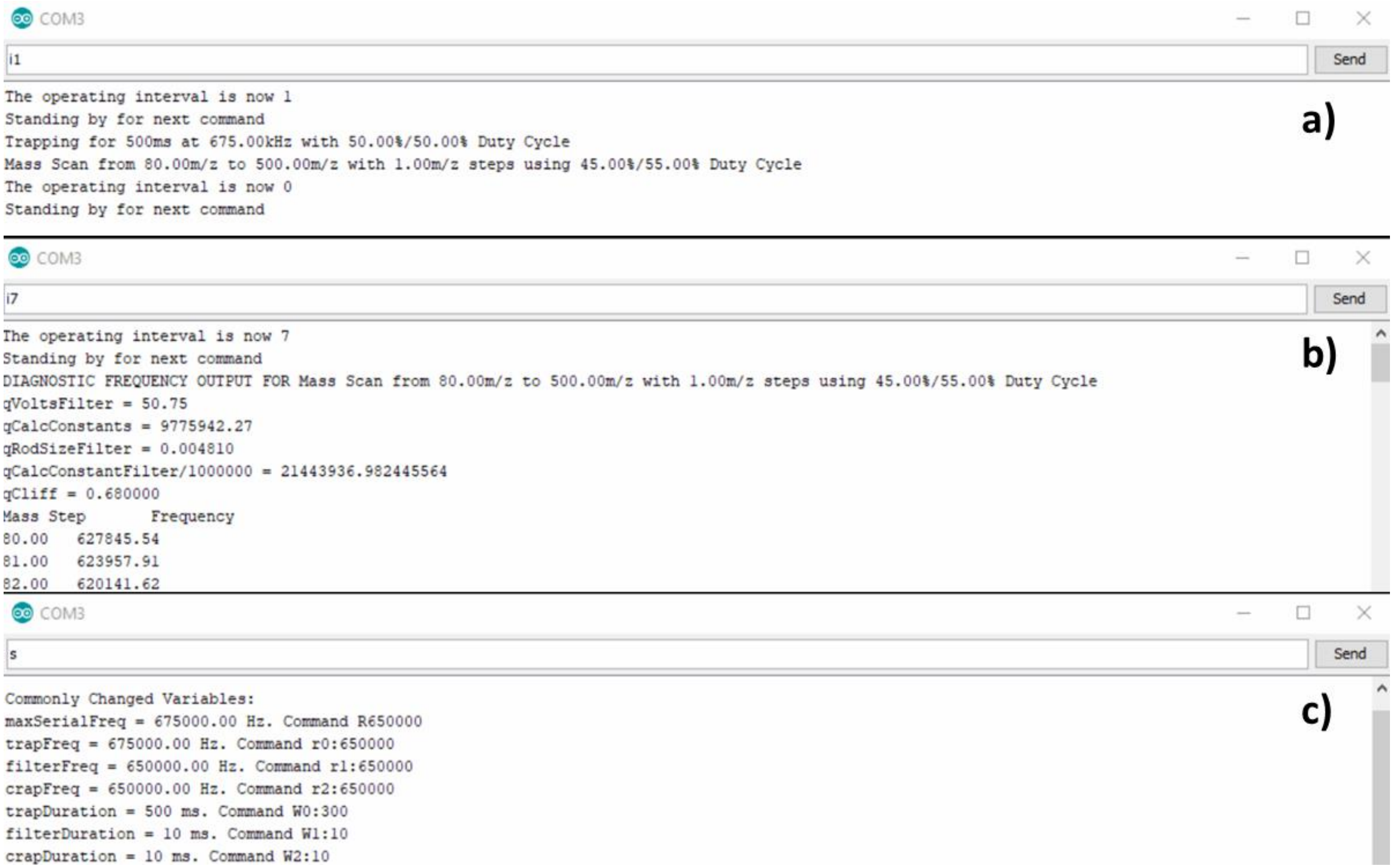

```
i1
```

```
The operating interval is now 1
Standing by for next command
Trapping for 500ms at 675.00kHz with 50.00%/50.00% Duty Cycle
Mass Scan from 80.00m/z to 500.00m/z with 1.00m/z steps using 45.00%/55.00% Duty Cycle
The operating interval is now 0
Standing by for next command
```

```
i7
```

```
The operating interval is now 7
Standing by for next command
DIAGNOSTIC FREQUENCY OUTPUT FOR Mass Scan from 80.00m/z to 500.00m/z with 1.00m/z steps using 45.00%/55.00% Duty Cycle
qVoltsFilter = 50.75
qCalcConstants = 9775942.27
qRodSizeFilter = 0.004810
qCalcConstantFilter/1000000 = 21443936.982445564
qCliff = 0.680000
Mass Step       Frequency
80.00   627845.54
81.00   623957.91
82.00   620141.62
```

```
s
```

```
Commonly Changed Variables:
maxSerialFreq = 675000.00 Hz. Command R650000
trapFreq = 675000.00 Hz. Command r0:650000
filterFreq = 650000.00 Hz. Command r1:650000
crapFreq = 650000.00 Hz. Command r2:650000
trapDuration = 500 ms. Command W0:300
filterDuration = 10 ms. Command W1:10
crapDuration = 10 ms. Command W2:10
```

Figure 7.11 Example user input and outputs via the Arduino "Serial Monitor" functionality.

Section 7.3 Electric Circuit PCBs, BoM, etc.

At the time of writing, access to a currently version of the HVHF circuit can be found with Blaise Thompson and Gina Roesch. Blaise offered to update the KiCAD file for this circuit, in an effort to accommodate new design changes to the board. There is a KiCAD file on the Garand group server under "Garand Group/ElectronicsCircuits/PCBs/NEW High Voltage High Frequency" that has the GERBER files required to print a new HVHF circuit. There was no accompanying circuit diagram during the last communication with Blaise. Gina Roesch has the most up-to-date BoM for this design. A fairly robust explanation of how the major components of this circuit function was given in **Chapter 3**. Additionally, the circuit diagram of KiCAD was never properly used by myself or Nathan Hoffman, the original author. An outdated BoM is provided at "Garand Group/ElectronicsCircuits/Bill of Materials/HVHF.xlsx".

For the LVWFG, the KiCAD information can be found at in the same PCBs folder of the Garand group server, "Garand Group/ElectronicsCircuit/PCBs/Low Voltage Waveform Generator" and the BoM can be found at "Garand Group/ElectronicsCircuit/Bill of Materials/LVWFG.xlsx". These circuits have not been altered since the original ordering and assembly. A detailed overview of how the LVWFG generated square waves was given in **Chapter 3**. Some subsections of the KiCAD circuit diagram is shown below.

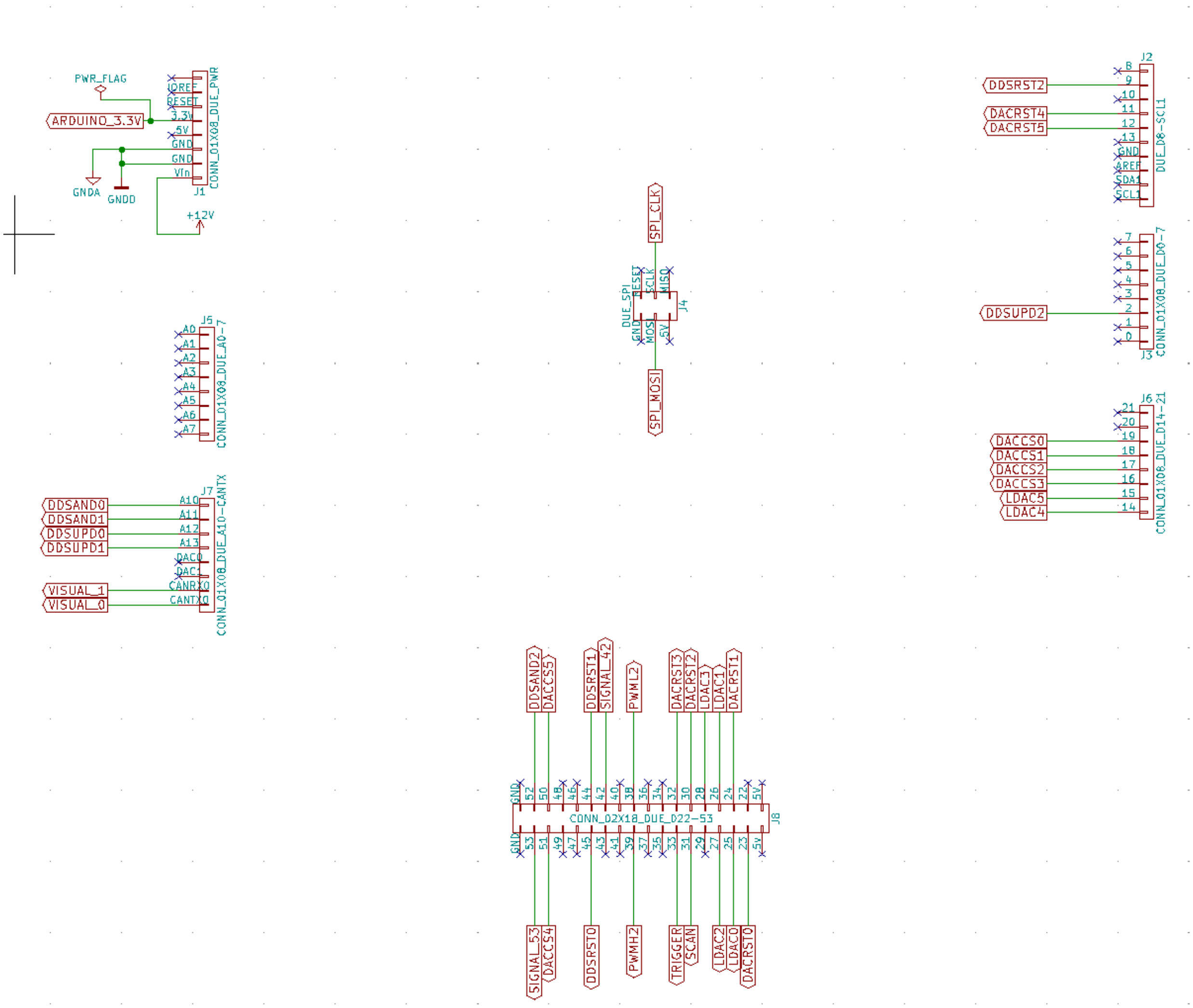

Figure 7.12 LVWFG Arduino Due pinout with labels.

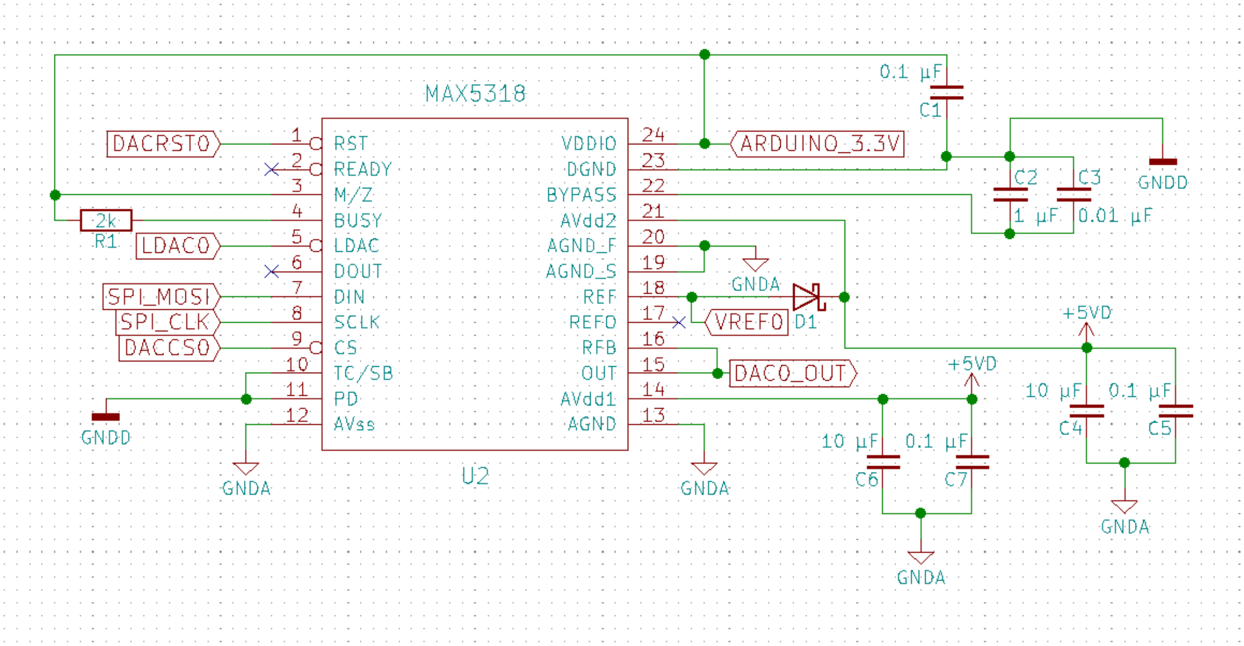

Figure 7.14 LVWFG DAC module with labels. One of six (remaining 5 not shown).

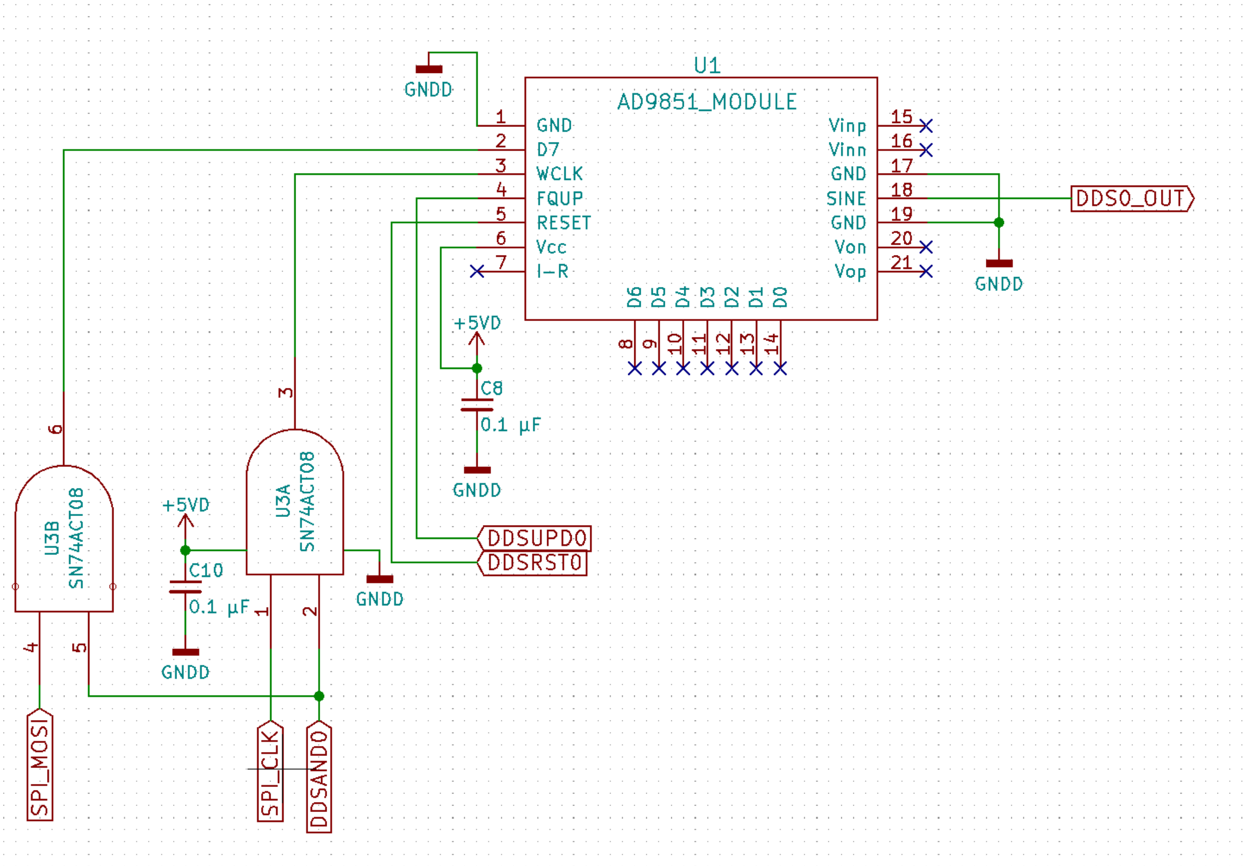

Figure 7.13 LVWFG DDS module with labels. One of three (remaining two not shown).

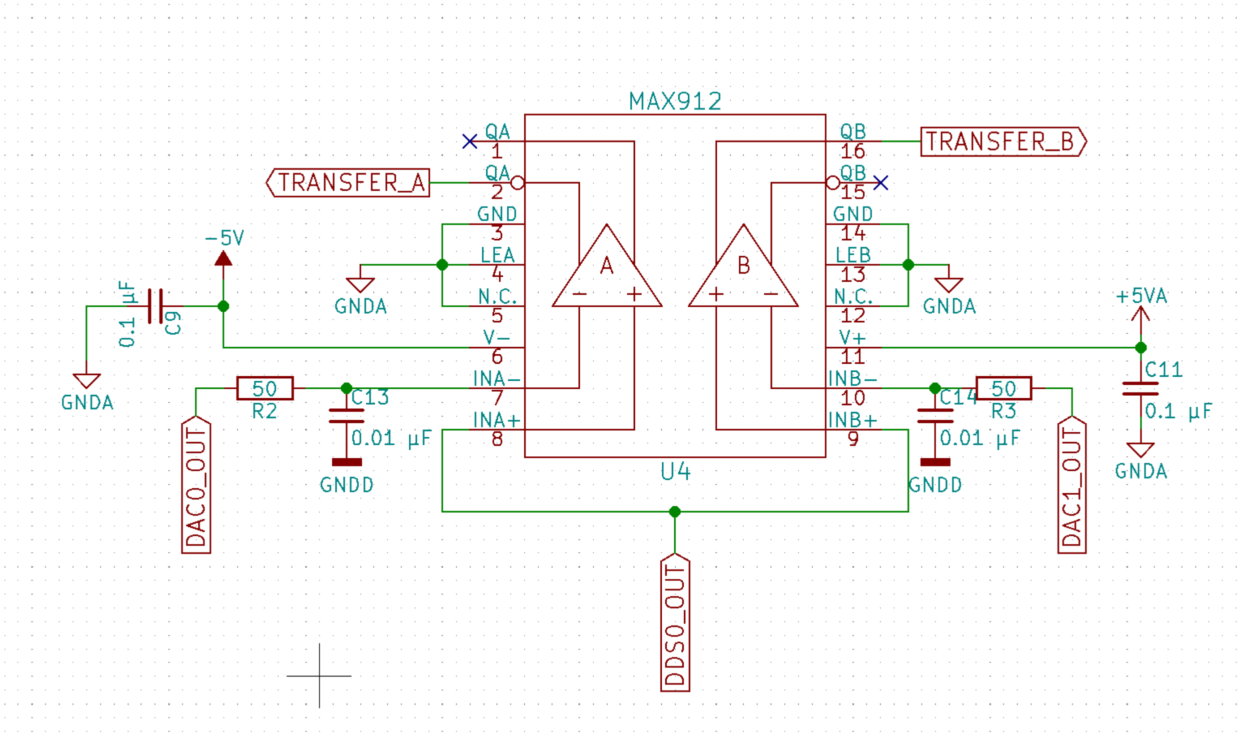

Figure 7.15 LVWFG high speed dual channel comparator with labels. One of three (remaining two not shown).